Sustainable Bio-based Adsorptive Concrete for Phosphorus Removal

DESIGN, PERFORMANCE AND DURABILITY

Fan Wu

Bouwstenen 371

Sustainable Bio-based Adsorptive Concrete for Phosphorus Removal

DESIGN, PERFORMANCE AND DURABILITY

Fan Wu

CIP-DATA LIBRARY TECHNISCHE UNIVERSITEIT EINDHOVEN

Sustainable Bio-based Adsorptive Concrete for Phosphorus Removal: Design, Performance and Durability / by Fan Wu

A catalogue record is available from the Eindhoven University of Technology Library

ISBN: 978-90-386-5839-1

Bouwstenen 371

NUR 955

Copyright © 2023 by Fan Wu

Cover design: Fan Wu

Ph.D. thesis, Eindhoven University of Technology, the Netherlands

All rights reserved. No part of this publication may be reproduced in any form or by any means without permission in writing form from the author.

Sustainable Bio-based Adsorptive Concrete for Phosphorus Removal

DESIGN, PERFORMANCE AND DURABILITY

PROEFSCHRIFT

ter verkrijging van de graad van doctor
aan de Technische Universiteit Eindhoven,
op gezag van de rector magnificus, prof.dr. S.K. Lenaerts,
voor een commissie aangewezen door het College voor Promoties,
in het openbaar te verdedigen op dinsdag 19 December om 13:30 uur

door

Fan Wu

geboren te Chongqing, China

Dit proefschrift is goedgekeurd door de promotoren en de samenstelling van de promotiecommissie is als volgt:

Voorzitter:	Prof. dr. ir. T.A.M. Salet
1e Promotor:	Prof. dr. ir. H.J.H. Brouwers
2e Promotor:	Prof. dr. Q.L. Yu (Wuhan University)
Co-promotor:	Dr. F. Gauvin
Promotiecommissieleden:	Prof. dr. H. Justnes (Norwegian University of Science and Technology)
	Prof. dr. W. Chen
	Prof. dr. S. Amziane (Université Clermont Auvergne)
	Prof. dr. S.R. van der Laan

Het onderzoek of ontwerp dat in dit proefschrift wordt beschreven is uitgevoerd in overeenstemming met de TU/e Gedragscode Wetenschapsbeoefening.

For my family

Do one thing at a time, and do it well.

Preface

My learning journey in the building materials group (TU/e) began in October 2018. Looking back, I am glad that I chose such a beautiful country for PhD studies. For the past several years, we have shared unforgettable memories here with the building materials group. The people I meet and the knowledge I gain here will be a treasure in my whole life. I could not have finished this thesis without all of your assistance.

I would like to appreciate Prof. H.J.H. (Jos) Brouwers, for giving me this unique learning opportunity, which changed the track of my life. In scientific research, you provided me with many invaluable suggestions and good working environments. Your assistance is indispensable for this thesis to be completed successfully. You spent more time revising my thesis and teaching me presentation skills many times. You inspired me with an optimistic attitude toward life and a hardworking attitude toward work. I will keep "*If Man Works Hard the Land Will Not Be Lazy*" in mind for my future work.

I would like to appreciate Prof. Qingliang Yu, for his invaluable assistance with this thesis and the application for the China Scholarship Council (CSC) Scholarship. Furthermore, I want to thank you for devoting your time to revising each paper. I have learned a lot from your feedback. You not only taught me how to write a scientific paper but also how to apply for scientific funding. These experiences I learned from you will be beneficial to my entire scientific career. You are like a guiding light for me, illuminating the path of my PhD studies and consistently providing assistance in my work.

I am grateful to Prof. Changwu Liu from Sichuan University for encouraging me to study abroad, for his guidance while I was studying at Sichuan University, and for his fatherly care in my life and career.

I am deeply thankful to Prof. Xiaoqing Chen from the Institute of Mountain Hazards and Environment (IMHE), Chinese Academy of Sciences (CAS), for fully supporting me to continue my studies at TU/e.

I would like to extend my sincere gratitude to Dr. F. (Florent) Gauvin for revising my manuscripts and providing assistance with the SEM training. I appreciate the opportunity to collaborate with Dr. dipl.-min. (Katrin) K. Schollbach, Prof. Sieger van der Laan, Dr. M.V.A. (Miruna) Florea, Dr. Nataliya Lushnikova and Prof. Alex van Herk in our group.

A special thanks to Ing. A.C.A. (Anneke) Delsing, who performed many IC tests for

me, I would not have been able to complete the most important part of my thesis (P-removal test) without your assistance. The same thanks to Ing. H.L.W. (Harrie) Smulders, Ing. Wout van Bommel for their assistance with the testing equipment. I would like to thank our previous secretaries, Mrs. L. (Leontine) Harmsen, Mrs. N. (Nathaly) Rombley, Mrs. Astrid Kemps, and our current secretaries, Mrs. Manon van Run, for creating a home-like office environment for us.

My gratitude to the professors who accepted to serve on my promotion committee: Prof. H. Justnes (Norwegian University of Science and Technology), Prof. W. Chen (Wuhan University of Technology, Eindhoven University of Technology), Prof. S. Amziane (Université Clermont Auvergne) and Prof. S.R. van der Laan (Tata Steel, Eindhoven University of Technology). Thank you all for taking the time to read and evaluate my work.

I would like to express my heartfelt gratitude to all of my friends from the Eindhoven University of Technology, who have provided me with invaluable assistance during my experiments and unforgettable memories of my abroad life. Thank you, Qadeer Alam and Veronica Caprai, for showing me an impressive Dutch PhD defense, which was the first defense I attended at the TU/e. Thank you, Peipeng Li, Yangyueye Cao and Gang Liu, for teaching me how to use many testing equipments in our laboratory. Thank you, Zhenyao Qu, for sharing with me the colourful PhD life in Eindhoven. Thank you, my neighbour, Hoss Karimi, for showing me a lovely life abroad and taking me to various lunch places in Eindhoven. Thank you, Yan Luo and Tao Liu, for taking me to collect the best road trip memories in Iceland together. Thank you, Jinyang Li, we had a wonderful road trip during the summertime in Norway. Thank you, Xuan Ling and Yanjie Tang, for teaching me a lot about chemical analysis knowledge. Thank you, my friends, Changliang Ye and Jianing Zhao, for helping me in my abroad life and sharing many beautiful sceneries in Europe. My sincere gratitude to all of my colleagues and friends: Anna, Ce Zhang, Huarong Li, Jawad, Kinga, Katerina, Kate, Perry, Shaohua Li, Xiaoxiao Zhang, Winnie Franco, Yuxuan Chen, Yuri, Zixiao Wang, Alex, Beatrice, Ceren, Charles, Daoru Liu, Felix, Helong Song, Iris, Jia He, Jiale Yuan, Jonathan, Leila, Marc, Marina, Naomi, Quan Liu, Ricardo, Samantha, Samuel, Shashank, Yanshuo Liu, Zixing Liu, Zhihan Jiang. It is my honour to work with all of you. I wish you all the best of luck and a wonderful life in future.

Eindhoven, February 2023

Fan Wu

Summary

Urban surfaces such as streets, parking lots and roofs are regarded as critical channels for contaminant transport from stormwater to nearby rivers. Various pollutants such as nitrate (N), phosphate (P), and heavy metals are carried by stormwater runoff to enter nearby rivers during the rainy season. Among these pollutants, P is one of the main pollutants from farmland, industry, domestic sewage and atmospheric pollution sediments, that cause eutrophication and algae blooms in water bodies. Recently, conventional pervious concrete has gained increasing attention for pollutant removal from stormwater runoff. However, the application of coarse aggregates without any adsorption capacity in pervious concrete is one of the major reasons for poor pollutant removal performance. Furthermore, the mechanical strength of the pervious concrete is rather low because of the single-graded aggregate structure. Besides, pervious concrete frequently comes into contact with polluted water, resulting in poor durability. Motivated by the above issues, this work aims to develop a bio-based adsorptive concrete that can reduce accelerated runoff, simultaneously remove pollutants and improve the quality of underlying soil water, focusing on its mechanical properties, adsorption performance and durability. This work can be condensed into the following three main sections:

In the first section, the selection and modification of highly adsorptive cementitious composites are investigated. Miscanthus (*x* giganteus) is modified using physical treatment (ball milling) and heat treatment methods. Heat-treated miscanthus has a positive influence on the compressive strength of miscanthus mortar. Powdery and long-fibre miscanthus are the recommended forms for using miscanthus in bio-based mortar in terms of low drying shrinkage, good thermal conductivity and mechanical strength. Furthermore, P-adsorption experiments are carried out to evaluate the P-removal capacity of several granular aggregates for potential application in highly adsorptive concrete, including industrial by-product (basic oxygen furnace steel slag), lightweight aggregate (expanded silicate), and bio-based material (miscanthus). Furthermore, basic oxygen furnace steel slag is combined with porous expanded silicate using a non-sintered pelletizing method to produce sustainable highly adsorptive aggregates, and miscanthus is added to further increase its porosity. The manufactured adsorptive aggregate has good mechanical strengths, high P-removal capacity, and excellent resistance to salt and freeze-thaw cycles, making it suitable for use as a highly adsorptive aggregate in adsorptive concrete.

In the second section, the structure optimization, mix design and adsorption performance of bio-based adsorptive concrete are investigated to enhance the

mechanical properties and adsorption performance of adsorptive concrete. A porous adsorptive paste is created by combining chemisorption and physisorption mechanisms to improve the adsorption performance. The adsorptive cement paste has an adsorption amount of 30.4-74.2 mg/g, at a corresponding P-concentration of 1215-2967 mg/L. This is attributed to the Ca^{2+} leached from the adsorptive cement paste reacting with the phosphate in solution to form Ca-P precipitates. A two-sized aggregate skeleton structure is proposed to improve the mechanical strength, adsorption performance and freeze-thaw resistance of adsorptive concrete. This is achieved by the small-sized steel slag filling the pores between the aggregates, reducing the porosity and permeability of adsorptive concrete. The Langmuir model and Elovich model can be used to fit the adsorption isotherm and kinetic results. Furthermore, the developed adsorptive concrete has a low P-releasing capacity, indicating that there is no secondary environmental risk.

In the third section, the long-term performance of bio-based miscanthus mortar is investigated. The major factor that limits the durability of miscanthus mortar is the natural degradation behaviour of miscanthus fibre. The mechanical strength degradation of miscanthus mortar mainly takes place in the first month after being soaked in water. Heat-treated miscanthus fibre can improve compressive and flexural strengths by 83% and 27%, respectively, as well as reduce the drying shrinkage, with a reduction of up to 25% at 90 days, compared to untreated miscanthus, because of the increased degree of cement hydration, reduced porosity and enhanced compatibility with the cement paste. Furthermore, heat-treated miscanthus fibre can promote cement hydration and strength development, improve the dimensional stability of miscanthus mortar and make it more durable in mortar.

Contents

Chapter 1 Introduction

1.1 Background

Human activities have a growing negative impact on the aqueous environment as industrialization and urbanization process [1]. Approximately 80% of the world's population is facing water scarcity [2], poor water quality and water pollution, which eventually becomes one of the world`s major environmental issues [3]. Urban surfaces such as streets, parking lots, and roofs are regarded as critical channels for contaminant transport [4,5]. Pollutants are usually transferred by three stages before causing water pollution: pollutant formation, runoff transfer, and pollutant accumulation (**Fig. 1.1**). Various pollutants such as fertilizers, pesticides, and heavy metals, enter directly into nearby rivers transferred by stormwater runoff during the rainy season, [6], posing a threat to ecological safety and public health [7].

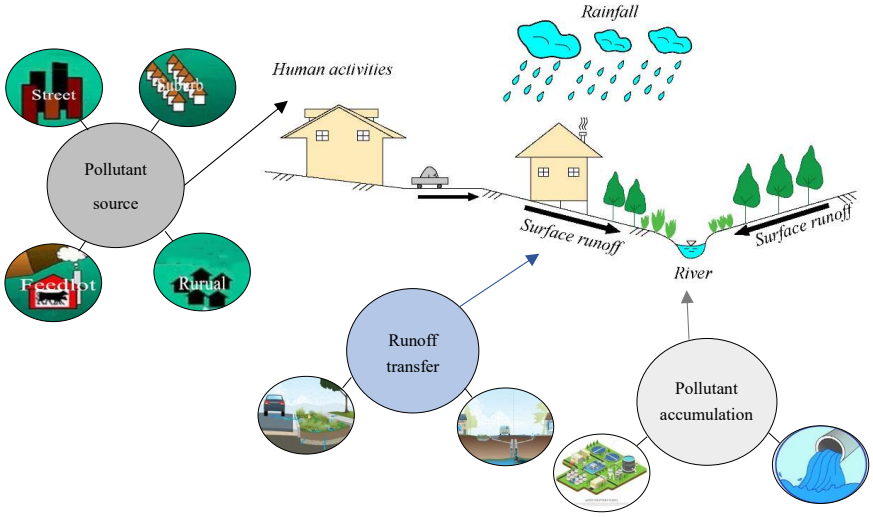

Fig. 1.1 Pollutant transfer process from the road surface to a nearby water body.

Stormwater runoff from urban catchment areas is the primary pathway for pollutants to be transferred from the pavement surface to a water body. Phosphate (P) is one of the main pollutants from farmland, industry, domestic sewage and atmospheric pollution sediments, etc. [8]. When the concentration of P in the water exceeds 0.03 mg/L, algae and aquatic plants grow at an abnormally fast rate, reducing the quality of the water [9]. Previous research indicates that stormwater runoff transports 75-90 % of P [10]. Therefore, avoiding accelerated stormwater runoff and removing P from stormwater

runoff is critical for providing underlying soil water and improving its water quality in ecological city construction.

Adsorption performance of traditional pervious concrete has recently gained attention for removing pollutants from stormwater runoff, [11–13]. Stormwater runoff is filtered from the road surface to the underlying soil layer and reused for urban flood management when pervious concrete is used. The pollution level of the water body caused by stormwater runoff will be significantly reduced if pollutants from stormwater runoff can be effectively removed by adsorption and physical filtration of pervious pavement. Previous research has shown that pervious concrete can adsorb a variety of pollutants during the rainwater infiltration process, including P [11], heavy metals (Mn, Co and Ni, etc.) [13], and fecal coliforms [14]. Therefore, pervious concrete has a high potential for removing pollutants from stormwater runoff.

Crushed rock (basalt, limestone, etc.) is commonly used as coarse aggregates in pervious concrete. Because crushed gravel lacks adsorption ability, traditional pervious concrete has poor adsorption performance, with a long reaction time and low adsorption capacity [15]. The poor reaction between the mortar matrix and the pollutants is responsible for low adsorption capacity. Furthermore, the strength of single-graded pervious concrete is very low, usually less than 15 MPa. Moreover, long-term contact with polluted water reduces the durability of pervious concrete. More importantly, the original purpose of pervious concrete is not to remove pollutants, rather, it is designed to allow stormwater runoff to pass through it, reducing urban flooding and reusing stormwater. In the face of rising stormwater pollution, traditional pervious concrete no longer meets the requirements of sustainable development of ecological cities for pollutant removal from stormwater. It is hypothesized that replacing conventional aggregates with highly adsorptive aggregates will potentially improve the adsorption capacity of concrete and meet pollutant removal requirements.

Miscanthus (*x* giganteus) (M) is a perennial biomass energy crop that is widely grown in Europe due to its being highly efficient in using water, nitrogen and sunlight [16,17]. In comparison to other natural fibres such as straw and hemp, the M fibre is considered strong and has adequate firmness and thermal insulating properties. Furthermore, M is a high-yielding renewable material with environmentally friendly properties. M is commonly used as a natural fibre for bio-based concrete due to its lightweight and porous properties [18]. Furthermore, M is a natural and porous material that can be used as an adsorbent material. Heat-treated bio-based material (biochar) is a charcoal-like product that results from the thermochemical conversion of organic materials or biomass in an oxygen-limited environment. The porosity of the biochar gives it a high

specific surface area, which allows it to remove contaminants from aqueous solutions such as heavy metals, organics, and total suspended solids. Therefore, it is reasonable to expect the application of these porous bio-based materials will improve the adsorption performance of concrete.

1.1.1 Waste materials applied as adsorbents for wastewater treatment

- *Bio-based materials applied as an adsorbent for pollutant removal*

Currently, various bio-based materials have been investigated as low-cost adsorbents for pollutant removal [19–21], including the shells and stones of fruits such as nuts, peanuts, olive wastes, almonds, apricot kernel shells, and cherries, also cereal wastes such as rice, maize and corn, as well as sugar cane bagasse and coir pith. These bio-based materials are typically used in their natural form or after some physical or chemical modification [22]. Previous research has shown that bio-based material has an adsorption capacity and can absorb nitrate, phosphate, heavy metals, suspended solids and other containments, etc. This is due to the well-developed micropores of these bio-based adsorbents for the physical adsorption of pollutants from an aqueous solution [23,24]. Bio-based materials are viable options for wastewater purification because of their unique chemical composition [25,26], availability in abundance, renewable nature, and low cost.

The adsorption capacity of pyrolyzed bio-based materials has been investigated in the last decades to improve the adsorption capacity of bio-based materials. Heat-treated bio-materials are carbon-rich, porous, with oxygen functional groups and aromatic surfaces, and have a good capacity for adsorption. Large specific surface area, porous structure, and surface functional groups of heat-treated bio-materials are the important features promising high contaminant removal efficiencies, with a wide application in constructed wetlands. Heat-treated bio-materials with micropore structure and high surface area can provide active sites for redox reactions, adsorption, and support microbial activities, resulting in overall greater wastewater treatment efficiency. However, very few studies have been conducted to investigate the use of heat-treated bio-materials in concrete for the production of porous adsorptive concrete.

- *Industrial waste materials applied as an adsorbent for pollutant removal*

In recent years, the adsorption properties of industrial by-products such as Basic Oxygen Furnace (BOF) steel slag (SS), fly ash and expanded clay have been investigated [27–29]. Among these materials, SS has a high adsorption capacity for pollutants and has been used as a water purification filter [30–32]. Basic Oxygen

Furnace (BOF)-steel slag is the main metallurgical by-product during the steelmaking process [33,34], which contains a high content of CaO, Fe_2O_3, SiO_2 and a minor amount of MgO, MnO, Al_2O_3, and other elements [35,36]. The main mineral components of SS are C_3S, C_2S, C_4AF, C_2F, RO phase (CaO-FeO-MnO-MgO solid solution), and free-CaO, which gives the SS cementitious properties [37,38]. Because the metal ions released by SS have an affinity for some anions in pollutants, the SS has been used as an adsorbent for pollutant removal. For example, 22.4 tons of P were removed in field wetlands during an 11-year experiment and the maximum adsorption capacity is 1.23 kg of P (per ton of steel slag) [39]. Furthermore, constructed wetlands made of SS achieve high P removal efficiency with near-neutral pH, which meets water discharge standards [40].

Chemical reactions between metal cations (e.g. Ca^{2+}, Fe^{3+} and Al^{3+}) and phosphate anion species (HPO_4^{2-} and PO_4^{3-}) are mainly removal mechanisms for P-removal [41]. Among these cations, Ca^{2+} is the most reactive ion with phosphate anion species, making it available for P-removal [42]. Ca^{2+} leached from the SS can react with phosphate in two steps [43]: first, the ion concentration of Ca^{2+} and OH^- increases due to SS dissolution, and then the Ca^{2+} and OH^- ions react with phosphate to form amorphous calcium-phosphate (Ca-P) and/or octacalcium phosphate precipitates. The driving mechanism during the P-crystallization adsorption process is primarily nucleation by precipitation of hydroxyapatite ($Ca_{10}(PO_4)_6(OH)_2$) [44], which has low solubility [30,43] and does not cause secondary pollution. Therefore, SS has a high potential for application as an ingredient to enhance the P-removal of concrete.

- *Influencing parameters of adsorption performance*

The adsorption capacity of bio-based materials is determined by microporous structure, which includes micropore volume, pore size and distribution characteristics [58]. The most important parameters that affect the total surface area of bio-based materials are absorption capability, pyrolysis temperature, and pyrolysis rate [59]. The well-developed micropore structure and high specific surface area of pyrolyzed bio-based materials allow them to absorb a variety of compounds, including heavy metals, nutrients, and other contaminants. The adsorption efficiency of heat-treated bio-materials is influenced by raw material properties, deashing treatment, pH, adsorbent dosage, competitive anions, and temperature. Furthermore, the adsorption behaviour of heat-treated bio-materials for various contaminants (e.g., heavy metals, organic matter, and other contaminants) differs and is well correlated with the properties of the contaminants. The adsorption mechanism may be affected by bio-based material properties such as surface functional groups, specific surface area, pore structure, and

mineral components.

Chemical adsorption, which is effective for specific pollutants, is attributed to the adsorption capacity of the SS [45]. Organic pollutants, nitrate, phosphate and heavy metals, for example, are commonly found in aqueous solutions. However, because of the dense structure of the SS, Ca^{2+} release from the SS is not always sufficient during P-removal [43]. Physical adsorption also plays an important role in the removal of pollutants for adsorptive aggregates in case of well-developed micropores for pollutant removal. Therefore, combining highly adsorptive SS powder with porous bio-based materials to produce artificial adsorptive aggregates with both chemical and physical adsorption capacity, not only reduces concrete cost but also improves the adsorption capacity of concrete.

1.1.2 Porous concrete applied for pollutant removal from stormwater

- *Adsorption performance of conventional porous concrete*

Previous studies have been conducted on the potential of using pervious concrete to adsorb pollutants such as P [20], heavy metals (Mn, Co and Ni, etc.) [13], and fecal coliform [21], for urban stormwater purification [19]. Furthermore, crushed concrete granules [24] and cementitious materials [25] have the potential to remove P from an aqueous solution. Titanium dioxide (TiO_2) is also applied to remove air pollutants from pervious concrete [22]. The adsorption capacity of conventional porous concrete for pollutant removal is summarized in **Table 1.1**. It is concluded that pervious concrete can be used for pollution removal. However, the adsorption capacity of traditional pervious concrete is very limited due to the lack of adsorption in gravel or sand. Moreover, even at a low initial pollutant concentration, a long reaction time is frequently required, [46]. To improve the adsorption performance of concrete, it is critical to select an adsorptive material with adequate strength and adsorption capacity.

Table 1.1 Adsorption capacity of conventional porous concrete for pollutants removal.

Types of concrete	Pollutants	Initial concentration	Removal capacity	Reaction time
Pervious concrete [13]	Cu, Co, Ni	0.1-1.3 mg/L	>75%	6 months
Fly ash pervious concrete [47]	P	2.58-3.4 mg/L	25-85%	0.5-8 hours
Iron oxide pervious concrete [11]	P	10 mg/L	>90%	72 hours
Pervious concrete [46]	Cu, Zn	20 µm/L, 100 µm/L	87%, 90%	10 cycles
Portland cement [12]	P	400 mg/L	20.75%	-
Aluminium hydroxide sand [48]	P	25 mg/L	0.239mg/g	24 hours

- *Improvement of adsorption performance of conventional porous concrete*

To improve the adsorption performance of pervious concrete, various materials with high adsorption capacity were used as concrete composites. For example, calcium sulfoaluminate cement and coal bottom ash aggregates are used to improve N and P removal of porous concrete [49]. Red mud is used in geopolymer-based porous concrete to improve heavy metal ions removal [50]. Chitosan is used to modify alkali-activated slag before it is used in porous concrete to increase the adsorption capacity for Pb removal [51]. Furthermore, because of its propensity to stimulate microbial degradation and its mechanical retention adsorption, biochar is added to porous concrete to increase the removal efficiency of N and P [52]. Mineral adsorbents (e.g. pumice, zeolite and perlite) are used as fine aggregates in porous concrete to improve water quality [53]. Generally, the adsorption capacity of concrete increases with the increase in adsorbent content used in concrete.

To achieve a porous structure and high permeability for rapid water penetration, pervious concrete is typically designed with no sand or a very small amount of sand [54]. Porous adsorptive concrete, unlike traditional pervious concrete, does not require a fast permeable function. Under saturated conditions, it only needs to allow water to slowly penetrate the concrete. Therefore, it must have some porosity, but the void is not as large as in pervious concrete. Furthermore, porous adsorptive concrete can not be completely sealed because stormwater runoff must flow into the concrete and contact the adsorbent material in order for contaminants to be removed. It is crucial to find an optimum of mechanical and adsorption properties in order to maintain good mechanical strength and high adsorption capacity. Moreover, a porous adsorption mortar should be designed using modified bio-material materials and adsorptive materials to improve the water permeability passage of the mortar and maximize its adsorption capacity.

1.1.3 Long-term performance of bio-based concrete

- *Biodegradability of bio-based materials*

The primary components of bio-based materials are cellulose, hemicelluloses and lignin. Biomass is a highly porous and water-absorption material, and extractive compounds such as starch, sugar, some phenols, and occasionally hemicelluloses and lignin can cause a delay in cement setting time [31]. The disadvantages of using bio-based materials in cementitious materials are self-evident: 1) Dimensional instability and high water absorption of bio-based materials due to the sensitivity of cellulose to ambient moisture; 2) Cellulose degradation after long-term application; 3) Weak bond between natural fibre and cementitious matrix. Therefore, pretreatment is critical to reducing the

degradation potential of bio-based materials and improving their performance prior to application in building materials.

Various treatment methods have been investigated to improve the compatibility of bio-based materials with cement matrix [22], such as physical treatment (milling [55], rolling compression [56], cutting [57]), chemical treatment (alkali, silane [58]), and heat treatment [59], etc. Treatment with an alkaline solution (e.g. lime, sodium hydroxide [33] and calcium hydroxide [36]) is an important step in the chemical treatment of natural fibre because it removes some lignins, hemicelluloses, pectins, and other minor components such as wax. However, chemical treatment continues to limit the biodegradability of bio-based materials. The alkalinity of the matrix and the volumetric instability of the bio-based materials are the primary causes for poor durability of the bio-based concrete [37]. Pyrolysis methods are used to treat bio-based materials to completely decompose organic matter [38, 39], which is the most effective method to remove soluble sugar and hemicellulose, to improve dimensional stability, and to reduce biological degeneration.

- *Durability of porous bio-based adsorptive concrete*

Porous adsorptive concrete is frequently applied in a saturated water environment to adsorb pollutants from stormwater runoff, cellulose degradation of bio-based materials in a long-term humid environment is an important limiting factor for the durability of bio-based concrete [59]. Bio-based materials are sensitive to moisture changes in the environment, and drying shrinkage and wet swelling of bio-based materials may jeopardize the durability of bio-based concrete. Therefore, the long-term physical and mechanical properties of bio-based mortar in aqueous conditions must be evaluated. Furthermore, the freeze-thaw resistance properties of concrete should be evaluated when used in northern European countries, such as the Netherlands, Denmark and Finland.

1.2 Motivation and objective

Motivated by the aforementioned issues, this research aims to develop bio-based adsorptive concretes that can reduce accelerated stormwater runoff while providing underlying soil water, simultaneously removing P to improve the quality of underlying water. The adopted research idea is to replace conventional cementitious composites with highly adsorptive materials to produce porous bio-based adsorptive concrete, and the investigated characteristics focus on adsorptive cementitious composites, performance evaluation and durability of bio-based adsorptive concrete. The primary

issue that must be addressed is the selection and modification of highly adsorptive materials. Secondly, the structure optimization and mix design of bio-based adsorptive concrete is an important factor that should be investigated. Finally, the durability of bio-based mortar must be evaluated. The following are the specific objectives of this work:

- *Selection and modification of highly adsorptive materials*

The application of conventional aggregates with no adsorption capacity is the major reason for the low adsorption performance of traditional pervious concrete. It is hypothesized that using highly adsorptive materials as adsorptive aggregates and mortar, as well as optimizing the micropores of skeleton structure will improve the adsorption performance of concrete. Therefore, the adsorption performance and adsorption mechanism of various potential adsorptive materials for highly adsorptive concrete are firstly evaluated, and then the facile pelletizing method is used to produce sustainable highly adsorptive aggregates with good mechanical properties.

- *Mix design and optimization of bio-based adsorptive concrete*

A dense paste layer will reduce the penetration potential of pollutants into the adsorptive aggregate, resulting in a significant reduction in the adsorption performance of concrete. A porous adsorptive cement paste is developed to reduce the effects of a dense paste layer on the adsorption performance of the paste-coasted aggregate by combining chemical and physical methods. Furthermore, a two-sized aggregate skeleton structure is designed for porous adsorptive concrete, and the optimum mix design is obtained using the orthogonal method.

- *Long-term performance of bio-based mortar*

The major factor limiting the durability of bio-based mortar is the long-term degradation characteristics of natural fibres. The physical and mechanical properties, long-term degradation characteristics, and dimensional stability of treated miscanthus mortar are investigated to reduce the negative impact of miscanthus fibre on the service life of bio-based mortar.

1.3 Outline of the thesis

The framework of this thesis is shown in **Fig. 1.2**. The following paragraphs briefly introduce the thesis chapters:

In Chapter 1, the motivation and background, problem statement, and methodology of the research topic of this thesis are discussed.

In Chapter 2, the physical treatment (ball milling) and heat treatment methods are used to modify miscanthus (*x* giganteus), the effects of heat-treated duration (2-hour, 3-hour, and 4-hour), size and shape of miscanthus fibre (long fibre, short fibre, and powder) on bio-based miscanthus mortar are investigated.

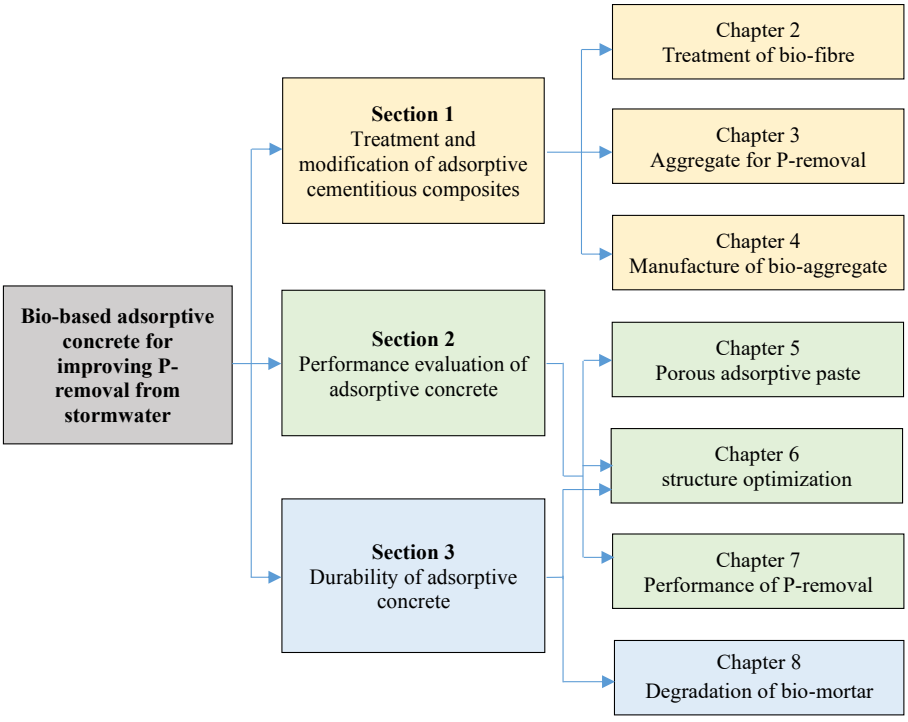

Fig. 1.2 The framework of this thesis.

In Chapter 3, the P-removal performance of various granular adsorptive aggregates is evaluated for potential applications in highly adsorptive concrete. The effects of material types, adsorption isotherms, adsorption kinetics, and different pH values on P-removal capacity are investigated. Potential adsorptive materials for the manufacture of adsorptive aggregates are obtained.

In Chapter 4, a porous and sustainable adsorptive aggregate combining both chemical and physical adsorption capacities is developed. Physical and mechanical properties, salt attack resistance, freeze-thaw resistance, and adsorption characteristics of highly adsorptive aggregates are investigated.

In Chapter 5, a porous adsorptive cement paste is developed using miscanthus powder and steel slag powder to increase the water passage of the cement paste and improve

the adsorption characteristics of the paste-coated aggregate.

In Chapter 6, a two-sized aggregate structure is proposed to optimize micropore skeleton structures of adsorptive pervious concrete. The effects of cement, sand, w/c and adsorptive aggregate content on physical and mechanical properties, adsorption performance, and freeze-thaw cycles of adsorptive pervious concrete are investigated.

In Chapter 7, the manufactured adsorptive aggregate is used to make adsorptive concrete with a higher P-removal capacity. Physico-mechanical properties, cyclic adsorption characteristics, P-removal mechanism and environmental impacts of concrete are investigated.

In Chapter 8, in order to reduce the negative impact of natural fibre on the service life of bio-based concrete. The effects of raw miscanthus, heat-treated miscanthus, and miscanthus powder on physical and mechanical properties, long-term degradation characteristics, and dimensional stability of bio-based miscanthus mortar are investigated.

In Chapter 9, the main conclusions of this work are presented, along with recommendations for future work.

Chapter 2 Effects of treated miscanthus on performance of bio-based cement mortar

Bio-based miscanthus cementitious composites as a sustainable building material have attracted more attention recently. The organic matter and physical properties (size, shape, etc.) of the miscanthus have a negative influence on the performance of cementitious composites. In this chapter, physical treatment (ball milling) and heat treatment methods are applied to modify miscanthus (*x* giganteus), the effects of heat-treated duration (2-hour, 3-hour and 4-hour), the size and shape of miscanthus on bio-based concrete are investigated. The results show that the heat-treated miscanthus has a positive influence on compressive strength. The irregular cavities of the parenchyma structure of the miscanthus are easily filled with fresh mortar and tightly embedded in the mortar, resulting in an enhanced bonding interface. Besides, the long-fibre miscanthus (2-3 cm) has a better fibre-bridging effect than other forms of the miscanthus, with an improvement in flexural strength of 24%. Physically treated miscanthus exhibits excellent heat-insulating performance, which is recommended for heat-insulating bio-concrete. The treated miscanthus significantly reduces the drying shrinkage, with a decrease of up to 25% at 90 days, compared to the untreated miscanthus. It is concluded that the physically treated miscanthus (e.g. long-fibre and powdery miscanthus) are recommended forms for application in sustainable bio-based cement mortar.

This chapter is partially reproduced from:

F. Wu, Q.L. Yu, H.J.H. Brouwers, F. Gauvin. Effects of treated miscanthus on performance of bio-based cement mortar. Journal of Sustainable Cement-Based Materials, 4, 12, 2022.

2.1. Introduction

Miscanthus (*x* giganteus) is a perennial energy crop in Europe because of its high biomass yield and adaptation to the European climate [60]. The utilization of miscanthus as a fibre or an aggregate has gained great attention in Europe [61–63], for example, lightweight fiberboards, plant pots and packaging materials made of miscanthus fibre have been investigated in previous studies [16]. The advantages of using miscanthus for the manufacture of bio-based cement mortar are that the miscanthus is renewable crop, abundant, with widespread availability and rapid growth [63]. The research on bio-based miscanthus mortar aims to develop sustainable building materials, reduce the environmental impact and recycle wastes from agricultural factories [64].

The organic matter and physical properties (e.g. size, shape, etc.) of miscanthus show a negative influence on the performance of bio-based miscanthus mortar. Due to the high porosity of miscanthus fibre, it is sensitive to changes in humidity in the ambient environment. As a result, the drying shrinkage and wet swelling of miscanthus fibre will affect the performance of the miscanthus mortar. The drying shrinkage of bio-based mortar is usually higher than that of inorganic mass-based mortar [65]. Moreover, during ageing, the degradation of miscanthus fibre may occur as a consequence of the dissolution of the hemicellulose, cellulose and lignin [66]. The extractive compounds from miscanthus fibre such as polysaccarides, phenols and starch, are known to delay cement hydration [67]. The weak bond between the bio-based fibre and the mortar interface is a key factor restricting the ultimate strength of bio-based mortar. Therefore, to reduce the drying shrinkage and improve the mechanical strength of miscanthus mortar, miscanthus fibre should be treated prior to use in bio-based cement mortar.

In this chapter, two methods are used to modify miscanthus fibre: heat treatment and physical treatment (ball milling). The raw miscanthus fibre is treated under nitrogen conditions at 250 ℃ for 2, 3 and 4 hours of exposure, and the ball milling is also used for the physical treatment of the miscanthus fibre. After ball milling, 2-3 cm, 0.4-1.5 cm and <0.05 cm miscanthus are used as long fibre, short fibre, and powdery fibre, respectively. The physical properties, morphology and mineralogical phase of miscanthus fibre before and after treatment are evaluated. The effects of different forms of miscanthus fibre on the physic-mechanical properties, microstructure and drying shrinkage of bio-based cement mortar are investigated. The recommended miscanthus treatment method is obtained based on the present results.

2.2. Materials and methods

2.2.1 Raw materials

The CEM I 52.5 R Portland cement is used as a binder (ENCI, the Netherlands). Commercial expanded silicate (ES) is used as coarse aggregate. To obtain a good particle packing, four sizes of the ES are used with the size of 0.09-0.3 mm, 0.5-1 mm, 1-2 mm and 2-4 mm in this study. The specific density and crushing strength of the ES are 2.26 g/cm^3 and 12-22 MPa [68], respectively. The raw miscanthus fibre with a length of 1-3 cm is supplied by NNRGY Company (The Netherlands). The external surface is stiff and smooth epidermis texture with round micropores, which provides the strength and toughness for the miscanthus fibre. The internal surface of the miscanthus is a parenchyma structure, which provides good thermal and sound absorption properties [62]. Fly ash and silica fume are used as supplementary cementitious materials. CEN-NORM sand satisfying European standards (EN 196-1) is used as fine aggregate. The polycarboxylate ether superplasticizer is used to improve the workability of the fresh mixture.

2.2.2 Treatment of miscanthus

The schematic diagram of the treatment methods of the miscanthus fibre is presented in **Fig. 2.1**. Generally, the pyrolysis temperature of miscanthus biomass varies from 200 °C to 400 °C [69]. The miscanthus easily turns to ash under high-temperature conditions, the low-temperature pyrolysis is selected in the present study. The raw miscanthus is placed in a vacuum furnace under nitrogen conditions at 250 °C for 2 hours, 3 hours and 4 hours, respectively.

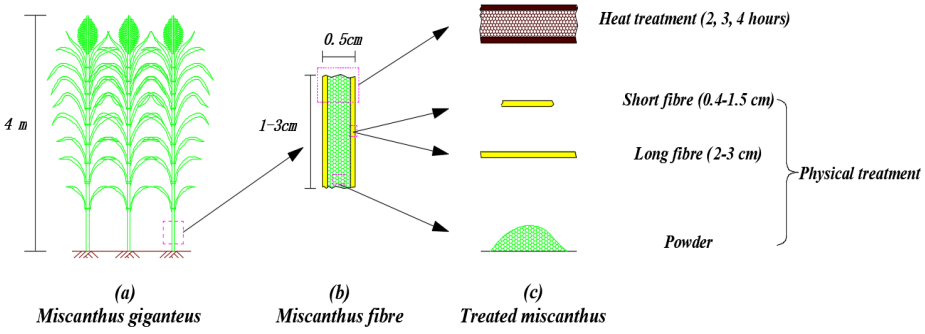

Fig. 2.1 Schematic diagram of the treatment of miscanthus.

In ball milling, the external surface of the miscanthus provides the long fibre and short fibre, while the porous internal surface becomes the powdery miscanthus. The detailed

process of ball milling is as follows: 10 porcelain milling balls of a total of 805.4 g mass with a diameter of 30 mm are placed in each porcelain ball mill pot of 50 ml bowl volume, and then 40 g miscanthus is added to per ball mill pot. The ball milling is run with a milling speed of 300 rpm for 10 minutes. After ball milling, the long fibres (2-3 cm), short fibres (0.4-1.5 cm) and powdery (<0.05 cm) miscanthus are obtained by a sieving machine, as shown in **Fig. 2.2**.

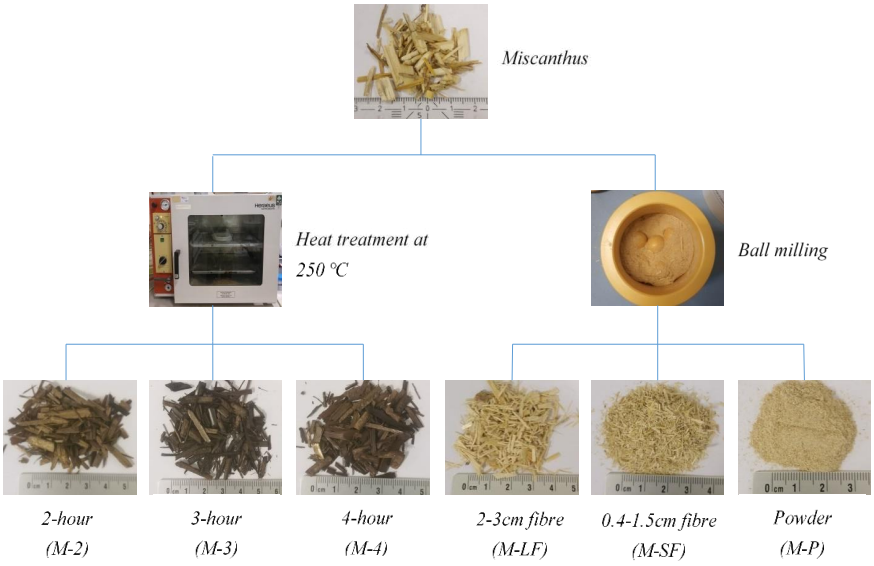

Fig. 2.2 Miscanthus fibre after treatment.

2.2.3 Mix proportion and specimen preparation

The treated miscanthus, including heat-treated 2 hours (M-2), 3 hours (M-3) and 4 hours (M-4), long fibre (M-LF), short fibre (M-SF) and powdery miscanthus (M-P) are used to replace the untreated miscanthus (M-0) by volume. A 1.5% V/V of the miscanthus is added to the mortar. The gradation distribution of the ES aggregate refers to the literature [68], and the contents of cement, fly ash and silica fume refer to the lightweight aggregate concrete [70]. The powdery miscanthus can not be submerged in water for the pre-wetting treatment, the same volume water of 24-h water absorption of the powdery miscanthus is added to the fresh mixture. The fresh mixture is compacted by a striking shaker. After that, all mixtures are covered with a plastic film and demoulded after 24 hours and then stored in the laboratory at a temperature of 20±2 ℃ and relative humidity of ≥95%. The mix proportions of concrete are shown in **Table 2.1**.

2.2.4 Test methods

The density of 100×100×100 mm^3 sample at 28 days is measured following EN 1015-6. The water absorption and porosity of 100×100×100 mm^3 sample at 28 days are determined according to ASTM C642-13. The compressive strength and flexural strength of 40×40×160 mm^3 sample at 28 days are determined according to EN 196-1, with a loading rate of 2400 N/s and 50 N/s, respectively. The average value of three samples is recorded as the final result. The specific density of the miscanthus fibre is determined by using an AccuPyc II 1340 gas pycnometer. The microscopic images of the miscanthus fibre before and after treatment are observed with SEM (Phenom ProX). The 100×100×100 mm^3 sample at 28 days is oven-dried at 105 °C for 24 hours to a constant mass, and then the surface midpoint position of the sample is used for the thermal conductivity measurement by ISOMET 2104, three surfaces are determined for each sample. The 40×40×160 mm^3 sample after demoulding is stored in the laboratory at a temperature of 20±2 ℃ and relative humidity of 65±3%, and then the drying shrinkage is determined by using a digital micrometer gauge with a resolution of 0.001 mm according to DIN 52450.

Table 2.1 The mix proportions of mortar (kg/m^3).

Materials	M-0	M-2	M-3	M-4	M-LF	M-SF	M-P
CEM I 52.5R	440	440	440	440	440	440	440
Fly ash	66	66	66	66	66	66	66
Silica fume	44	44	44	44	44	44	44
ES 0.09-0.3 mm	119.2	119.2	119.2	119.2	119.2	119.2	119.2
ES 0.5-1 mm	74.2	74.2	74.2	74.2	74.2	74.2	74.2
ES 1-2 mm	83.4	83.4	83.4	83.4	83.4	83.4	83.4
ES 2-4 mm	96.7	96.7	96.7	96.7	96.7	96.7	96.7
Sand	692	692	692	692	692	692	692
Water	192.5	192.5	192.5	192.5	192.5	192.5	192.5
Superplasticizer	6.1	6.1	6.1	6.1	6.1	6.1	6.1
Miscanthus fibre	24.6	21.5	18.8	15	22.1	24.3	23.6

2.3. Results and discussion

2.3.1 Characterization of the miscanthus after treatment

- *Physical properties of the treated miscanthus*

The physical properties of the treated miscanthus fibre are shown in **Table 2.2**. As expected, heat treatment reduces the density of the miscanthus, whereas, the ball milling treatment has a negligible effect on the density. The densities of heat-treated miscanthus

at 2-hour, 3-hour and 4-hour are reduced by 13%, 24% and 39%, respectively, as compared to the untreated miscanthus (M-0). This may be attributed to the organic matter being pyrolyzed and a carbon skeleton and microporous structure formed during the process, which leads to a reduction in the mass of the bio-materials [71]. The results also show that the powdery miscanthus and heat-treated miscanthus have a higher water absorption than other forms of the miscanthus. However, the long-fibre and the short-fibre miscanthus possess lower water absorption because the parenchyma structure with high water absorption is separated from the miscanthus surface.

Table 2.2 Properties of treated miscanthus fibre.

Sample code	Treatment method	Specific density (g/cm^3)	Relative change from M-0 (%)	24-h water absorption (%)	Relative change from M-0 (%)
M-0	-	1.64	-	269 ± 15	-
M-2	Heat	1.43	-13	287 ± 18	+7
M-3	Heat	1.25	-24	350 ± 21	+30
M-4	Heat	1.00	-39	398 ± 20	+48
M-LF	Physical	1.47	-10	190 ± 11	-29
M-SF	Physical	1.62	-1	230 ± 13	-15
M-P	Physical	1.57	-4	525 ± 23	+95

- *Morphology*

The SEM micrographs of the miscanthus fibre after 4-hour heat treatment are shown in **Fig. 2.3**. The surface colour of the heat-treated miscanthus turns from yellow to black, which indicates that the volatile components in the organic matter have been expelled and relatively carbon remains [72]. Cracks appear along the longitudinal direction of the stem due to the dehydration of the miscanthus (**Fig. 2.3a**). Moreover, surface peeling is observed on the external surface of the miscanthus. Similar to the external surface, cracks also occur on the surface of the parenchyma structure and the fragment of the cavity is peeled off from the parenchyma, and a dispersed laminated structure is formed on the internal surface (**Fig. 2.3b**). The increase in surface cracks by heat treatment provides a path for the flowing mortar to penetrate the interior of the cavity of the miscanthus [73], making the miscanthus more tightly embedded in the mortar achieving a better bonding interface.

- *Mineralogical phase analysis*

The cellulose chain molecule in the amorphous area is irregularly arranged, resulting in a diffuse reflection and no peaks are generated in XRD [74]. The XRD patterns of the untreated and heat-treated miscanthus fibre are presented in **Fig. 2.4**. The results show that both untreated and heat-treated miscanthus are amorphous because of the presence

of graphite. Bio-materials such as peanut, walnut and chestnut, etc. have typical peaks at 22.6° due to the presence of crystalline cellulose [74]. Previous studies show that the crystalline cellulose of peach and apricot shells decreases after heat treatment and that a broad wide graphitic peak at the diffraction angle of 26.7° [59]. The reduction in the crystallinity of cellulose is mainly caused by the loss of oxygen from the heat-treated bio-materials.

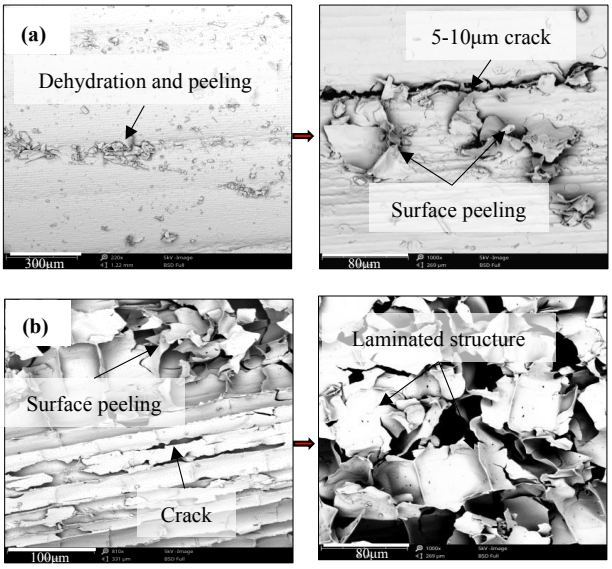

Fig. 2.3 SEM micrographs of (a) external surface (b) internal surface of 4-hour heat-treated miscanthus fibre.

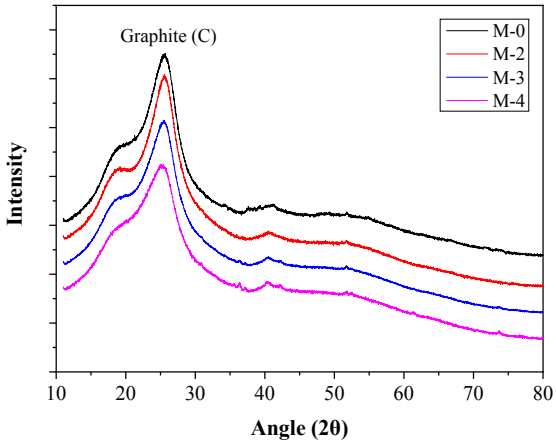

Fig. 2.4 XRD patterns of the untreated and heat-treated miscanthus fibre.

2.3.2 Physical properties of miscanthus mortar

- *Density*

As shown in **Fig. 2.5a**, as the duration of heat treatment increases, the density of the mortars gradually decreases, because the heat treatment increases the closed pores of the miscanthus over time [69]. The oven-dry density of the reference mortar (M-0) is 1498 kg/m^3, and the M-4 mixture obtains the lowest oven-dry density of 1439 kg/m^3, which is 4% less than the M-0 mixture. For physical treatment, the M-SF results in more reduction in the density of mortar, compared to the M-LF and the M-P, with a decrease of 2.3%. This may be attributed to the weak bond between the smooth external surface of miscanthus fibre and the mortar resulting in more micropores in the interfacial transition zone (ITZ) [75].

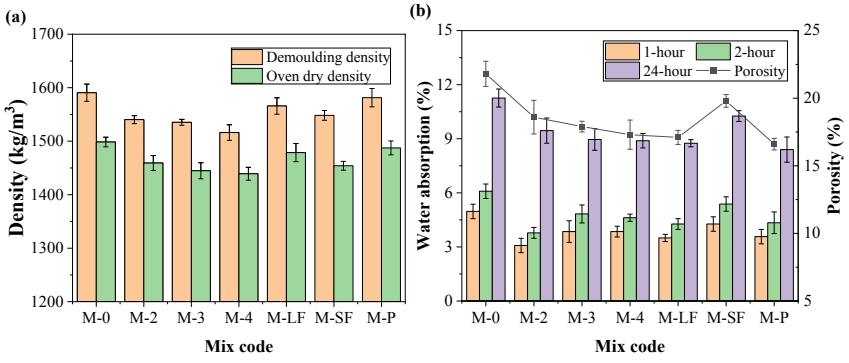

Fig. 2.5 (a) density and (b) water absorption and porosity of mortar.

- *Water absorption and porosity*

As shown in **Fig. 2.5b**, the 24-hour water absorption of miscanthus mortar varies from 8% to 11%, and the porosity is between 17% and 22%. The treated miscanthus significantly decreases the water absorption and porosity of the mortar. The water absorption and porosity of the M-P mixture decreased by 26% and 24%, respectively, compared to the M-0 mixture. After ball milling, the small particles of the miscanthus are more tightly wrapped by the mortar, which results in a decrease in porosity and water absorption [76]. For the heat treatment, with the increase in the pyrolysis duration, the volatile components gradually are lost, causing the carbon content to increase relatively with the decomposition of organic matter, affecting the bonding ability at the mortar interface [59,77], and consequently, reducing the porosity and water absorption of mortar.

- *Thermal conductivity*

The thermal conductivity of the mortars varies from 0.56 W/(m·K) to 0.73 W/(m·K), as shown in **Table 2.3**. The treated miscanthus significantly reduces the thermal conductivity, volume heat capacity and thermal diffusivity of mortar. The thermal conductivity of the M-4 and M-LF mixtures is reduced by 19% and 23%, respectively, as compared to the M-0 mixture. After ball milling, the particle size of the miscanthus becomes smaller, they are more tightly and uniformly dispersed into the mortar and form tiny closed voids, resulting in an improvement in the heat absorption capacity of the miscanthus mortar. It can be concluded that the physically treated miscanthus (M-LF and M-SL series) is recommended for the manufacture of heat-insulating bio-based mortar.

Table 2.3 Thermal properties of mortar.

Mix code	Thermal conductivity λ (W/m·K)	Volume heat capacity Cρ (M J/m^3·K)	Thermal diffusivity a (10^{-6} m^2/s)
M-0	0.73	1.7	0.44
M-2	0.59	1.6	0.38
M-3	0.59	1.6	0.38
M-4	0.59	1.5	0.37
M-LF	0.56	1.6	0.35
M-SL	0.56	1.6	0.34
M-P	0.62	1.7	0.38

2.3.3 Mechanical properties

- *Compressive strength and flexural strength*

The compressive strength and flexural strength of the mortars are shown in **Fig. 2.6**. The results show that the treated miscanthus significantly increases the compressive strength of the mortar. Moreover, the compressive strength of mortar containing heat-treated miscanthus improves as the heat treatment duration increases. However, considering the energy consumption and exhaust emissions caused by heat treatment, it is not preferred for treating miscanthus.

The 28-day compressive strengths of the M-LF and M-P mixtures are increased by 17% and 26%, respectively, compared to the M-0 mixture. The results also show that the M-LF and M-P significantly improve the 28-day flexural strength of the mortar, with an increase of 24% and 12%, respectively, as compared to the M-0 mixture. The large particle size and waxy surface of the untreated miscanthus results in weak bonding with the mortar [62]. The untreated miscanthus increases the air voids of mortar, resulting in

a reduction in mechanical strength.

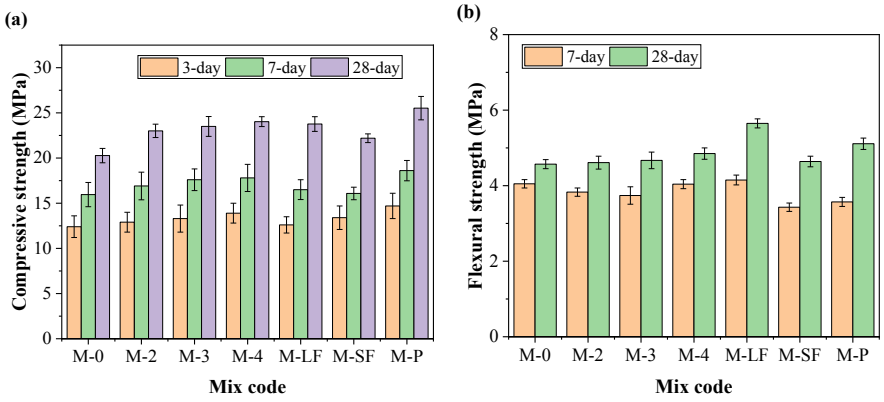

Fig. 2.6 (a) compressive strength and (b) flexural strength of mortar.

- *Microstructure*

The SEM micrographs of miscanthus mortar are shown in **Fig. 2.7**, the mortar is present on the untreated miscanthus and a small amount of mortar is observed on the surface (M-0) along the fibre. Some surfaces of heat-treated miscanthus are covered with mortar (M-4). The crack development process of bio-based miscanthus mortar (M-0) is shown in **Fig. 2.8**. The failure of mortar depends on the characteristics of the miscanthus, lightweight aggregate strength, as well as interfacial adhesion between the miscanthus and the mortar. The microscopic pores easily develop on the surface of the mortar around the miscanthus. The crack is developed along with the weak bonding interface under external load and the low-strength miscanthus is also penetrated by the crack. When the crack passes through the lightweight aggregate, the failure of mortar occurs. Therefore, an effective method to improve the mechanical strength of the miscanthus mortar is to increase the bonding ability between the miscanthus and the mortar through heat treatment and physical treatment.

2.3.4 Drying shrinkage

- *Drying shrinkage and mass loss*

As shown in **Fig. 2.9**, the treated miscanthus significantly decreases the drying shrinkage and mass loss of mortar. Moreover, most of the drying shrinkage and mass loss of the miscanthus mortar happen within the first two weeks due to the high porosity of miscanthus mortar. At 90 days, the drying shrinkage of the M-LF and M-P mixtures are 831 με and 788 με, respectively, which are reduced by 21% and 25%, respectively,

compared to the M-0 mixture. Previous studies show that the drying shrinkage of oil palm shell concrete [78] and wood sand concrete [79] at 90 days are about 450-550 με and 1200-1900 με, respectively. Therefore, the drying shrinkage of the miscanthus mortar in this study is acceptable compared to those bio-based concretes.

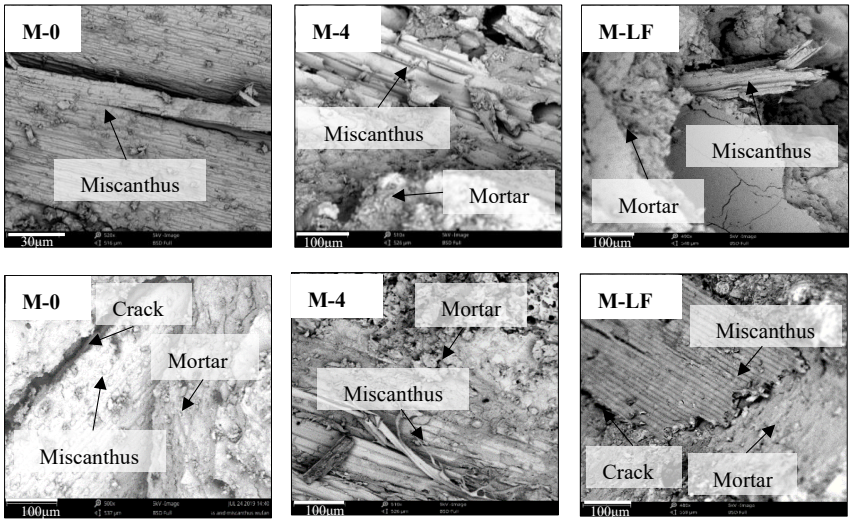

Fig. 2.7 SEM micrographs of miscanthus mortar.

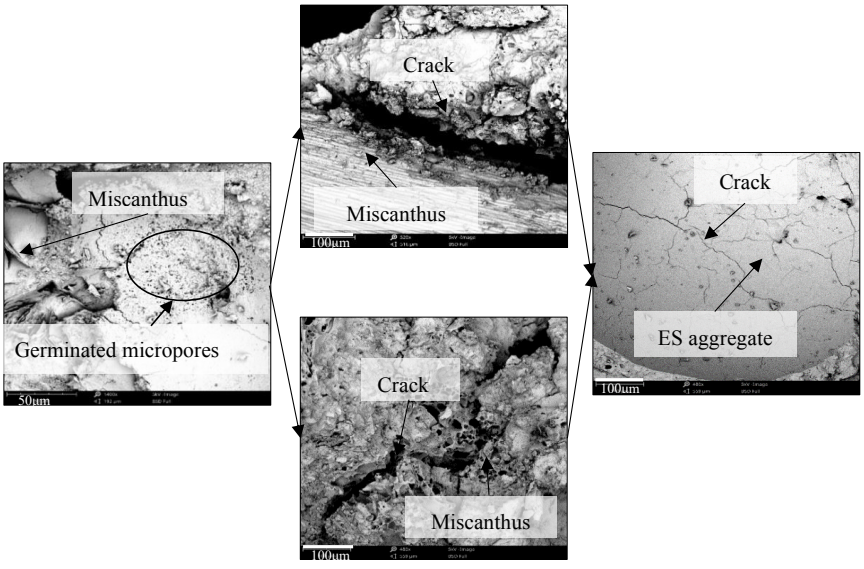

Fig. 2.8 SEM micrographs of crack development of miscanthus mortar.

The drying shrinkage is generally caused by the loss of water in the capillary from the interior of concrete [80–82], which is related to relative humidity [83,84] and porosity [85,86]. Under the same conditions, low-porosity concrete usually has less drying shrinkage [87]. Large particle aggregates are more prone to dry shrinkage than small particle aggregates [88]. Since mortar containing powdery miscanthus has a smaller particle size and less porosity than mortar containing untreated miscanthus, this results in a significant reduction in the drying shrinkage.

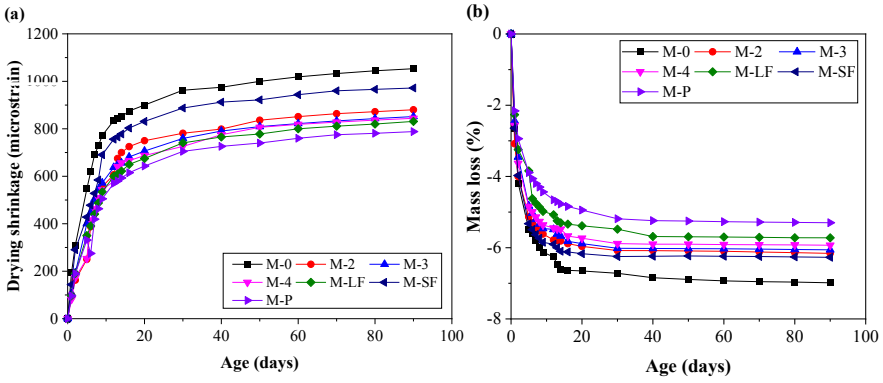

Fig. 2.9 (a) drying shrinkage and (b) mass loss of miscanthus mortar.

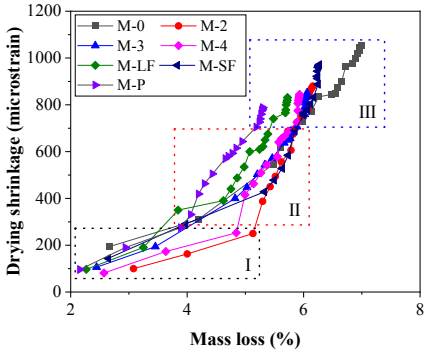

Fig. 2.10 Relationship between mass loss and drying shrinkage of miscanthus mortar.

- *Relationship between mass loss and drying shrinkage*

The relative humidity inside the concrete may affect the drying shrinkage [85]. The mass loss of concrete can be used to evaluate relative humidity [80], especially for the high water absorption aggregate [89]. As shown in **Fig. 2.10**, the relationship between drying shrinkage and mass loss can be divided into three stages. In the first stage, the mass loss increases significantly with a small drying shrinkage due to the rapid loss of free water from the larger pores of the miscanthus mortar. The treated miscanthus

reduces the mass loss of the miscanthus mortar in this stage because of the reduction in the porosity of the mortar. In the second stage, a good linear relationship is observed between drying shrinkage and mass loss. A similar trend is observed in other previous studies [80,83,87]. In the third stage, the mass loss of concrete is maintained at a steady state, while the dry shrinkage rate is gradually reduced [85].

2.4. Conclusions

(1) Heat treatment significantly reduces the density of the miscanthus fibre and increases water absorption, which is not recommended for miscanthus treatment. The crack appears on the surface of the miscanthus after heat treatment, and the fragment is peeled off the surface. Water absorption of the miscanthus is lower for the short fibre (0.4-1.5 cm) and long fibre (2-3 cm).

(2) Milling miscanthus reduces the density, water absorption, porosity and thermal conductivity of the mortar significantly. The small particle of the miscanthus is more easily enclosed by the mortar after ball milling, resulting in a decrease in water absorption and porosity of the M-P mixture.

(3) Using milled miscanthus improves the compressive strength of the mortar significantly. The irregular cavities of the parenchyma structure of the powdery miscanthus are easily filled with fresh mortar and tightly embedded in the mortar, resulting in an enhanced bonding interface. Moreover, long fibres of miscanthus have a better fibre-bridging effect than other forms of miscanthus.

(4) Powdery miscanthus and long-fibre miscanthus are superior in terms of reducing drying shrinkage, thermal conductivity, and improving the mechanical strength of the miscanthus mortar, and are the preferred forms for using miscanthus in sustainable bio-based cement mortar.

Chapter 3 Phosphorus removal from aqueous solutions by adsorptive concrete aggregates

The purpose of this chapter is to investigate the adsorption characteristics of granular aggregates under identical experimental conditions for potential applications in highly adsorptive concrete. The industrial by-products (steel slag), lightweight aggregates (expanded silicate) and bio-based materials (peach shell and miscanthus) are used for phosphate (P) removal from aqueous solutions. The effects of several parameters such as the initial P-concentrations, reaction time and pH value on adsorption capacity and removal efficiency of P are investigated using an IC analyzer. Results show that the P-adsorption of all absorbents follows the adsorption isotherms with a varying P-concentration from 5 mg/L to 700 mg/L, and the adsorption isotherms data is fitted well by the Langmuir model. The steel slag exhibits a higher P-adsorption capacity and adsorption efficiency compared to lightweight aggregates and bio-based materials, with an estimated maximum adsorption capacity by steel slag of 20.4 mg/g. Heat treatment is used to increase the adsorption capacity of the miscanthus by making use of the change in pore structure characteristics determined by BET. The adsorption kinetic data of the steel slag follows a pseudo-second-order model. The ICP-AES, XRD and SEM-EDS analyses show that the P-adsorption of the bio-based material follows physical adsorption, whereas the adsorption mechanism of the steel slag can be attributed to the Ca^{2+} released from the steel slag, which can react with phosphate and form a stable Ca-P precipitate. It is suggested that steel slag can function as an effective adsorptive aggregate for the manufacture of highly adsorptive concrete.

This chapter has been published as:

F. Wu, Q.L. Yu, F. Gauvin, H.J.H. Brouwers, C.W. Liu. Phosphorus removal from aqueous solutions by adsorptive concrete aggregates. Journal of Cleaner Production, 278, 123933, 2021.

3.1 Introduction

Phosphate is one of the main pollutants from stormwater runoff [90]. In extreme conditions, the excess supply of P causes eutrophication and excessive algal blooms [91]. With the requirements of sustainable development, different low-cost and high-adsorption materials are gradually employed for water purification, such as fly ash [12], pumice [92], steel slag [43], porous lightweight materials [93], peach shell (PS) [94], miscanthus (M) [95], plantage ovata [96], etc. The P-adsorption mechanism of these materials is attributed to ion exchange, chemical precipitation, biological processes and physical adsorption, etc. [97]. Although most of these materials have good adsorption characteristics, not all of them are suitable as adsorptive aggregates considering size and strength requirements. Besides, most of the current studies mainly focus on the adsorption capacity of powdery materials. The adsorption performance of the low-cost, available and highly adsorptive aggregates for highly adsorptive concrete should be evaluated by granular aggregate rather than powder.

BOF steel slag (SS) is a by-product of the steel industry, which is mainly used for road-base or sand replacement, or otherwise landfilled or stockpiled. The main dominant components of the SS are calcium oxide (CaO) and iron oxide (Fe_2O_3), which are the result of the addition of the fluxing agent during the steelmaking process [43]. The high content of metal oxide makes it a potential adsorbent, and it has attracted more attention for phosphate removal from wastewater [5]. The release of calcium ions (Ca^{2+}) from the SS can be combined with phosphate (PO_4^{3-}) by Ca-P precipitation-coagulation mechanism [27]. More than 70% of the BOF-SS is composed of calcium-containing minerals [98], indicating sufficient calcium ions can be supplied for the precipitation-coagulation process.

Adsorptive aggregates should be low-cost, eco-friendly and available, thus bio-based aggregates may be feasible for recyclable adsorptive materials for pollutant removal due to the well-developed pore structure. However, the different experimental conditions affect physico-chemical properties of adsorbent materials, and the same material exhibits different adsorption capacities with varying conditions such as initial concentration, reaction time, pH, temperature and agitation mode, etc [43]. The adsorption properties of different adsorptive aggregates under identical experimental conditions should be investigated and the optimized aggregates for potential application in highly adsorptive concrete should be obtained.

The purpose of this chapter is to investigate the adsorption characteristics of granular aggregates under identical experimental conditions for potential applications in highly

adsorptive concrete. The industrial by-product (BOF steel slag), lightweight aggregate (expanded silicate) and bio-materials (peach shell and miscanthus) are used for P-removal from aqueous solutions. The effects of the initial P-concentration, reaction time and pH on the adsorption capacity and efficiency of P are investigated with ion chromatography (IC). The adsorption isotherms and adsorption kinetics models of P-absorption are derived. The pore structural properties of the materials are analyzed using Brunauer Emmett Teller (BET) method. The removal mechanism of phosphate is discussed based on the results from inductively coupled plasma atomic emission spectroscopy (ICP-AES), X-ray diffraction (XRD) and scanning electron microscope combined with an energy dispersive spectrometer (SEM-EDS).

3.2 Materials and methods

3.2.1 Materials

The BOF steel slag (SS) (TATA Steel, The Netherlands), commercial expanded silicate material (ES), miscanthus (M) (NNRGY, The Netherlands) and commercial peach shell biochar (PS) are used as absorptive materials in this study. The heat-treated miscanthus (M-3hour) under nitrogen conditions at 250 ℃ for 3 hours is also used as an absorbent for comparison [69]. All raw materials selected for the investigations of the adsorption performance have a particle size of 1-2 mm. They are washed twice with distilled water to remove any contaminations, and then oven-dried at 105 ℃ for 24 hours and stored in air-tight containers until the test.

Table 3.1 Chemical composition of raw materials (wt.%).

Oxides	Cement	Steel slag[34]	Expanded silicate
CaO	64.6	40.3	2.0
SiO_2	20.1	14.1	55.0
Al_2O_3	5.0	2.0	22.0
Fe_2O_3	3.2	26.7	3.0
SO_3	3.1	-	-
MgO	2.0	7.8	1.0
MnO	0.1	4.7	-
TiO_2	0.3	1.4	0.5
V_2O_5	-	1.0	-
P_2O_5	0.4	1.6	-
K_2O+Na_2O	0.8	-	14.0
LOI	0.4	0.6	4.0

The high content of metal oxides contributes to a strong affinity for P-adsorption [99]. The chemical compositions of raw materials are determined by X-ray fluorescence

spectroscopy (XRF), as presented in **Table 3.1**. The main chemical components of the SS are CaO (40.3%), Fe_2O_3 (26.7%) and SiO_2 (14.1%). The ES is mainly composed of SiO_2 (55.0%), Al_2O_3 (22.0%), K_2O and Na_2O (14.0%). The PS and M are organic matter, and their chemical compositions are mainly composed of C, H, O and N [59]. The SEM images of the adsorbents are shown in **Fig. 3.1**. Many micropores are observed on the surface of the PS, ES and M-3hour (**Fig. 3.1a**, **3.1c** and **3.1e**). The SS displays a densified surface, but microscopic cracks with a width of smaller than 5 μm are observed on the surface (**Fig. 3.1b**). The internal surface of the M is parenchyma-like a cavity structure (**Fig. 3.1d**).

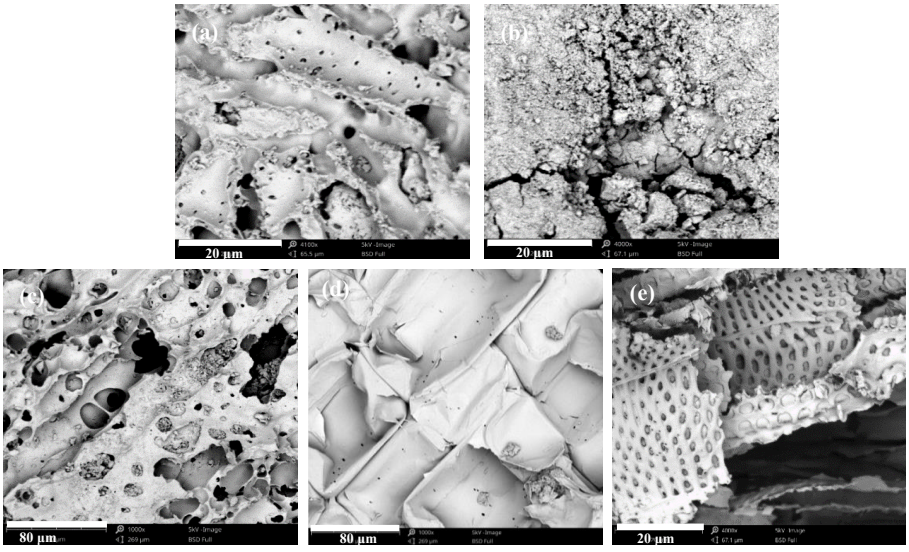

Fig. 3.1 SEM images of topography of (a) PS, (b) SS, (c) ES, (d) M and (e) M-3hour.

3.2.2 P-adsorption experiments

An artificial P solution is prepared for the adsorption test in this study. A stock P solution of 1000 mg/L is prepared by dissolving the chemically pure potassium dihydrogen phosphorus (KH_2PO_4) in distilled water, i.e., 4.394 g of KH_2PO_4 is weighed and placed in a 200 mL beaker with distilled water, the solution is transferred to a 1000 mL volumetric flask, dilute with distilled water to the mark line and the 1000 mg/L P solution is obtained. 1 mL of this solution contains 1 mg of phosphorus. All standard P solutions with the desired concentration are prepared by diluting the stock P solution with distilled water.

- *Effect of different adsorbents on adsorption*

A preliminary experiment is conducted to evaluate the adsorption capacity of different raw materials. 1 g of the adsorbent material is added to a 25 ml P solution with a concentration of 50 mg/L. The mixture is stirred at 225 rpm in the thermostatic shaker for 24 h and then filtered by a 0.45 μm membrane. The extracted supernatant is used for the P concentration test.

The P-adsorption amount (q, mg/g) and P-removal fraction (P_R, %) are calculated as follows:

$$q = \frac{C_0 - C_e}{M} \times V \quad (3.1)$$

$$P_R = \frac{C_0 - C_e}{C_0} \times 100\% \quad (3.2)$$

Where C_0 is the initial P concentration (mg/L), C_e is the P concentration in the solution at equilibrium (mg/L), M is the mass of sample (g), and V is the volume of solution (L).

- *Adsorption isotherms*

The adsorption isotherms of P are evaluated with batch experiments. For the sorption isotherms, 1g of the adsorbent is loaded in a 50 ml polyethene centrifuge tube and mixed with 25 ml of various P solutions (5-700 mg/L). The flask is covered and stirred at 225 rpm for 24 h to ensure approximate equilibrium. After P adsorption, the solution is filtered through a 0.45 μm membrane filter and then analyzed for P concentration.

The Langmuir and Freundlich equations are used for analyzing the adsorption isotherms of adsorbents, as described below:

Langmuir equation:

$$A_e = \frac{Q_m K_L C_e}{1 + K_L C_e} \quad (3.3)$$

Freundlich equation:

$$A_e = K_F C_e^{\frac{1}{n}} \quad (3.4)$$

Where A_e is the adsorption removal capacity (mg/g), C_e is the P concentration in the solution at equilibrium (mg/L), Q_m is maximum adsorption capacity in Langmuir isotherm, K_L is adsorption constant in Langmuir isotherm, K_F is the constant of Freundlich isotherm, n is heterogeneity factor of Freundlich isotherm.

- *Adsorption kinetics*

The adsorption kinetics experiments are performed using a procedure similar to the one used for the adsorption isotherm test. A series of bottles with 1g of adsorbent and 100 ml of solution with a set P concentration of 100 mg/L, then mixed and shaken for different contact times (0.25, 0.5, 1, 2, 4, 6, 8, 12, 16 and 24 h). The solution is filtered and determined for residual concentration.

The Lagergren pseudo-first-order equation, pseudo-second-order equation and simple Elovich equation are used for describing the adsorption kinetics of adsorbents in this study:

Pseudo-first-order equation:

$$\frac{dA_t}{dt} = k_1(A_e - A_t) \quad (3.5)$$

Pseudo-second-order equation:

$$\frac{dA_t}{dt} = k_2(A_e - A_t)^2 \quad (3.6)$$

Simple Elovich equation:

$$q = \alpha + \beta \ln t \quad (3.7)$$

Where A_t is the amount of P adsorbed by the adsorbent at any time (mg/L), A_e is the adsorption removal capacity (mg/g), K_1 and K_2 are the rate constant of Lagergren pseudo-first-order and pseudo-second-order kinetic models.

- *Effect of pH on adsorption capacity*

The effects of pH on P-adsorption are determined by a series of experiments with constant initial P concentration (100 mg/L) and adsorbent dosage (1g) and various pH values (3, 5, 7, 9 and 11). 1M NaOH and 0.5 M HCl are used to adjust the pH value of the tested P solution.

3.2.3 P-desorption experiments

In this study, an artificial P solution is prepared for the adsorption test. A stock P solution of 1000 mg/L is prepared by dissolving the chemically pure potassium dihydrogen phosphorus (KH_2PO_4) in distilled water. All standard P solutions with the desired concentration are prepared by diluting the stock P solution with distilled water.

P-saturated adsorbent (1g) with 50 mg/L P-solution is placed in a 50 ml tube with 25

ml distilled water. After that, the tube is continuously shaken in a shaker at 225 rpm for 24 h. The mixture is centrifuged and filtered, and the P is determined by the same method described above.

P-desorption amount (q_d, mg/g) is calculated:

$$q_d = \frac{CV}{M} \tag{3.8}$$

The P-desorption fraction (P_d) is calculated:

$$P_d = \frac{CV}{T_P} \times 100\% \tag{3.9}$$

where C is the P concentration in the solution (mg/L), M is the mass of sample(g), V is the volume of the solution(L), and T_P is the P content in the P-saturated sample.

3.2.4 Analytical methods

The microstructural properties of all samples including BET-surface area, pore volume and pore size are determined by the nitrogen adsorption/desorption test. The mineralogical composition of all samples before and after absorption of P is determined by XRD. The microstructure of all samples before and after the test is observed by SEM-EDS. Before SEM-EDS analysis, all samples are Au-coated to observe the sample surface. Metal ions such as calcium (Ca^{2+}), iron (Fe^{2+}), magnesium (Mg^{2+}), etc. are measured through ICP-AES. The concentration of P is analyzed by IC.

3.3 Results and discussion

3.3.1 Pore structure of materials

The P-adsorption capacity depends on the differences in chemical composition, microstructure, and pore characteristics [100]. Most powders or aggregates such as clay, pigment, and cement exhibited Type II isotherms, and the narrow hysteresis loop is generated by inter-particle capillary condensation [101]. As shown in **Fig. 3.2**, the adsorption-desorption isotherm curves of all materials belonged to the Type II isotherms based on the International Union of Pure and Applied Chemistry (IUPAC) classification [101]. Moreover, a narrow hysteresis loop is observed in the adsorption-desorption isotherms curve, which indicates that the micropores and mesopores are well-developed [102,103]. The results also show that the PS adsorbed more nitrogen than other materials under the same relative pressure conditions, which indicates that the PS has more developed pore structures.

The pore size of adsorbents can be divided into micropores (<2nm), mesopores (2-50nm) and macropores (>50nm) [104]. The pore size distribution of the material is estimated by the Barrett-Joyner-Halenda (BJH) method from the desorption data of the BET test, as shown in **Fig. 3.3**. The pore structure properties of the material are shown in **Table 3.2**. As shown in **Fig. 3.3**, most of the pores of the PS and SS are less than 10 nm, which indicates that they may have better adsorption capacity compared to the ES and the M. Generally, the mesopores mainly play the role of the channel for the solution to enter the interior of the PS. Most of the pore volume of the ES and M is less than 50 nm, and they are in the range of mesopores. Heat treatment reduces the pore volume and pore size of the M, consequently increasing the specific surface area, as shown in **Table 3.2**. Therefore, the M-3hour may have better uptake of pollutants because of the well-developed mesoporous structure and high specific surface area compared to the untreated M [69].

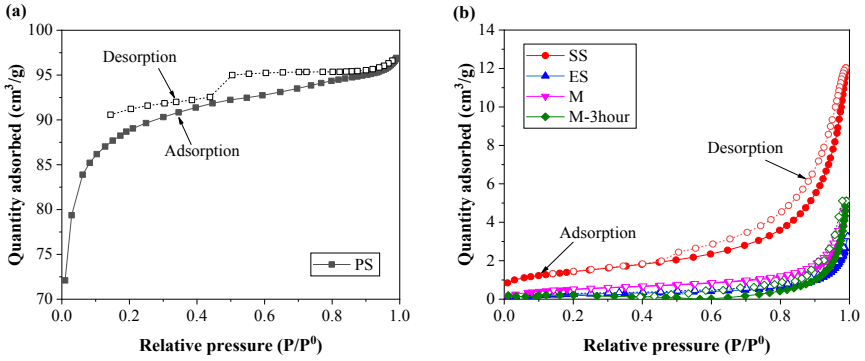

Fig. 3.2 The nitrogen adsorption-desorption isotherms of the material.

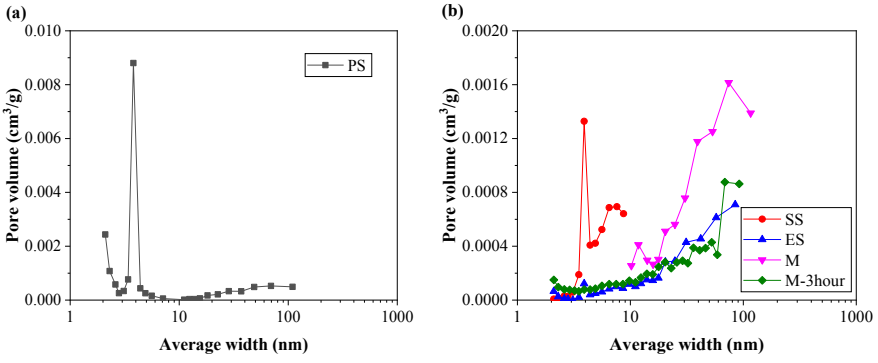

Fig. 3.3 The Barrett-Joyner-Halenda (BJH) pore size distribution of the material.

3.3.2 P-adsorption

- *Effect of different materials on adsorption*

The P-adsorption amount and removal fraction of the material after 24 h in a P solution of 50 mg/L are shown in **Fig. 3.4**. The results show that the SS and ES have a higher amount for P removal compared with other bio-materials. The P-removal fraction of P with the SS is 100%, while the adsorption capacity of other materials for P removal is very limited, with a range of 8%-19%. The high P adsorption capacity of the SS is attributed to the calcium ions leached from the SS surface, which can be bound with P ions in the solution to form a stable precipitate [100,105].

Table 3.2 Physical properties of materials.

Materials	BET surface area (m^2/g)	Micropore area (m^2/g)	Pore size (nm)	Pore volume (cm^3/g)
PS	297	237	2.0	0.15
SS	5.1	0.6	13.2	0.002
ES	1.0	0.1	14.5	0.004
M	0.1	0.5	30.7	0.007
M-3hour	2.0	1.4	12.8	0.006

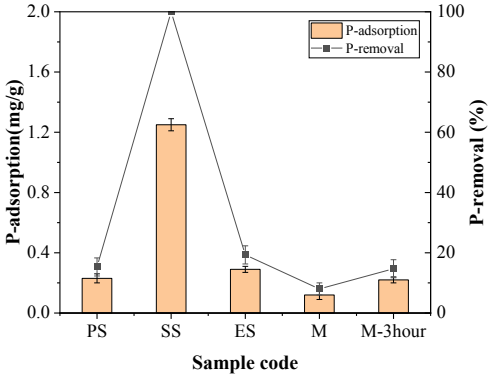

Fig. 3.4 P-removal capacity and rate of the material in the P solution of 50mg/L. (Adsorbent: 1g, P solution volume: 25 ml, Revolution per minute: 225, Time: 24 hours).

Some metals ions such as K, Na and Mg ions do not significantly affect the P-adsorption capacity [106,107], whereas metal ions (i.e. Ca, Fe, Al) released from the materials have a strong affinity with P. Previous studies have reported that the relative effects of the different cations on P-adsorption capacity [106], with the order of Ca > Mg > K > Na [108]. Hence, among the metal ions, the Ca^{2+} concentration is one of the key parameters for the Ca-P precipitation [43]. Although sodium ions are also leached from the solution of the SS, the sodium ions have no significant effect on the adsorption of P, as reported

by Bowden et al. [27] and Yin et al. [105]. For the SS, the P-removal capacity is dominated by a chemical process, a large amount of calcium ions leach from the SS surface to supply enough dissolved calcium ions to the solution and react with phosphate and precipitate in the form of hydroxyapatite following the chemical reactions [43]:

$$CaO + H_2O \rightarrow Ca^{2+} + 2OH^- \quad (3.10)$$

$$5Ca^{2+} + 3PO_4^{3-} + OH^- \rightarrow Ca_5(PO_4)_3(OH) \downarrow \quad (3.11)$$

However, the PS and M are organic matter, which is mainly composed of C, N and O elements, indicating that the P-removal is achieved by pore-filling and electrostatic attraction [109]. The high specific surface area and more mesoporous structure are crucial for improving the uptake capacity of P [102]. The results confirm that the M-3hour increases the adsorption capacity compared to the M. Previous research shows that the bio-materials made from bamboo, maize residue and soybean stover have a low P-removal rate with a range of 2-9% [102]. The results also indicate that the SS has better P-adsorption capacity and adsorption efficiency compared to lightweight aggregates and bio-materials.

- *Adsorption isotherms*

The adsorption isotherms of the materials are presented in **Fig. 3.5**. The results show that the P-adsorption amount increases as the initial P concentration increases. However, the P-removal fraction decreases with the increase in P concentration. At the initial P concentration of 700 mg/L, the maximum adsorption amount of the SS is 9.8 mg/g, while the adsorption amount of other materials varies from 1.5 mg/g to 1.8 mg/g. When the initial P concentration is less than 200 mg/L, the P-removal fraction of the SS reaches 100%. When the initial P concentration further increases, the P-removal fraction of the SS decreases. For instance, the removal fraction of the SS slows down to about 55% at the initial P concentration of 700 mg/L.

The P-adsorption isotherms are analyzed by Langmuir and Freundlich equations, respectively, as shown in **Fig. 3.6**. The Langmuir and Freundlich isotherm parameters for P-adsorption are presented in **Table 3.3**. The results show that both Langmuir and Freundlich models fitted the experimental data well with a very high correlation coefficient (R^2). The estimated maximum adsorption amount of the SS is 20.4 mg/g according to the Langmuir model. The maximum adsorption capacity of the M-3hour is very close to that of the PS. The extraction of P from the M and the M-3hour may more easily occur than other materials because of the low holding capacity [102].

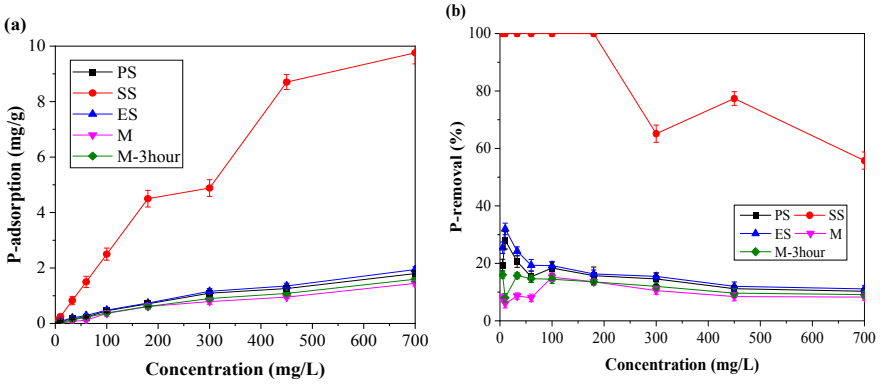

Fig. 3.5 The adsorption isotherms of the materials (a) P-removal amount and (b) P-removal fraction (Adsorbent: 1g, P solution volume: 25 ml, Revolution per minute: 225, Time: 24 hours).

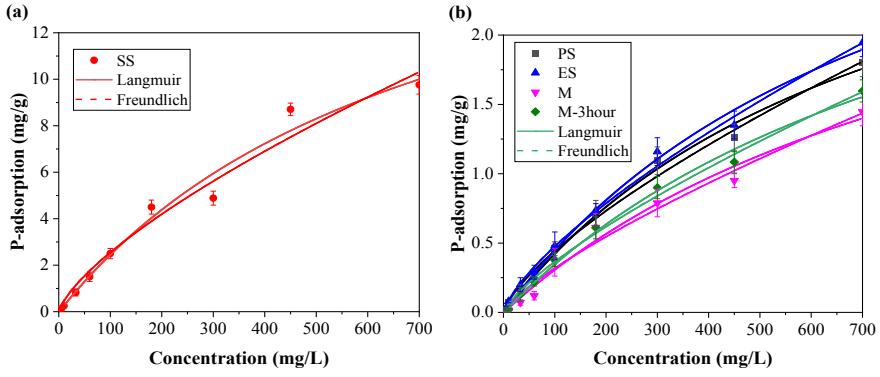

Fig. 3.6 The Langmuir and Freundlich isotherms of the materials.

Table 3.3 Langmuir and Freundlich isotherm parameters of the materials.

Materials	Langmuir model			Freundlich model		
	Q_m	K_L	R^2	K_F	n	R^2
PS	3.7	0.0013	0.99	0.02	1.39	0.99
SS	20.4	0.0014	0.98	0.10	1.40	0.97
ES	4.1	0.0013	0.99	0.02	1.39	0.99
M	3.4	0.0010	0.98	0.01	1.30	0.98
M-3hour	3.7	0.0011	0.99	0.01	1.33	0.99

- *Adsorption kinetics*

Kinetic studies are usually used to evaluate the relationship between reaction time and the maximum adsorption amount [102]. The adsorption fraction of the adsorbent usually increases rapidly during the initial reaction time and then slowly reaches equilibrium [110]. As shown in **Fig. 3.7**, the adsorption amount of all materials

increases as the reaction time increases. At the end of 2 hours, the adsorption amount of the SS only reaches 52% of the adsorption equilibrium amount. The results also show that the adsorption fraction of the SS gradually reduces with contact time increases until reaching the equilibrium after 16 hours. The equilibrium time of the SS and ES are significantly longer than that of bio-materials. The varying equilibrium time may be attributed to the distinguishing characteristics of the materials, which leads to different adsorption processes and adsorption mechanisms [105].

However, the adsorption amount of the M rapidly increases in the first 2 hours, which reaches 92% of the adsorption equilibrium amount. Previous research reported that the adsorption amount of the peanut shell biochar exceeds 80% of its maximum adsorption amount within the first 4 hours [102]. This is attributed to a large amount of mesopores available for adsorption at the first contact time [110]. Moreover, the high water absorption of the M results in the mesopores being rapidly filled by the P solution in the first 2 hours, and then the adsorption fraction rapidly decreases until reaching equilibrium. However, the use of the SS to remove P is a slow and continuous process, indicating sufficient calcium ions gradually leach from the SS surface and then react with P for the precipitation-coagulation process. Besides, the precipitation also needs time to finish the reaction [111]. Therefore, as long as calcium ions are continuously released from the SS surface, the P-removal process will keep proceeding.

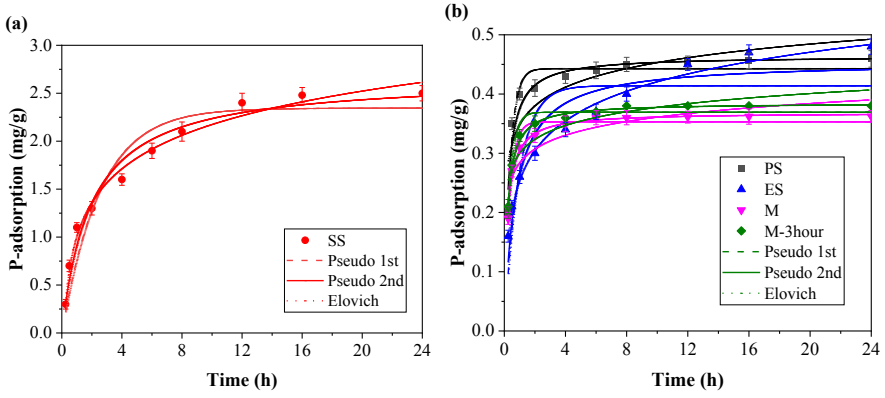

Fig. 3.7 Adsorption kinetics of the materials.

The experimental data are matched by the pseudo-first-order, pseudo-second-order and simple Elovich kinetic models. As shown in **Fig. 3.7**, the experimental data of P-adsorption in this study can be described well by the pseudo-second-order kinetic model. The evaluated kinetic parameters are presented in **Table 3.4**. The values of the calculated adsorption amount are close to the experimental data according to the

pseudo-second-order model. Although the Elovich model also can fit the adsorption kinetic data of the SS and the ES, the fitting quality for the M and PS is poor.

Table 3.4 Kinetic parameters of the materials.

Materials	Pseudo-first-order			Pseudo-second-order			Elovich		
	Q	K_1	R^2	Q	K_2	R^2	α	β	R^2
PS	0.44	2.7	0.95	0.46	9.2	0.93	0.35	0.05	0.72
SS	2.35	0.4	0.92	2.67	0.2	0.97	1.02	0.50	0.99
ES	0.41	1.1	0.74	0.46	3.0	0.89	0.26	0.07	0.99
M	0.35	2.9	0.94	0.37	12.9	0.99	0.29	0.03	0.79
M-3hour	0.37	3.0	0.94	0.39	13.3	0.99	0.30	0.03	0.81

- *Effect of pH on adsorption capacity*

The high pH causes the adsorbent surface to carry a more negative charge, which significantly repulses negatively charged solutes, consequently, a high pH generally reduces the adsorption amount of P due to the presence of repulsive forces [112]. As shown in **Fig. 3.8**, the adsorption amount of all materials decreases by 11%-19% when the pH value increases from 3 to 11. This result is consistent with previous studies reported by Yin et al. [105] and Bolan et al. [113], with a maximum P-adsorption amount appearing at a pH value of around 3-4. When the pH value of the solution is less than 2, the species of the P predominantly exist in H_3PO_4, which is difficult to attach to exchange sites for anion exchange. When the pH value varies from 3 to 5, the $H_2PO_4^-$, HPO_4^{2-} and PO_4^{3-} are major species for the P solution, which are available for ion exchange, especially $H_2PO_4^-$. When the pH value is more than 8, the more OH^- ion exists in solution, which may compete with the species of the P for ion exchange, resulting in the reduction in the P-adsorption [114].

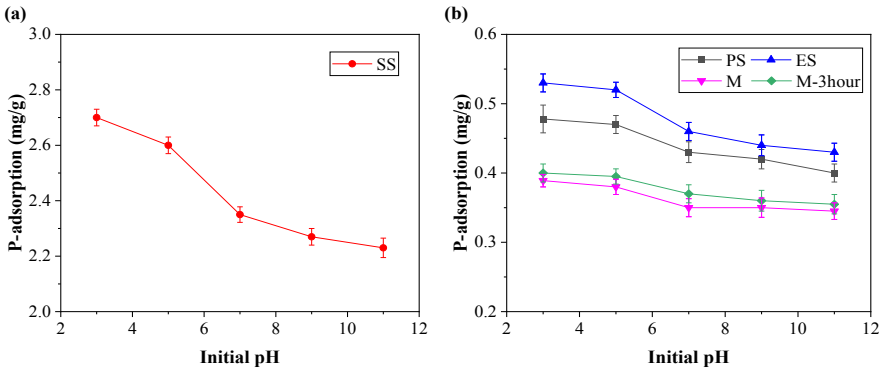

Fig. 3.8 Effects of pH values on the adsorption amount (Adsorbent: 1g, P solution: 25 ml, Initial P concentration: 100 mg/L).

The results also show that the adsorption amount of the SS reduces sharply when the pH values of the P solution change from acidic to alkaline. Previous studies indicate that the amount of Ca^{2+} ions leaching from the adsorbent decreases with an increase in the pH value of the initial solution [105,115]. Moreover, when the pH value of the solution decreased, the positively charged surface sites formed on the adsorbent promote P-adsorption because of the electrostatic attraction [115]. An approximate 20% reduction in P adsorption amount is observed in the calcium-rich sepiolite adsorbent [105]. This is because the positive charge surface of the adsorbents is more easily combined with P in an acidic solution due to electrostatic attraction [115]. Besides, the types of P ions in the solution are affected by the pH value of the solution. When the pH value varies between 3 and 7, the predominant species of P are negatively charged $H_2PO_4^-$, which could react with the dissolved Ca^{2+} to form the precipitation.

3.3.3 P-desorption

The P-desorption amount and desorption fraction of the material are shown in **Fig. 3.9**. The results show that the P-desorption fraction of the M and the M-3hour is significantly higher than that of other materials, which are more than 60%. This phenomenon indicates that the M is an unstable physical absorption, and the adsorbed P could easily be desorbed from the M, which is a reversible adsorption process, resulting in secondary pollution in the aquatic environment. It should be noted that no desorbed P is detected in the SS solution, which confirms that the combination of Ca-P is a stable precipitation process and barely desorption occurs once bonding is formed [105,116]. Therefore, the SS can be safely used as adsorptive aggregates in concrete for P-removal from water and no secondary pollution occurs.

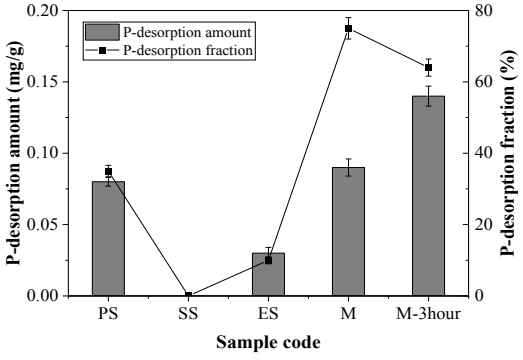

Fig. 3.9 The P-desorption amount and desorption fraction of the material (Adsorbent: 1g, Distilled water: 25 ml, Revolution per minute: 225, Time: 24 hours).

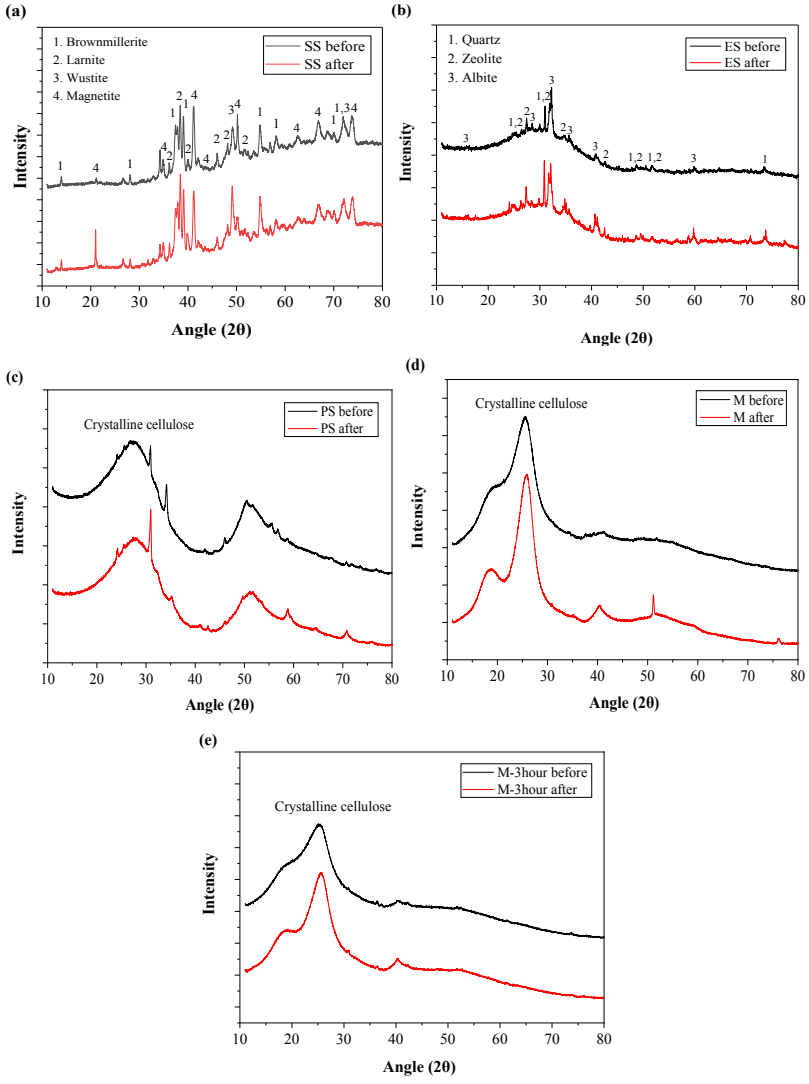

Fig. 3.10 The XRD patterns of the material before and after the test (a) SS, (b) ES, (c) PS, (d) M and (e) M-3 hour.

3.3.4 Characterization of the adsorbents after P-adsorption

- *Mineralogical phase analysis*

The main mineral components of the SS are brownmillerite, larnite, wustite and magnetite, as shown in **Fig. 3.10a**. The adsorption effect of the SS on P can be explained by the hydrolysis of calcium-containing oxides [117]. The calcium-containing oxides are involved in the P-removal by chemical bonding on the surface or chemical reaction

with the surface, which leads to a better adsorption capacity of the SS than other materials. The crystalline compounds of the ES are quartz, zeolite and albite, but the ES is predominantly amorphous. Metal elements such as sodium, potassium and aluminium also contributed to the P-adsorption [118].

Similar to other bio-materials such as wood, soybean, bamboo, etc., the structure of the PS is crystalline cellulose and a distinct peak appears near the diffraction between 25° and 30°. The shape of the diffraction curve of the M and M-3hour is similar to that of the PS. The M-3hour shows a wide diffraction peak compared to the M due to the heat treatment effect [59,119]. PS and M are mainly composed of C and O, which account for about 90% of the total dry weight [120,121]. They cannot react with P to form a new crystal structure. Therefore, the changes in the peaks of the M and the M-3hour after P-adsorption near the diffraction angle of 18° and 40° are caused by the amorphous P on the surface or micropores of the material [117].

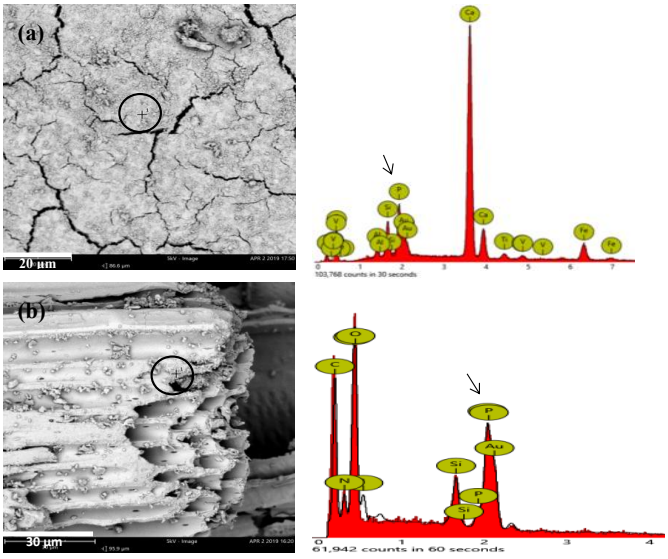

Fig. 3.11 The SEM images and EDS analysis of the material after adsorption test (a) SS and (b) M-3hour.

- *SEM-EDS analyses*

The SEM images and the EDS analyses of the material after P adsorption are shown in **Fig. 3.11**. Several small spots are selected and analyzed on the surface of the materials and a crystalline substance appears distributed on the M-3hour surface. The finely distributed P crystals are observed on the surface of the SS by EDS analysis, which is the precipitate of Ca/P/O. The same phenomenon is also observed by other researchers

in other materials, such as furnace slag [111], oil-shale ash [99], and sepiolite [105], namely suspended Ca-P precipitation formed on the surface of the adsorbent after P-adsorption. In this study, the strong peak of P is observed in all EDS spectra and the P is detected on the surface of all materials. The surface structure of the SS has no significant effect on the P-adsorption, the chemical adsorption is predominant to the SS for P adsorption due to the dissolution of calcium and precipitation of hydroxyapatite [43].

3.3.5 Low-cost materials used for P-adsorption

Table 3.5 Low-cost materials used for P-adsorption.

Materials	Particle size (mm)	Adsorption capacity (mg/g)	Initial concentration (mg/L)	Agitation mode (rpm)	Contact time (h)	P-removal (%)
Industrial materials						
Steel slag this study	1-2	9.8	700	225	24	55
Furnace slag [111]	0.8-2.3	2.8	-	4000	24	-
Steel slag [43]	5-10	2.5	100	125	24	>90
Furnace slag [122]	<5	8.9	400-600	200	24	-
Fly ash [12]	<0.3	32	400	120	16	-
Coal ash [29]	<2.8	0.9	35-45	-	12	-
Synthetic materials						
Fe-Cu binary oxide [9]	Powder	35.2	30	160	24	-
Aluminium oxide [123]	Powder	35	8	600	4	-
Iron hydroxide [8]	Powder	28.8	-	-	24	-
Natural materials						
Palygorskite [115]	<0.15	42	1000	200	24	-
Modified sepiolite [105]	<0.15	32	100	160	24	86
Quartz sand [48]	0.5-2	0.3	25	140	24	87.7
Bio-based materials						
Peanut shell [102]	Powder	3.8	5	200	48	61.3
Bamboo [124]	Powder	<2.5	6.5	200	24	42.15
Juniper fiber [125]	Powder	<0.5	10	150	24	-
Date palm fiber [126]	Powder	1.8	50	200	2	-

The low-cost materials used for P-adsorption including industrial by-products, synthetic materials, natural and bio-based materials are presented in **Table 3.5**. The results indicate that the SS generally has better P adsorption capacity than most of the bio-materials and unmodified natural materials, but lower than synthetic materials and modified natural materials. SS is known for its volume instability by hydration reaction of free-lime phase and also has issues with leaching. The same negative properties as the synthetic and modified aggregates. Although synthetic materials have higher

adsorption capacity, they are powdery and are not suitable for application as aggregates in concrete. Similar to the modified natural aggregates coated with chemical solvents, the use of synthetic materials in concrete may lead to secondary pollution of the water environment [119].

Bio-based activated carbon such as bamboo, juniper fibre and date palm fibre has been widely used as adsorbents in water treatment, but the adsorption capacity of bio-materials is relatively limited compared to the SS. Besides, they are generally elongated and flaky particles, and their application as aggregates results in a weak interfacial transition zone and low mechanical properties of concrete [59]. However, the granular SS has a much higher strength than other biological materials, which is feasible to be directly used as aggregates in concrete. Therefore, SS can be considered as an effective adsorptive aggregate to replace the non-adsorptive aggregate for increasing the P-removal of adsorptive concrete because of its excellent mechanical and adsorption properties.

3.4 Conclusions

(1) BOF steel slag exhibits a high P-adsorption capacity and adsorption efficiency, compared to lightweight aggregates and bio-based materials. Adsorption kinetics are fitted well by the pseudo-second-order kinetic model. Steel slag has very low P-desorption, indicating that it can be used safely as adsorptive aggregates in concrete for P-removal.

(2) The steel slag adsorption mechanism is attributed to Ca^{2+} leached from the SS surface, which can react with phosphate to form Ca-P precipitate. Moreover, the chemisorption process is continuous and stable, indicating that enough calcium ions gradually leach from the steel slag surface and then react with phosphate for the precipitation-coagulation process. It is proposed that steel slag can serve as effective adsorptive aggregates in the production of highly adsorptive concrete.

(3) Heat treatment can be used to increase the adsorption capacity of the miscanthus. The adsorption amount of the miscanthus after a 3-hour heat treatment increases from 3.4 mg/g to 3.7 mg/g due to the change in pore structure characteristics. P-adsorption of bio-based materials follows a physical adsorption mechanism because of the well-developed mesoporous structure and high specific surface area. However, high water absorption of the miscanthus results in rapid P-adsorption in the initial reaction time, as well as high P-desorption.

Chapter 4 A facile manufacture of highly adsorptive aggregates using steel slag and porous expanded silica for phosphorus removal

Natural adsorptive materials are mainly based on physical adsorption and have limited adsorption capacity. Artificial adsorptive aggregates possess great potential in improving water quality for pollutant removal from stormwater. This chapter aims to develop a porous and sustainable adsorptive aggregate combining both chemical and physical adsorption capacities. Industrial by-product steel slag (SS) powder is used in conjunction with porous expanded silicate (ES) powder applying a non-sintered pelletizing method for producing sustainable highly adsorptive aggregates, and bio-based miscanthus (M) is applied to further increase its permeability and porosity. The results show that the bulk density of the resulting adsorptive aggregates varies from 570 kg/m^3 to 882 kg/m^3, with a bulk crushing strength of up to 5.1 MPa. Moreover, all adsorptive aggregates have outstanding resistance to salt and freeze-thaw cycles. Phosphate adsorption tests show that the adsorptive aggregates remove the P in an aqueous solution. The present result demonstrates that sustainable highly adsorptive aggregates with good mechanical properties can be produced by applying the facile pelletizing method, suitable for the application in adsorptive concrete.

This chapter has been published as:

F. Wu, Q.L. Yu, F. Gauvin, H.J.H. Brouwers. A facile manufacture of highly adsorptive aggregates using steel slag and porous expanded silica for phosphorus removal. Resources, Conservation and Recycling, 166, 105238, 2021.

4.1 Introduction

To recycle industrial wastes and develop sustainable adsorbent materials, the adsorption characteristics of industrial by-products, such as steel slag (SS), fly ash and expanded clay, have been investigated in recent years [27–29]. Among these materials, the SS exhibits an excellent adsorption capacity for pollutants and has been used as a filter for water purification in the field of wastewater treatment [30–32]. However, calcium ions for the hydroxyapatite precipitation are mainly released from the surface of the SS. The release of Ca^{2+} from the SS is not always sufficient during P-removal [43] because of the dense structure of the SS. Moreover, the adsorption capacity of the material usually increases as the particle size decreases, because of the increase in specific surface area [127]. The adsorption capacity of the SS is attributed to chemical adsorption, which is effective for specific pollutants, such as phosphate [45]. The aqueous solution usually contains a variety of pollutants, such as organic pollutants, nitrate, phosphate and heavy metals. Physical adsorption also plays an important role in adsorptive aggregates because it utilizes well-developed micropores for pollutant removal. Therefore, a combination of high-adsorption SS powder and porous materials produces artificial adsorptive aggregates with both chemical and physical adsorption capacity, which not only significantly reduces the density of the adsorptive aggregates for easy transportation but also makes the polluted water more easily in contact with the SS, will result in more calcium precipitated for the formation of Ca-P precipitation.

High permeability and porosity are essential for adsorptive aggregates because the pollutants can more easily penetrate inside the adsorptive aggregate, and then the pollutants in the water can be quickly absorbed by the adsorbent material within the adsorptive aggregate. Moreover, the increase in micropores of adsorptive aggregates can adsorb contaminants through pore-filling and electrostatic attraction [109]. Bio-based materials can significantly increase the permeability and porosity of the cement paste due to the well-developed micropores [59,128]. Previous studies show that ground miscanthus (M) exhibits high porosity and lightweight properties due to the high content of porous parenchyma with a pore size of approximately 50 μm [62]. Besides, the M powder can absorb about 5 times water of its weight, indicating high adsorption potential for pollutant removal from wastewater. The adsorption capacity of the M for Cd can reach 13.2 mg/g after slow pyrolysis with a temperature of more than 500 ℃ [129]. Besides, the M has a better adsorption capacity for heavy metals removal and rapidly reaches equilibrium within 5 minutes [19]. Therefore, the M can be used to further increase the permeability of the adsorptive aggregate, making pollutants easily penetrate the adsorptive aggregate and be adsorbed and precipitated by the adsorptive

aggregate.

This chapter aims to develop a porous and sustainable adsorptive aggregate combining both chemical and physical adsorption capacity for the improvement of the P-removal performance of adsorptive concrete. Basic Oxygen Furnace (BOF) steel slag (SS) powder is used in conjunction with porous expanded silicate (ES) powder by non-sintered pelletizing for the manufacture of high adsorptive aggregates and the miscanthus (M) is used to further increase its permeability and porosity. The physical properties, mechanical strength, durability characteristics, and P-removal capacity of adsorptive aggregates are investigated. The mineralogical phase and microstructure of adsorptive aggregates are analysed by XRD and SEM, respectively. The present research provides a high adsorptive aggregate with good mechanical properties and high P-removal performance, which is suitable for application in the field of stormwater purification such as adsorptive concrete, constructed wetlands or rainwater gardens.

4.2 Materials and methods

4.2.1 Materials

BOF steel slag (SS) (supplied by TATA Steel, The Netherlands) powder, a commercial lightweight expanded silicate (ES) powder and miscanthus (M) (supplied by Vibers, The Netherlands) are used as main components for the manufacture of adsorptive aggregates in this study. CEM I 52.5 R Portland cement (supplied by ENCI, The Netherlands) is used as the binder. The SS is mainly composed of calcium and iron oxides, while the ES mainly contains silicon and aluminium oxides. However, the interior of the ES and the M is porous, so it may be feasible to use them to reduce the density of the adsorptive aggregates and increase the permeability.

4.2.2 Adsorptive aggregates preparation

The specific density of the SS and ES are 3.9 g/cm^3 and 2.3 g/cm^3, respectively. To reduce the density of the adsorptive aggregate, three mixing proportions including different SS and ES content are investigated. Considering the total content of raw materials by weight is 100% when the SS content are 25% (SS25), 50% (SS50) and 75% (SS75) and the corresponding ES content are 75%, 50%, and 25%, respectively. To increase the permeability of the adsorptive aggregate, the raw miscanthus (M) and heat-treated miscanthus (HM) under nitrogen conditions at 250℃ for 3 hours are added to the mixture. The dosage of miscanthus in most mixtures is 3% of raw materials by weight (designated M3 in all Mix), except for the SS75M5 with 5% miscanthus. All

mixtures contain 15 wt.% added cement as binder. The mixture without any miscanthus (Mix No. with M0) is used as a control, including SS25M0, SS50M0 and SS75M0. The mix compositions of adsorptive aggregate are presented in **Table 4.1**.

Table 4.1 Mix compositions of adsorptive aggregates.

Mix No.	Composition (by weight)				
	RM[a]	M[b]/RM	W[c]/RM	Cement/RM	M Type
SS25M0		0%	15%	15%	-
SS25M3	25%SS[d]+75%ES[e]	3%	15%	15%	Raw
SS25HM3		3%	15%	15%	Heat-treated
SS50M0		0%	15%	15%	-
SS50M3	50%SS+50%ES	3%	15%	15%	Raw
SS50HM3		3%	15%	15%	Heat-treated
SS75M0		0%	15%	15%	-
SS75M3	75%SS+25%ES	3%	15%	15%	Raw
SS75HM3		3%	15%	15%	Heat-treated
SS75M5		5%	15%	15%	Raw

[a] Raw material, the mixture of steel slag and expanded silicate, [b] Miscanthus, [c] Water, [d] Steel slag
[e] Expanded silicate.
e.g. for SS25M3, SS25 indicates that the steel slag (SS) content in the mixture is 25%, and M3 means that the miscanthus (M) content is 3%. In other mixtures, HM3 indicates that the content of heat-treated miscanthus (HM) is 3%.

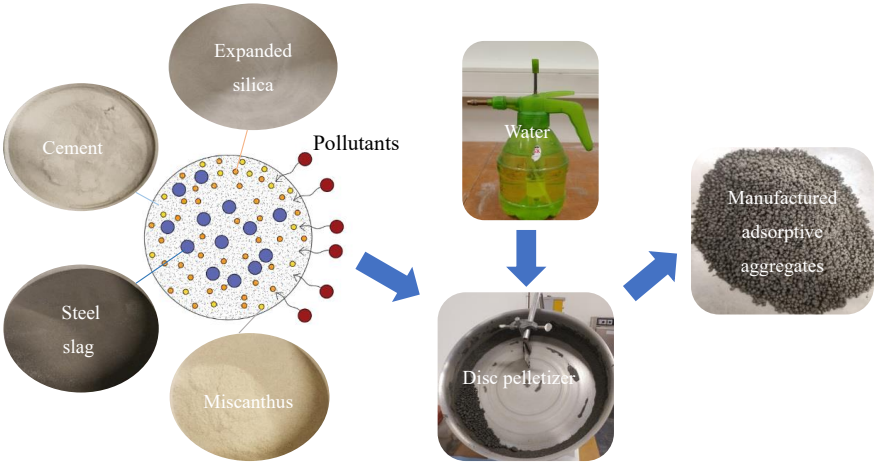

Fig. 4.1 The manufacturing process of the adsorptive aggregate.

The manufacturing process of adsorptive aggregates is shown in **Fig. 4.1**. Firstly, all raw materials are evenly mixed in a mixer for 3 minutes. Then, the disc pelletizer is turned on at a speed of 200 rpm and a small amount of water is sprayed on the surface of the rotating disc. When the mixture powder is added to the disc, water is immediately

sprayed on the dried powder surface to form spherical particles. After about 5 minutes, the particles are removed from the disc. After that, the mixture is added to the disc again and sprayed with water, and repeat the previous steps until enough particles are obtained.

4.2.3 Test methods

- *Physical properties test*

The particle size distribution of adsorptive aggregates is determined by the sieving method according to EN 933-1:2012, and the mesh size is 16 mm, 8 mm, 5 mm, 3 mm and 1 mm, respectively. The particle density is determined by using an AccuPyc II 1340 gas pycnometer. The bulk density and water absorption are determined according to EN 1097-6. Besides, the mineralogical phase of adsorptive aggregates is measured by XRD, and the microstructure is analysed by SEM.

- *Mechanical strength test*

The bulk crushing strength of adsorptive aggregates is determined according to EN13055:2016. When the adsorptive aggregate is used for adsorptive concrete, it may be prone to damage during mixing with other course or fine aggregates. The shearing strength is determined to evaluate the resistance to abrasion. The test process is as follows: firstly, 8 g of the adsorptive particles with a particle size of 3-5 mm is placed in the porcelain ball mill pot. Then, 20 g of porcelain is added to the ball mill pot. The ball milling is turned on with a milling speed of 140 rpm. The mass loss of the adsorptive particles is recorded at 1 min, 2 min, 4 min, 8 min, 12 min and 16 min, respectively.

- *Durability test*

When applied to adsorptive concrete, adsorptive aggregates will frequently contact water, especially polluted water, which would potentially lead to the disintegration of the adsorptive aggregate. In this study, a NaCl solution with a 5% concentration by weight is used to evaluate the durability of the adsorptive aggregate in the aqueous solution. The adsorptive aggregate with a size of 5-8 mm is used for the salt resistance test. The change in mass of the adsorptive aggregate is measured at 1, 3, 7, 10, 15, 20, 25 and 30 days.

When the adsorptive aggregate is applied in cold regions, the expansion of the water inside the saturated adsorptive aggregate during the freezing stage will generate expansion force, which will potentially damage the aggregate. Therefore, freeze-thaw resistance is an important index for evaluating the durability of adsorptive aggregates.

In this study, the resistance to freezing and thawing is determined according to EN 1367-1. The temperature of the freeze-thaw test is set from -17.5 ℃ to 20 ℃ and 24 hours for each cycle. The change in mass of adsorptive aggregates is measured at 1, 3, 7, 10, 15, 20, 25 and 30 freeze-thaw cycles, respectively.

- *Adsorption test*

Phosphate is a major pollutant in an aqueous solution, and it is used to simulate polluted water in this study. 1g of the adsorptive aggregate is added to a 25 ml P solution with an initial concentration of 168 mg/L. The mixture is stirred at 225 rpm in the thermostatic shaker for 24 hours and then filtered by a 0.45 μm membrane. The extracted supernatant is used for analysing the P concentration by using IC. The mineralogical phase and microstructure of SS50M3 after the adsorption test is measured by XRD and SEM-EDS, respectively, for analysing the adsorption mechanism. The P-adsorption amount (q, mg/g) and P-removal fraction (P_R, %) are calculated by Eqs. (3.1) and (3.2), respectively.

The ions leached from adsorptive aggregates are determined according to EN 12457-2 by ICP-AES. The adsorptive aggregates and deionized water are mixed with a liquid-solid ratio of 10, using a dynamic shaker with a speed of 250 rpm for 24 hours. The leachates are filtered by the 0.22 μm filter and acidified with concentrated HNO_3 for the leaching test.

4.3 Results and discussion

4.3.1 Physical properties of adsorptive aggregates

- *Particle size distribution*

According to the EN standard (EN12620:2002), aggregates with a particle size of less than 4 mm are defined as fine aggregates, and larger than 4 mm are coarse aggregates. As shown in **Fig. 4.2**, the diameter of most adsorptive particles mainly distributes from 1 mm to 4 mm, which accounts for 56%-80% of the total particle size distribution. Adsorptive particles with a size of 4 mm-16 mm account for 20%-41%, while adsorptive particles with a size of more than 16 mm account for only 1%-7%. Moreover, when the adsorptive particle size is less than 8 mm, the shape of the adsorptive particles is mainly spherical, while the particles are larger than 8mm, the flatness of the adsorptive particles increases, as shown in **Fig. 4.3**.

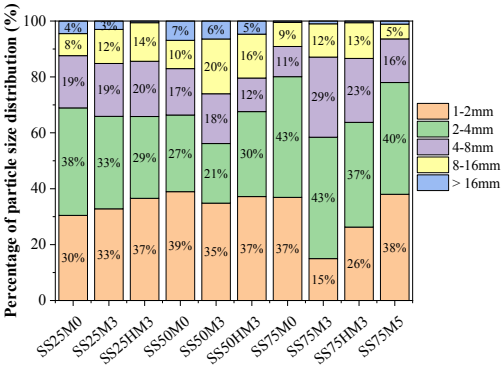

Fig. 4.2 The particle size distribution of adsorptive aggregates.

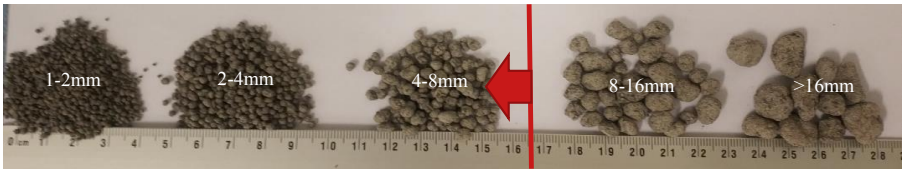

Fig. 4.3 SS50NoM adsorptive particle.

- *Mineralogical phase analysis*

The X-ray diffraction patterns are shown in **Fig. 4.4**. The results show that the mineralogical phase of all materials contains calcium silicate hydrate (C-S-H) and calcium hydrate (CH) as cement is used as a binder for all mixtures. However, there are significant differences in diffraction peaks at diffraction angles of 13°, 22°, 32°, 55°, 67° and 72°. When the steel slag content increases from 25% (SS25) to 75% (SS75), the diffraction peaks at 13° and 32° are significantly reduced, and the diffraction peaks at 22°, 55°, 67° and 72° are increased. This is because when the steel slag content is 25%, the composition of the material is mainly expanded silicate (75%), which is predominantly amorphous with minor quartz, zeolite and albite, so more obvious diffraction peaks at 13° and 32°. However, the main components of steel slag are oxides of calcium and iron. When the content of steel slag is 75%, more larnite, magnetite, brownmillerite and wustite are observed at a diffraction angle of 22°, 55°, 67° and 72°.

- *Densities*

The density of the adsorptive aggregates is shown in **Fig. 4.5**. As expected, the addition of miscanthus reduces the density of the adsorptive aggregates, especially the heat-treated miscanthus (HM3). Because the heat treatment decomposes organic matter and increases the microporous structure of miscanthus [130]. Moreover, the density of the

adsorptive aggregates increases significantly with the increase of the steel slag content because the density of steel slag (SS) is much higher than that of lightweight expanded silicate (ES). The apparent density of the adsorptive aggregates varies from 1933 kg/m^3 to 2633 kg/m^3, and bulk density ranges from 570 kg/m^3 to 882 kg/m^3. EN 13055 stipulates that materials with a particle density lower than 2000 kg/m^3 or a loose bulk density lower than 1200 kg/m^3 can be used as lightweight aggregates. Although most of the adsorptive aggregates have a density of more than 2000 kg/m^3, the bulk densities are within the range of lightweight aggregates, therefore they may be used to produce lightweight aggregate concrete (LWAC).

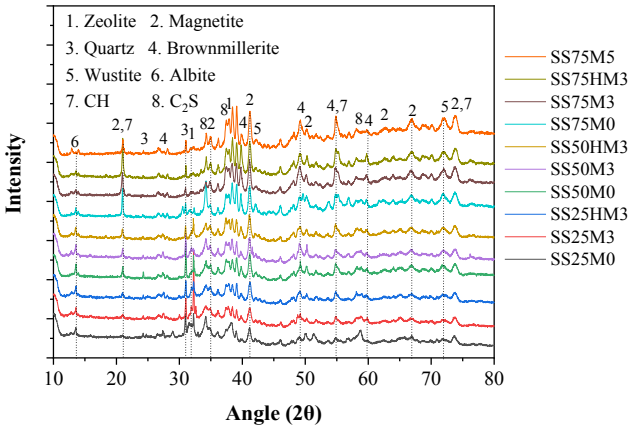

Fig. 4.4 XRD patterns of adsorptive aggregates.

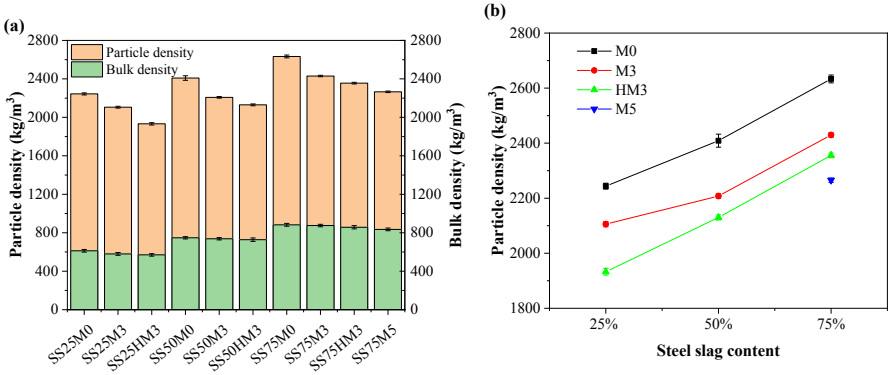

Fig. 4.5 Density of adsorptive aggregates.

- *Water absorption*

For ordinary aggregates, high water absorption generally reduces the workability and mechanical properties of concrete, as well as increases the micropores inside the

concrete. However, for adsorptive aggregates, high water absorption means that the polluted water can quickly penetrate the interior of the adsorptive aggregate and react with the adsorbent materials for pollutant removal. As shown in **Fig. 4.6**, all adsorptive aggregates have high initial water absorption, and the water absorption gradually increases with time. Nevertheless, after 8 hours, the increase in water absorption becomes insignificant. This phenomenon indicates that all adsorptive aggregates have a microporous structure, which can quickly absorb polluted water during the initial contact with the aqueous solution. The same phenomenon is observed in artificial dredged sediment aggregates [131]. Moreover, with the increase of steel slag content, the water absorption gradually decreases. This may be due to the dense structure of the steel slag, which leads to the low water absorption of the steel slag. Hoff [132] reported that the 24-h water absorption of structural-grade lightweight aggregates varies from 5% to 25%. In this study, except for SS25M3 and SS25HM3, the water absorption of other adsorptive aggregates is similar to the Hoff range for lightweight aggregates.

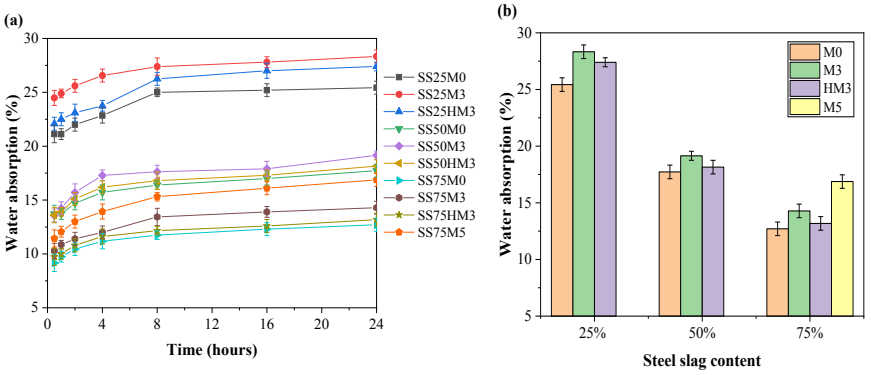

Fig. 4.6 Water absorption of adsorptive aggregates.

- *Microstructure*

As shown in **Fig. 4.7**, a lot of micropores exist inside the adsorptive aggregates, which is the reason for the high water absorption. These micropores are mainly formed by the porous structure of lightweight expanded silicate and the weak bonding between steel slag or miscanthus and cement paste. For most adsorption materials, the chemical composition, microporous structure and pore characteristics are critical for the adsorption capacity [100]. Compared to ordinary aggregates, the micropores can be used as a channel for polluted water to enter the interior of the adsorptive aggregates. Once polluted water is in contact with steel slag, porous expanded silicate and miscanthus, it can be adsorbed by chemical or physical adsorption.

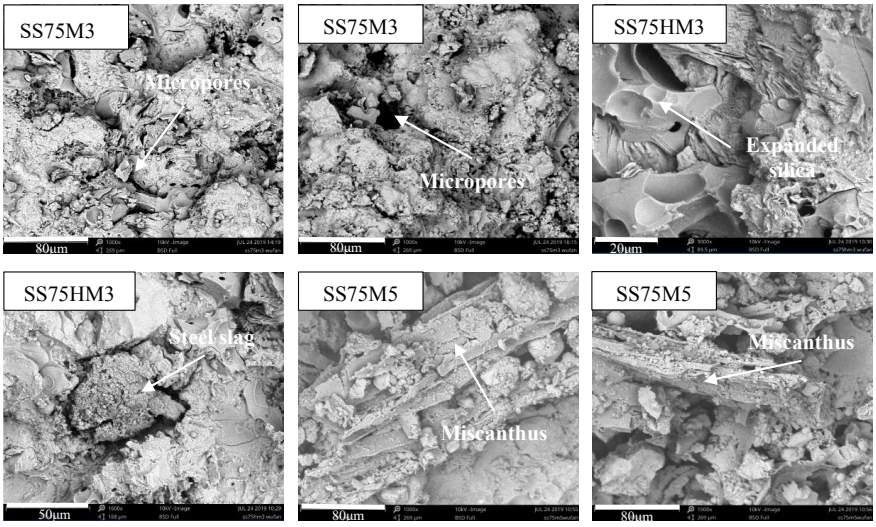

Fig. 4.7 SEM micrographs of adsorptive aggregates.

4.3.2 Mechanical properties of adsorptive aggregates

- *Bulk crushing strength*

As shown in **Fig. 4.8**, the bulk crushing strength of all adsorptive aggregates varies from 1.9 MPa to 5.1 MPa. When steel slag content increases, the bulk crushing strength increases significantly due to the high strength of steel slag. Steel slag contributes to the high bulk crushing strength of adsorptive aggregates and the addition of miscanthus significantly weakens the bulk crushing strength. When the content of miscanthus is 5%, SS75M5 has a minimum bulk crushing strength of 1.9 MPa, which is 63% lower than the adsorptive aggregate without any miscanthus (SS75M0).

Generally, sintered artificial lightweight aggregates have better mechanical strength than non-sintered aggregates. Lau et al. [133] showed that the lightweight aggregate made of palm oil fuel ash and lime-treated sewage sludge possesses a crushing strength of 8.1 MPa. Lo et al. [134] reported that the high-calcium fly ash aggregates sintered at the temperature of 1150℃ have a crushing strength of 6.3 MPa. Although sintered artificial aggregates usually possess high mechanical strength, fossil fuels are consumed for providing high temperatures, accompanied by high carbon emissions. Peng et al. [131] manufactured non-sintered dredged sediment aggregates with a crushing strength varying from 0.3 MPa to 2.5 MPa. Therefore, the mechanical strength of the adsorptive aggregates manufactured in this study is significantly better than ordinary non-sintered artificial aggregates.

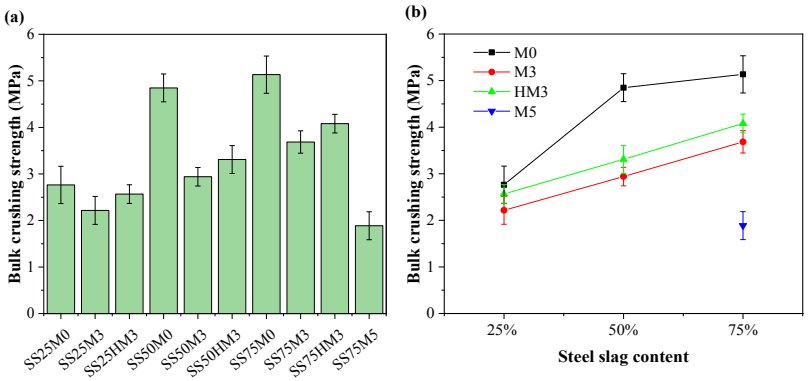

Fig. 4.8 Bulk crushing strength of adsorptive aggregates.

- *Shearing strength*

The percentage of damage of adsorptive aggregates is shown in **Fig. 4.9**. The results show that the percentage of damage of all adsorptive aggregates increases with time. When steel slag content is 25%, the abrasion of adsorptive aggregates increases rapidly within the first 4 minutes and further increases slowly till 16 minutes. This may be because high-density steel slag plays a core role in the process of particle formation, and low-density expanded silicate is wrapped on the surface of the steel slag during the disc rotation. Therefore, low-strength expanded silicate on the outer surface of adsorptive aggregates is more likely to be damaged first, leading to a rapid decrease in mass during the first 4 minutes. For the adsorptive aggregates containing 75% steel slag, the percentage of damage increases more linearly with time, which indicates that they have better abrasion resistance.

4.3.3 Durability of adsorptive aggregates

- *Salt resistance*

The mass losses of adsorptive aggregates during the salt resistance test are shown in **Fig. 4.10**. The results show that the increase in steel slag content improves the resistance of the adsorptive aggregate to salt attack. This may be because the high content of porous expanded silicate significantly increases the porosity of adsorptive aggregates, and NaCl penetrates the adsorptive aggregate easily, resulting in severe erosion of the adsorptive aggregate. In addition, the addition of 5% miscanthus significantly reduces salt resistance. SS75M5 has a maximum mass loss of 9% when exposed to a 5% NaCl solution for 30 days, while the mass loss of other mixtures ranges from 2% to 5%. This indicates that high miscanthus content significantly reduces the salt resistance of

adsorptive aggregates.

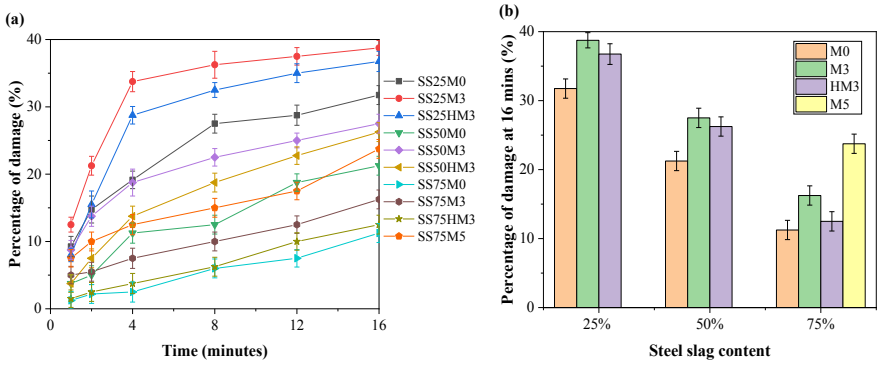

Fig. 4.9 Percentage of damage of adsorptive aggregates.

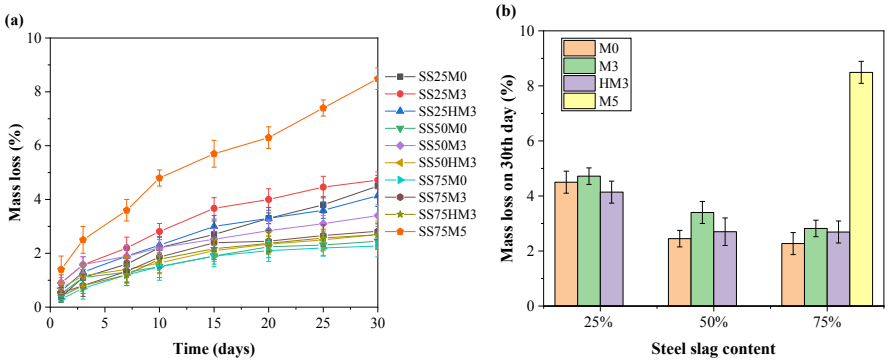

Fig. 4.10 Mass loss of adsorptive aggregates during salt resistance test.

- *Freeze-thaw resistance*

As shown in **Fig. 4.11**, the addition of 3% miscanthus slightly increases the mass loss during the freeze-thaw test. The resistance to freeze-thaw of SS75M5 is significantly lower than other adsorptive aggregates because 5% miscanthus significantly increases the porosity of the adsorptive aggregate, resulting in an increase in water absorption and a reduction in mechanical strength [128]. However, heat-treated miscanthus has no significant effect on mass loss compared to the adsorptive aggregate without any miscanthus (M0).

Generally, freeze-thaw resistance depends on the content of micropores, the degree of connectivity, and the pore characteristics [135]. Connected micro-cracks act as a path for water to transport inside of adsorptive aggregates. When the water in the micro-cracks is frozen and turns to ice, the expansion force causes freeze-thaw damage.

Compared to lightweight expanded silicate, the adhesion between steel slag and paste is weak, and obvious cracks exist in the interfacial transition zone (ITZ) between steel slag and mortar (**Fig. 4.7**). Due to the freeze-thaw expansion force, more micro-cracks are formed in the ITZ, which results in the adsorptive aggregate containing high content of steel slag being more easily damaged.

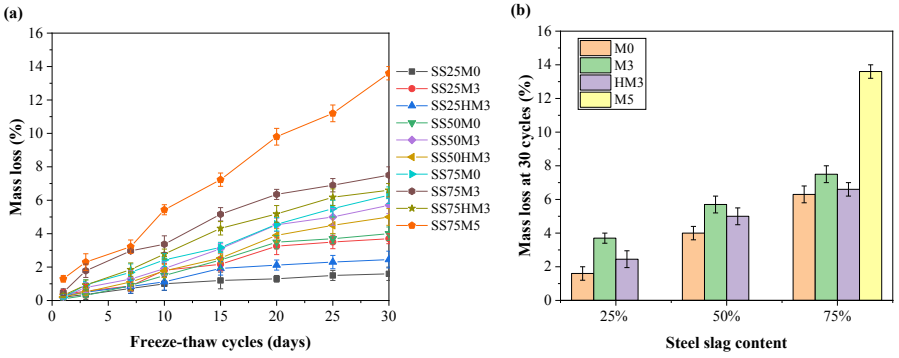

Fig. 4.11 Mass loss of adsorptive aggregates during freeze-thaw resistance test.

4.3.4 Adsorption of adsorptive aggregates

- *Adsorption capacity*

The results show that no P is detected in the solution after the adsorption test, and all P-solutions with an initial concentration of 168 mg/L are adsorbed by the adsorptive aggregate. The excellent adsorption capacity of the adsorptive aggregate is attributed to the calcium leached from the steel slag and cement paste, which can combine with the P to form Ca-P precipitates [27]. Moreover, the microporous structure of lightweight expanded silicate and miscanthus adsorb P through physical adsorption [136,137]. The adsorption capacity of bio-based materials is usually lower than that of industrial or synthetic materials, and the adsorption capacity for P-removal is generally 0.5-3.8 mg/g [124–126]. The adsorption amount of adsorptive aggregates in this study is 4.2 mg/g with an initial concentration of 168 mg/L P-solution, which is greatly higher than that of ordinary sand and bio-based materials, especially compared to the common concrete materials, indicating that it is possible to improve the P-adsorption capacity of concrete applying the developed adsorptive aggregates.

- *Adsorption mechanism*

The hydration products of cement are mainly hydrated calcium silicate (C-S-H) and calcium hydroxide (CH). After adsorption, the pH of the solution varies from 11.5-11.6,

11.6-11.7 and 11.8-11.9 for the SS25 series, SS50 series and SS75 series, respectively, while the initial pH of the phosphate solution is 5.2. Previous studies have shown that not all metal ions (i.e. K^+, Na^+ and Mg^{2+}) have significant effects on the adsorption of P, but some metal ions such as Ca^{2+}, Fe^{2+} and Al^{3+} have a strong affinity with phosphate ions [106,107], and the order of the binding ability to phosphate ion is Ca^{2+}>Mg^{2+}>K^+>Na^+ [108]. Therefore, when the P solution contacts the adsorptive aggregate, the phosphate ion can react with metal ions (Mg^{2+}, Al^{3+}, Fe^{3+}) [138,139], mainly calcium ions (Ca^{2+}) by chemical reactions as follows [43,111]:

$$CaO + H_2O \rightarrow Ca^{2+} + 2OH^- \quad (4.1)$$

$$5Ca^{2+} + 3PO_4^{3-} + OH^- \rightarrow Ca_5(PO_4)_3(OH) \downarrow \quad (4.2)$$

Calcium ions leached from the adsorptive aggregate are more than 1000 mg/kg, and the sodium and potassium ions are 100-200 mg/kg. Besides, aluminium, iron and magnesium and other leaching ions are also detected in the solution, as shown in **Table 4.2**. Previous studies [138] showed a simultaneous decrease in PO_4^{3-}, calcium, magnesium and aluminium when a chemical reaction of phosphate removal occurs. The results also show that the more expanded silicate in adsorptive aggregates, the more aluminium ions are detected in SS25M0, SS25M3 and SS25HM3 because the expanded silicate mainly contains aluminium oxide. The potential environmental hazards of the heavy metals leached from the adsorptive aggregate are analyzed in the following section 4.3.5.

The ultimate goal of the manufactured adsorptive aggregate is to replace the normal aggregate without any adsorption properties and significantly improve the adsorption capacity of porous concrete for pollutant removal from stormwater. The adsorption process and mechanism of different aggregates for P-removal are shown in **Fig. 4.12**. Since normal aggregates (basalt, limestone, etc.) do not have high permeability and adsorption, the P solution cannot be adsorbed when it contacts with such kind of aggregate. Porous lightweight aggregates such as expanded lightweight silica and bio-based aggregates generally possess a lot of micropores, and thus, a small amount of P solution can be adsorbed by a pore-filling effect, but the P-bonding of physical adsorption is usually weak, and as a result, the P solution absorbed by micropores exists only on the surface of porous lightweight aggregates [15]. However, for adsorptive aggregate, the porous M mainly provides porosity and permeability of the adsorptive aggregate for wastewater penetration, and then more P solution is prone to penetrate inside the aggregate, and the SS and cement paste contribute good adsorption because the P reacts with calcium ions leached from the SS and cement paste to form Ca-P precipitation [100]. Besides, the ES provides lightweight and adsorption. Therefore,

compared to normal aggregate or porous lightweight aggregate, the designed adsorptive aggregate has significantly superior adsorption characteristics, which can possibly improve the adsorption capacity of porous concrete.

Table 4.2 Ions leached from adsorptive aggregates (mg/kg).

Element	Samples										Limit values [a]
	SS25 M0	SS25 M3	SS25H M3	SS50 M0	SS50 M3	SS50H M3	SS75 M0	SS75 M3	SS75H M3	SS75 M5	
Al	>155	>130	>134	79	32	42	15	8	10	12	-
Fe	0.2	0.7	0.3	0.1	≤0.3	≤0.3	≤0.4	≤0.4	≤0.4	≤0.4	-
Mg	0.1	0.1	0.1	0.1	0.1	0.1	0.1	0.1	0.1	0.1	-
As	≤0.2	≤0.2	≤0.2	≤0.2	≤0.2	≤0.2	≤0.2	≤0.2	≤0.2	≤0.2	0.9
Ba	-	0.3	0.9	1.8	6.6	3.2	6.5	10.7	10.4	5.3	22
Co	≤0.4	≤0.4	≤0.4	≤0.4	≤0.4	≤0.4	≤0.4	≤0.4	≤0.4	≤0.4	0.54
Cr	1.4	2.7	1.1	0.4	-	-	0.2	0.1	-	-	0.63
Cu	≤0.3	0.4	≤0.2	≤0.4	≤0.3	≤0.3	≤0.4	≤0.2	≤0.4	≤0.1	0.9
Pb	≤0.6	≤0.5	≤0.5	≤0.6	≤0.5	≤0.6	≤0.6	≤0.5	≤0.5	≤0.5	2.3
Zn	≤0.4	≤0.3	≤0.3	≤0.4	≤0.4	≤0.4	≤0.4	≤0.4	≤0.4	≤0.4	4.5
Mn	≤0.6	≤0.6	≤0.6	≤0.6	≤0.6	≤0.6	≤0.6	≤0.6	≤0.6	≤0.6	-
Mo	0.4	1.2	0.5	0.1	0.1	0.1	≤0.1	-	-	-	1
Se	≤0.1	-	≤0.1	≤0.1	≤0.1	≤0.1	≤0.1	≤0.1	≤0.1	≤0.1	0.15
V	4.4	1.7	0.7	0.5	≤0.1	≤0.1	-	≤0.1	≤0.1	-	1.8

[a] Limit values refer to the maximum emission values for building materials according to the Dutch Soil Quality Decree (2015).

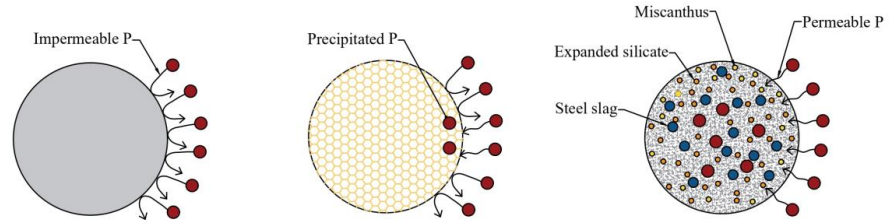

Fig. 4.12 Hypothesized adsorption process and mechanism of different aggregates for P-removal.

- *Mineralogical phase analysis*

After the adsorption test, the diffraction peaks at 22° are significantly lower than the diffraction peaks before adsorption, as shown in **Fig. 4.13**. The peak at 22° is related to calcium hydroxide. This phenomenon confirms that calcium ions participate in the reaction process of Ca-P precipitation. However, no obvious peaks related to Ca-P precipitate are observed in the XRD pattern, and the same phenomenon is reported by Han et al. [117], the precipitation of Ca-P is below the detection limit of XRD.

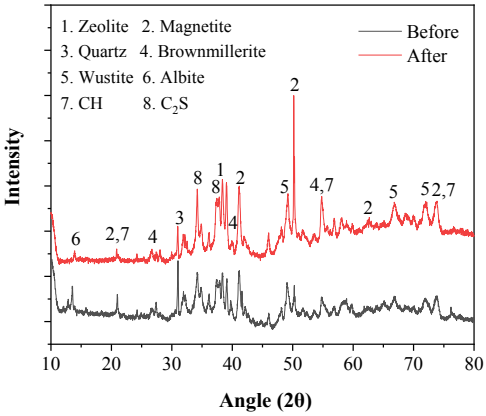

Fig. 4.13 X-ray diffraction patterns of the SS50M3 after adsorption.

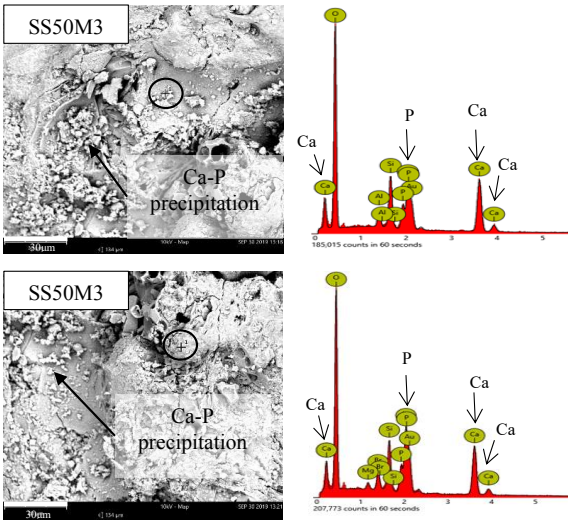

Fig. 4.14 SEM-EDS analysis of the SS50M3 after adsorption.

- *SEM-EDS analysis*

After adsorption, the surface of the adsorptive aggregate is analyzed by SEM-EDS, as shown in **Fig. 4.14**, and some small white spots are observed on the surface of the adsorptive aggregate. Its components are mainly O, Ca, Si and P, which indicate that suspended Ca-P precipitation is formed on the adsorptive aggregate surface. The same finely distributed P crystals are reported in previous studies [99,105,111]. Compared to the adsorptive aggregate containing 25% steel slag, the adsorptive aggregate containing 75% steel slag is more suitable as an adsorptive aggregate due to the presence of more calcium hydroxide based on mineralogical phase analysis.

4.3.5 Environmental and economic assessment

- *Environmental analysis*

In order to evaluate the potential environmental problems of the synthesized adsorptive aggregates, the leaching results of all samples are analyzed through a series of chemical tests. The ions leached from adsorptive aggregates are presented in **Table 4.2**. The emission limit values for building materials in unshaped materials according to the Dutch Soil Quality Decree (2015) are also shown in **Table 4.2**. The results show that most of the analyzed leaching elements (As, Ba, Co, Cu, Pb, Zn and Se) released from the synthesized adsorptive aggregate are far below the maximum emission limit values, except for Cr (all SS25 series), V (SS25M0 and SS25M3) and Mo (only SS25M3). The limit values of Cr, V and Mo in unshaped materials should be lower than 0.6 mg/kg, 1.8 mg/kg and 1 mg/kg, respectively. In this study, the leaching values of Cr, V and Mo released from the SS25 series are 1.1-2.7 mg/kg, 0.7-4.4 mg/kg and 0.4-1.2 mg/kg, respectively. This may be attributed to the fact that the heavy metals such as Cr, V and Mo leached from the SS are prone to be immobilized in the alkaline matrix. The pH values of the SS75 series are slightly higher than the SS25 series, which further contributes to a better immobilization capacity. Moreover, the water absorption of the SS25 series (25%-28%) is significantly higher than that of the SS75 series (13%-17%), resulting in much higher porosity and permeability, i.e. an easier leaching potential of Cr, V and Mo. Therefore, the SS50 and SS75 series can be used as artificial adsorptive aggregates without any environmental risk. Nevertheless, it should be noted the analyzed results here are only valid for the steel slag used in this study and for wider applicability, more investigation is still needed.

Due to the fact that the production of synthetic aggregates usually consumes energy, the carbon footprints of the manufactured adsorptive aggregates in this study have been evaluated [141], as shown in **Table 4.3**. Compared to the carbon emissions of normal aggregates without adsorption capacity (0.041 kg CO_2-e/kg) [142], adsorptive aggregates have a high carbon emission. This is because ordinary Portland cement with an additional amount of 15% of the SS and ES by weight is used as a binder for the manufacturing of adsorptive aggregates. Cement accounts for approximately 38 %, 40 % and 43 % of the total CO_2 emissions of the SS25 series, SS50 series and SS75 series respectively. Therefore, future work on reducing the cement content can significantly decrease the carbon footprint of the adsorptive aggregate, for example, by using alkali-activated materials to manufacture adsorptive aggregates because it shows an advantage in carbon dioxide emission (CO_2-e) towards Portland cement [143]. Moreover, the SS75 series have lower carbon emissions than the SS25 series due to their lower content

of artificial lightweight aggregates. Currently, the SS has been used for CO_2 storage through carbonization [144]. Firstly, the hydration and dissolution of CO_2 form carbonic acid (H_2CO_3), and then the Ca^{2+} and Mg^{2+} ions leach from the SS and finally the precipitation of carbonates containing calcium and magnesium. Studies have estimated up to 17 % of CO_2 uptake by carbonating steel slag wastes [145]. Therefore, the application of the SS as an ingredient in adsorptive aggregates not only increases adsorption capacity but also shows a potential application to reduce CO_2 emission by carbonation.

Table 4.3 Carbon footprints of adsorptive aggregates by calculation (kg CO_2-e/ kg).

Samples	proportion	Steel slag	Expanded silicate	Heat-treated miscanthus	Cement	Total CO_2 emissions
SS25M0	25%SS+75%ES	0.04	0.17	-	0.12	0.32
SS25M3	25%SS+75%ES+3% M	0.04	0.17	-	0.12	0.32
SS25HM3	25%SS+75%ES+3% HM	0.04	0.17	0.002	0.12	0.33
SS50M0	50%SS+50%ES	0.07	0.11	-	0.12	0.30
SS50M3	50%SS+50%ES+3% M	0.07	0.11	-	0.12	0.30
SS50HM3	50%SS+50%ES+3% HM	0.07	0.11	0.002	0.12	0.31
SS75M0	75%SS+25%ES	0.11	0.06	-	0.12	0.29
SS75M3	75%SS+25%ES+3% M	0.11	0.06	-	0.12	0.29
SS75HM3	75%SS+25%ES+3% HM	0.11	0.06	0.002	0.12	0.29
SS75M5	75%SS+25%ES+5% M	0.11	0.06	-	0.12	0.29

The estimated CO_2 emission values of raw materials refer to previous literature. The CO_2 emission value of cement is 0.816 kg CO_2-e per kg reported by Barcelo et al. [146] and slag is 0.143 kg CO_2-e per kg reported by Gao and Yu [143], and the heat-treated miscanthus is 0.052 kg CO_2-e per kg refer to the biochar pellet carbon footprint [147]. The CO_2 emissions value of expanded lightweight silicate is assumed to be 0.220 kg CO_2-e per kg refers to a commercial-scale lightweight aggregate [148].

- *Economic analysis*

The economic analysis of adsorptive materials is estimated according to the price of the local building market, as shown in **Table 4.4**. The prices per ton of cement and lightweight expanded silicate are about 100 €/t and 1800 €/t, respectively, following the local building market. The price of steel slag is assumed to be 8 €/t [149]. Miscanthus is considered as agricultural waste at no cost, but considering energy consumption for heat treatment, the price of heat-treated miscanthus is assumed to be 2 €/t.

The results show that with the increase of the SS content, adsorptive aggregate has a better price advantage in the construction market, because the market price of porous

lightweight ES is much higher than the price of the SS and cement. The main purpose of adding ES is to reduce the density of the adsorptive aggregate, especially for the aggregate containing high SS content. Because the high content of the SS will significantly increase the constant weight of the building structure. Therefore, in future research, low-cost porous aggregates can be used instead of ES to reduce the cost of adsorptive aggregates. Based on the analysis results, considering environmental and economic benefits, as well as good mechanical properties and adsorption characteristics, the SS75 series is recommended as an adsorptive aggregate to replace normal aggregates for highly adsorptive concrete design.

Table 4.4 Economic estimations of the manufacture of adsorptive aggregates (€/t).

Samples	Proportion	Steel slag	Expanded silicate	Miscanthus	Cement	Total price
SS25M0	25%SS+75%ES	2	1350	-	15	1367
SS25M3	25%SS+75%ES+3% M	2	1350	--	15	1367
SS25HM3	25%SS+75%ES+3% HM	2	1350	0.06	15	1367.06
SS50M0	50%SS+50%ES	4	900	-	15	919
SS50M3	50%SS+50%ES+3% M	4	900	-	15	919
SS50HM3	50%SS+50%ES+3% HM	4	900	0.06	15	919.06
SS75M0	75%SS+25%ES	6	450	-	15	471
SS75M3	75%SS+25%ES+3% M	6	450	-	15	471
SS75HM3	75%SS+25%ES+3% HM	6	450	0.06	15	471.06
SS75M5	75%SS+25%ES+5% M	6	450	-	15	471

4.4 Conclusions

(1) The content of steel slag in the adsorptive aggregate has a significant impact on its physical and mechanical properties, as well as its durability. When the adsorptive aggregate contains 75 wt.% steel slag, it shows excellent mechanical properties and salt resistance. Moreover, as steel slag content increases, more calcium ion (Ca^{2+}) is released, which benefits the chemical adsorption capacity of the adsorptive aggregate.

(2) The addition of porous materials (expanded silicate and miscanthus) significantly reduces the density of the adsorptive aggregate while increasing its permeability, providing enough micropores for physical adsorption capacity. The high dosage of raw miscanthus (5 wt.%), on the other hand, has negative effects on mechanical properties and durability, whereas heat-treated miscanthus with a dosage of no more than 3 wt.% is recommended for the adsorptive aggregate.

(3) The resulting adsorptive aggregates have a bulk density ranging from 570 kg/m^3 to 882 kg/m^3 and a bulk crushing strength of up to 5.1 MPa. Moreover, all adsorptive

aggregates have good resistance to salt and freeze-thaw cycles.

(4) The developed adsorptive aggregates have a high P-binding capacity. This is attributed to the Ca-P precipitation formed by the chemical reaction of calcium ion (Ca^{2+}) leached from steel slag and cement paste with phosphate (PO_4^{3-}), together with the physical adsorption provided by the micropores of expanded silicate and miscanthus.

(5) SS75 series is recommended as an adsorptive aggregate to replace conventional aggregates in highly adsorptive concrete due to its environmental and economic benefits, as well as its good mechanical properties and adsorption characteristics.

Chapter 5 Phosphorus removal enhancement by porous adsorptive paste using miscanthus and steel slag for highly adsorptive concrete

The low permeability and low adsorption capacity of conventional cement paste are the decisive reasons for the poor adsorption performance of the adsorptive aggregates applied to adsorptive concrete. In this chapter, a porous adsorptive paste is developed by combining chemical and physical methods to enhance permeability and adsorption performance. Porous heat-treated miscanthus (HM) (0.5 wt.% and 1.0 wt.%) powder and steel slag (SS) (5.0 wt.% and 10.0 wt.%) powder with different dosages are investigated in this new adsorptive paste. Results show the excellent adsorption capacity of the adsorptive paste of 30.4-74.2 mg/g, with a corresponding initial P-concentration of 1215-2968 mg/L. The leaching result, ICP-AES, XRD, FTIR, TG-DTG and SEM-EDS analyses confirm the Ca^{2+} leached from the adsorptive paste and the SS, reacting with the PO_4^{3-} to form Ca-P precipitates in solution. Moreover, the porous HM significantly improves the permeability of the developed paste. It is can be concluded that the HM with a dosage of 0.5 wt.% and the SS with a dosage of 10.0 wt.% can be recommended for the highly adsorptive paste to improve P-removal capacity from stormwater, without obvious sacrifices on other properties.

This chapter has been published as:

F. Wu, Q.L. Yu, H.J.H. Brouwers. Phosphorus removal enhancement by porous adsorptive mortar using miscanthus and steel slag for highly adsorptive concrete. Construction and Building Materials, 295, 123686, 2021.

5.1 Introduction

The adsorption capacity of porous adsorptive materials usually depends on the microstructure and pore characteristics [100]. In particular, the increase in well-developed micropores (< 2 nm) and specific surface area can improve the physisorption capacity of adsorptive materials [104]. The porous miscanthus (M) may be used to improve the micropores of the adsorptive mortar and promote the penetration of pollutants into the mortar layer that will be then absorbed by the adsorptive aggregate.

The P-removal mechanism is generally based on chemical reactions between metal cations (e.g. Ca^{2+}, Fe^{3+} and Al^{3+}) and the phosphate anion species (HPO_4^{2-} and PO_4^{3-}) [41]. The driving mechanism during the adsorption process of P-crystallization consists essentially of nucleation by precipitation of hydroxyapatite ($Ca_{10}(PO_4)_6(OH)_2$) [44]. However, crushed rock (basalt, limestone, etc.) is usually used as coarse aggregates in conventional pervious concrete. However, the lack of adsorption ability of crushed rock results in a poor adsorption performance of conventional pervious concrete. The adsorption capacity is only attributed to the reaction of mortar and P in the solution. The adsorption performance of potentially adsorptive aggregates is analyzed in our previous work (Chapter 3) [15].

The manufacture of a highly adsorptive aggregate made from the SS and the heat-treated M with physical and chemical adsorption is reported in previous work (Chapter 3) [55]. Similar to conventional aggregates, when highly adsorptive aggregates are applied to the concrete matrix, their surface will be coated with mortar. The P-removal potential of adsorptive aggregate pellets is generally controlled by their permeability, which is related to the ability to release Ca^{2+} into the solution. A highly dense mortar layer will significantly reduce the penetration potential of pollutants into the adsorptive aggregate, resulting in a significant reduction in the adsorption performance. Therefore, a porous permeable mortar with good permeability and adsorption is developed in this chapter to improve the adsorption performance of mortar-coated aggregates.

The chemical method by adding adsorptive materials (SS) and the physical method by adding porous materials (heat-treated miscanthus (HM)) are used to increase the adsorption capacity of the cement mortar. Firstly, the effects of the SS and the HM powder on cement hydration are analyzed by a TAM air isothermal calorimeter. Then the physical, mechanical properties, and adsorption characteristics of adsorptive mortar are investigated. The effects of the adsorptive mortar on the adsorption capacity of the aggregate are also analyzed. Moreover, the leaching test results (ICP-AES), mineralogical phase (XRD), microstructure (SEM-EDS), Fourier transform infrared

spectra (FTIR) and thermal gravimetric results (TGA-DTG) of adsorptive mortar before and after P-removal test are analyzed for a better understanding of Ca-P precipitate mechanism.

5.2 Materials and methods

5.2.1 Materials

Miscanthus (M) powder (Vibers, The Netherlands) and BOF steel slag (SS) powder (TATA Steel, The Netherlands) are used as porous materials and adsorption materials, respectively, to improve the permeability and adsorption characteristics of the adsorptive mortar in the present study, as shown in **Fig. 5.1**. Portland CEM I 52.5 R cement is used as the binder, provided by ENCI (The Netherlands). The raw M is heat-treated for 3 hours at a temperature of 250 ℃ under nitrogen gas to improve its adsorption characteristics by increasing the microporous structure [15]. The specific density of the heat-treated miscanthus (HM) and the SS is 1.3 g/cm^3 and 3.9 g/cm^3, respectively. The 24-h water absorption of the HM is 350±21%. The BET specific surface areas of the HM and the SS are 5.1 m^2/g and 2.0 m^2/g, respectively.

Fig. 5.1 Heat-treated miscanthus powder and steel slag powder and their microscopic images.

5.2.2 Preparation of adsorptive mortar

The schematic diagram of the improvement of permeability and adsorption performance of cement mortar is shown in **Fig. 5.2**. When the adsorptive aggregate is coated by conventional mortar, it is difficult for pollutants to reach the highly adsorptive aggregate or only a small amount of pollutants could penetrate the adsorptive aggregate due to the low permeability of normal mortar. To improve the permeability of the mortar-coated aggregates, the HM is adopted in the present study to form a porous structure inside the mortar for the improvement of adsorption performance by physical

method. When the permeability of the mortar is increased by the HM, more pollutants can penetrate the paste, then contact the adsorptive aggregate, and subsequently be absorbed by the highly adsorptive aggregate. The SS is applied as a chemisorbing material to improve the P-adsorption capacity of the mortar. The P in the solution can be removed by the SS while passing through the adsorptive mortar [55].

A paste containing 400 g cement and 200 g water is used as the control mix (C0) with a water-to-cement (w/c) of 0.5 referring to the preparation method of standard mortar (EN 196-1:2005). The high content of miscanthus [75] and steel slag [150] will significantly reduce the mechanical strength and durability of mortar. An HM content of 0.5 wt.%, 1 wt.% and 5 wt.%, 10 wt.% of SS with respect to cement are added to the other four batches of paste, which are labelled as HM0.5, HM1, SS5 and SS10, respectively. The mix proportions of cement pastes are shown in **Table 5.1**.

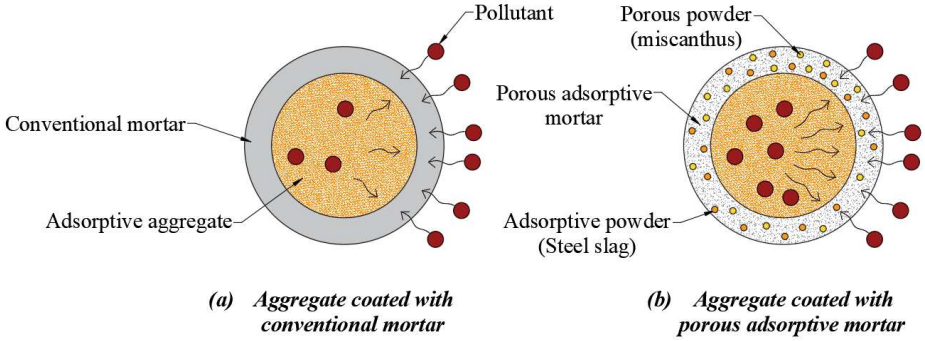

Fig. 5.2 Schematic diagram of the improvement of permeability and adsorption performance of adsorptive mortar.

Table 5.1 Mix proportions of cement pastes.

Mix code	Cement (g)	Water (g)	HM (g)	SS (g)
C0	400	200	-	-
HM0.5	400	200	2	-
HM1	400	200	4	-
SS5	400	200	-	20
SS10	400	200	-	40

5.2.3 Effects of adsorptive mortar on adsorption performance of aggregates

When the adsorptive aggregate is coated with paste, its adsorption characteristics will be affected by factors such as the permeability and adsorption capacity of the cement mortar. To investigate the effects of the mortar containing the M and the SS on the actual adsorption performance of the adsorptive aggregate, the previously manufactured adsorptive aggregates (SS75) with a size of 2-5 mm are applied in the present study.

The adsorptive aggregate is produced through 75 wt.% steel slag and 25 wt.% lightweight expanded silicate, which shows high adsorption and good mechanical properties. The P-adsorption amount and removal fraction of the adsorptive aggregate are 4.2 mg/g and 100%, respectively, with an initial P-concentration of 168 mg/L and P-solution to aggregate of L/S = 25. The detailed manufacturing process and characteristics of this adsorptive aggregate are shown in our previous research [55]. The properties of adsorptive aggregates are shown in **Table 5.2**.

Table 5.2 Properties of adsorptive aggregates.

Adsorptive aggregate	Size (mm)	Apparent density (kg/m^3)	24-h water absorption (%)	Crushing strength (MPa)
SS75	2-5	2633	13	5.1

The preparation process of coating aggregates with adsorptive mortar is presented in **Fig. 5.3**. Firstly, the adsorptive aggregate is poured into the prepared fresh paste (**Fig. 5.3a**, **5.3b**), and then the adsorptive aggregate and the mortar are mixed until the adsorptive aggregate is evenly coated by the mortar (**Fig. 5.3c**). After that, the mortar on the surface of the aggregate is rounded manually, and the resulting thickness of the mortar layer is about 0.5-1 mm (**Fig. 5.3d**). Finally, the aggregates coated with the mortar are stored in a standard curing room until the adsorption test.

5.2.4 Test methods

- *Cement hydration test*

Generally, bio-based materials have an adverse effect on cement hydration due to the presence of organic matter [57]. The influence of the M and the SS on the hydration characteristics of cement is measured using a TAM air isothermal calorimeter at a constant temperature of 20 ℃. Using the same mix proportions as in the cement paste for the mortars. After mixing, all samples are placed in the calorimeter to determine the hydration behavior of the cement.

- *Physical and mechanical test*

The density, water absorption and permeable pore of all samples are determined according to ASTM C642-13. Samples with dimensions of 40×40×40 mm^3 and 40×40×160 mm^3 at a curing age of 28 days are used for determining the compressive strength and flexural strength, respectively, according to EN 196-1. The constant loading rates of compressive strength and flexural strength test are 2400 N/s and 0.05 MPa/s, respectively. The average value of three samples is reported as the test result.

The microscopic image of the sample is observed by a scanning electron microscope (SEM).

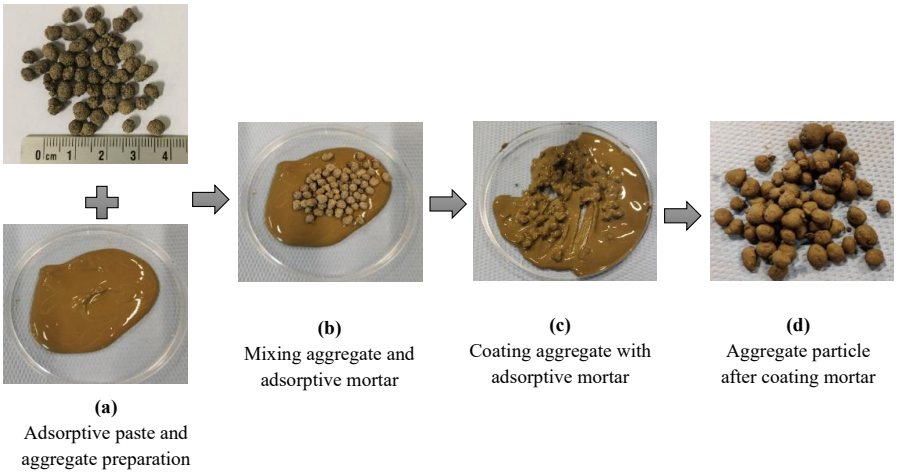

Fig. 5.3 Preparation process of coating adsorptive aggregates with adsorptive mortar.

- *Adsorption test*

In this study, a phosphate solution is used to simulate the polluted water for the adsorption test. Because of the good adsorption characteristics of our aggregates, three high-concentration P solutions (1215 mg/L, 1849 mg/L and 2968 mg/L) are used for mortar adsorption testing and for the mortar-coated aggregate testing in this study. Firstly, 1g of mortar (or mortar-coated aggregate) is added to a small plastic bottle with a 25 ml P solution. Secondly, the plastic bottle with mortar and P solution is stirred at 225 rpm in the shaker for 24 hours and then filtered using a 0.45 μm membrane to obtain the extracted supernatant. The change in the P-concentration of the solution is determined using IC (Thermo Dionex Aquion). The P-adsorption amount (q, mg/g) and P-removal fraction (P_R, %) are calculated by Eqs (3.1) and (3.2), respectively.

To investigate the adsorption mechanism of the adsorption mortar, ions leached from the adsorptive mortar are determined according to EN 12457-2. Firstly, adsorptive mortar and distilled water are mixed with a liquid-solid ratio of 10, i.e. 10 g adsorptive mortar is mixed with 100 ml of distilled water, and then shaken using a dynamic shaker with a speed of 250 rpm for 24 hours. Finally, the leachates are filtered by a 0.22 μm filter and acidified with concentrated HNO_3 for the leaching test by ICP-AES (SPECTROBLUE). The mineralogical phase and microstructure of samples before and after the adsorption test are measured by XRD and SEM-EDS, respectively, and the

sample is further analyzed by Fourier transform infrared spectroscopy (FTIR) (PerkinElmer) and thermogravimetry (TG-DTG) (STA 449 F1 Jupiter) for better understanding of adsorption mechanism of adsorptive mortar.

5.3 Results and discussion

5.3.1 Hydration behavior of adsorptive mortar

As shown in **Fig. 5.4**, at 80 hours, the total released heat of HM1 is only reduced by 2% (**Table 5.3**), compared to the control mortar (C0). Heat treatment changes the biomass content (cellulose, hemicellulose and lignin) of the HM, and oxygen-containing saccharides are pyrolyzed and more carbon is formed during the pyrolysis process, which ultimately eliminates their effects on cement hydration [130,151]. Boix et al. [58] reported that the alkali-treated miscanthus accelerates the hydration of cement compared to the untreated miscanthus, and a direct inverse relationship is found between the sugar content extracted from the fibre and the mechanical strength of miscanthus concrete. Therefore, the HM works better to increase the porosity of adsorptive mortar because it will have little negative impacts on the cement hydration and mechanical strength of the mortar. From other studies, it is known that the total released heat of cement hydration decreases with increasing dosage of the SS [152]. However, for the heat flow curve, no obvious delay is observed in the SS5 and SS10 curves. It is concluded that adding the SS up to 10 wt.% in this study does not significantly alter the hydration of cement.

5.3.2 Physical and mechanical properties of adsorptive mortar

- *Density, water absorption and porosity*

The density of adsorptive mortar is shown in **Fig. 5.5a**. As expected, the addition of the HM slightly decreases the density of adsorptive mortar, while the SS significantly increases the density. The changes in the oven-dry density of HM0.5, HM1, SS5 and SS10 are -2%, -3%, +3% and +8%, respectively, compared to the control mortar (C0). These results are consistent with the previous studies [62,153], i.e. the addition of the bio-based miscanthus reduces the density of concrete due to its porosity and lightweight properties, and the SS significantly increases the density of concrete structure [144].

Water absorption is a very important indicator of the adsorption performance of adsorptive concrete. The pollutants can be quickly absorbed by adsorptive concrete, which is usually related to the amount and size of the micropores, as well as the connectivity. As shown in **Fig. 5.5b**, both the M and the SS increase the water

absorption and permeable pore of the adsorptive mortar. The water absorption of the HM0.5, HM1, SS5 and SS10 increases by 3%, 10%, 4% and 8%, respectively, and the corresponding permeable pore increases by 6%, 13%, 4% and 10%, respectively, compared to the control mortar (C0). Due to the highly porous structure of the HM, it can generally absorb several times water higher than its mass. The water absorption of the miscanthus is related to the particle size and the 48-hour water absorption of 2-4 mm, 0-2 mm and powdery miscanthus is about 290%, 400% and 525%, respectively, as reported by Chen et al. [62].

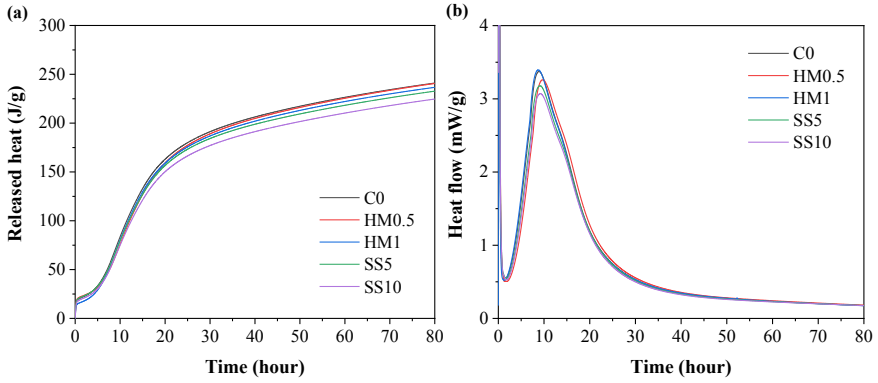

Fig. 5.4 Effects of miscanthus and steel slag powders on (a) released heat and (b) heat flow of cement hydration.

Table 5.3 Released heat comparison of adsorptive mortar (80 hours).

Items	C0	HM0.5	HM1	SS5	SS10
Total heat (J/g)	241	241	237	233	225
Heat deviation (J/g)	-	-0.4	-4.4	-8.3	-16.4
Reduction (%)	-	-	2	3	7

- *Compressive strength and flexural strength*

The mechanical properties of adsorptive mortar are the decisive factors in the mechanical strength of adsorptive concrete. The compressive strength and flexural strength of adsorptive mortar are shown in **Fig. 5.6**. The results show that the M reduces the compressive strength of adsorptive mortar and the SS does not significantly affect the compressive strength. Moreover, the mechanical strength of the adsorptive mortar decreases with the increasing dosage of the M and the SS. This may be because the addition of the M and the SS increases the porosity of the adsorptive mortar, resulting in a decrease in mechanical strength. The 28-day compressive strengths of the HM0.5, HM1, SS5 and SS10 are 59.7 MPa, 57.8 MPa, 63.2 MPa and 60.5 MPa, respectively.

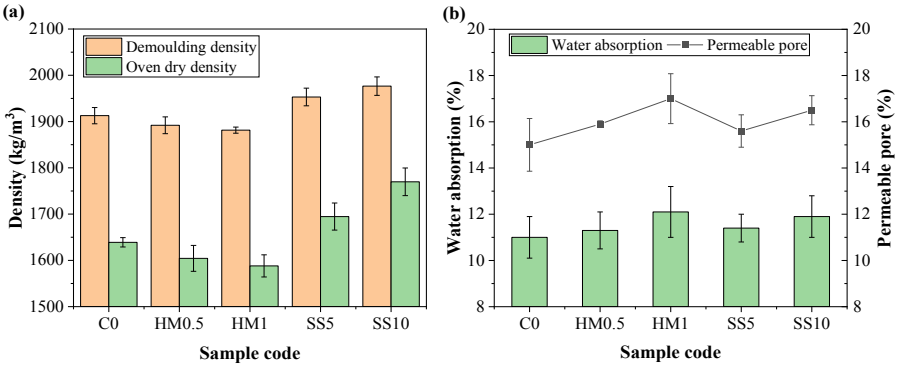

Fig. 5.5 (a) density and (b) water absorption and permeable pore of adsorptive mortar.

Generally, the addition of waste has a significant impact on the mechanical properties of concrete [154,155]. The addition of bio-based materials significantly reduces the mechanical strength of concrete because of the low strength, high porosity and organic matter of bio-based materials [156]. The same phenomenon is observed in bio-based lightweight concrete, such as miscanthus concrete [62], oil palm shell concrete [157], apricot shell concrete [128], and wood concrete [158]. However, the heat-treated bio-based material has better dimensional stability and less organic content, resulting in a less negative effect on the mechanical strength of concrete compared to untreated bio-based materials [59].

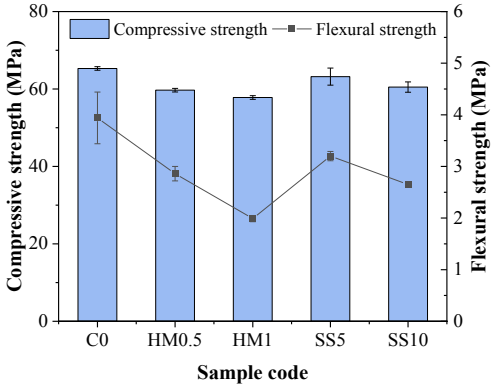

Fig. 5.6 Compressive and flexural strengths of adsorptive mortar at the age of 28 days.

The results also show that the addition of the M and the SS results in a more significant reduction in flexural strength than compressive strength. The 28-day flexural strengths of the HM0.5, HM1, SS5 and SS10 are 2.89 MPa, 1.99 MPa, 3.20 MPa and 2.65 MPa, respectively. Based on the results, the high content of the HM powder (e.g. more than

1.0 wt.%) is not recommended for adsorptive mortar due to the significant decrease in mechanical strength.

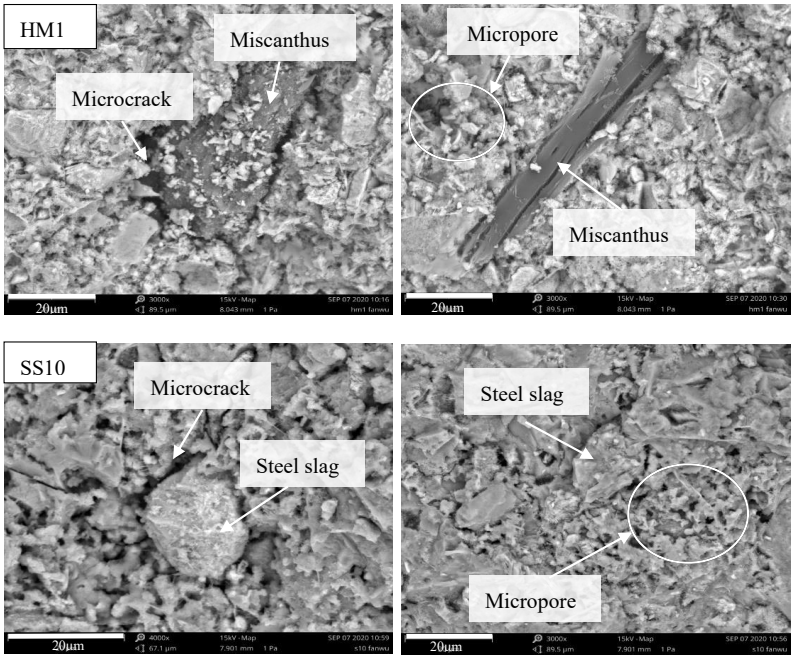

Fig. 5.7 SEM micrographs of adsorptive mortar.

- *Microstructure*

The SEM micrographs of adsorptive mortar (HM1 and SS10) are shown in **Fig. 5.7**. Micropores are observed on the surface of the HM1 and the SS10 sample. Moreover, the surface of the M and the SS does not closely bond with the mortar interface, and obvious microcracks exist in the interfacial transition zone. The same phenomenon has also been reported in bio-based lightweight concrete such as oil palm shell concrete [159], wood sand concrete [79] and bamboo-reinforced concrete [160]. These microcracks and micropores increase the water absorption of the adsorptive mortar, increasing the easiness for the pollutants to penetrate the mortar layer. However, these microcracks are also one of the primary reasons for the mechanical strength reduction of the adsorptive mortar. Enough transport channels for the number of cracks are also observed on the HM surface because of the increase in brittleness of the HM after heat treatment. Luo et al. [69] reported that the average pore size of the miscanthus after heat treatment at 300 °C is 1.03 μm, which can provide physical adsorption. Heat treatment not only reduces the pore size of the HM but also increases its specific surface area and ion exchange capacity. Therefore, the well-developed micropores and high

BET specific surface area of the HM after pyrolysis endow it with an adsorption capacity for pollutant removal from wastewater [15].

5.3.3 Adsorption performance of adsorptive mortar

- *Adsorption capacity*

The results show that no phosphate is detected in the solution after the adsorption test, except for the HM0.5 under a high initial P-concentration of 2697.5 mg/L condition, which indicates that the P is completely removed by the adsorptive mortar even at a high initial P-concentration. The P-adsorption capacity of the adsorptive materials depends on the initial concentration of the P solution [15] and the L/S. When the initial P-concentration is 1215 mg/L, 1849 mg/L and 2968 mg/L, the adsorption capacity of most adsorptive mortars (except for HM0.5) is 30 mg/g, 46 mg/g and 74 mg/g, respectively. The excellent adsorption capacity of the adsorptive mortar is attributed to the Ca^{2+} leached from the SS and mortar, which can react with the PO_4^{3-} to form Ca-P precipitates [18]. Besides, the porous miscanthus can also adsorb P through physical adsorption [15] and increase the permeability of the adsorptive mortar, which helps the leaching of Ca^{2+} from the adsorptive mortar surface.

The adsorption capacity of the developed adsorptive mortar is significantly higher than most of the adsorptive materials, including industrial by-products (fly ash [12], coal ash [29] and furnace slag [111]), natural material (sepiolite [105], palygorskite [115]) and bio-based material (peanut shell [102], bamboo [124] and juniper fibre [125]). More importantly, other adsorptive materials usually focus on P-removal with a low P-concentration (i.e. less than 1000 mg/L) [11,12]. The adsorptive mortar in this study completely removes all P from the P-solution with a high concentration of up to 2968 mg/L, showing an outstanding adsorption capacity. Therefore, it can be concluded that the developed adsorptive mortar can be applied to significantly improve the P-adsorption performance of porous adsorptive concrete.

- *Adsorption mechanism of adsorptive mortar*

The adsorption of materials can generally be divided into physical adsorption and chemical adsorption. The adsorption of adsorptive mortar for P-removal is mainly dominated by chemical adsorption supplied by the mortar and the SS. The microporous structure formed by the HM contributes to physical adsorption by pore-filling and electrostatic attraction [109]. P-removal rate by hydroxyapatite crystallization is affected by pH, temperature and concentration of PO_4^{3-} and Ca^{2+} [41]. The Ca^{2+}, K^+ and Na^+ ions are the main ions leached from the adsorptive mortar. The Ca^{2+} ion has a strong

affinity with phosphate, whereas other metal ions such as K^+, Na^+ and Mg^{2+} ions do not significantly affect the P-adsorption capacity [106,107]. The hydration products of mortar are mainly hydrated calcium silicate and calcium hydroxide.

As presented in **Table 5.4**, the content of calcium oxide (CaO) is slightly reduced after the adsorption test, which indicates that it keeps dissolving in the 25 ml+1g mortar shaking experiment. In addition, P_2O_5 is found in the HM0.5, HM1 and SS5, which proves that P has a chemical reaction with the adsorptive mortar. The changes in the concentration of Ca^{2+} ion released from phosphate-loaded mortar in the solution are shown in **Fig. 5.8**. When leaching the mortars exposed to different P-solutions (1215 mg/L, 1849 mg/L and 2968 mg/L), the concentration of the Ca^{2+} after adsorption decreases, compared to the initial concentration of the Ca^{2+} before adsorption.

Table 5.4 Chemical compositions of adsorptive mortar before and after adsorption (wt.%).

Oxides	C0		HM0.5		HM1		SS5		SS10	
	Before	After	Before	After	Before	After	Before	After	Before	After
CaO	60.9	60.9	60.6	60.0	60.8	59.8	59.3	59.0	57.6	55.1
SiO_2	16.0	15.9	15.9	15.5	15.9	15.4	15.6	15.3	15.3	14.3
Al_2O_3	6.7	6.8	7.1	7.0	6.9	7.1	6.7	6.5	6.8	6.8
Fe_2O_3	3.6	3.6	3.6	3.6	3.6	3.7	5.1	5.3	6.3	6.3
SO_3	2.8	2.8	2.8	2.6	2.8	2.6	2.5	2.5	2.4	2.2
MgO	1.4	1.3	1.4	1.3	1.4	1.2	1.7	1.6	1.9	1.7
P_2O_5	-	-	-	0.1	-	0.5	-	0.6	0.2	-

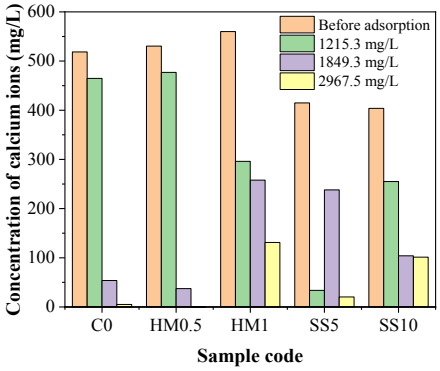

Fig. 5.8 Changes in the concentration of calcium ion released from adsorptive mortar.

- *FTIR analysis*

The infrared spectra of the SS5 before and after adsorption are presented in **Fig. 5.9a**. The spectrum presents an intense narrow band at 3635 cm^{-1}, which is a stretching vibration generated by the hydrogen bonds (O–H) bonds in portlandite ($Ca(OH)_2$) that

is formed in the cement hydration [161]. The hydroxyl group with an O-H bond usually appears at the wavelength of 3434 cm^{-1} due to symmetric and antisymmetric stretching vibration of water bounding from the hydrated products [162]. Moreover, an absorption band (H-O-H) at the wavelength of 1639 cm^{-1} shows the deformation vibration of water molecules [163,164]. The adsorptive mortar after adsorption has an obvious peak at 3434 cm^{-1} and 1639 cm^{-1}, which may be due to the influence of the bound water in the sulfate ettringite ($Ca_6Al_2(SO_4)_3(OH)_{12}\cdot 26H_2O$) (Aft phase). Furthermore, a narrow sharp band appears at 1112 cm^{-1}, which is associated with the stretching vibration of the SO_4^{2-} group, supporting the presence of sulfate ettringite [165]. The hydrated products of cement show the typical characteristic of the Si-O asymmetric stretching vibration with a peak for the C-S-H at 970 cm^{-1} [166]. Calcium carbonate ($CaCO_3$) is originally present in mortar because of the chemical reaction between portlandite and atmospheric carbon dioxide (CO_2), resulting in C-O bending vibration and stretching with a peak appearing at 713 cm^{-1}, 872 cm^{-1} and 1417 cm^{-1} [162,166].

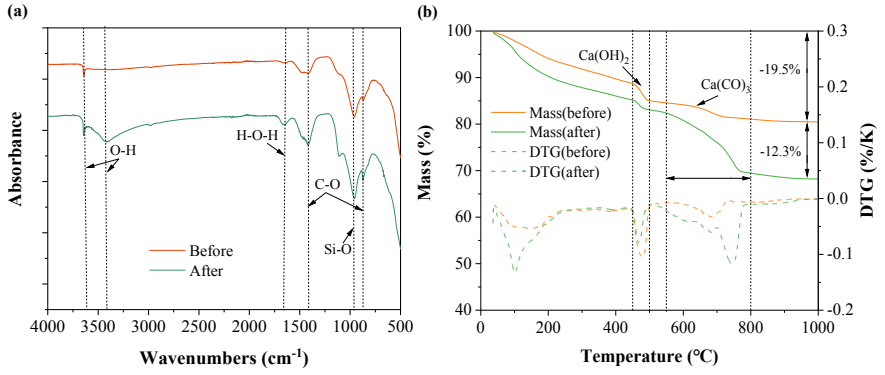

Fig. 5.9 (a) Infrared spectra and (b) TG-DTG of the SS5 before and after adsorption.

- *TG-DTG analysis*

The thermal gravimetric results of the SS5 are illustrated in **Fig. 5.9b**. Generally, a distinct mass loss for cementitious materials at a temperature of 130-200 ℃, 400-500 ℃ and 500-800 ℃, indicates the dehydration, the dihydroxylation or calcination of ettringite, the decomposition of $Ca(OH)_2$ and the decarbonation of $CaCO_3$, respectively [152]. The TG curves show that all adsorptive mortars have a similar endothermic peak within 1000 ℃ before or after adsorption. The SS5 has a lower mass loss than C0 and HM0.5, indicating that fewer hydration products are generated due to the retardation of cement hydration by SS [152]. A mass-loss peak appears at around 100 ℃ in the DTG curve related to the free moisture loss [167]. Besides, the dehydration of C-S-H appears below 200 ℃, which also matches the weight loss description in the mass loss curve

[168,169]. A sharp decline of mass is observed at a temperature range of 450-500 ℃ for all adsorptive mortar, which corresponds to the decomposition of $Ca(OH)_2$ [144,170]. The result is consistent with the XRD analysis. A significant mass loss is observed at the temperature of 550-800 ℃, which is related to the thermal decomposition of $CaCO_3$ [171].

- *SEM-EDS analysis*

The mortars HM1 and SS10 after adsorption are analyzed by SEM-EDS, as shown in **Fig. 5.10**, the C-S-H gel has a dense network structure, which indicates that enough hydration products are formed. A strong peak of P appears in the EDS spectra and P is detected on the adsorptive mortar surface. Previous studies have reported that the small white crystalline substance on the surface is the suspended Ca-P precipitation [99,105]. The results also show that many micropores are observed on the surface of the HM1 and SS5. This may be due to the addition of the HM and the SS increasing the porosity of the adsorptive mortar, causing more P-solution to penetrate the mortar layer and favor the combination with Ca^{2+} to form Ca-P precipitation.

5.3.4 Effects of adsorptive mortar on the performance of aggregates

- *Adsorption capacity of aggregates coated with adsorptive mortar*

For the adsorptive aggregate (SS75), coated with different adsorptive mortars, the adsorption capacity is presented for different initial P concentrations (**Fig. 5.11**). The adsorptive aggregate is immersed in P-solution with an initial concentration of 1215 mg/L, 1849 mg/L and 2968 mg/L, the adsorption capacity of the aggregate pellets coated with normal mortar (P-C0) decreases by 18%, 25% and 48%, respectively, compared to the aggregate (SS75) without coating. The results also show that the porous adsorptive mortar significantly improves the adsorption capacity of the aggregate, compared to the P-C0. When the P-concentration is 1215 mg/L, 1849 mg/L and 2968 mg/L, the P-adsorption capacity of the adsorptive mortar is 11.0-13.5 mg/g, 12.8-18.0 mg/g and 11.5-16.5 mg/g, respectively, and the P-removal rate is 36-44%, 39-28%, 22-15%, respectively. Compared to previous studies, the adsorption capacity is significantly higher than that of most porous concrete, bio-based materials and industrial by-products. In this study, the P-HM1 shows the highest adsorption capacity and removal rate for the mortar-coated adsorptive aggregates, and its adsorption capacity increases by 20%, 24% and 35%, respectively, with an initial P-concentration of 1215 mg/L, 1849 mg/L and 2968 mg/L, compared to the P-C0. The increase in the adsorption capacity of the mortar-coated adsorptive aggregate is mainly attributed to the increase in the micropores and permeability. Considering a balance between

mechanical strength and adsorption capacity, the HM with a dosage of 0.5 wt.% and the SS with a dosage of 10 wt.% are recommended for the adsorptive mortar.

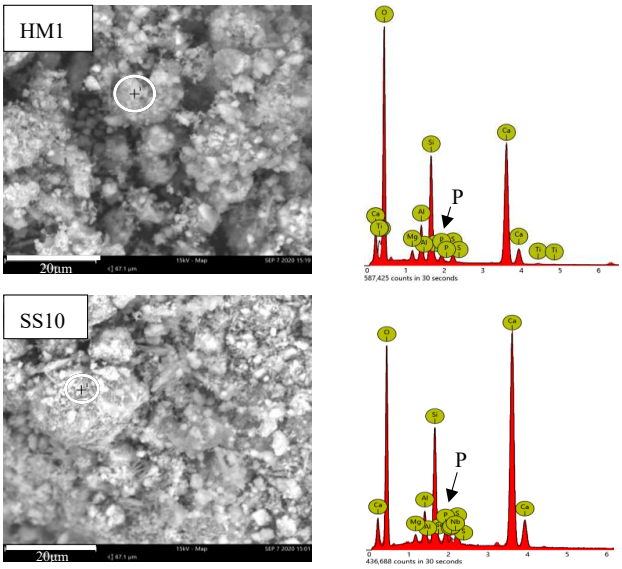

Fig. 5.10 SEM-EDS analysis of adsorptive mortar after adsorption.

- *Adsorption mechanism of adsorptive aggregates*

Both physisorption and chemisorption mechanisms can be used to increase the adsorption capacity of adsorptive materials. Physical modifications such as increasing the amount of micropores, connectivity or specific surface area [100], and chemical modifications such as increasing the leaching of Ca^{2+} ion for promoting its binding to phosphate and the formation of P-Ca precipitation are often utilized [15]. In this study, both physical and chemical modification is applied to improve the adsorption performance of cement-coated adsorptive aggregates. The porous HM is applied to physically modify the porosity and permeability of mortar to increase the leaching of Ca^{2+} ions. The SS is applied to further increase the chemisorption capacity of the mortar-coated aggregate.

The schematic diagram of the adsorption process and mechanism of mortar-coated adsorptive aggregates for P-removal is shown in **Fig. 5.12**. When a conventional aggregate is coated by conventional mortar, most of the phosphate can not be in contact with the conventional aggregate (**Fig. 5.12a**). More importantly, conventional aggregates do not have the adsorption capacity, thereby a small amount of the phosphate

can be adsorbed by the Ca^{2+} ion leached from the mortar itself, which explains the low P-removal capacity of conventional porous concrete.

In contrast, for adsorptive aggregate coated with conventional mortar, due to the high adsorption capacity of the adsorptive aggregate (SS75), as shown in **Fig. 5.11**, as long as the phosphate can penetrate the coating layer of the conventional mortar, it can be adsorbed by the adsorptive aggregate and mortar. It has to be noted that only a small amount of phosphate can reach the adsorptive aggregate because of the restrictive permeability of the conventional mortar (**Fig. 5.12b**).

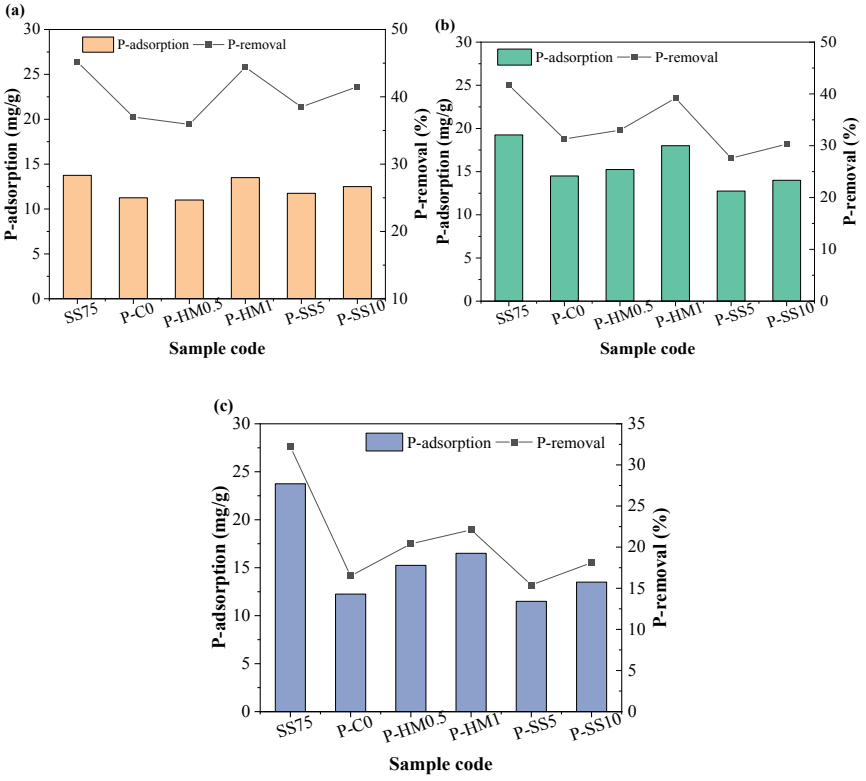

Fig. 5.11 P-adsorption amount and removal fraction of adsorptive aggregates with an initial P concentration (a) 1215.3 mg/L, (b) 1849.3 mg/L and (c) 2967.5 mg/L.

However, when the adsorptive aggregate is coated by a porous adsorptive mortar, due to the increase in the permeability of the adsorptive mortar, more phosphate can penetrate the coating layer and reach the adsorptive aggregate, and finally, be absorbed by the internal adsorptive aggregate and the external adsorptive mortar layer (**Fig. 5.12c**). In addition, the adsorptive mortar itself contributes to phosphate removal with

its own improved adsorptive properties.

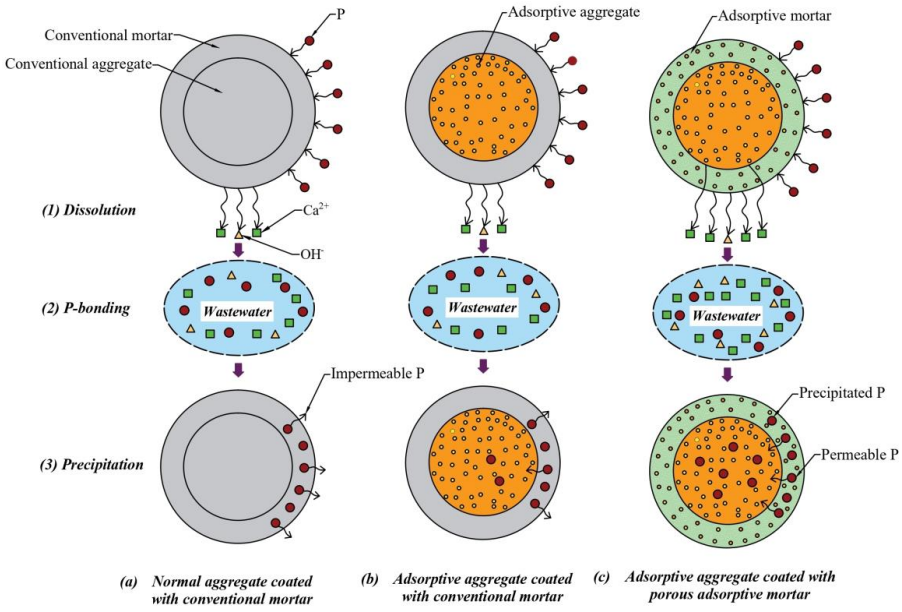

Fig. 5.12 Schematic diagrams of the adsorption process and mechanism of adsorptive aggregates coated with porous adsorptive mortar for P-removal.

5.4 Conclusions

(1) Heat-treated miscanthus (HM) (0.5 wt.% and 1 wt.%) shows an insignificant effect on cement hydration thanks to the pyrolysis of oxygen-containing saccharides. The addition of steel slag (SS) (5 wt.% and 10 wt.%) slightly reduces the total heat of cement hydration by 3-7%.

(2) HM slightly decreases the density of adsorptive paste (up to 3%), whereas the SS significantly increases it (up to 8%). The HM can be applied to improve the permeability of adsorptive paste (up to 10%). However, the high content of the HM (≥1 wt.%) would result in a significant decrease in mechanical strength.

(3) The adsorptive paste has a high adsorption capacity, namely 30.4 mg/g, 46.2 mg/g and 74.2 mg/g, with corresponding initial P-concentrations of 1215 mg/L, 1849 mg/L and 2968 mg/L. The mortar-coated aggregate (P-HM1) has the highest adsorption capacity and removal rate for P-removal, with an increase of 20-35%, compared to the P-C0. Ca^{2+} leached from the paste and the SS is one of the main metal ions for the

formation of Ca-P precipitates in the solution. Besides, the porous HM contributes to physical adsorption by increasing the micropores of the adsorptive paste.

(4) Porous HM and the SS can significantly improve the adsorption performance of the mortar-coated aggregate by increasing permeability and Ca^{2+} ion release. The HM with a dosage of 0.5 wt.% and the SS with a dosage of 10.0 wt.% are recommended for the adsorptive paste, without obvious sacrifices in other properties.

Chapter 6 Mechanical, absorptive and freeze-thaw properties of pervious concrete applying a bimodal aggregate packing model

To optimize the pore skeleton structure of pervious concrete to enhance its phosphate (P) removal from stormwater, small-sized adsorptive aggregate (1-2 mm steel slag) and large-sized natural aggregate (2-5 mm basalt), are applied for the manufacture of two-sized aggregate pervious concrete. Physico-mechanical properties, adsorption performance and freeze-thaw resistance are investigated. The results show that the small-sized steel slag aggregate fills the pores between the large-sized natural aggregates and reduces the porosity and permeability of pervious concrete, significantly improving the mechanical strength and freeze-thaw resistance. Pervious concrete in this study shows an excellent P-adsorption capacity, all P is removed from the aqueous solution with an initial concentration of 168 mg/L and 307 mg/L. The harmful elements (Cr, Sr and V, etc.) leached from the concrete are lower than the maximum limit value. The orthogonal results show that cement and steel slag are the main factors affecting the P-adsorption performance of pervious concrete. Based on the current results, sample 3 (cement: 350 kg/m^3, sand: 500 kg/m^3, w/c: 0.37, 1-2 mm steel slag: 1385.8 kg/m^3 and 2-5 mm basalt: 361.3 kg/m^3) shows good P-removal capacity, which is an optimal mix for pervious concrete to remove P from stormwater, with suitable strength and durability.

This chapter is partially reproduced from:

F. Wu, Q.L. Yu, H.J.H. Brouwers. Mechanical, absorptive and freeze-thaw properties of pervious concrete applying a bimodal aggregate packing model. Construction and Building Materials, 333, 127445, 2022.

6.1 Introduction

Conventional pervious concrete is typically composed of single-sized coarse aggregates, cement and water or a small amount of fine aggregate [54], which has many advantages, including good drainage properties, noise absorption and urban heat island reduction [172,173]. In recent years, for removing pollutants from stormwater, such as phosphate (P), nitrate (N) and heavy metals etc., more and more attention has been paid to the adsorption performance of pervious concrete. For example, the expanded shale aggregate is used for permeable pavement for the P and N removal [174]. Besides, pervious concrete is applied to remove heavy metals such as zine, lead [175,176] and cesium [177] and excess nutrients in the water body [178]. However, single-sized aggregates without adsorption capacity are currently the primary aggregates for conventional pervious concrete, consequently, the adsorption capacity and removal rate of conventional pervious concrete is low and usually require a long reaction time. Therefore, it is hypothetically to improve the P-removal performance of pervious concrete by using materials with adsorption capacity as aggregates and optimizing the micropores of the skeleton structure between the aggregates.

The behavior of concrete is related to aggregate characteristics [179]. The adsorptive materials have been applied to conventional pervious concrete to improve the pollutants removal from stormwater recently. For example, nano-titanium dioxide (TiO_2) is used in pervious concrete to improve the purification efficiency of pollutants (N, P and methylene blue), with an efficiency of 60%-90% [180]. The use of 0.6-1.2 mm mineral adsorbents (zeolite and pumice) improves the compressive strength of pervious concrete and decrease the suspended solids by 40% [53]. Red mud in geopolymer pervious concrete for heavy metal removal with a removal rate of 53-77% because the geo-polymeric gel and red mud have good adsorption for heavy metals, but red mud shows a negative effect on mechanical strength [50]. In addition, a porous bio-based material, biochar is also added to pervious concrete for N and P removal [52]. Therefore, it is of significance to choose an adsorptive material with appropriate strength and adsorption capacity to improve the adsorption performance of pervious concrete.

In this chapter, steel slag is applied as adsorptive aggregates to replace conventional aggregates, a two-sized aggregate structure is firstly proposed for improving the adsorption performance, mechanical properties and durability of pervious concrete, and then the effects of cement, sand, water-cement ratio (w/c) and steel slag content on adsorption performance are investigated based on an orthogonal test result. The present work resulted in an optimal mix design of two-sized aggregate pervious concrete with excellent adsorption capacity together with desired mechanical properties and

durability for engineering applications.

6.2 Two-sized aggregate structure for pollutants removal

Natural aggregate is here modelled to be a spherical particle, the structure comparison of conventional pervious concrete and two-sized aggregate pervious concrete is shown in **Fig. 6.1**. Conventional pervious concrete often contains a single-sized aggregate for high permeability and good anti-clogging properties. However, for two-sized aggregate pervious concrete, low permeability is desirable as long as the pollutants can penetrate the concrete matrix with water flow and be absorbed by adsorptive ingredients. Besides, the low void can lead to an improvement in mechanical properties [181]. Therefore, the two-sized aggregate structure is applied to improve the adsorption and purification function of pervious concrete in this study. Natural aggregates with larger particle sizes are used as the skeleton, and the small-sized adsorptive particles are filled into the skeleton voids as the main body for pollutant removal by physical and chemical adsorption. The large-sized natural aggregates and small-sized adsorptive aggregates form a two-sized structure. Furthermore, the large-sized aggregates can also be replaced with adsorptive aggregates to further improve the adsorption capacity of pervious concrete.

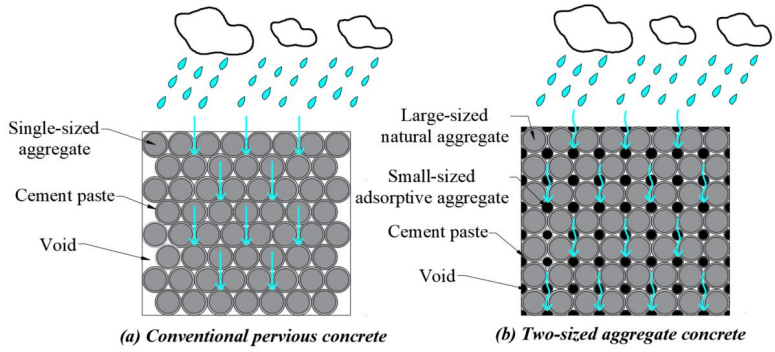

Fig. 6.1 Structure comparison of conventional pervious concrete and two-sized aggregate pervious concrete.

The mathematical relationship of the particle size between the natural aggregate and the adsorptive aggregate is shown in **Fig. 6.2**. The optimized particle packing can enhance the mechanical properties and durability of pervious concrete [182,183]. When the natural aggregate is single-sized, usually two arrangements (triangular array and square array) exist between aggregates from a two-dimensional perspective. There are three types of holes formed by two aggregate arrangements, including cube pore,

octahedral pore and tetrahedral pore. For example, when using natural aggregates as a skeleton with a particle size of R_1=5 mm, the maximum particle size of the adsorptive aggregate is R_2=1.15 mm, 2.05 mm or 3.65 mm based on three packing modes. Due to the angular effect of natural aggregates, most natural aggregates belong to a close-packed array structure, thus the formed pores are mainly tetrahedral and octahedral holes. When the particle size of the natural aggregate is selected as 5 mm, the adsorptive aggregate size should not exceed 2.05 mm to make small-sized adsorptive aggregate smoothly fill the pore structure for a good micropore structure of pervious concrete. The small-sized adsorptive aggregate can fit into these holes, theoretically, the particle size of the adsorptive aggregate can be estimated for good packing modes using:

$$R_2 = \left(\sqrt{3} - 1\right)R_1 \tag{6.1}$$

$$R_2 = \left(\sqrt{2} - 1\right)R_1 \tag{6.2}$$

$$R_2 = \left(\frac{\sqrt{6}}{2} - 1\right)R_1 \tag{6.3}$$

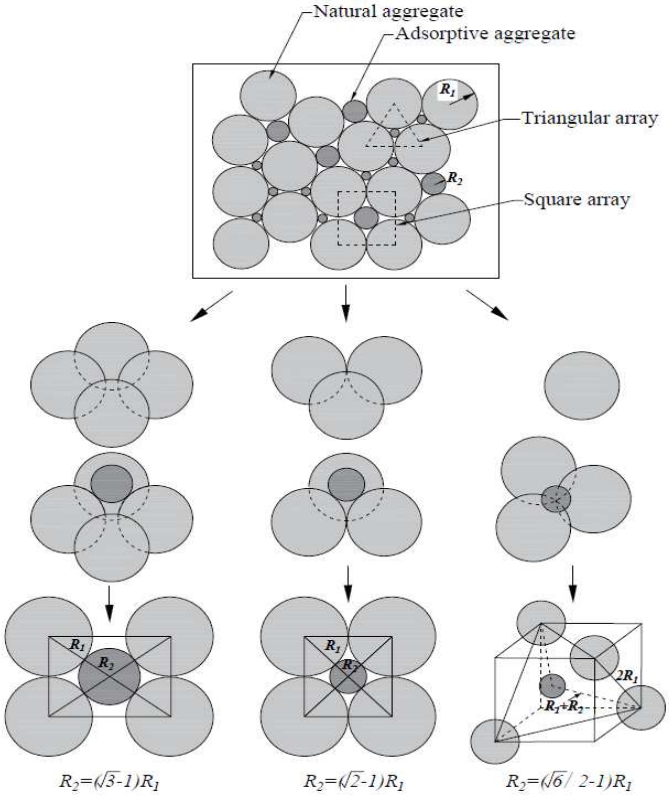

Fig. 6.2 Three packing forms of two-sized aggregates (R_1: normal aggregate size; R_2: adsorptive aggregate size).

6.3 Materials and Methods

6.3.1 Materials

Basalt with a particle size of 2-5 mm is used as coarse aggregates. BOF steel slag (TATA Steel, The Netherlands) with 1-2 mm particle size is used as an alternative for the fine aggregates (**Fig. 6.3**). The specific densities of the basalt and the steel slag are 3.1 g/cm^3 and 3.9 g/cm^3, respectively. Portland cement CEM I 52.5 R (ENCI, The Netherlands) is used as the binder. CEN-NORM sand satisfied with European standards (EN 196-1) is used as fine aggregates.

Fig. 6.3 (a) BOF steel slag and (b) Basalt.

6.3.2 Mix proportion and specimen preparation

- *Effects of the steel slag on the performance of pervious concrete*

Firstly, the effects of the small-sized steel slag on the physical and mechanical properties, adsorption performance and freeze-thaw resistance of pervious concrete are evaluated. A mixture containing 301 kg/m^3 cement, 110 kg/m^3 sand, 111.4 kg/m^3 water and 1574 kg/m^3 basalt is used as the control mix, which refers to the mix proportion of pervious concrete as reported by Nguyen et al [184]. The 2-5 mm basalt is replaced by 1-2 mm steel slag to form a two-sized skeleton structure in the other four batches, and other parameters are kept constant. The alternative volume ratios are set as 12.5%, 25%, 37.5% and 50%, respectively. The mix proportions of pervious concrete are presented in **Table 6.1**.

- *Mix proportion of orthogonal test*

The orthogonal test is used to investigate the optimal mixing ratio of two-sized aggregate pervious concrete. The effects of four factors (including cement, sand, w/c and the volumetric content of steel slag in total aggregates) on physical and mechanical

properties, adsorption performance and freeze-thaw resistance of pervious concrete are investigated, and each factor is designed as three levels, as shown in **Table 6.2**. The orthogonal table $L_9(3^4)$ is applied in the orthogonal test, the mix proportions of pervious concrete are shown in **Table 6.3**.

Table 6.1 Mix proportions of pervious concrete.

Samples	Cement (kg/m^3)	Sand (kg/m^3)	Water (kg/m^3)	Aggregates		Steel slag /total aggregates (Vol.%)
				1-2 mm Steel slag (kg/m^3)	2-5 mm Basalt (kg/m^3)	
Control	301	110	111.4	0	1574	0
SS12.5	301	110	111.4	251.6	1377.3	12.5
SS25	301	110	111.4	503.2	1180.5	25
SS37.5	301	110	111.4	754.7	983.8	37.5
SS50	301	110	111.4	1006.3	787	50

Table 6.2 Factors and levels of the orthogonal test.

Three levels	Four factors			
	Cement (kg/m^3)	Sand (kg/m^3)	W/C	1-2 mm steel slag/ total aggregate (Vol.%)
1	350	400	0.33	25
2	400	450	0.35	50
3	450	500	0.37	75

6.3.3 Test methods

- *Physical and mechanical properties*

The density of the sample is measured following EN 12390-7. The porosity of the samples is determined according to ASTM C1754/C1754M-12. The cross-section of the sample after the flexural test is captured by a high-definition camera for evaluation of internal pore properties including pore area fraction and average pore size, etc. are analyzed based on the image analysis method by the Image J software [185]. A random location of 40×40 mm^2 on the casting surface of the sample is used as the surface pore analysis. Considering the apparent differences in the casting surface of the sample, the change in porosity of the entire casting surface along with the length of the sample is analyzed.

The 28-day compressive strength and flexural strength of the sample are determined according to EN 196-1. Fragments of the sample are collected after the compression test for microstructure analysis using SEM.

The porosity can be calculated according to:

$$P = \left[1 - \left(\frac{M_{dry} - M_{sub}}{\rho_{water} \times V_s}\right)\right] \times 100\% \quad (6.4)$$

where P is the total porosity of the sample (%); M_{dry} is the dry mass of the sample (kg); M_{sub} is the submerged mass of the sample in water (kg); V_s is the volume of the sample (m^3); ρ_{water} is the density of water (kg/m^3).

The water permeability of the sample is determined using the falling head method, and the coefficient of water permeability is calculated based on Darcy`s Law as shown by:

$$k = \frac{a \times L}{A \times t} ln\left(\frac{h_1}{h_2}\right) \quad (6.5)$$

where k is the water permeability coefficient (mm/s); a is the cross-sectional area of pipe (mm^2); A is the cross-sectional area of the cylindrical sample (mm^2); L is the length of the sample (mm); t is the time when the water head varies from h_1 to h_2; $h_1$is the initial water head (mm); h_2 is the final water head (mm).

Table 6.3 Mix proportions of the orthogonal test.

Samples No.	Cement (kg/m^3)	Sand (kg/m^3)	w/c	Water (kg/m^3)	Aggregates			
					1-2 mm Steel slag (kg/m^3)	Steel slag /total aggregate (Vol.%)	2-5 mm Basalt (kg/m^3)	Basalt/total aggregate (Vol.%)
1	350	400	0.33	115.5	511.4	25	1199.9	75
2	350	450	0.35	122.5	973.4	50	761.2	50
3	350	500	0.37	129.5	1385.8	75	361.3	25
4	400	400	0.35	140	1415.4	75	369.0	25
5	400	450	0.37	148	446.1	25	1046.6	75
6	400	500	0.33	132	887.5	50	694.1	50
7	450	400	0.37	166.5	860.5	50	673.0	50
8	450	450	0.33	148.5	1289.6	75	336.2	25
9	450	500	0.35	157.5	403.2	25	945.9	75

- *Adsorption performance*

The adsorption performance of pervious concrete is evaluated by the P-solution removal test in this study. Considering the high P-removal performance of steel slag aggregates [15], different initial concentrations of P-solution, including low-concentration (168 mg/L and 307 mg/L) and high-concentration (1869 mg/L and 2898 mg/L) P-solutions are prepared for the P-adsorption test by dissolving the chemically pure potassium dihydrogen phosphorus (KH_2PO_4) in distilled water. After that, the P-solution is stirred at 225 rpm in a thermostatic shaker for 24 hours for the dissolution

of the solid P-particle before the adsorption test.

The P-adsorption test of pervious concrete in this study refers to the laboratory setup method for the removal of stormwater pollutants reported by Haselbach et al. [46], as shown in **Fig. 6.4**. The 40×40×160 mm^3 sample is cut into a small cube block (approximately 4×4×4.5 mm^3) for the P-adsorption test. Firstly, 100 ml of P-solution is poured into a glass container, and then the control valve is opened, the P-solution is slowly dripped onto the surface of the concrete block with a flow rate of 3-5 ml/min, and a beaker at the bottom is used to collect the filtrate. When the P-solution is completely filtered by the concrete block, the collected filtrate is immediately poured into the upper glass container to continue the next cyclic P-adsorption test. After P-solution is adsorbed by the concrete block for 1, 3 and 5 times, about 3 ml of filtrate is collected by an injecter and then filtered by a 0.45 μm membrane filter and the P-concentration of the filtrate is determined using an IC analyzer. The mass of the small cube block for the cyclic adsorption test is shown in **Table 6.4**. The P-adsorption amount (q, mg/g) and P-removal fraction (P_R, %) are calculated according to Eqs. (3.1) and (3.2), respectively.

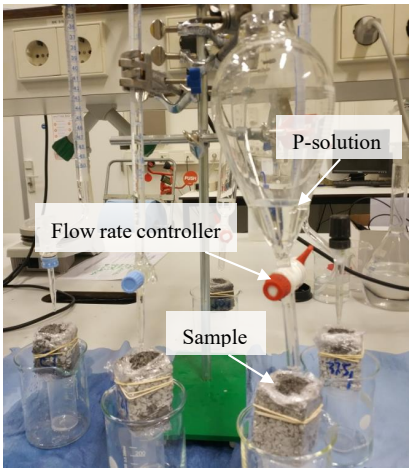

Fig. 6.4 Laboratory setup for P-adsorption test.

- *Freeze-thaw test*

The resistance to freeze-thaw cycles of pervious concrete is evaluated according to EN 1338. The temperature of the freeze-thaw test varies from -18 ℃ to 20 ℃ for 24 h. The prism samples of 40×40×160 mm^3 are completely immersed in the water, and the water surface is 5±2 mm above the surface of the sample. The mass loss and apparent change of the sample after each freeze-thaw cycle is evaluated.

Table 6.4 Mass of the small cube block for cyclic adsorption test.

P-concentration	Sample mass (g)								
(mg/L)	1	2	3	4	5	6	7	8	9
1869	144	147	140	151	144	154	169	167	176
2898	153	154	148	156	137	159	171	167	179

6.4 Results and discussion

6.4.1 Effects of steel slag content on the performance of pervious concrete

- *Density, porosity and permeability*

The aggregate size and shape have a significant effect on the porosity and permeability of pervious concrete [179]. As shown in **Fig. 6.5**, the replacement of basalt aggregate with small-sized steel slag aggregate increases the density of pervious concrete and reduces the porosity and permeability coefficient. When 50% basalt (2-5 mm) is replaced by 1-2 mm steel slag, the density increases by 26% and the porosity and permeability coefficient reduce by 36% and 63%, respectively. The phenomenon of smaller aggregate size leading to a lower permeability of pervious concrete is reported in previous studies [186]. The tendency of an increase in pore sizes of pervious concrete with the increase of aggregate particle sizes can be easily noticed [185].

The pores have a relatively uniform distribution as the pores are smaller and regular [187]. In this study, the pores of the SS50 concrete are more uniform than that of the control concrete. Besides, it can be observed that the small-sized steel slag fills the large pores between aggregates, resulting in a significant decrease in porosity. The mechanical strength and permeability of pervious concrete mainly depend on micropores, cement paste and aggregate characteristics [188]. The reduced porosity through the small-sized aggregate can contribute to the strength enhancement of pervious concrete.

- *Compressive strength and flexural strength*

The relationship between 28-day mechanical strength and porosity of pervious concrete is shown in **Fig. 6.6**. As the content of small-sized steel slag increases, the 28-day compressive strength and flexural strength of pervious concrete gradually increase. When the coarse aggregate is replaced by 50% steel slag, the compressive and flexural strengths are 14.3 MPa and 5.19 MPa, respectively, with an increase of 151% and 131%, compared to the control concrete. This may be attributed to the good packing, low porosity and particle interlock formed by the two-sized aggregates [189]. It can be

concluded that the mixing of 1-2 mm steel slag aggregate and 2-5 mm natural aggregate results in an increased aggregate packing density, contributing to the improvement of the mechanical strength.

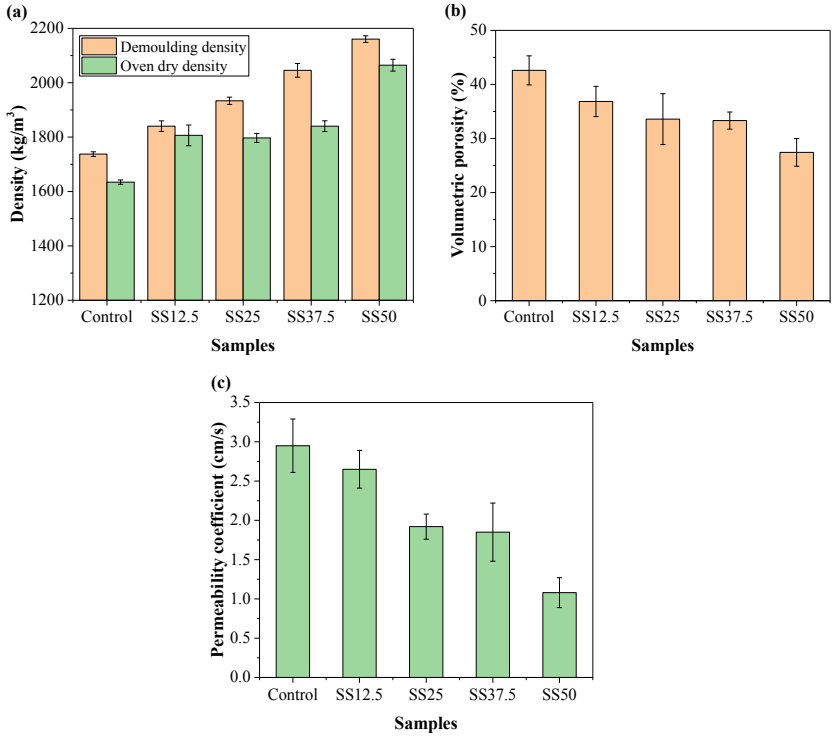

Fig. 6.5 Density, volumetric porosity and permeability coefficient of pervious concrete.

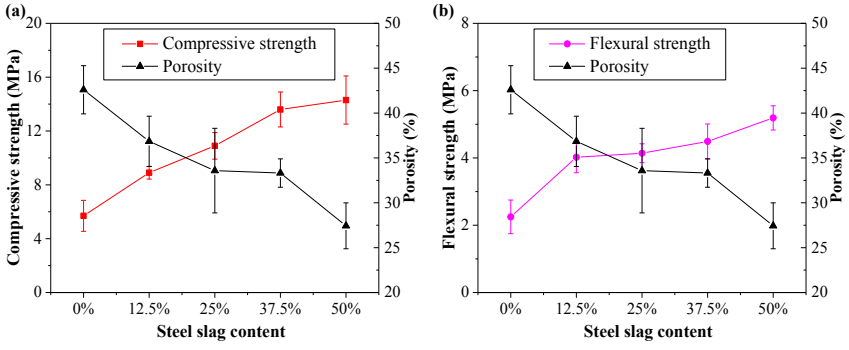

Fig. 6.6 Relationship between 28-day compressive strength and flexural strength and porosity of pervious concrete.

Generally, the interfacial transition zone (ITZ) is the weakest part of conventional

concrete, which dominates the performance of the concrete [190]. However, the designed porosity is the weakest part of pervious concrete. In this study, small-sized steel slag fills the pores between the aggregates and decreases the porosity of pervious concrete, thus improving the mechanical strength. Moreover, steel slag has a higher density and strength than basalt aggregate. The application of high-strength waste aggregates (e.g. copper slag [179], steel slag [191], etc.) can enhance the mechanical strength due to the strong interlocking effect [190]. The use of cement, fine aggregates, polymeric materials, fibres, etc. will further improve the mechanical properties of pervious concrete [192–195].

Microscope images of the ITZ of pervious concrete are shown in **Fig. 6.7**. A good bond between basalt and mortar is observed, however, a small number of microcracks is produced between the ITZ and the surface of basalt aggregate during the compression test (**Fig. 6.7a**). The micro-cracks are observed in the ITZ between steel slag and mortar, but no steel slag cracking (**Fig. 6.7b**), indicating that the ITZ between steel slag and mortar is the weakest part of pervious concrete, which needs to be strengthened in future work.

- *P-adsorption performance*

The initial concentration of the P-solution is 168 mg/L and 307 mg/L, respectively. The results show that no P is detected in the filtrate, indicating that all P in the solution is adsorbed by pervious concrete. This may be attributed to the calcium ions (Ca^{2+}) and hydroxide ions (OH^-) released from the pervious concrete reacting with the phosphate to form Ca-P precipitates. Moreover, when the pervious concrete is immersed in water for a long time, the aquatic microbes attached to the porous structures also contribute to biological adsorption [196], and the internal micropores have physical adsorption for the suspended substances from stormwater [197]. Therefore, the P-removal performance of pervious concrete depends on the connected pore structure of pervious concrete, in addition to the adsorption capacity of the adsorptive aggregate and the mortar matrix.

The comparison of pollutant removal of different concretes from stormwater runoff is shown in **Fig. 6.8**. For conventional concrete, stormwater containing pollutants can not penetrate the conventional concrete, only the surface contact with pollutants, and the pollutant removal of the conventional concrete can be ignored (**Fig. 6.8a**). During the infiltration of stormwater into the pervious concrete, the ions (calcium, iron, aluminium and hydroxide ions, etc.) leached from the cement paste of pervious concrete can react with a small amount of pollutants (methylene blue, phosphate, nitrate and heavy metals, etc.) through surface complexation, ion exchange and precipitation [180,198].

Conventional single-sized pervious concrete exhibits a certain adsorption capacity for pollutants (**Fig. 6.8b**), however, it usually has a low adsorption capacity and a long contact time [15]. Due to the high adsorption capacity of the adsorptive aggregate, more pollutants can be combined with the adsorptive aggregate and cement matrix, significantly improving the pollutant removal capacity of pervious concrete by a two-sized aggregate structure (**Fig. 6.8c**). Moreover, when the large-sized natural aggregate is completely replaced by the adsorptive aggregates, the adsorption capacity of pervious concrete would be further improved.

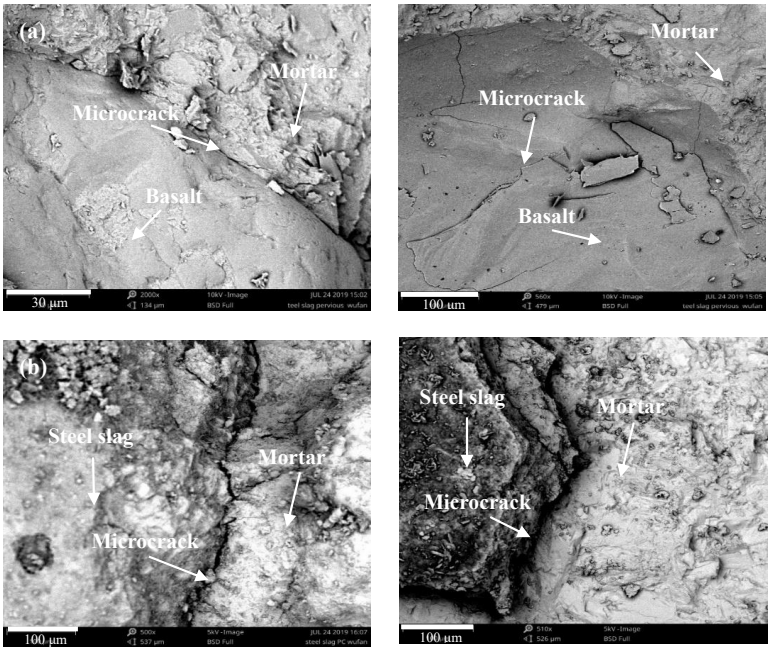

Fig. 6.7 Microscope images of the ITZ (a) Basalt and (b) Steel slag.

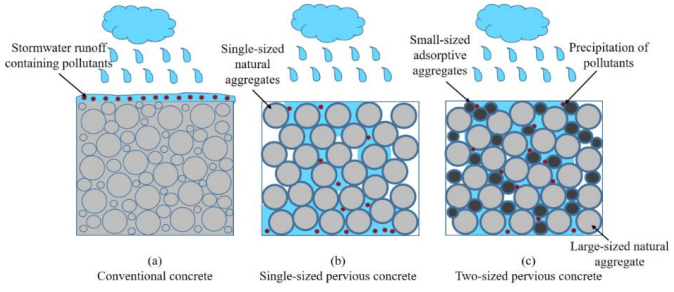

Fig. 6.8 Comparison of pollutant removal from stormwater runoff by (a) conventional concrete, (b) single-sized pervious concrete and (c) two-sized pervious concrete.

During the rainy season, the stormwater penetrates the voids of pervious concrete, which then dissolves the hydration products of cement paste [199]. The dissolved ions are then washed out from the pervious concrete by stormwater. Therefore, when steel slag is used as aggregates for pervious concrete, the leaching behavior should be evaluated in this study, and the leaching results are shown in **Table 6.5**. The amount of sodium and potassium is 50-100 mg/kg and the calcium ion is above 500 mg/kg. Some harmful metal ions such as As, Cr, V, etc. leached from the steel slag particle and pervious concrete are far below the maximum limit values for building materials according to the Dutch Soil Quality Decree [140]. The results confirm that the pervious concrete produced in this study can be used for P-removal without any environmental risk.

Table 6.5 Leaching results of steel slag and two-sized pervious concrete (mg/kg).

Elements	Al	As	Ba	Cr	Fe	Mg	Sr	V
Steel slag	3.49	≤0.18	0.004	0.13	≤0.25	0.55	0.37	≤0.95
Control	1.41	≤0.18	3.44	0.05	≤0.15	0.04	21.2	≤0.22
SS12.5	0.06	≤0.18	3.80	0.05	≤0.22	0.04	21.3	≤0.22
SS25	≤0.02	≤0.18	3.12	0.04	≤0.23	0.04	21.0	≤0.22
SS37.5	≤0.31	≤0.18	3.32	0.05	≤0.22	0.04	21.1	≤0.21
SS50	≤0.28	≤0.18	3.54	0.07	≤0.25	0.02	21.0	≤0.22
Limit value	-	0.90	22	0.63	-	-	-	1.80

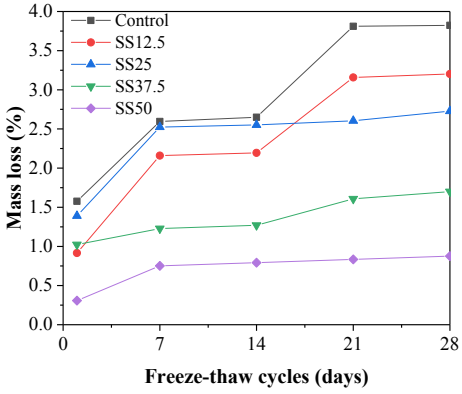

Fig. 6.9 Mass loss of pervious concrete during the freeze-thaw test.

- *Freeze-thaw resistance*

Pervious concrete is applied to remove pollutants from stormwater runoff and is often in contact with an aqueous solution, the resistance to freeze-thaw cycles of pervious

concrete should be evaluated when it is applied in a cold region. As shown in **Fig. 6.9**, the SS50 concrete has the best resistance to freeze-thaw cycles, compared to the control concrete. The use of small-sized steel slag instead of basalt significantly improves the freeze-thaw resistance of pervious concrete. After 28 freeze-thaw cycles, the mass loss of the control, SS12.5, SS25, SS37.5 and SS50 concrete are 4%, 3%, 3%, 2% and 1%, respectively. The mass loss of the SS50 concrete decreases by 74%, compared to the control concrete. The spalling of aggregates from the concrete surface may lead to an increase in mass loss, for example, a significant increase in mass loss of the SS12.5 concrete is observed at 21 freeze-thaw cycles. Therefore, freeze-thaw characteristics of pervious concrete can be improved by using a two-sized aggregate structure composed of fine steel slag and normal coarse aggregate.

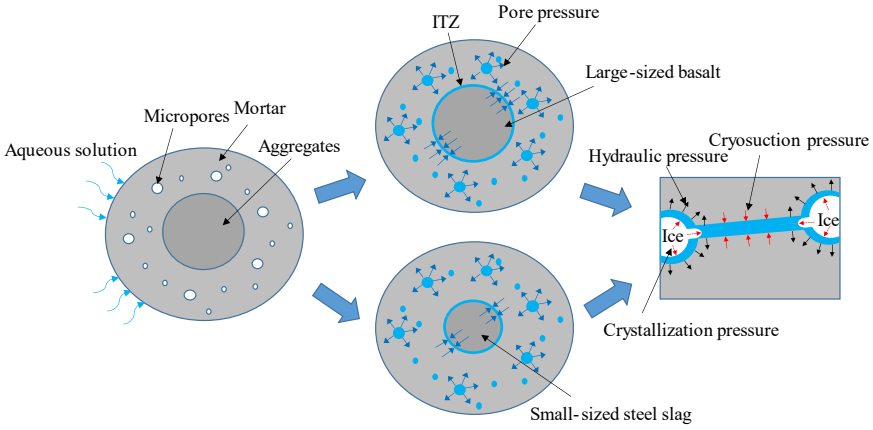

(a) Concrete containing micropores (b) Ice formation in micropores (c) Pore pressure in micropores

Fig. 6.10 Schematic diagrams of the freeze-thaw failure mechanism of two-sized aggregate pervious concrete.

The main degradation form of freeze-thaw damage is the cracking and spalling of the concrete surface [65,200]. The effects of pore pressures on the micropores of two-sized aggregate pervious concrete during freeze-thaw cycles are illustrated in **Fig. 6.10**, the freeze-thaw damage is mainly caused by the pore pressure due to the ice formation [200,201]. The pore pressure is composed of hydraulic pressure (ice volume expansion), cryosuction pressure (surface tension of the water) and crystallization pressure (shape of ice crystals), depending on the thermodynamics between ice crystal and unfrozen water [202–204]. The hydraulic pressure mainly relies on the increased ice volume due to expansion, while the cryosuction pressure and crystallization pressure depend on pore size and temperature [202]. In this study, when the basalt is replaced by small-sized steel slag, the internal defects or micropores of the pervious concrete are reduced, and the hydraulic pressure generated by the ice expansion also significantly decreases,

which contributes to the good freeze-thaw resistance of two-sized aggregate pervious concrete.

The effects of freeze-thaw cycles on the mechanical strength of pervious concrete are analyzed, as shown in **Table 6.6**. The results show that the compressive strength and flexural strength significantly decrease after freeze-thaw cycles. However, when the basalt is replaced by small-sized steel slag, the reduction in mechanical strength is rather limited. After 15 freeze-thaw cycles, the reduction in the compressive strength and flexural strength of the SS50 concrete is only 4% and 7%, respectively, which is significantly lower than the reduction in the strength of the control concrete.

The degrading effect of freeze-thaw cycles on the mechanical properties of concrete has been observed in previous studies [205]. The cracks caused by freeze-thaw damage are the main reasons for strength reduction [206]. According to the degradation model of strength as reported by Sun et al. [205], the relative compressive strength of conventional concrete after 15 freeze-thaw cycles is approximately 0.96, with a compressive strength loss of about 4%. It is noted that SS50 developed in this work shows a comparable compressive strength loss with conventional concrete, indicating its excellent durability performance.

Table 6.6 Mechanical strength loss of pervious concrete after 15 freeze-thaw cycles.

Samples	Compressive strength (MPa)			Flexural strength (MPa)		
	Before	After	Reduction in %	Before	After	Reduction in %
Control	5.7	4.5	21	2.25	2.06	8
SS12.5	8.9	8.0	10	4.02	3.68	9
SS25	10.9	9.5	13	4.14	3.64	12
SS37.5	13.6	11.0	19	4.49	4.32	4
SS50	14.3	13.8	4	5.19	4.81	7

6.4.2 Orthogonal results of two-sized aggregate pervious concrete

- *Physical properties*

The surface texture of pervious concrete is shown in **Fig. 6.11**. The results show that samples 2, 3, and 4 have a perfect surface, the small-sized steel slag is tightly embedded between the basalt aggregates, and the overall surface is relatively smooth compared to samples 1 and 5. The surfaces of samples 8 and 9 are covered by mortar, most of the micropores are filled with mortar and the porosity is lower. No micropores are observed on the surface of sample 9 and all micropores are blocked by mortar, which will significantly affect the penetration of pollutants into the pervious concrete and reduce its adsorption performance.

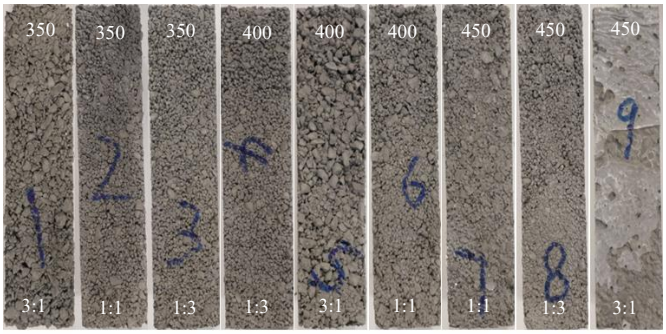

Fig. 6.11 Surface texture of pervious concrete (top values: cement content, below values: LA:SA).

The target grading line is calculated by the modified Andreasen and Andersen model using [207]:

$$P(D) = \frac{D^q - D_{min}^q}{D_{max}^q - D_{min}^q} \quad (6.6)$$

Where D is the particle size of the materials; D_{min} and D_{max} are the minimum and maximum particle size of the materials, and their values are 0.3 μm and 5000 μm in this study, respectively; *P(D)* is the cumulative fraction of the total solids being smaller than the particle size of D; q is the distribution modulus, and 0.30 is used in this study.

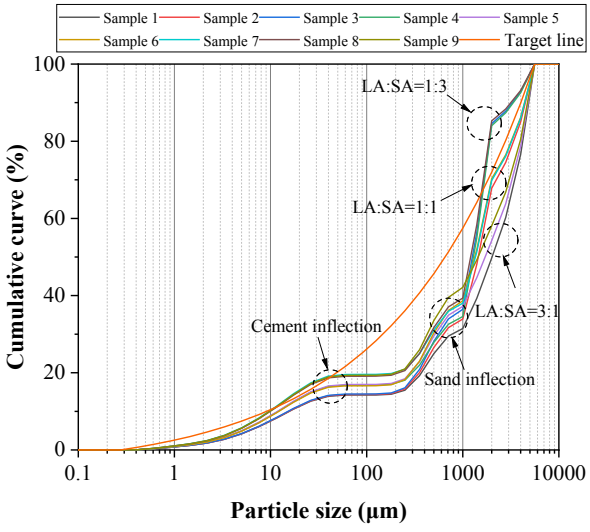

Fig. 6.12 Cumulative curves of particle size distribution of pervious concrete.

Generally, different types of concrete can be designed using Eq. (6.6) by applying various distribution modulus values (q), which determine the proportion between the

fine and coarse aggregates in the mixture. Higher distribution modulus values (q>0.5) are leading to coarse mixtures whereas smaller values (q<0.25) are resulting in mixtures which are rich in fine particles [208]. The distribution modulus of 0.23 is recommended for ultra-high-performance concrete [209]. An optimum range of the distribution modulus of 0.22-0.25 and 0.35-0.40 for self-compacting concrete and earth-moist concrete, respectively [208,210,211]. The distribution modulus values of 0.25 and 0.32 are used for cement-based lightweight composites [212]. The distribution modulus values of 0.30 and 0.35 are designed for pumpable low-shrinkage flowing concrete [213]. Due to higher coarse particles in pervious concrete, a distribution modulus value of 0.30 is used for the target line based on the particle packing method.

The cumulative curves of the particle size distribution of pervious concrete are shown in **Fig. 6.12**. The results show that the volume ratio of large-sized aggregate (LA) to small-sized aggregate (SA) has a significant effect on the cumulative curves of particle size distribution. When the volume ratio of large-sized aggregate to small-sized aggregate is 1:3, which is close to the target line, and the surface texture of the sample is suitable for permeable adsorptive concrete.

Table 6.7 Porosity, water absorption and density of concrete.

Samples	Internal pore obtained by image analysis		Surface pore obtained by image analysis		Volumetric porosity obtained by test (%)	24-hour water absorption (%)	Oven-dry density (kg/m^3)
	Area fraction of pores (%)	Average pore size (mm)	Area fraction of pores (%)	Average pore size (mm)			
1	10	0.06	12	0.06	14	6	2081
2	9	0.04	11	0.04	16	7	2084
3	6	0.03	11	0.05	17	7	2013
4	9	0.04	16	0.07	17	7	2132
5	2	0.03	12	0.10	13	6	2048
6	5	0.04	12	0.05	14	6	2198
7	4	0.04	3	0.02	11	5	2390
8	10	0.02	4	0.03	12	5	2325
9	1	0.04	0.1	0.01	9	4	2484

The porosity, water absorption and density of pervious concrete are shown in **Table 6.7**. The results show that the area fraction and the average pore size of the surface pore of the most pervious concrete are higher than that of the internal pore. The calculated area fraction of surface pores of samples 7, 8, and 9 are very low because these three samples have more cement content (450 kg/m^3), resulting in the blockage of the pores of the concrete by the excessive cement paste, consequently showing lower water absorption and higher density compared to other sample series. Generally, the target porosity of

pervious concrete should be 15-35% considering the requirements of the anti-clogging characteristic [214]. The low-porosity pervious concrete may have a clogging problem, and further research is needed in future work.

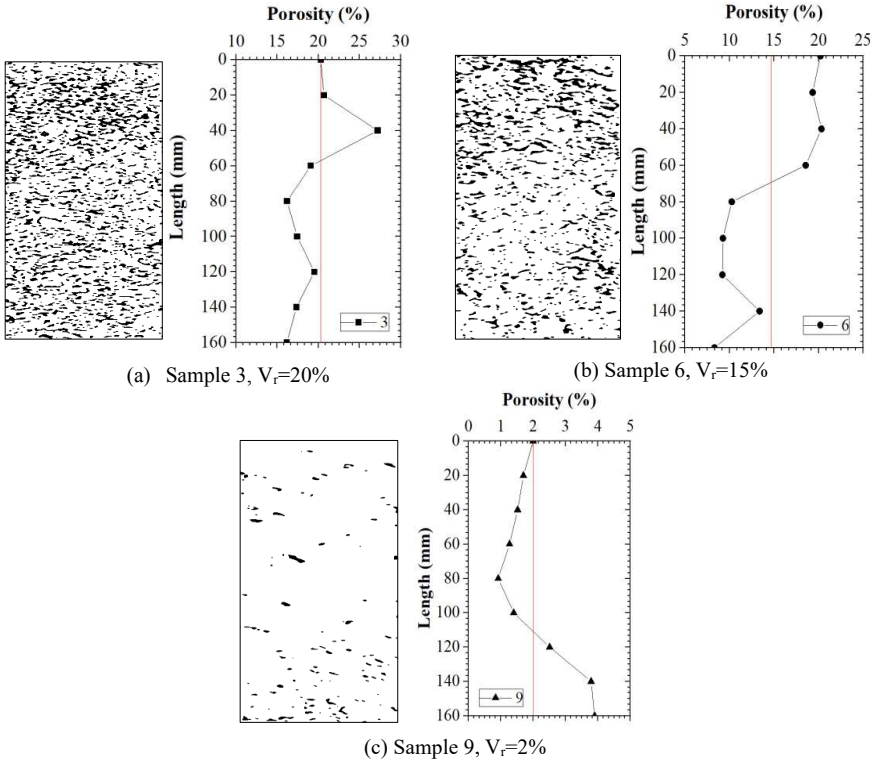

(a) Sample 3, V_r=20%

(b) Sample 6, V_r=15%

(c) Sample 9, V_r=2%

Fig. 6.13 Changes in porosity of the entire casting surface of pervious concrete with its length (black areas are pores).

The change in porosity of the entire casting surface along with the length of samples 3, 6 and 9 is analyzed by Image J software, as shown in **Fig. 6.13**. The porosity of the entire casting surface of samples 3, 6 and 9 are unevenly distributed along with the length, with a range of 16-27%, 8-20% and 1-4%, respectively. In the length range, the average porosity of the entire casting surface of samples 3, 6 and 9 is 20%, 15% and 2%, respectively. The porosity of the entire casting surface of sample 3 more evenly distributes along with the length compared with samples 6 and 9, which is helpful for pollutant removal by pervious concrete.

- *Mechanical properties*

The compressive strength and flexural strength of samples 1, 2, and 3 series with a

cement content of 350 kg/m^3, are significantly different from those of sample 4, 5, and 6 series (cement: 400 kg/m^3) and sample 7, 8, and 9 series (cement: 450 kg/m^3), as shown in Fig. 6.14. These results are consistent with the porosity results, that is, samples 1, 2, and 3 series with a high porosity result in a low compressive strength (27.0-31.3 MPa), while samples 7, 8, and 9 series with a low porosity show a higher compressive strength (45.7-71.7 MPa). The compressive strengths of samples 4, 5 and 6 series vary from 31.5 MPa to 39.4 MPa. Similar to the compressive strength, the flexural strength in this study shows a similar trend. The flexural strengths of sample 1-3, 4-6 and 7-9 series vary between 6.21-6.25 MPa, 6.91-7.20 MPa and 8.08-8.47 MPa, respectively, indicating sample 1-3 series in this study have relatively good strength for structural applications including sidewalks, parking lots and parkways, etc., compared to conventional pervious concrete.

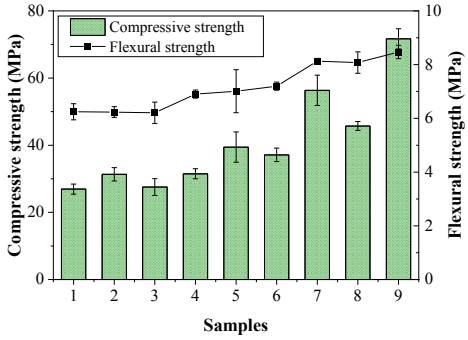

Fig. 6.14 28-day compressive strength and flexural strength of pervious concrete.

- *P-adsorption capacity and removal rate*

Considering the low-concentration P solution (168 mg/L and 307 mg/L) is totally adsorbed by pervious concrete in the first part, a much higher concentration of P solution (1869 mg/L and 2898 mg/L) is applied to the present adsorption test. As shown in **Fig. 6.15**, the P-adsorption amount and P-removal fraction of different pervious concrete have a significant difference. The P-adsorption amount and removal fraction of samples 1, 2, and 3 series are better than other samples series. When the P-concentration is 1869 mg/L, the P-adsorption amount of sample 1-3, 4-6 and 7-9 series varies between 0.15-0.30 mg/g, 0.06-0.29 mg/g and 0.01-0.04 mg/g, respectively, the corresponding P-removal fractions are 11-22%, 5-23% and 1-4%, respectively. The high P-removal rate of samples 1, 2, and 3 series may be attributed to the relatively high porosity and water absorption, therefore, phosphate in the solution can easily contact calcium ions for Ca-P precipitates. Although samples 7, 8, and 9 series have high mechanical strength, the adsorption capacity is very low, compared to other sample series.

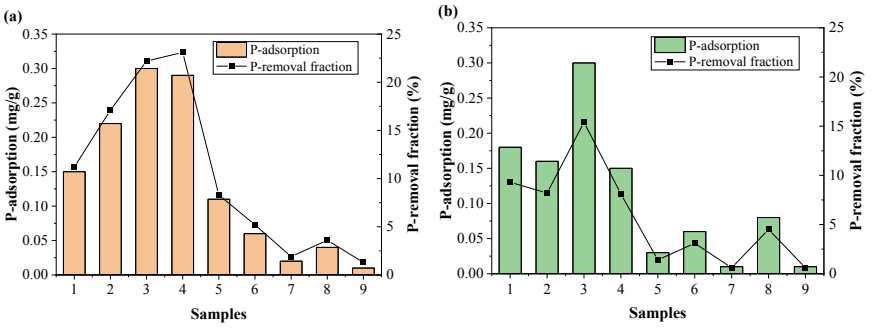

Fig. 6.15 P-adsorption amount and removal fraction of pervious concrete in P- solution of (a) 1869 mg/L and (b) 2898 mg/L.

The significance of cement, sand, w/c and small-sized steel slag content on the adsorption capacity are analyzed through the variance analysis. The calculated results are shown in **Table 6.8**. The deviation analysis of the orthogonal test results of P-adsorption capacity is calculated based on [215]:

$$K = \sum_{l=1}^{r} K_{jl} \tag{6.7}$$

$$P = \frac{1}{n} K^2 \tag{6.8}$$

$$Q = \sum_{i=1}^{n} p_i^2 \tag{6.9}$$

$$Q_j = \frac{1}{m} \sum_{l=1}^{r} K_{jl}^2 \tag{6.10}$$

$$S_j^2 = Q_j - P \tag{6.11}$$

$$S_T^2 = \sum_j S_j^2 \tag{6.12}$$

where, n is the number of experiments; r is the level of each factor; m is the number of occurrences of each level; the values of the n, r and m in this study are 9, 3 and 3, respectively; K_{jl} is the sum of the test results (P_i in **Table 6.8**) of the corresponding factor level l (l=1,2,3,⋯,r) in the column j; P and Q are an intermediate value to facilitate calculation of S_j^2 and S_T^2; S_j^2 is the sum of squares for each factor in the column j; S_T^2 is the sum of squares for total deviations.

Considering the orthogonal table L9 (3^4) is completely filled in this study, the sand has no significant effect on the P-adsorption capacity, with the smallest sum of squares (S_j^2) than other factors (cement, W/C and steel slag), thereby it is used as the error group for the further variance analysis. The variance analysis results are shown in **Table 6.9**. As expected, cement and steel slag content have significant effects on the P-adsorption capacity, especially the cement, the water-cement ratio has no significant effect on the

adsorption capacity. According to the deviation calculation results (**Table 6.8**) and the P-adsorption results, sample No. 3 shows excellent P-removal ability, which is recommended as the optimum mix for pervious concrete.

Table 6.8 Deviation calculation of the orthogonal results of P-adsorption capacity.

Sample No. (n)	Cement (kg/m^3)	Sand (kg/m^3)	W/C	1-2 mm steel slag/ total aggregate (Vol.%)	Adsorption capacity in 1869 mg/L P-solution (mg/g) (p_i)
	j=1	j=2	j=3	j=4	
1	350	400	0.33	25	0.15
2	350	450	0.35	50	0.22
3	350	500	0.37	75	0.30
4	400	400	0.35	75	0.29
5	400	450	0.37	25	0.11
6	400	500	0.33	50	0.06
7	450	400	0.37	50	0.02
8	450	450	0.33	75	0.04
9	450	500	0.35	25	0.01
K_{j1}	*0.67*	*0.46*	*0.25*	*0.27*	*K=1.2*
K_{j2}	*0.46*	*0.37*	*0.52*	*0.30*	*P=0.16*
K_{j3}	*0.07*	*0.37*	*0.43*	*0.63*	*Q=0.263*
Q_j	*0.222*	*0.162*	*0.173*	*0.187*	
S_j^2	*0.062*	*0.002*	*0.013*	*0.027*	S_T^2=*0.103*

Table 6. 9 Variance analysis of dependent variable of P-adsorption capacity.

Source of variance	Sum of squares	Degree of free	Mean square	F value	Significance
Cement	0.062	2	0.031	34.3	*
W/C	0.013	2	0.006	7.0	
Steel slag	0.027	2	0.013	14.8	(*)
Error	0.002	2	0.001		
Total (S_T^2)	0.103	8			

The symbols * and (*) represent the significance results under the condition of the significance level of α=0.10 and 0.05, respectively, and the corresponding critical F values are 9.0 and 19.0, respectively.

The particle size has a significant effect on P-removal efficiency, smaller particle size will release more calcium ions and hydroxide ions to combine with phosphate [216]. The pervious concrete with high void and small-sized aggregates has superior P-removal ability due to the large specific surface area [196]. The permeable pavement made of expanded shale aggregate can reduce the P-concentration from 0.2 mg/L to 0.04 mg/L by simulated storm test [174]. The pervious concrete treated with TiO_2 has a P removal of nearly 90%, with an initial concentration of 1000 mg/L [180]. In this study, the high-concentration P solution (1869 mg/L and 2898 mg/L) and the concrete blocks with a particle mass of 144-179 g are used for the P-adsorption test, thereby the

P-removal ability of pervious concrete blocks is acceptable.

- *Effects of cycles on P-adsorption performance*

The effects of adsorption cycles on P-adsorption amount and P-removal fraction are evaluated and the results are presented in **Fig. 6.16**. With the increase in the adsorption cycles, the P-adsorption amount and P-removal fraction of all pervious concrete increases, especially for samples 3 and 4. When the adsorption cycles increase from 1 to 5, the P-adsorption amount of sample 3 increases from 0.3 mg/g to 0.6 mg/g, and the P-removal fraction increases from 15% to 31%. This indicates that enough calcium ions are released from the pervious concrete for the chemisorption process of Ca-P precipitates, and the adsorption cycles do not reduce the adsorption capacity.

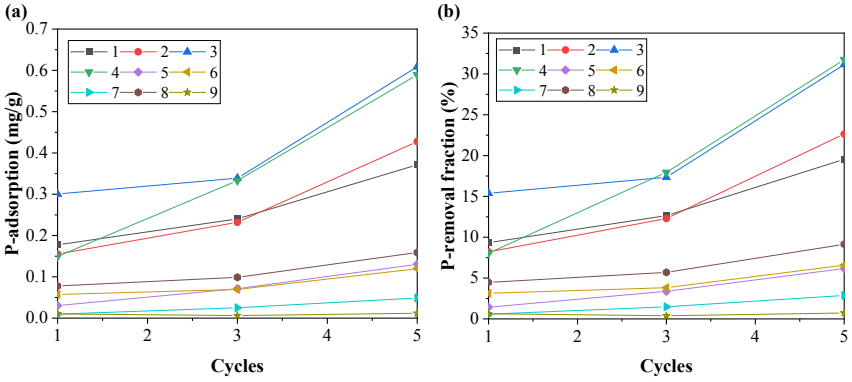

Fig. 6.16 Effects of cycles on P-adsorption amount and P-removal fraction of pervious concrete.

All adsorptive materials will reach saturation at a certain moment. Because only 5 cycles are used for the adsorption test, no saturation point is observed in this study, more adsorptive cycles need to be carried out for determining the saturation cycles. Moreover, the methods for extending the service life of the pervious concrete after pollutant saturation should be considered in future work, for example, to collect absorbed phosphate used as fertilizer for plants [217,218] or cultivate microbial communities in the micropores structure of pervious concrete to decompose absorbed organic matter [178].

- *Durability*

The mass loss of pervious concrete during the freeze-thaw cycles is presented in **Fig. 6.17a**. The mass loss of all concretes is relatively low, except for sample 1. At the 42 freeze-thaw cycles, the mass loss of sample 1 is 3%, and the mass loss of other sample series varies from 1% to 2%. The freeze-thaw damage mainly occurs on the surface of

the concrete and the four corners, which is manifested by the peeling of aggregate particles from the concrete surface (**Fig. 6.17b**). Compared to the freeze-thaw resistance results of the first part of this study, the freeze-thaw characteristics of pervious concrete have been significantly improved through the optimized mix design. Although samples 5 and 6 show the best freeze-thaw resistance, the P-adsorption amount and removal faction are relatively low compared to sample 3 (**Fig. 6.15**). Considering the high P-adsorption capacity and suitable strength and durability of sample 3, it is recommended as the optimum mix for pervious concrete.

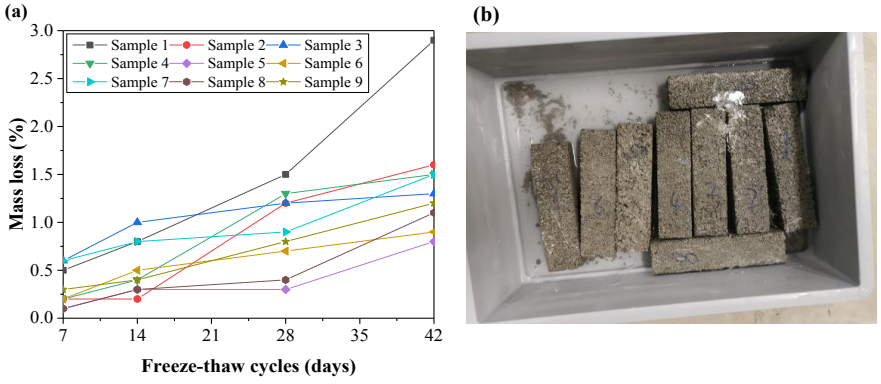

Fig. 6.17 (a) Mass loss of pervious concrete and (b) Changes in the concrete surface after 42 freeze-thaw cycles.

6.5 Conclusions

(1) When pervious concrete contains 50% steel slag (1-2 mm), compressive strength and flexural strength increase by 151% and 131%, respectively, and mass loss caused by freeze-thaw cycles decrease by 74%, compared to control concrete. This is attributed to the fact that small-sized steel slag fills the pores between the aggregates and gradually reduces porosity and permeability, which is beneficial for improving the mechanical strength and freeze-thaw resistance of pervious concrete.

(2) Two-sized aggregate pervious concrete has an excellent P-adsorption capacity, all P is removed from the aqueous solution because the calcium (Ca^{2+}) ion and hydroxide (OH^-) ion released by the pervious concrete react with the phosphate to form Ca-P precipitates. Moreover, the harmful elements (Cr, Sr and V, etc.) leached from pervious concrete are much lower than the maximum limit value for building materials, confirming no environmental risk.

(3) According to the results of orthogonal testing, cement and steel slag are the main factors affecting the adsorption performance of pervious concrete. Sample 3 (cement: 350 kg/m^3, sand: 500 kg/m^3, w/c: 0.37, 1-2 mm steel slag: 1385.8 kg/m^3 and 2-5 mm basalt: 361.3 kg/m^3) shows excellent adsorption capacity for high-concentration P-removal and can be used as the optimum mix for two-sized aggregate pervious concrete. Moreover, when the cycle number increases from 1 to 5, the P-adsorption capacity of sample 3 increases from 0.3 mg/g to 0.6 mg/g, and the P-removal rate increases from 15% to 31%.

Chapter 7 Improvement of phosphorus removal capacity of pervious concrete using highly adsorptive aggregates

Pervious concrete has been widely used in building engineering such as pavements, parking lots and rain gardens for urban runoff management. However, the low adsorption capacity of conventional aggregates greatly limits the pollutant removal capacity of pervious concrete. To improve the phosphate adsorption capacity of pervious concrete from stormwater runoff, BOF steel slag and manufactured aggregates are applied to improve the P-removal capacity. The physico-mechanical properties, adsorption performance, adsorption mechanism and environmental impacts of highly adsorptive pervious concrete are investigated. Results show that the adsorptive concrete and steel slag concrete exhibit excellent P-adsorption capacity, increasing by 31% and 52%, respectively, compared to the conventional aggregate concrete. The Ca^{2+} released from concrete is the dominant ion for the chemisorption of Ca-P precipitation. The P-adsorption amount and removal faction of adsorptive pervious concrete increase with P-concentration and reaction time. Langmuir model and Elovich model provide appropriate fitting for the adsorption isotherm of adsorptive pervious concrete. Moreover, the developed adsorptive pervious concretes show a low P-releasing capacity, indicating that they can be safely used for P-removal from stormwater runoff in building engineering, without potentially negative environmental impact.

This chapter is partially reproduced from:

F. Wu, Q.L. Yu, H.J.H. Brouwers. Improvement of phosphorus removal capacity of pervious concrete using highly adsorptive aggregates. Manuscript.

7.1 Introduction

Concrete slurry [219] or mortar powder [220] shows excellent adsorption capacity for P-removal due to the dissolved Ca^{2+} from $CaOH_2$, $CaCO_3$ and other phases in the hydrated cement matrix. The hydration product of Portland cement is a calcium-rich product, and the dissolved Ca^{2+} has a good adsorption capacity for P-removal [176]. The adsorption capacity of conventional aggregates such as crushed limestone, basalt and river gravel, etc. is limited since they do not exhibit any adsorption performance during the adsorption process [48]. Current research aims to improve the adsorption capacity of pervious concrete from the perspective of improving the adsorption capacity of mortar, for example, by adding aluminium hydroxide [48], fly ash and iron oxide [11], etc., however, the role of adsorptive aggregate in the adsorption process is ignored. Moreover, since the adsorption material usually reaches saturation after long-term service, the adsorption performance and environmental influence of pervious concrete after the cyclic adsorption test should be evaluated.

Industrial wastes such as steel slag (SS), furnace slag, fly ash, etc., are potential absorbents for P-removal [15,39]. Previous studies show that concrete blocks after heat treatment can be applied to remove boron and fluorine from an aqueous solution [221] because the ettringite phase ($Ca_6Al_2(SO_4)_3(OH)_{12}\cdot 26H_2O$) is dehydrated to form the meta-ettringite phase under the high temperature. Moreover, the dissolved portlandite reacts with SO_4^{2-} to form expansive gypsum for sulphate removal [13]. To improve the adsorption performance of pervious concrete by replacing conventional aggregates with highly adsorptive aggregates, an absorptive aggregate with physical and chemical adsorption capacity, good mechanical properties and durability are developed in Chapter 4 [55]. In this chapter, the adsorption capacity after the cyclic adsorption test and the adsorption mechanism of adsorptive pervious concrete is investigated.

The steel slag (SS) and manufactured adsorptive aggregate (AD) are applied as adsorptive aggregates for adsorptive pervious concrete in this chapter, and basalt (B) is used as the reference aggregate for comparison. The physical characteristics, mechanical properties and P-removal performance of adsorptive pervious concrete are investigated. The cyclic adsorption characteristics, precipitate mechanism and environmental impacts of adsorptive pervious concrete are analyzed. The adsorption results are analyzed by adsorption isotherms and kinetics models. The developed adsorptive pervious concretes show excellent low P-releasing capacity and can be safely applied for P-removal from stormwater runoff.

7.2 Materials and methods

7.2.1 Materials

CEM I 52.5 R Portland cement (ENCI, The Netherlands) is used as a binder in this study. Commercial basalt (B), BOF steel slag (SS) (TATA Steel, The Netherlands) and manufactured adsorptive aggregate (AD) are applied as coarse aggregates, with a particle size of 1-2 mm and 2-5 mm, as shown in **Fig. 7.1**. The specific density of the B, SS and AD aggregates are 3.1 g/cm^3, 3.9 g/cm^3 and 2.6 g/cm^3, respectively. The AD is produced using 75 wt.% SS and 25 wt.% expanded silicate, with a crushing strength of 5.1 MPa. The detailed manufacturing process is presented in Chapter 4 [55]. CEN-NORM standard sand is used as the fine aggregate, which meets the requirement of the EN196-1 Standard.

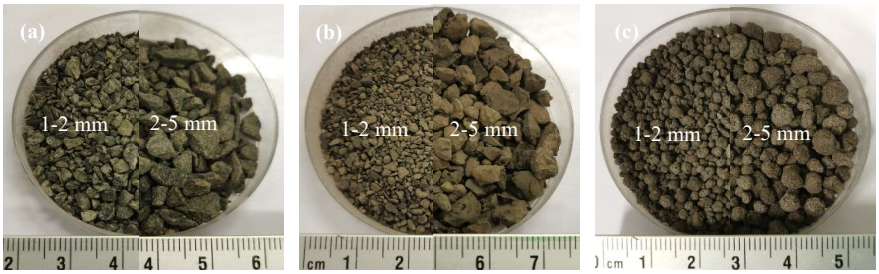

Fig. 7.1 (a) Basalt aggregate, (b) Steel slag aggregate and (c) Adsorptive aggregate.

Table 7.1 Mix proportions of adsorptive pervious concrete and their densities (kg/m^3).

Sample	Cement	Sand	Water	Aggregates		Density
				1-2 mm	2-5 mm	
B	350	500	129.5	1083.8	361.3	1843
SS	350	500	129.5	1385.8	461.9	1970
AD	350	500	129.5	934.5	311.5	1467

7.2.2 Mix proportion and sample preparation

Two-sized aggregates (1-2 mm and 2-5 mm) are used in this study for the manufacture of adsorptive pervious concrete, on the consideration of enhancing its mechanical properties from the improved packing perspective [207]. The volume ratios of large-sized aggregate and small-sized aggregate in the mix proportion are chosen at 25% and 75%, respectively, based on the preliminary tests concerning both the mechanical properties and durability [55]. The mix proportions of the adsorptive pervious concrete are shown in **Table 7.1**.

7.2.3 Test methods

- *Physical and mechanical properties*

The water absorption of concrete is determined according to ASTM C642-13, at the age of 28 days. The water permeability of concrete is determined using the Falling Head Method [179], and the coefficient of permeability known as saturated hydraulic conductivity, can be calculated based on Darcy`s Law as described in [222]. The porosity test is performed based on ASTM C1754/C1754M-12.

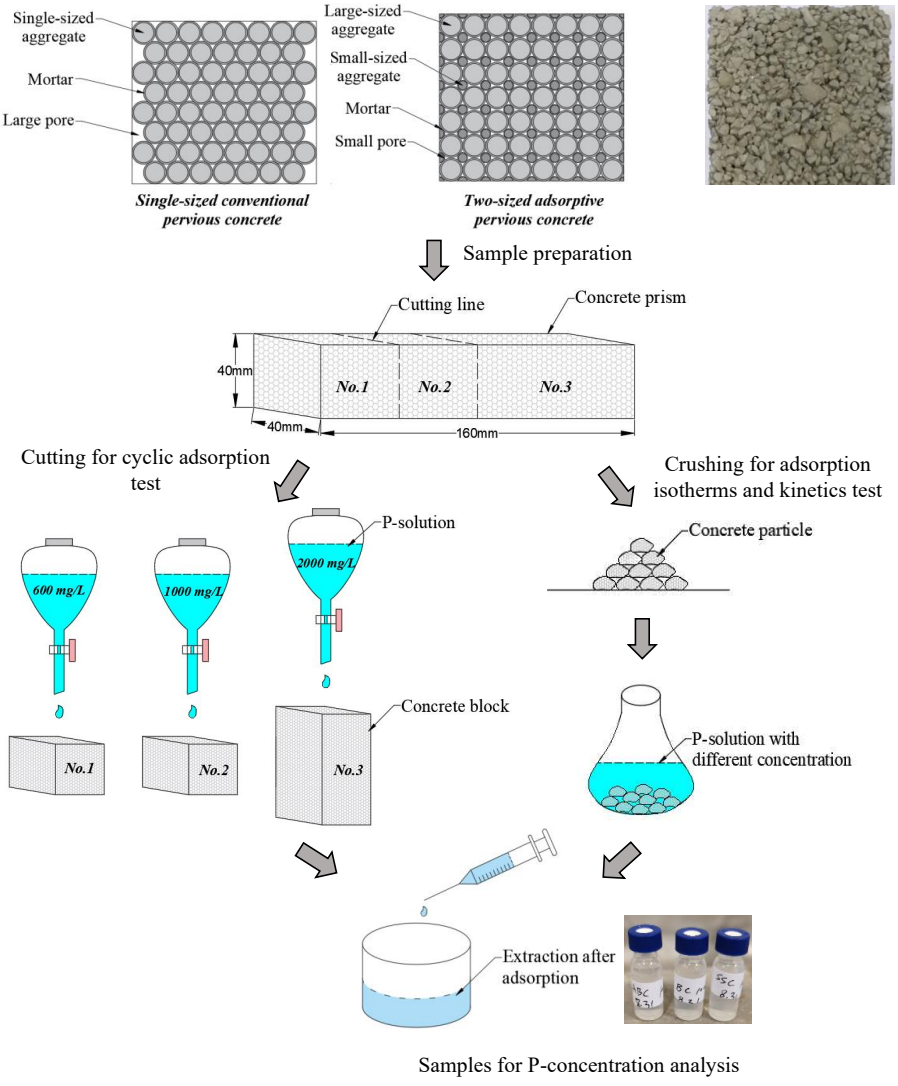

Fig. 7.2 Schematic diagram of sample preparation process for P-adsorption test.

The compressive and flexural strengths of concrete at a curing age of 28 days are determined in accordance with EN 196-1, with a corresponding loading rate of 2400 N/s and 50 N/s, respectively. The average value of the three samples is reported as the test result.

- *Cyclic adsorption performance*

The adsorption performance of the adsorptive material will be gradually decreased after a long-term application, eventually, the materials will reach saturation. In the present study, the effects of the number of cycles on the adsorption performance of adsorptive pervious concrete are investigated. 40×40×160 mm^3 sample is cut into three small cubes, labelled as No.1, No.2 and No.3, respectively, as shown in **Fig. 7.2**. To prevent the leakage of P-solution from the surroundings of the sample, melted wax is used to seal the surrounding surfaces of the small cube sample, and then a plastic film and a rubber ring are wrapped around the sample to make sure that the water flow only passes in vertical direction. The laboratory setup for the cyclic adsorption test of the adsorptive concrete block is presented in **Fig. 7.3**. During the cyclic adsorption test, 100 ml of the prepared P-solution is poured into the upper opening of the glass container, and then the flow rate controller is opened to assure the P-solution drips slowly with a rate of 3-5 ml/min. After each cycle, the filtrate is filtered and collected for pH value and P-concentration measurement.

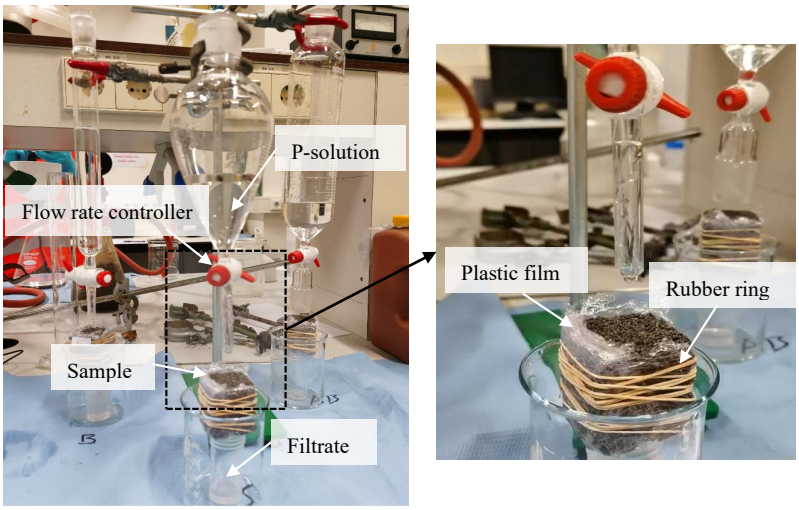

Fig. 7.3 Laboratory setup for cyclic adsorption test of adsorptive pervious concrete.

P-solutions with three designed high-concentration of 600 mg/L, 1000 mg/L and 2000 mg/L, respectively, are applied for the cyclic adsorption test. To ensure the accuracy of

the concentration of the P-solution for the adsorption test, the actual P-concentration is measured using IC, as described in **Table 7.2**. After 1, 3 and 5 cycles, 2 ml of the filtrate of sample No.1 and sample No. 2 is collected for P-concentration analysis.

The P-concentration of sample No. 3 is determined after 1, 3, 5 and 7 cycles. After each cyclic adsorption test, the pH value of the filtrate is measured by a pH meter. The microscopic image of the sample is observed by a scanning electron microscope (SEM). The released Ca^{2+} ion from cementitious materials is one of the main ions reacting with phosphate for Ca-P precipitates, and the concentrations of Na^{+}, K^{+} and Ca^{2+} ions released from adsorptive pervious concretes are determined by an IC analyzer. The P-adsorption amount (mg/g) and P-removal fraction (%) are calculated using the formula described in our previous study [15]. The environmental risk of metal ions released from concrete components is evaluated according to EN 12457-2 through ICP-AES.

Table 7.2 Parameters of adsorptive pervious concrete block for cyclic adsorption test.

Samples	No.	Length (cm)	With (cm)	Height (cm)	Mass (g)	P-concentration (mg/L)
	B1	4	4	4.3	123	649
B	B2	4	4	4.3	126	944
	B3	4	4	6.5	199	2268
	SS1	4	4	4.3	99	486
SS	SS2	4	4	4.2	99	891
	SS3	4	4	6.5	155	1531
	AD1	4	4	4.2	134	664
AD	AD2	4	4	4.3	139	1086
	AD3	4	4	6.4	194	2147

- *Adsorption isotherms and kinetics*

The adsorption isotherms of adsorptive pervious concrete for P-removal are evaluated by the batch experiment. Firstly, concrete samples after the compressive test are collected and oven-dried for the adsorption test. Then, approximately 1 g of the sample is placed in a 50 ml plastic bottle and then mixed with 25 mL of P-solution with different concentrations (13-392 mg/L) (**Table 7.3**). After that, the plastic bottle with concrete particles and P-solution is stirred in a shaker at 225 rpm for 24 hours to reach equilibrium. The solution is filtered using a 0.45 μm membrane filter for P-solution concentration analysis using an IC analyzer. The Langmuir and Freundlich models are selected for the adsorption isotherms analysis of concrete.

Similar to the adsorption isotherm procedure, the adsorption kinetics of P-adsorption of the adsorptive pervious concrete is carried out. A series of samples with a mass of about 20 g and 25 mL of P-solution (L/S of 25/20) with a constant concentration of

2921 mg/L (measured using the IC analyzer) are prepared and shaken for different reaction times (1 day, 7 days, 14 days and 35 days). After that, the solution is collected for residual P-concentration measurement. The Lagergren pseudo-first-order, pseudo-second-order and Elovich models are used for the adsorption kinetics analysis.

Table 7.3 Parameters of adsorptive pervious concrete for adsorption isotherms and kinetics test.

Adsorption isotherms test				Adsorption kinetics test			
P-concentration (mg/L)	Sample mass (g)			P-concentration (mg/L)	Sample mass (g)		
	B	SS	AD		B	SS	AD
13	0.8	1.0	0.8	2921	21.2	16.3	16.0
34	1.3	2.1	0.9				
70	1.6	1.7	0.7				
131	1.8	1.1	1.0				
260	2.0	1.6	1.2				
392	2.9	2.4	2.2				

- *P-releasing test*

If the adsorbed P is leached from the concrete, it will result in a negative effect on the environment and even cause secondary pollution. Therefore, the P-releasing properties of adsorptive pervious concrete are investigated. After adsorption saturation, the concrete particle samples with a mass of 1 g in the three different P-concentrations of 260 mg/L, 392 mg/L and 2921 mg/L are oven-dried and placed in a plastic bottle with 25 mL of distilled water (L/S of 25/1). The bottle is shaken at 225 rpm for 24 hours using a shaker. The solution is filtered and collected to determine P-concentration, and the P-releasing amount (mg/g) and fraction (%) are calculated based on the testing results.

7.3 Results and discussion

7.3.1 Physical and mechanical properties

- *Density and water absorption*

The physical properties of adsorptive pervious concrete are shown in **Table 7.4**. The adsorptive aggregate (AD) concrete has a low density and high water absorption compared to the basalt aggregate (B) concrete and steel slag aggregate (SS) concrete, owing to the porous structure of the AD aggregate. Compared to the B concrete, the water absorption of the SS concrete does not change significantly, only with an increase of 3%. The adsorption performance of the SS aggregate mainly relies on the released Ca^{2+} for precipitation of Ca-P by chemical adsorption, as physical adsorption does not

contribute significantly to the adsorption of the SS aggregate [15]. Therefore, high water absorption of the AD concrete means the pollutants can penetrate the concrete surface and be absorbed by the adsorptive aggregate, which also contributes to physical adsorption by micropores [55].

Table 7.4 Physical properties of adsorptive pervious concrete.

Samples	Oven-dry density (kg/m^3)	24-h water absorption (%)	Permeability (mm/s)	Porosity (%)
B	1843±40	6.5±1	1.1±0.1	15±2
SS	1970±35	6.7±1	1.3±0.2	17±1
AD	1467±21	12.8±1	1.5±0.1	20±1

- *Permeability and porosity*

As shown in **Table 7.4**, the porosity and permeability of the SS and the AD concrete are higher than that of the B concrete, the porosity increases by 13% and 28%, respectively, and the corresponding permeability has an increase of 18% and 36%. Generally, conventional pervious concrete has a porosity of 15-30% [223] and water permeability of 2-12 mm/s [172] for rapid water permeability, anti-clogging properties and suitable mechanical strength. The relationship between porosity and permeability of pervious concrete is shown in **Fig. 7.4**. The water permeability and porosity of adsorptive pervious concrete in this study are significantly lower than that of conventional pervious concrete, such as municipal waste concrete [224], polymer-modified concrete [225], and recycled aggregate concrete [226] and other aggregates concrete [227,228]. This is attributed to the small-sized aggregate added to the mixture, which leads to a lower permeability of pervious concrete [53,186]. The main function of adsorptive pervious concrete is to reduce pollutants from stormwater runoff, and thus as long as the pollutants can penetrate the concrete and contact the adsorptive aggregate, relatively low permeability and porosity are acceptable for adsorptive pervious concrete.

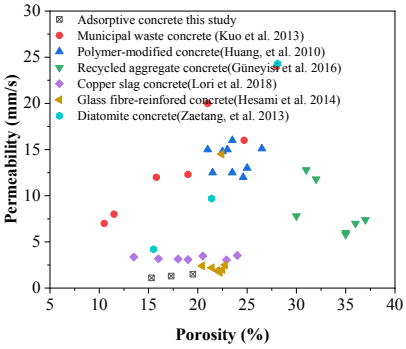

Fig. 7.4 Relationship between porosity and permeability of pervious concrete.

- *Mechanical properties*

The compressive and flexural strengths of adsorptive pervious concrete are shown in **Fig. 7.5**. The SS and AD concrete have lower compressive strength and flexural strength compared to the B concrete. In this study, the 28-day compressive strengths of the B, SS and AD concretes are 19.8 MPa, 14.7 MPa and 12.9 MPa, and the corresponding flexural strengths are 5.58 MPa, 3.59 MPa and 2.72 MPa, respectively. Because the manufactured adsorptive aggregate has a low crushing strength (5.1 MPa) compared to the conventional aggregate.

Conventional pervious concrete has a typical low compressive strength of less than 20 MPa [223]. The geopolymer-based pervious concrete containing 30 wt.% red mud for the removal of heavy metals has a compressive strength of 18.5 MPa, which also can be used in pavement [50]; Biochar pervious concrete has a compressive strength of 15.5-21.7 MPa [52]; Hardened geopolymer pastes used for fecal coliforms and P-removal after 7 days curing has a compressive strength of 3.9-15.8 MPa [14]. Therefore, the mechanical strength of adsorptive pervious concrete in this study is acceptable for application in some building engineering, such as sidewalks, parking lots and parkways etc. The mechanical strength of adsorptive pervious concrete can be improved by adding natural sand [225], admixture (silane, latex) [192,225] and fibre [227], and using ultra-high-performance paste [229], etc.

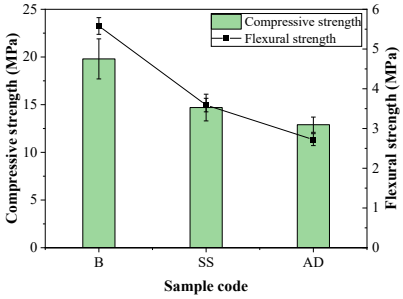

Fig. 7.5 Compressive strength and flexural strength of adsorptive pervious concrete (28 days).

From the SEM micrographs of concrete (**Fig. 7.6**), micropores exist on the surface of the SS and the AD series. The SS aggregate is not tightly bound with the cement paste interface, and obvious micropores are shown in the interfacial transition zone (ITZ), which is one of the reasons for the low compressive strength of the SS concrete. The micropores of the AD concrete are mainly from the porous structure of the expanded silicate because the adsorptive aggregate is made of 25 wt.% expanded silicate. These micropores can make the pollutants easily penetrate the cement paste layer and be

adsorbed by well-developed micropores and adsorptive materials [55].

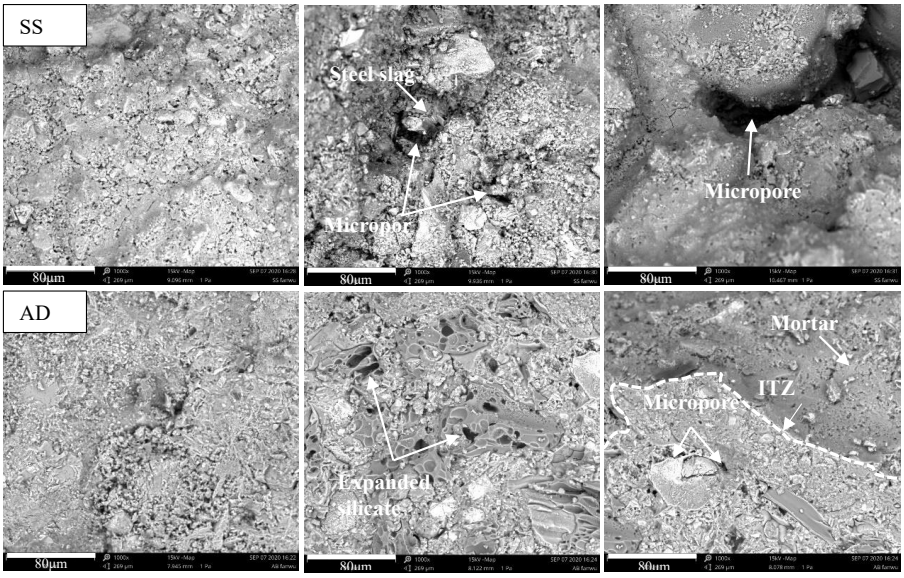

Fig. 7.6 SEM micrographs of concrete.

7.3.2 Cyclic adsorption performance

- *Adsorption capacity*

The effects of cycles on the adsorption capacity of concrete in different P-solution are shown in **Fig. 7.7**. The P-adsorption capacity of all concretes increases with the increase of the number of cycles. The adsorption capacity is generally evaluated by the adsorption capacity of the unit mass of the adsorbent. The AD concrete exhibits the highest adsorption capacity. When the initial P-concentrations are 600 mg/L, 1000 mg/L, and 2000 mg/L, the adsorption capacity of the AD concrete at the fifth cycle increases by 13%, 13% and 33%, respectively, compared to the B concrete. Even after 7 cycles, all concrete blocks still have a high adsorption capacity. The adsorption capacity of the B, the SS and the AD concrete is 0.38 mg/g, 0.36 mg/g and 0.49 mg/g, respectively, as the P-concentration of 2000 mg/L.

The Ca^{2+} and OH^- released from the cement paste and the SS and AD aggregates, combined with phosphate is the main reason for the formation of Ca-P precipitation [219,230]. Previous studies show that the P-removal capacity of fine particles of concrete waste increases as its particle size decreases because the concrete waste with smaller particle size has more Ca-rich and porous hardened cement paste powder [216].

This is attributed to the smaller particles with a higher specific surface area that can release more calcium ions. Since a concrete block is used for P-removal in this study, its P-adsorption capacity is lower than that of pure cement paste [220] and adsorptive aggregates [55]. However, the adsorptive pervious concrete in this study has a higher P-removal at high-concentration P-solution conditions, with a short reaction time, and it is possible to be applied as permeable pavements to improve the P-removal capacity from stormwater runoff.

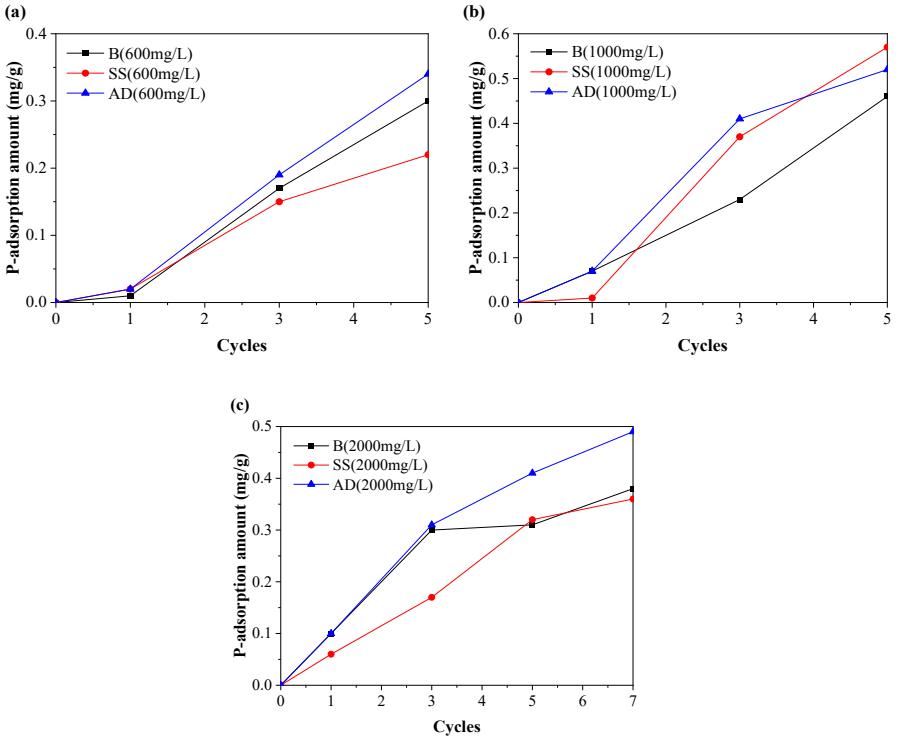

Fig. 7.7 Effects of cycles on the adsorption amount of concrete with three designed P-concentration of (a) 600 mg/L, (b) 1000 mg/L and (c) 2000 mg/L.

- *Precipitate mechanism*

The Ca^{2+} has a strong affinity with the PO_4^{3-} compared to other metal ions such as Mg^{2+}, Na^{+} and K^{+} [106,107], which is the dominant ion for the chemical reaction of Ca-P precipitation [43]. The hydrated cement products are mainly calcium hydroxide (CH) and hydrated calcium silicate (C-S-H). The excellent adsorption capacity of the adsorptive aggregate is mainly attributed to the Ca^{2+} released from the aggregates [55], which can combine with the PO_4^{3-} for Ca-P is bound by chemisorption [18] (**Fig. 7.8**).

Moreover, the microporous structure adsorbs P through physical adsorption by electrostatic attraction and pore-filling [109].

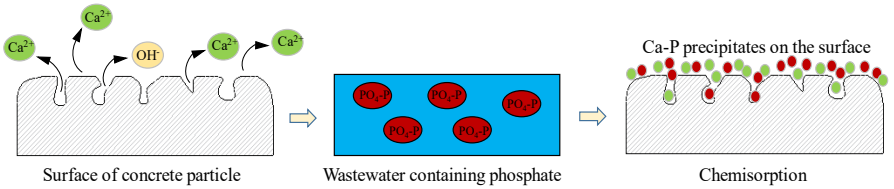

Fig. 7.8 Schematic diagrams of the adsorption mechanism between concrete and phosphate solution.

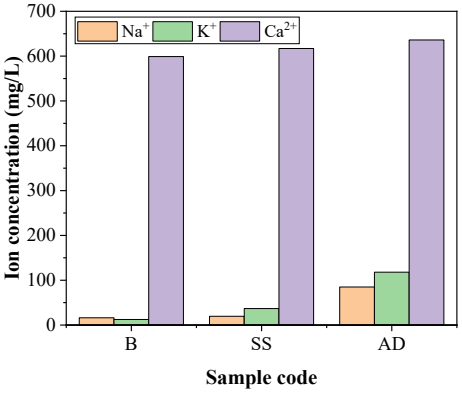

Fig. 7.9 Released sodium, potassium and calcium ions of adsorptive pervious concrete (2.5 g sample, 25 ml distilled water).

The released Na^+, K^+ and Ca^{2+} of the adsorptive pervious concrete block are shown in **Fig. 7.9**. The results show that the AD and the SS concrete release more ions (Na^+, K^+ and Ca^{2+}) than the B concrete. The concentration of Ca^{2+} released from the SS and the AD concrete increases by 3% and 6%, respectively, compared to the B concrete.

7.3.3 Adsorption isotherms and kinetics

- *Adsorption isotherms*

The P-adsorption capacity of concrete increases with the increase of P-concentration, while the P-removal rate has a decreasing trend, as shown in **Fig. 7.10a**. All the P in the solution is almost removed as the initial P-concentration is lower than 50 mg/L. As the P-concentration further increases the P-removal rate of concrete decreases. When the P-concentration is 392 mg/L, the P-adsorption capacities of the B, SS and AD concretes are 2.25 mg/g, 2.94 mg/g and 3.41 mg/g, respectively, and the corresponding P-removal

rates are 67%, 72% and 76%. The AD and SS concrete exhibit better P-removal performance than the B concrete, and the adsorption capacity increases by 31% and 52%, respectively. In addition, the adsorption performance of the concrete particles during the adsorption isotherm test is significantly higher than that of the concrete blocks during the cyclic adsorption test. This phenomenon indicates that concrete with sufficient surface to contact with P-solution would be beneficial to improve the P-adsorption capacity.

The adsorption isotherms are fitted by Langmuir and Freundlich models [111], respectively, as shown in **Fig. 7.10b**. The Langmuir and Freundlich isotherm parameters are shown in **Table 7.5**. The results indicate that both models can well describe the adsorption, nevertheless, the Langmuir model fits the experimental results better than the Freundlich model, with a higher correlation coefficient (R^2).

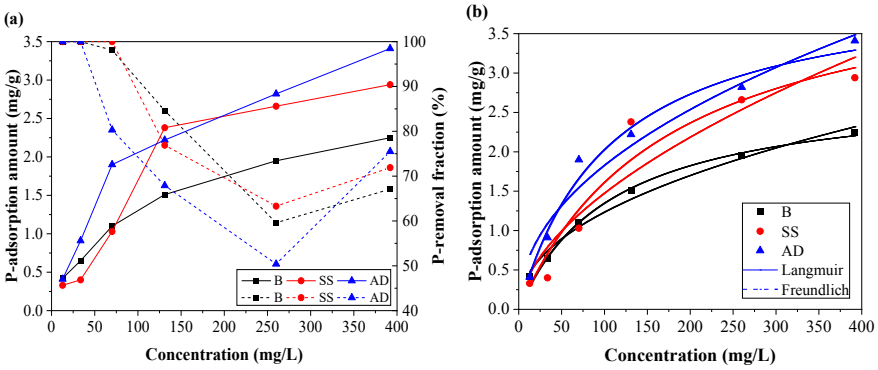

Fig. 7.10 (a) Adsorption isotherms of concrete (solid line: P-adsorption amount; Dotted line: P-removal fraction) and (b) Fitting results of adsorption isotherms by Langmuir and Freundlich models.

Table 7.5 Langmuir and Freundlich isotherm parameters of concrete.

Samples	Langmuir model			Freundlich model		
	Q_m	K_L	R^2	K_F	n	R^2
B	2.82	0.009	0.99	0.15	2.17	0.98
SS	4.43	0.006	0.93	0.11	1.77	0.87
AD	4.18	0.010	0.98	0.21	2.12	0.95

- *Adsorption kinetics*

The adsorption kinetics of adsorptive pervious concrete are shown in **Fig. 7.11**. The P-adsorption capacity and P-removal rate of concrete increase with the reaction time. The P-adsorption capacity and removal rate of concrete continues to increase, even after a 35-day reaction time. The P-adsorption capacities of the B, SS and AD concrete at 35-day are 2.40 mg/g, 3.88 mg/g and 4.13 mg/g, respectively, and the corresponding P-

removal rates are 70%, 87% and 90%, respectively. This indicates that adsorptive pervious concrete can release enough Ca^{2+} for the precipitation-coagulation process of Ca-P, with a potential ability for long service life.

The experimental results are fitted by Lagergren pseudo-first-order model, pseudo-second-order model and Elovich kinetic model, as shown in **Fig. 7.11c**. The kinetic parameters are presented in **Table 7.6**. The results show that the experimental data can be fitted well by the Elovich model with a good correlation coefficient (R^2). The Lagergren pseudo-first-order and pseudo-second-order are not suitable for fitting the kinetic curves of P-adsorption of concrete.

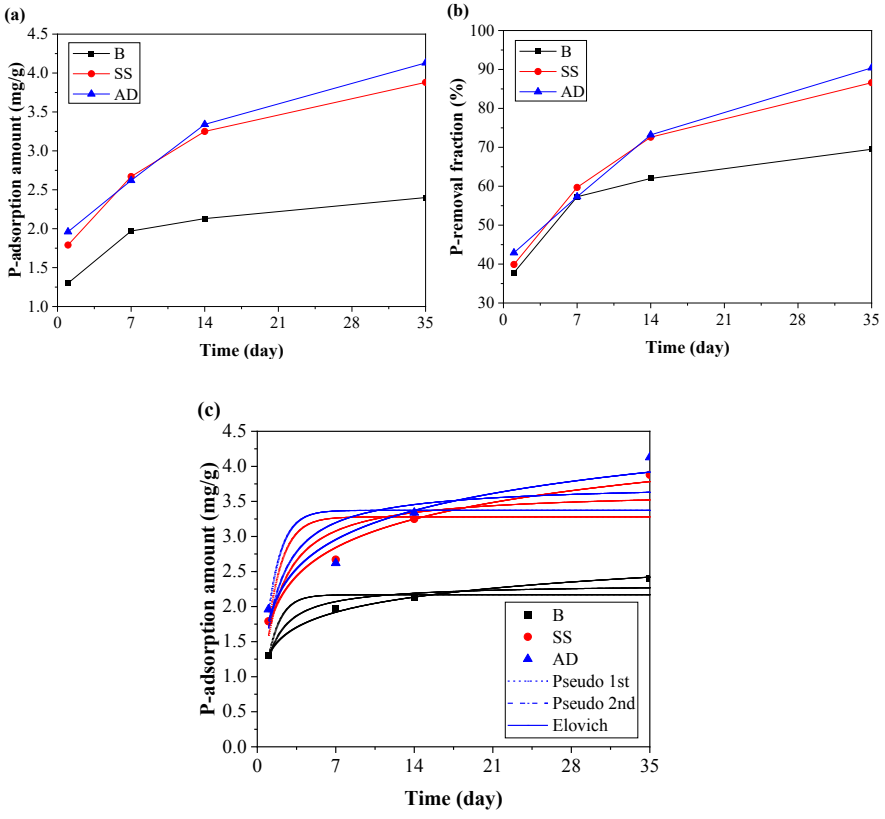

Fig. 7.11 Adsorption kinetics of concrete (a) P-adsorption amount, (b) P-removal fraction and (c) Fitting results of adsorption kinetics.

7.3.4 Environmental evaluation

- *P-releasing capacity*

A stable precipitation process for adsorption is essential to reduce the environmental secondary pollution caused by releasing adsorbed pollutants. The P-releasing results of adsorptive pervious concrete are shown in **Table 7.7**. When the P-concentration is 260 mg/L, all concretes have no P-releasing behaviour. As the concentration increases, the P-releasing of the B concrete appears. When the P-concentration is very high with a value of 2921 mg/L, the AD concrete has a low P-releasing capacity. However, no adsorbed P is desorbed from the SS concrete because the SS aggregate has a lower P-releasing fraction due to the stable adsorption process [15]. The P-releasing fraction of AD concrete is 20%, which is relatively low compared to B concrete. The developed SS and AD concrete in this study shows a low P-releasing capacity, indicating that they can be safely used for P-removal from stormwater runoff, and the most of adsorbed P will not release from the adsorptive pervious concrete to cause environmental secondary pollution.

Table 7.6 Kinetic parameters of concrete.

Samples	Pseudo-first-order			Pseudo-second-order			Elovich		
	Q	K_1	R^2	Q	K_2	R^2	α	β	R^2
B	2.17	0.91	0.79	2.32	0.51	0.92	1.32	0.31	0.99
SS	3.28	0.76	0.55	3.65	0.21	0.78	1.71	0.58	0.97
AD	3.37	0.85	0.35	3.76	0.22	0.62	1.80	0.60	0.89

- *Leaching results*

The potential environmental impacts of the components of adsorptive pervious concrete are evaluated by the leaching test, as shown in **Table 7.8**. The results show that all elements including heavy metals (Cr, Mo and V etc.) leached from the SS and AD aggregates are far below the limit values according to the Dutch Soil Quality Decree [140]. This is in agreement with previous research as cementitious materials have shown excellent in immobilizing heavy metals [55]. Therefore, the developed adsorptive pervious concrete (AD and SS) can be used to remove P from stormwater without any leaching hazards.

Table 7.7 P-releasing results for adsorptive pervious concrete.

Samples	B			SS			AD		
Initial P-concentration (mg/L)	260	392	2921	260	392	2921	260	392	2921
P-releasing amount (mg/g)	-	0.6	0.3	-	-	-	-	-	0.4
P-releasing fraction (%)	-	27	23	-	-	-	-	-	20

Table 7.8 Ions leached from adsorptive pervious concrete components (mg/kg).

Elements	Al	Fe	Mg	As	Ba	Cr	Pb	Zn	Mo	Se	V
Steel slag	0.1	≤0.6	0.3	≤0.5	0.8	0.2	-	-	-	-	≤0.4
Adsorptive aggregate	15.2	≤0.4	0.1	≤0.2	6.5	0.2	≤0.6	≤0.4	≤0.1	≤0.1	-
Limit values [a]	-	-	-	0.9	22	0.63	2.3	4.5	1	0.15	1.8

[a] Limit values refer to the maximum emission values for building materials according to the Dutch Soil Quality Decree (2015).

7.4 Conclusions

(1) Adsorption performance of adsorptive pervious concrete is significantly influenced by the type of adsorptive aggregate used. Concretes containing adsorptive aggregate and steel slag aggregate exhibit excellent P-adsorption capacity, compared to basalt aggregate concrete, with an increase of 31% and 52%, respectively. P-adsorption capacities of adsorptive aggregate concrete and steel slag concrete at 35 days are 4.13 mg/g and 3.88 mg/g, respectively, with corresponding P-removal fractions of 87% and 90%. The Langmuir model and Elovich models fit the adsorption isotherm and kinetic results of adsorptive pervious concrete well, with a good correlation coefficient.

(2) P-adsorption capacity of adsorptive pervious concrete enhances as P-concentration and reaction time increase. The adsorptive aggregate concrete has a high adsorption capacity. At an initial P-concentration of 2000 mg/L, the adsorption capacity of adsorptive aggregate concrete increases by 32% over basalt aggregate concrete after 5 cycles. Moreover, the concentration of Ca^{2+} released from adsorptive pervious concrete exceeds that of K^{+} and Na^{+}, which is the dominant ion for the chemisorption of Ca-P precipitation.

(3) Adsorptive aggregate concrete and steel slag aggregate concrete exhibit excellent low P-releasing capacity, indicating that they can be used for P-removal from stormwater runoff, with minimal environmental impact. Moreover, the adsorptive pervious concrete releases enough Ca^{2+} for the precipitation-coagulation process of Ca-P, with the potential for long-term service life.

Chapter 8 Long-term performance of bio-based miscanthus mortar

The long-term degradation characteristics of embedded natural fibres are one of the key factors restricting the durability of bio-based mortars and concretes. In this chapter, to reduce the negative impact of miscanthus fibre on the service life of bio-based adsorptive concrete, the effects of the raw miscanthus (RM), heat-treated miscanthus (HM) and miscanthus powder (MP) on the physical and mechanical properties, long-term degradation characteristics and dimensional stability of bio-based miscanthus mortar are investigated. The results show that the HM fibres improve the compressive strength and flexural strength by 83% and 27%, respectively, compared to the RM fibre, thanks to the increased degree of cement hydration, reduced porosity and better compatibility with mortar. The mechanical strength degradation of miscanthus mortar mainly occurs in the first month after being soaked in water due to the saturation of mortar. The alkaline environment of mortar will cause the dissolution of some cellulosic components, resulting in the degradation of the miscanthus fibre. The removal of sugar from the miscanthus fibre by heat treatment is conducive to cement hydration, strength development and durability of miscanthus mortar. It is concluded that heat-treated miscanthus fibres can be applied to reduce the dimensional stability and degradation characteristics of bio-based miscanthus mortar.

This chapter is partially reproduced from:

F. Wu, Q.L. Yu, H. J. H. Brouwers. Long-term performance of bio-based miscanthus mortar. Construction and Building Materials, 324, 126703, 2022.

8.1 Introduction

Natural fibres are mainly composed of cellulose, hemicellulose and lignin, etc., the drawbacks of applying bio-based materials in cementitious materials include hygroscopicity, incompatibility and degradability, etc. [231]. The low affinity between bio-based materials and cement paste is one of the main reasons for poor mechanical strength [232]. In addition, the alkaline solution in the concrete pore will dissolve the cellulose of the natural fibre, resulting in a strong degradation of the natural fibre, and eventually reducing the service life of bio-based concrete. The sugar released from natural fibre has a significantly negative effect on cement hydration and delays the setting and hardening of concrete matrix [153] because the extractives from natural fibre affect the production of calcium-silicate-hydrate (C-S-H) and portlandite.

Compared to other natural fibres such as straw, hemp, etc., miscanthus is considered a strong fibre, and possesses enough firmness and thermal insulating properties. Besides, miscanthus is a high-yield renewable material with environmentally friendly characteristics. Thanks to its lightweight and porous properties, miscanthus is commonly used as a natural fibre for bio-based lightweight concrete [18]. Although miscanthus fibre is covered in a closed environment after being applied to concrete, the alkaline environment has a dissolving effect on the cellulosic components of miscanthus fibre, which will affect the mechanical properties, long-term degradation and durability of cementitious miscanthus materials. Previous studies show that many sugars are released from the miscanthus under the alkali condition as the miscanthus is exposed to the concrete formation [58]. Besides, miscanthus fibre has a strong affinity with water and possesses a high water absorption capacity, and the shrinkage and swelling of miscanthus have strong negative effects on the durability of miscanthus concrete. Compared to normal-weight concrete, miscanthus concrete generally has a higher porosity and water absorption, however, the mechanical strength, degradation characteristics and dimensional stability will be affected by the humidity of the ambient environment. Therefore, the long-term degradation behavior, drying shrinkage and wet swelling characteristics of miscanthus mortar should be investigated systematically.

This chapter focuses on investigating the physical and mechanical properties, long-term degradation and dimensional stability of miscanthus mortar. The effects of the raw miscanthus (RM), heat-treated miscanthus (HM) and miscanthus powder (MP) on the degradation characteristics of miscanthus mortar are investigated systematically. The degradation mechanism of miscanthus fibre in water and cement solution is evaluated by FTIR, XRD and SEM analyses. The hydration behavior, physical and mechanical properties of miscanthus mortar, as well as strength degradation after being submerged

in water for 90 days are analyzed. The dimensional stability of miscanthus mortar including drying shrinkage and wet swelling are investigated. Based on the present results, the HM fibre shows outstanding performance in improving the dimensional stability and degradation resistance characteristics, which can be applied to improve the service life of miscanthus mortar.

8.2 Materials and methods

8.2.1 Materials

Raw miscanthus (RM) and miscanthus powder (MP) supplied by Vibers (The Netherlands) are used in this study, as shown in **Fig. 8.1**. The RM is heat-treated using a vacuum furnace under nitrogen gas at 250℃ for 3 hours, and then the heat-treated miscanthus (HM) is milled using a ball milling machine to obtain the HM powder. The purpose of heat treatment is to chemically alter the biomass (destroy the sugars) of the RM and investigate the effects of the HM on the physical mechanics and degradation characteristics of miscanthus mortar. The specific densities of the RM, HM and MP are determined by using an AccuPyc II 1340 gas pycnometer, which are 1.64 g/cm^3, 1.25 g/cm^3 and 1.57 g/cm^3, respectively. CEM I 52.5R Portland cement (ENCI, The Netherlands) and CEN-NORM standard sand are used as the binder and fine aggregates, respectively.

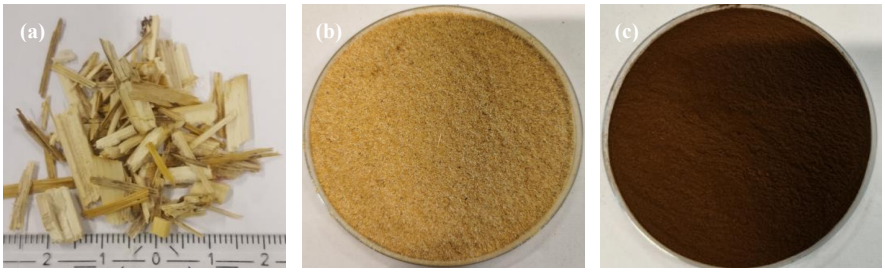

Fig. 8.1 Miscanthus used in this study (a) Raw miscanthus (RM), (b) Miscanthus powder (MP) and (c) Heat-treated miscanthus (HM).

8.2.2 Mix proportion and sample preparation

The mixing ratio of cement, sand and water of the miscanthus mortar refers to the mix proportion and preparation process of standard mortar (EN 196-1:2005). A high content of miscanthus fibre has a negative effect on the mechanical strength [62], and thus the RM and the HM in the amount of 1.0 vol.% of cement is added to the mixture as the references. Also investigated in this study are the effects of MP at different levels of

addition of 1.0 vol.%, 1.5 vol.% and 2.0 vol.% on the physical and mechanical properties of miscanthus mortar. The mix proportions of miscanthus mortar are shown in **Table 8.1**.

Table 8.1 Mix proportions of miscanthus mortar.

Sample	Cement (g)	Sand (g)	Water (g)	Miscanthus (Vol.%)
RM1	450	1350	225	1
HM1	450	1350	225	1
MP1	450	1350	225	1
MP1.5	450	1350	225	1.5
MP2	450	1350	225	2.0

8.2.3 Test methods

- *Effects of miscanthus on the hydration of cement*

The hydration kinetics test is performed using a TAM Air Isothermal calorimeter under a constant temperature of 20 ℃ to analyze the hydration degree of the miscanthus mortar. The RM, HM and HM are mixed with cement and water, and the water-to-cement ratio is kept as constant for all mixtures (w/c=0.5). The amount of miscanthus added to the mixture is 1 wt.% of the cement, and the MP of 2 wt.% is also added to the mixture to investigate the effects of the miscanthus content on the hydration of cement. After mixing, the fresh mixture is measured in the calorimeter for released heat and heat flow, the values are used for calculation of the hydration degree of cement.

- *Physical and mechanical properties*

The density, water absorption and porosity of the sample at the age of 28 days are determined according to ASTM C642-13. The thermal conductivity and ultrasonic pulse velocity (UPV) of the miscanthus mortar with a size of 100×100×100 mm^3 are determined using a thermal conductivity meter (ISOMET 2104) and ultrasonic instrument (Proceq 200), respectively. The compressive and flexural strengths of the sample at the age of 28 days are determined by EN 196-1. The microstructures of the interfacial transition zone between the miscanthus and the mortar are analyzed using an SEM analyzer (Phenom ProX).

- *Strength degradation of miscanthus mortar*

Bio-based concrete usually has high porosity due to the high water absorption of bio-based materials and low compatibility with the mortar interface. The mechanical strength degradation characteristics of miscanthus mortar are investigated in this study.

The samples (RM1, HM1 and MP1) with a curing age of 90 days are submerged in water for 30, 60 and 90 days, and then removed from the water for compressive strength and flexural strength test (**Fig. 8.2a**). The changes in mechanical strength of the miscanthus mortar before and after the submersion test are analyzed.

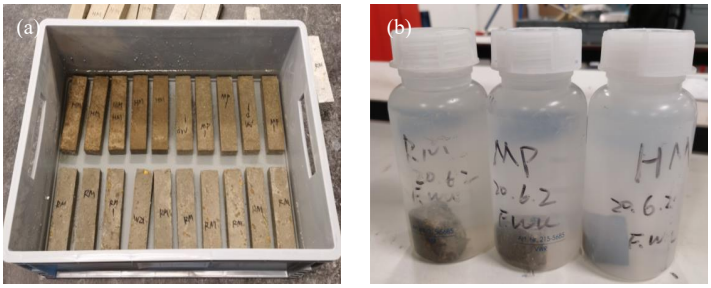

Fig. 8.2 Miscanthus mortar samples submerged in water for (a) Submersion test and (b) Leaching test.

The ion concentration leached from the miscanthus mortar during the degradation process is also investigated (**Fig. 8.2b**). The samples RM1, HM1 and MP1 and the deionized water are mixed with a liquid-to-solid ratio of 10 according to EN 12457-2, and then leachates are periodically collected and filtered using a 0.22 μm filter for leaching analysis. The potassium (K^+), calcium (Ca^{2+}) and sodium (Na^+) ions leached from the sample are measured with ion chromatography (IC, Thermo Dionex Aquion), and other metal ions (Al, Fe, Mg, Cr, Sr, Zn, etc.) are measured with inductively coupled plasma atomic emission spectroscopy (ICP-AES, SPECTROBLUE).

- *Long-term degradation of miscanthus fibre*

The mixture of cement and water is applied to simulate the cementitious environment in that the miscanthus fibre stays in cementitious materials. The degradation characteristics of miscanthus fibre in an aqueous solution and cement solution are investigated. The mixing ratio of miscanthus and water refers to the leaching test method (EN 12457-2) with a liquid-to-solid ratio of 10. The mix proportions of miscanthus and solution are presented in **Table 8.2**.

After mixing, the mixtures are shaken using a dynamic shaker with a constant speed of 250 rpm for 24 hours and then the mixture is kept in the plastic bottle (**Fig. 8.3**). After being soaked for 20, 40, 60, 80 and 100 days, the samples are taken out from the plastic bottle and then oven-dried at 38 ℃ for no less than 48 hours following the drying method in ASTM C1754/C1754M-12. The degradation characteristics of the miscanthus before and after submersion, using FTIR in the range from 4000 to 500 cm^{-1} with a 4 cm^{-1} resolution. The XRD (Bruker AXS D4 endeavor) and SEM (Phenom

ProX) are applied to analyze the crystal structure and micromorphology of miscanthus fibre during the degradation test. The change in the pH value of the solution with time is periodically measured using a pH meter.

Table 8.2 Mix proportions of miscanthus fibre for degradation test.

Sample	Cement (g)	Miscanthus (g)	Water (g)	Miscanthus type
MP	-	10	100	Raw
CMP	10	10	100	Raw
HM	-	10	100	Heat-treated
CHM	10	10	100	Heat-treated

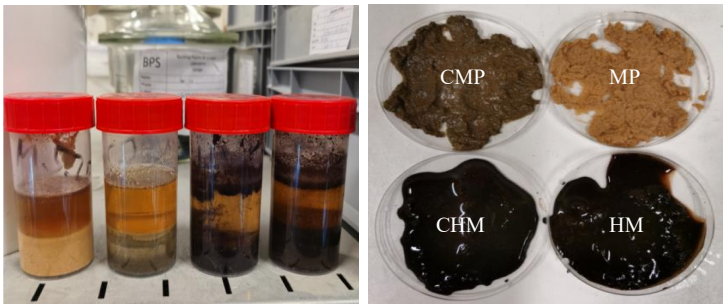

Fig. 8.3 Miscanthus fibre used for degradation test.

- *Drying shrinkage of miscanthus mortar*

Miscanthus fibre is sensitive to the humidity in the environment, which will affect the dimensional stability of bio-based miscanthus concrete. The drying shrinkage and wet swelling characteristics of miscanthus mortar are investigated in this study. The drying shrinkage test is performed with a prism of 40×40×160 mm^3 according to DIN 52450 (at RH of 50% ±5% and 23°C). As the drying shrinkage of concrete generally changes significantly after demolding, the drying shrinkage and mass loss are recorded every two days in the first month after demolding. One month later, the drying shrinkage and mass loss are measured once a week. The microscopic morphology of the miscanthus mortar after the drying shrinkage test is analyzed by SEM.

- *Wet swelling of miscanthus mortar*

The dimensional stability of miscanthus mortar under a saturated environment is investigated. The prismatic samples of 40×40×160 mm^3 after demolding are stored in water with a temperature of 20±2 ℃ and a water cover of at least 10 mm. Similar to the drying shrinkage test method, the axial wet swelling and changes in the mass of the samples are measured periodically. The wet swelling characteristics of miscanthus

mortar in the water environment are evaluated according to the test results.

8.3 Results and discussion

8.3.1 Hydration behavior of miscanthus mortar

The released heat and heat flow of miscanthus mortar are shown in **Fig. 8.4**. The results show that the type and content of miscanthus have a significant effect on the hydration of cement. As shown in **Table 3**, the HM1 and the MP1 significantly increase the released heat by 5% and 2%, respectively, compared to the RM1. When the content of the miscanthus increases from 1% to 2%, the released heat of the MP2 decreases by 3.8%. Moreover, the heat flow curve (**Fig. 8.4b**) shows that the HM1 slightly accelerates the hydration process due to the pyrolysis of oxygen-containing saccharides [130,151], compared to the RM1, the MP1 has no obvious effect on the hydration process, but the MP2 significantly delays the cement hydration.

Previous studies have shown that glucose and xylose are the main released sugars from miscanthus stems, which increases the setting time of cement hydration and decreases the amounts of hydrates such as calcium-silicate-hydrate (C-S-H) and portlandite [58]. The released sugars from bio-based materials have a negative effect on the mechanical strengths of bio-based concrete [233]. Based on the results, compared to untreated miscanthus, the heat-treated miscanthus and low-content miscanthus powder (1 vol.%) have an insignificant effect on the cement hydration, which may be conducive to the enhancement of mechanical strength and resistance to degradation of bio-based miscanthus concrete.

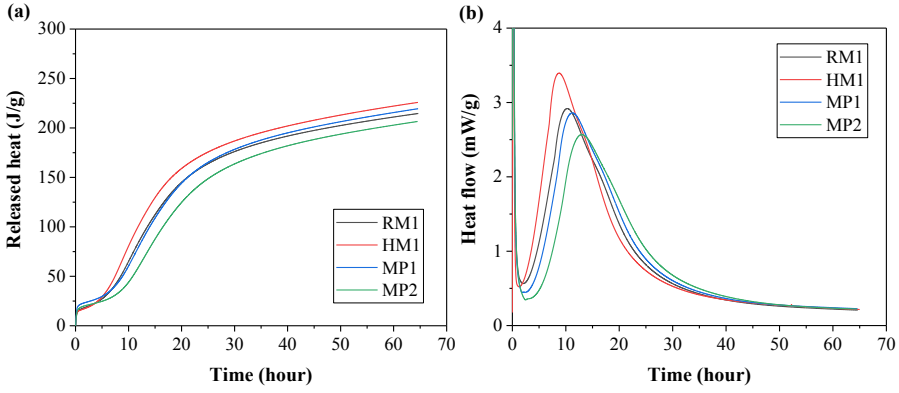

Fig. 8.4 (a) Released heat and (b) Heat flow of miscanthus mortar.

Table 8.3 Released heat comparison of miscanthus mortar (65 hours).

Samples	RM1	HM1	MP1	MP2
Total heat (J/g)	215	226	220	207
Heat deviation (J/g)	-	+11	+5	-8
Heat change in (%)	-	+5	+2	-4

8.3.2 Physical and mechanical properties of miscanthus mortar

- *Density, porosity and water absorption*

As shown in **Table 8.4**, the mortar HM1 slightly increases the oven-dry density of the miscanthus mortar and significantly reduces the porosity and water absorption, with a reduction of 10% and 15%, respectively, compared to the mortar RM1. This may be attributed to the good compatibility between the heat-treated materials and the mortar [59], which leads to the decrease of the microporous structure in the interfacial transition zone. The low porosity and water absorption can reduce the passage for the ion exchange between the interior of the mortar and the external environment, which is helpful to improve the bio-degradation resistance of bio-based concrete.

The results show that the high content of miscanthus powder (MP1.5 and MP2) significantly reduces the oven-dry density of miscanthus mortar and increases the porosity and water absorption of miscanthus mortar. When the miscanthus powder content is 2% (MP2), the oven-dry density of miscanthus mortar reduces by 13%, compared to the mortar RM1. Therefore, the miscanthus powder is more effective than raw miscanthus when the miscanthus fibre is applied for the manufacture of lightweight, acoustic absorption and heat-insulating building materials.

Table 8.4 Density, porosity and water absorption of miscanthus mortar.

Sample	Oven-dry density (kg/m^3)	Changes in %	Porosity (%)	Changes in %	24-h water absorption (%)	Changes in %
RM1	1932±19	-	17	-	9	-
HM1	2006±26	+4	15	-10	7	-15
MP1	1893±23	-2	18	+5	9	+6
MP1.5	1809±18	-6	19	+11	10	+17
MP2	1688±28	-13	19	+14	11	+26

- *Thermal insulating properties and UPV*

The thermal insulating characteristics of bio-based miscanthus concrete have a strong relationship with porosity [75]. Generally, the higher the porosity, the lower the thermal conductivity [65]. As shown in **Table 8.5**, the heat-treated miscanthus (HM1) shows an

insignificant effect on the thermal insulating characteristics. The mortars MP1, MP1.5 and MP2 reduce the thermal conductivity, volumetric heat capacity and thermal diffusivity, compared to the mortar RM1, with a decreasing trend as the MP content increases. Therefore, miscanthus powder shows great potential for application in bio-based thermal insulating concrete.

Table 8.5 Thermal insulating properties and UPV of miscanthus mortar.

Sample	Thermal conductivity λ (W/m·K)	Volumetric heat capacity Cρ (M J/m^3·K)	Thermal diffusivity a (10^{-6} m^2/s)	UPV (m/s)
RM1	1.77	1.93	0.92	3846
HM1	1.91	1.88	1.01	3831
MP1	1.55	1.89	0.82	3719
MP1.5	1.26	1.42	0.89	3165
MP2	1.15	1.59	0.73	2937

The defects and pores in the miscanthus mortar are evaluated by the UPV test, the results are shown in **Table 8.5**. Generally, when the ultrasonic pulse velocity is 3.66-4.58 km/s, indicating no obvious defects and cracks in the concrete [234]. Similar to the results of porosity and thermal conductivity, the mortars MP1, MP1.5 and MP2 significantly reduce the ultrasonic pulse velocity, indicating that more defects and micropores exist in the miscanthus powder mortars. The mortar HM1 has fewer defects and micropores, with good integrality, compared to the mortar MP series.

- *Compressive strength and flexural strength*

The mechanical strengths of miscanthus mortar are shown in **Fig. 8.5**. The mortar HM1 significantly improves the compressive strength and flexural strength of the miscanthus mortar. The 28-day compressive strength and flexural strength of the mortar HM1 are 52.8 MPa and 8.86 MPa, respectively, with an increase of 83% and 27%, respectively, compared to the mortar RM1. This may be attributed to the sugar removal of miscanthus after pyrolysis increasing the adhesion to the mortar, and the HM1 has a better degree of cement hydration and lower porosity. There is an inverse relationship between miscanthus sugar content and mechanical strength [58]. The use of heat-treated bio-based materials to improve mechanical strength has been reported in previous studies, for apricot kernel shell [65], oil palm shell [235] and biochar [236], prior to blending in a mortar. The removal of sugar from bio-based materials by heat treatment and alkali treatment methods etc. is the key to enhancing the mechanical strength of bio-based concrete.

The raw miscanthus has a large size and flat shape, the pores formed inside the mortar are larger than that of the miscanthus powder. Compared to the RM, the MP1 series

shows a significant increase in compressive strength, with an increase of 17%. However, the increase in flexural strength is not obvious due to the reduced fibre-bridging effect caused by miscanthus powder compared to untreated miscanthus fibre. The content of miscanthus has a significant effect on mechanical strength. When the miscanthus powder content is 2%, the compressive strength and flexural strength of the mortar MP2 reduce by 35% and 40%, respectively, compared to the mortar RM1. The added miscanthus content should be considered with caution for the application of bio-based miscanthus concrete in the structural elements.

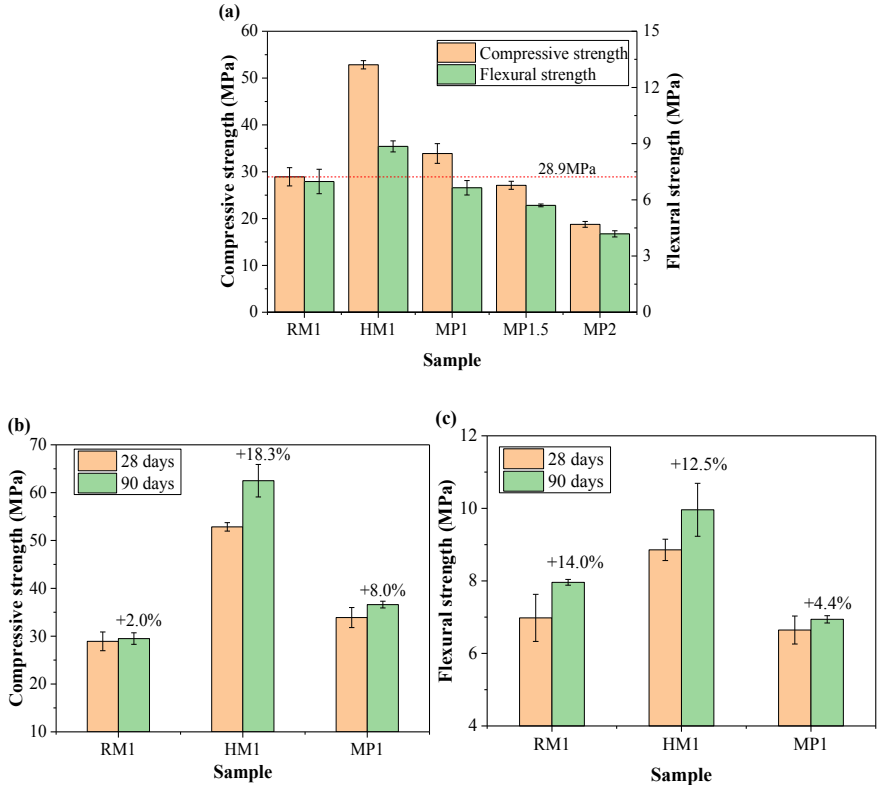

Fig. 8.5 Mechanical strengths of miscanthus mortar (a) 28-day mechanical strength, (b) compressive strength and (c) flexural strength.

As the curing time increases, the compressive strength and flexural strength of the miscanthus mortar increase, especially for the mortar HM1. This may be due to the fact that bio-based materials delay the hydration of cement in the early stage of curing. As the curing time increases, unhydrated cement gradually hydrates, resulting in an enhancement in the strength in the later curing stage. Therefore, a long curing time is needed for the ultimate strength development of bio-based miscanthus concrete.

- *Microstructure analysis*

The compatibility between bio-based materials and mortar is one of the main factors restricting the mechanical strength of bio-based concrete. As shown in **Fig. 8.6**, weak adhesion between miscanthus fibre and mortar is observed on the surface of the RM and MP. The HM shows good compatibility with mortar, which is also one of the main reasons for the better mechanical strength of the mortar HM1. Due to the shrinkage and swelling characteristics of the miscanthus fibre, the changes in humidity of the environment will have a significant impact on the dimensional stability of bio-based miscanthus concrete.

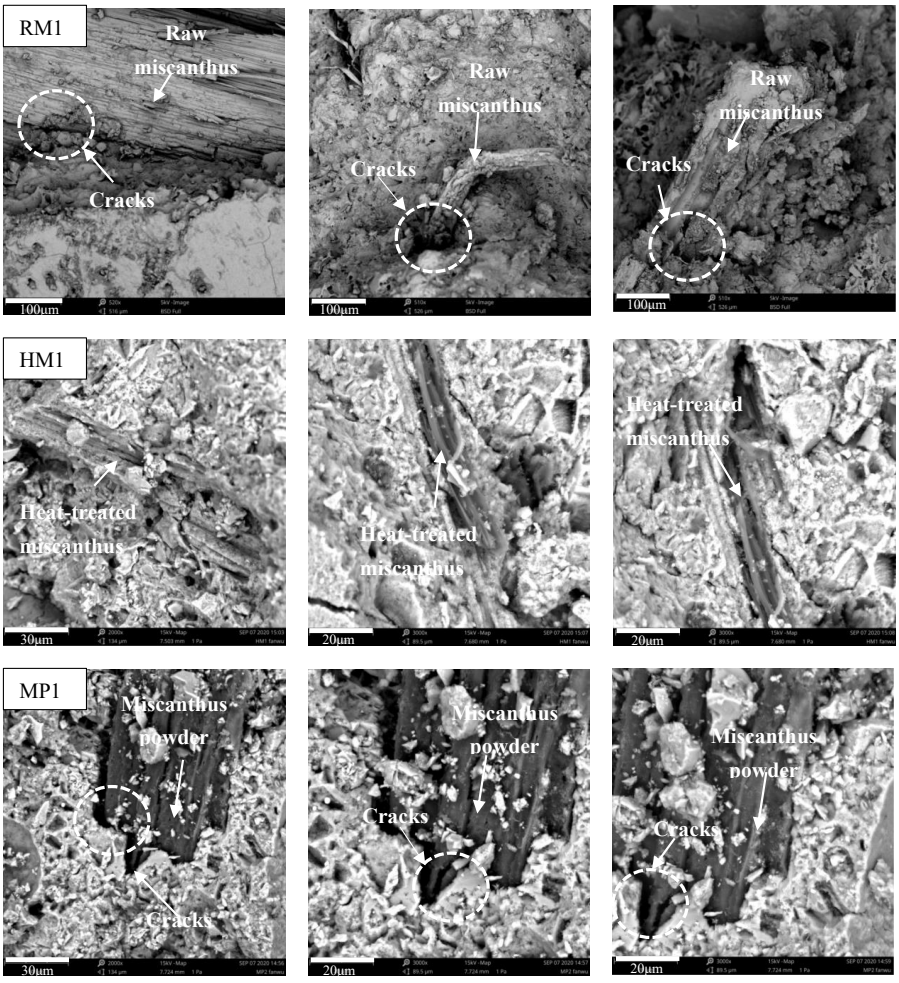

Fig. 8.6 Microscopic images of miscanthus mortar.

- *Strength degradation of miscanthus mortar*

As shown in **Fig. 8.7**, the compressive strength and flexural strength of all miscanthus mortars decrease in the initial soaking stage of 30 days, and then the reduction in mechanical strengths becomes unobvious. The compressive strength of the mortars RM1, HM1 and MP1 decreases by 18%, 24%, and 17%, respectively, and the corresponding flexural strength decreases by 30%, 38%, and 17%, respectively, after being submerged in water for 30 days. This may be because miscanthus mortar gradually absorbs water until saturation, the saturated miscanthus mortar has a negative effect on the mechanical strength. The wet swelling test results (Section 8.3.4) confirm that the mass and wet swelling values of miscanthus mortar gradually increase within the first month. The slight deformation of the miscanthus mortar may be the main reason for the rapid decrease in mechanical strength in the first month.

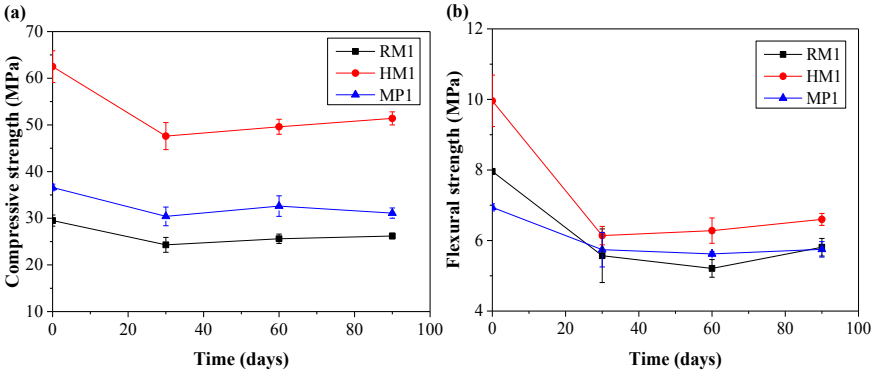

Fig. 8.7 Changes in mechanical strength of miscanthus mortar after being submerged in water.

8.3.3 Degradation characteristics of miscanthus mortar and miscanthus fibre

The results also show that the mechanical strength of the saturated miscanthus mortars at the 30-day and the 90-day have no obvious difference, indicating that the degradation of the miscanthus fibre has limited influence on the strength degradation of miscanthus mortar, and the saturation of miscanthus mortar may be the main reason for the strength degradation. Moreover, when miscanthus fibre is soaked in an alkaline solution, it will produce a more fibrillated surface [231], which is conducive to the strength stability of the miscanthus mortar.

The ions leached from miscanthus mortar are presented in **Table 8.6**. The results show that calcium, potassium and sodium ions are the main ions leached from miscanthus mortar, much higher than the concentration of other ions. All ions released from the

miscanthus mortar increase with the immersion time. Most of the ions leached from the mortar HM1 are less than that of the mortars RM1 and MP1 due to the low porosity of the mortar HM1. The high content of calcium ions leached from miscanthus mortar creates an alkaline environment, and some sugars or other cellulosic components can dissolve in the alkaline solution [231]. The sugar removal from miscanthus fibre is beneficial to the cement hydration, strength development and durability of miscanthus mortar. In addition, the airtight alkaline environment also delays the degradation of miscanthus fibre.

Table 8.6 Metal ions leached from the miscanthus mortar.

Ions	Sample	Changes in the ion concentration with soaking time (mg/L)			
		30 days	60 days	70 days	90 days
Ca	RM1	31	278	353	403
	HM1	114	251	306	348
	MP1	125	297	384	438
K	RM1	82	104	107	112
	HM1	69	84	89	95
	MP1	73	97	99	105
Na	RM1	22	35	37	40
	HM1	21	28	32	35
	MP1	16	29	32	35
Al	RM1	0.6	0.9	1.0	1.1
	HM1	0.6	0.6	1.1	1.4
	MP1	0.2	0.2	0.5	0.7
B	RM1	0.007	0.007	0.008	0.007
	HM1	0.005	0.006	0.007	0.007
	MP1	0.004	0.005	0.006	0.006
Ba	RM1	0.3	0.7	0.8	1.0
	HM1	0.5	0.6	0.8	0.9
	MP1	0.4	0.7	0.9	1.0
Cr	RM1	0.005	0.01	0.01	0.02
	HM1	0.004	0.006	0.01	0.01
	MP1	0.003	0.009	0.01	0.02
Li	RM1	0.2	0.3	0.4	0.4
	HM1	0.2	0.2	0.3	0.3
	MP1	0.1	0.3	0.3	0.3
Mg	RM1	0.01	0.01	0.009	0.008
	HM1	0.009	0.01	0.008	0.007
	MP1	0.02	0.007	0.006	0.004
Sr	RM1	1.3	3.9	4.6	5.4
	HM1	2.6	3.5	4.1	4.7
	MP1	2.0	3.8	4.7	5.3

- *Degradation characteristics of miscanthus fibre*

The FTIR results of miscanthus fibre after being submerged in solution are shown in **Fig. 8.8**. A broad band for the hydroxyl group (O-H) of cellulose and hemicellulose is observed in the range between 3600 and 3000 cm^{-1}. The O-H bond of the hydrated products usually appears at 3434 cm^{-1} [162]. When miscanthus is immersed in cement solution, more obvious peaks appear in the range of the O-H group for the CMP and CHM series. The increase in soaking time has no obvious effect on the O-H group.

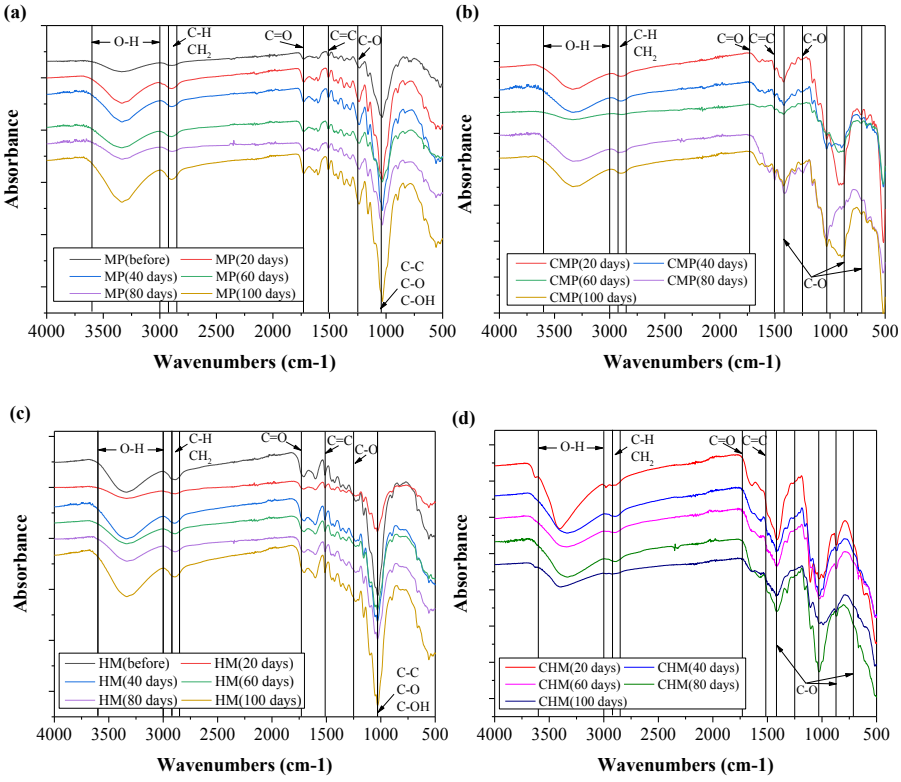

Fig. 8.8 FTIR data of miscanthus fibre after being submerged in the solution.

The C-H or CH_2 stretching of cellulose and hemicellulose are in the range between 2850 to 2920 cm^{-1}. The CM and CHM series show an insignificant vibration peak at 2850-2920 cm^{-1}. Boix et al. [58] reported that a small amount of hemicellulose can be extracted by water but not for cellulose, while the cellulose and xylose of miscanthus are significantly reduced after being soaked in a cement-water-sand mixture. This is because some cellulosic components are dissolved in an alkaline environment. As shown in **Table 8.7**, the leachates of the CMP and CHM series are a high alkaline

solution with pH values of 11.4-12.5, while the MP and HM series are weakly acidic environments with pH values of 5.1-6.3.

The MP shows an obvious band at 1730 cm^{-1}, corresponding to carboxyl groups (C=O), while after being heat-treated (HM) or soaked in cement solution (CMP and CHM), the CM and the CHM show a disappearance of the C=O band. These results are consistent with the results of alkali-treated miscanthus, which is attributed to the removal of some hemicellulose and lignin in carboxyl groups (C=O) [231]. The C-O stretching band in the range of 1240 and 1250 cm^{-1} also shows a similar trend, a decreased intensity almost to disappearance. This may be because of the alkali hydrogen bonding dissociation of hemicellulose and cellulose, as well as the hydrolysis of the hemicellulosic ester bonds [237].

The C=C aromatic symmetrical stretching of lignin at 1515 cm^{-1} does not show obvious changes for the MP and the HM because of the low pyrolysis temperature (250 ℃) applied in this study. The degradation temperature for cellulose, hemicellulose and lignin are 200-260 ℃, 240-350 ℃ and 280-500 ℃, respectively [238]. The low pyrolysis temperature in this study does not reach the level for lignin decomposition. Only the CMP and the CHM show the disappearance of some C=C group, possibly because part of the lignin is decomposed in a highly alkaline solution.

Different from the miscanthus soaked in water (MP and HM), an obvious C-O stretching band is also observed at 713 cm^{-1}, 872 cm^{-1} and 1417 cm^{-1} for the CMP and CHM. This may be because of the chemical reaction between portlandite ($Ca(OH)_2$) from the hydrated product of cement and atmospheric carbon dioxide(CO_2) [162]. An obvious peak at 1043 cm^{-1} is attributed to C-C, C-O stretching or C-OH bending of cellulose and hemicellulose [231,232].

Table 8.7 pH value of the leachates of the miscanthus fibre.

Sample	Duration of miscanthus fibre submerged in the solution				
	10 days	20 days	30 days	60 days	100 days
MP	5.3	5.1	6.3	5.7	5.2
CMP	11.4	11.6	11.6	11.6	11.6
HM	5.8	5.8	5.7	5.5	5.7
CHM	12.0	12.2	12.4	12.5	12.5

Generally, among the cellulose, hemicellulose, lignin, waxes, pectin, etc. only cellulose possesses a crystalline structure. The XRD results of miscanthus fibre before and after water immersion are shown in **Fig. 8.9a**, all miscanthus fibres are amorphous because of the irregular distribution of the cellulose chain molecule in the amorphous area, resulting in a diffuse reflection and no peaks [74]. However, a distinct peak occurs at

the diffraction angle (2θ) of 25-30 because of the crystalline cellulose. The HM series has a wider peak than the RM series owing to the destruction of some cellulose crystals during the pyrolysis process. Similar phenomena are observed in heat-treated bio-based materials [59]. Besides, the RM and the HM after being soaked in water for 60 days show a higher crystallinity because some non-crystalline compounds such as waxes, pectin, etc. are removed. The same phenomenon has also been observed in the alkali-treated miscanthus [231].

Compared to miscanthus soaked in water (MP and HM), the surface of miscanthus soaked in cement solution (CMP and CHM) is covered with cement paste. The XRD pattern of the CMP and CHM includes some hydration products such as calcium silicate hydrate and calcium hydroxide, and calcium carbonate from hydrated products reacts with carbon dioxide in the atmosphere (**Fig. 8.9b**). An obvious C-O stretching band from the calcium carbonate is observed (**Fig. 8.8b**, **8.8d**). In this study, for samples CMP and CHM, the hydration products on their surfaces are difficult to completely remove before the FTIR test due to the precipitation effect. Therefore, the changes in the crystal structure of the miscanthus soaked in the cement solution should be further determined in future work.

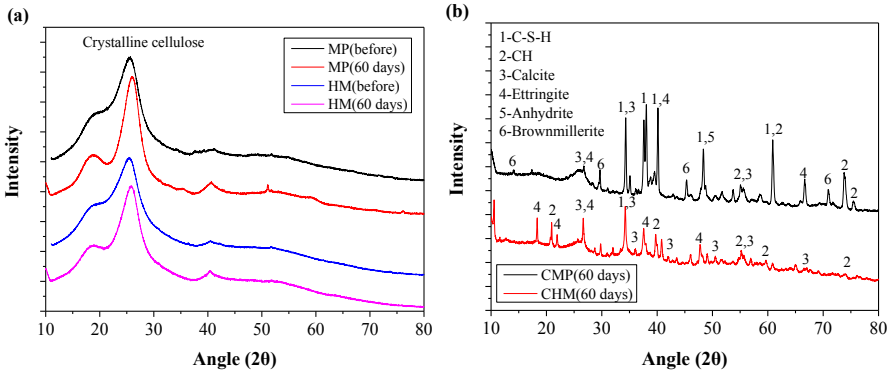

Fig. 8.9 XRD results of miscanthus fibre before and after water immersion.

The microscopic images of the miscanthus fibre after being submerged in the solution for 100 days are shown in **Fig. 8.10**. The results show that small miscanthus fragments appear on the surface of the MP and the HM, and an obvious fibrillated surface is observed. This may be because part of non-cellulosic compounds is extracted by an aqueous solution. Previous studies show that more rough and fibrillated surfaces are observed in alkali-treated miscanthus due to the removal of some lignocellulosic components [231]. For miscanthus soaked in cement solution (CMP and CHM), some hydrated cement products are observed on the miscanthus surface, especially for the

CHM. This may be due to heat treatment leading to better bonding between the CHM and the cement paste. Moreover, some cellulose and xylose leached from miscanthus can be absorbed by cement paste particles [58] to further improve the compatibility of miscanthus fibre and cement paste.

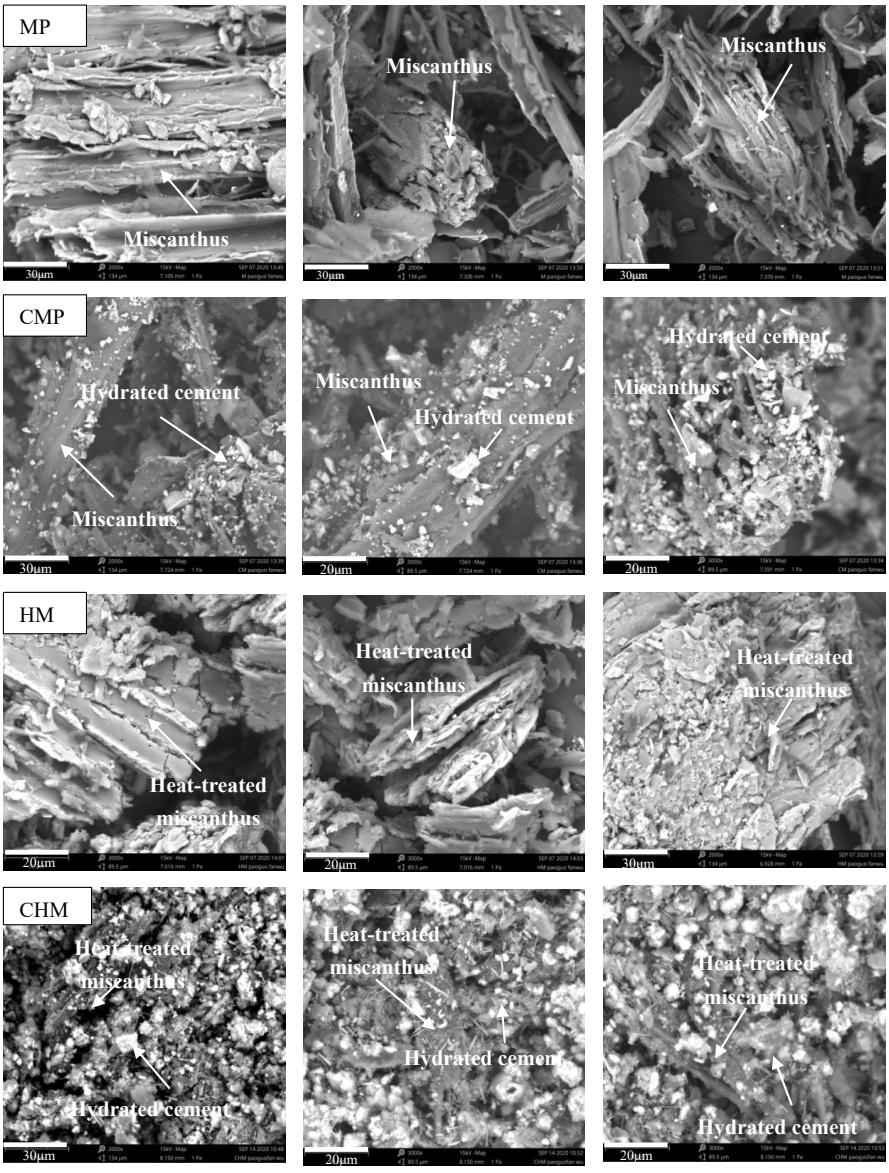

Fig. 8.10 Microscopic images of the miscanthus fibre after being submerged in the solution for 100 days.

The element calcium is detected on the surface of the CMP and the CHM by SEM-EDS

analysis. Moreover, the heat-treated miscanthus (HM and CHM) have a higher content of carbon (C) and less oxygen (O) elements, compared to the raw miscanthus (MP and CMP). Silica is also observed on the surface of the CMP and the CHM fibre indicating the presence of hydrated cement products.

8.3.4 Dimensional stability of miscanthus mortar

- *Drying shrinkage*

The bio-based materials are quite sensitive to humidity in the environment, and the shrinkage and swelling of bio-based materials have a negative impact on the performance of bio-based concrete. As shown in **Fig. 8.11a**, the drying shrinkage of miscanthus mortar increases rapidly within the first month after demolding, the drying shrinkages of the mortars RM1, HM1 and MP1 at 30 days account for 86%, 83% and 87% of the total drying shrinkage value. Besides, mortar HM1 significantly reduces the drying shrinkage by 8% at 114 days, mortar MP1 has no obvious effect on the drying shrinkage, with an increase of 1%, compared to mortar RM1. However, as the content of miscanthus powder increases from 1% to 2%, the drying shrinkage of the mortars MP1.5 and MP2 increases.

Previous studies show that the miscanthus ash obtained by heat treatment exhibits high efficiency in reducing the autogenous shrinkage of cementitious materials [17]. This may contribute to the good compatibility with the mortar, resulting in a decrease in micropores between the miscanthus fibre and the mortar matrix interface. In addition, pyrolysis can improve the dimensional stability of bio-based materials and significantly reduce the drying shrinkage of bio-based concrete [65].

The drying shrinkage of concrete is mainly caused by the water loss in the capillary pores, depending on the relative humidity [28] and porosity [29]. As shown in **Fig. 8.11b**, the mass loss of miscanthus mortar shows a trend similar to drying shrinkage, which significantly reduces within the first month. The mass loss of the mortars RM1, HM1 and MP1 at 30 days corresponds to 97%, 98% and 99% of the total mass loss value at 114 days.

The SEM images of miscanthus mortar after the drying shrinkage test are shown in **Fig. 8.12**, the shrinkage cracks between miscanthus and cement paste are observed in the mortars RM1 and MP1. The interface bonding between heat-treated miscanthus and cement paste is relatively good. Therefore, the heat treatment of miscanthus fibre appears to be an effective method to reduce the drying shrinkage of miscanthus mortar.

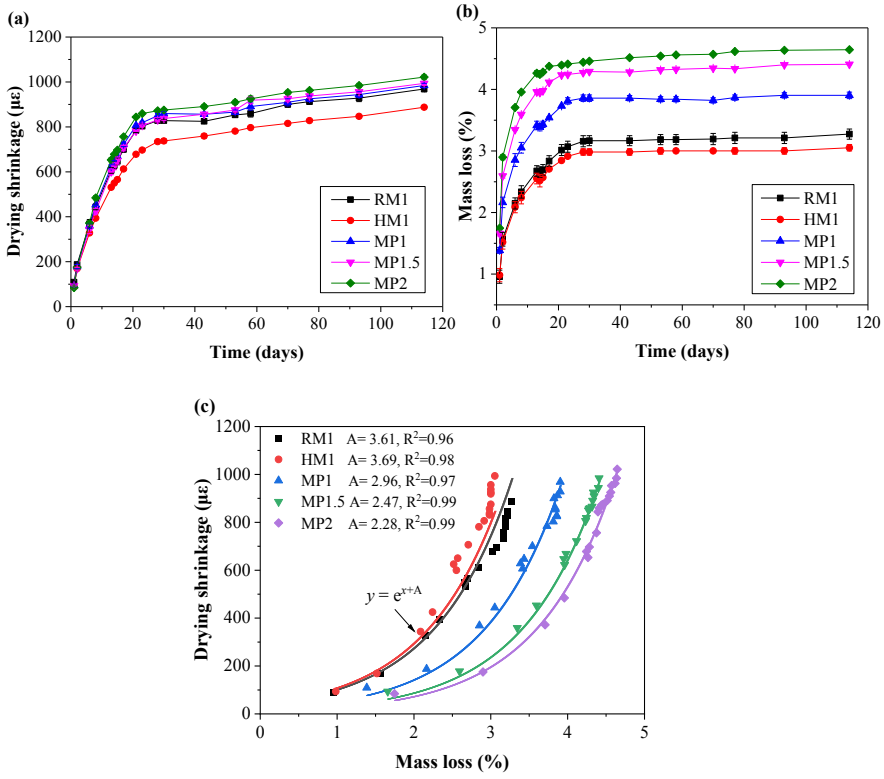

Fig. 8.11 (a) Drying shrinkage, (b) Mass loss and (c) Relationship between mass loss and drying shrinkage of miscanthus mortar.

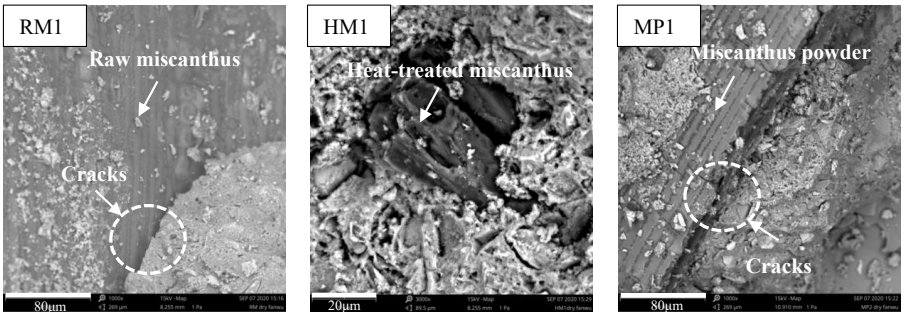

Fig. 8.12 SEM images of miscanthus mortar after drying shrinkage test.

After the miscanthus mortar is cast, cement paste and miscanthus fibre are close to the saturated state. For miscanthus mortar, the drying shrinkage is mainly caused by the moisture loss from the C-S-H matrix and the porous miscanthus fibre, which will affect the volumetric stability. The relationship between mass loss and drying shrinkage of miscanthus mortar can be fitted as:

$$y = e^{x+A} \tag{8.1}$$

where y is the drying shrinkage of miscanthus mortar (in με); x is the mass loss of miscanthus mortar (%); A is the empirical constant obtained by the experiment, the larger the value of A in Eq. (8.1), indicating that the miscanthus mortar has less mass loss when reaching the same drying shrinkage.

- *Wet swelling*

The wet swelling and mass increase of miscanthus mortar are shown in **Fig. 8.13**. The wet swelling of the mortars HM1 and RM1 shows the same trend, and the wet swelling of the mortar MP1 is higher than that of the mortars HM1 and RM1 due to the high porosity of the mortar MP1. The wet swelling of miscanthus mortar is mainly the volume change caused by the water gradually entering the miscanthus mortar from the microporous channels. The mass increase of the mortar HM1 is significantly lower than that of the mortars RM1 and MP1. The water entering the miscanthus mortar is one of the main reasons for the strength degradation of the miscanthus mortar and the dissolution of some cellulosic components. Therefore, increasing the dimensional stability of miscanthus by heat treatment has a positive effect on reducing the wet swelling characteristics of miscanthus mortar.

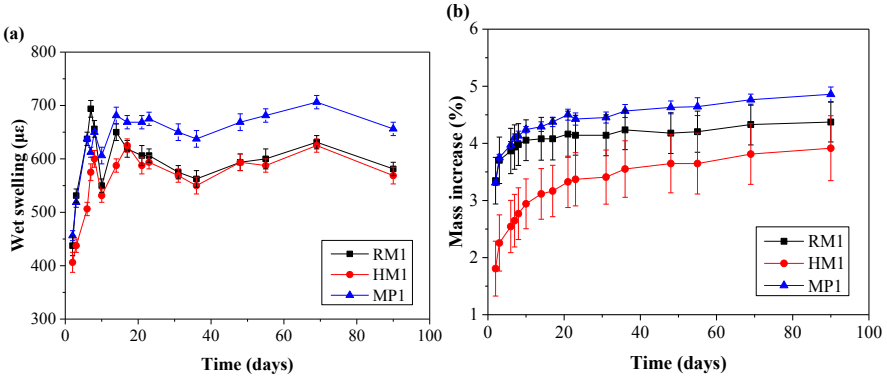

Fig. 8.13 (a) Wet swelling and (b) Mass increase of miscanthus mortar

8.4 Conclusions

(1) The mortar containing heat-treated miscanthus of 1 vol.% (HM1) shows an outstanding compressive strength and flexural strength, with an increase of 83% and 27%, respectively, compared to the control mortar containing raw miscanthus (RM1), thanks to the increased degree of cement hydration, lower porosity and enhanced

compatibility between fibres and mortar matrix.

(2) The mechanical strength degradation of bio-based miscanthus mortar after being soaked in an aqueous solution mainly takes place in the first month. The pyrolysed miscanthus fibre is beneficial for the strength development, resistance to degradation and dimensional stability of bio-based miscanthus mortar.

(3) The higher crystallinity of miscanthus fibre after being soaked in water for 60 days is attributed to the removal of some non-crystalline compounds (waxes, pectin, etc.). Microscopic image analysis detects miscanthus fibre degradation, such as small miscanthus fragments and a fibrillated surface on the miscanthus fibre surface.

(4) The morphology and content of miscanthus fibre have an obvious influence on the dimensional stability of miscanthus mortar. Drying shrinkage and wet swelling of miscanthus mortar increase rapidly within the first month because of moisture loss from the mortar matrix and the porous miscanthus fibre. Heat-treated miscanthus fibre improves the dimensional stability of bio-based miscanthus mortar and makes it more durable in mortar.

Chapter 9 Conclusions and recommendations

9.1 Conclusions

The goal of this work is to develop bio-based adsorptive concrete that can remove phosphate and improve the quality of underlying soil water. The treatment and modification of adsorptive cementitious composites, mix design and optimization of bio-based adsorptive concrete, and the long-term performance of bio-based adsorptive concrete are investigated from the standpoint of adsorptive aggregate, adsorptive cement paste, and porous structure. The following are the innovative conclusions of this work:

9.1.1 Miscanthus and steel slag as ingredients for highly adsorptive composites

The adsorption characteristics of several granular aggregates, including industrial by-product (basic oxygen furnace steel slag), lightweight aggregate (expanded silicate), and bio-material (miscanthus) are investigated to obtain potential highly adsorptive composites that can be applied to improve the adsorption performance of porous concrete. Basic oxygen furnace steel slag can be used as an effective adsorptive ingredient in the production of highly adsorptive concrete. The P-removal mechanism can be attributed to Ca^{2+} released from cement paste and steel slag, which can react with phosphate and form a stable Ca-P precipitate. Heat treatment can be used to increase the adsorption capacity of miscanthus because of the increase in specific surface area. Furthermore, steel slag is used in conjunction with porous expanded silicate by applying a non-sintered pelletizing method to produce sustainable highly adsorptive aggregates. Heat-treated miscanthus can be used to increase the porosity of adsorptive aggregates. The highly adsorptive aggregate with good mechanical strength, salt and freeze-thaw resistance can be produced by applying the non-sintered pelletizing method.

A porous adsorptive paste is created by combining chemisorption and physisorption mechanisms to enhance the adsorption performance of the paste-coated aggregate. The porous adsorptive cement paste has an adsorption capacity of 30.4-74.2 mg/g, at a corresponding initial P-concentration of 1215-2968 mg/L. The results confirm that Ca^{2+} leached from the adsorptive cement paste reacts with phosphate in solution to form Ca-P precipitates. Moreover, porous miscanthus improves the adsorption performance of the paste-coated aggregate thanks to the increase in porosity. Heat-treated miscanthus with a dosage of 0.5 wt.% and steel slag with a dosage of 10.0 wt.% can be

recommended for the highly adsorptive paste to improve P-removal capacity without sacrificing other properties.

9.1.2 Two-sized aggregate skeleton structure for porous adsorptive concrete

To improve the mechanical strengths and P-removal performance of porous adsorptive concrete by optimizing the porous skeleton structure, a two-sized aggregate containing 1-2 mm steel slag and 2-5 mm basalt is applied for the adsorptive concrete structure. Small-sized aggregates fill the pores between the large-sized aggregates, gradually reducing porosity and permeability and improving the mechanical strength and freeze-thaw resistance of adsorptive concrete. The optimum mix for adsorptive concrete is obtained based on orthogonal test results. The adsorptive concrete exhibits excellent P-removal capacity, with adequate mechanical strength and durability. The P-removal amount of adsorptive concrete increases with the increase of P-concentration and reaction time, indicating has enough Ca^{2+} can be released from concrete for Ca-P precipitate reaction. Hazardous elements (Cr, Sr, V, etc.) leached from adsorptive concrete are far below the maximum limit value, indicating no environmental risk.

The physico-mechanical properties, long-term adsorption characteristics, P-precipitate mechanism, and environmental impacts demonstrate that adsorptive concrete exhibits excellent P-removal capacity, with an adsorption amount increasing by 31-52%, compared to traditional pervious concrete. The P-adsorption amount and removal fraction of adsorptive concrete increase as the number of cycles increases. The Langmuir model and Elovich model are suitable for fitting adsorption isotherm and kinetic results of adsorptive concrete. Moreover, the adsorptive concrete exhibits a low P-releasing capacity, indicating that it can be safely used for P-removal from stormwater runoff.

9.1.3 Improvement of long-term performance of bio-based miscanthus mortar

The effects of organic matter and physical properties (size, shape, etc.) on the performance of bio-based miscanthus mortar are evaluated. Miscanthus (*x* giganteus) is modified using physical treatment (ball milling) and heat treatment methods, and heat-treated miscanthus has a positive impact on compressive strength. However, a high dosage of raw miscanthus (e.g. 5 wt.%) has a negative effect on the mechanical properties and durability of the mortar. The heat-treated miscanthus with a dosage of no more than 3 wt.% is recommended for adsorptive cement paste. Treated miscanthus significantly reduces drying shrinkage, with a reduction of up to 25% at 90 days, compared to untreated miscanthus. Powdery and long fibre of miscanthus are the recommended forms for application in sustainable bio-based mortar, in terms of

reducing drying shrinkage and thermal conductivity, as well as improving the mechanical strength of miscanthus mortar.

The effects of raw miscanthus, heat-treated and powdery miscanthus on the physical and mechanical properties, long-term degradation characteristics and dimensional stability of the miscanthus mortar are investigated. Thanks to an increased degree of cement hydration, reduced porosity and enhanced compatibility with the mortar matrix, heat-treated miscanthus increases the compressive and flexural strengths by 83% and 27%, respectively, compared to untreated miscanthus. The mechanical strength of the miscanthus mortar degrades primarily during the first month after being soaked in water. Heat-treated miscanthus fibre improves cement hydration, strength development and dimensional stability of miscanthus mortar. Therefore, heat-treated miscanthus fibre can be used to improve the dimensional stability and degradability resistance of bio-based miscanthus mortar.

9.2 Recommendations

This work investigates the physical and mechanical properties, adsorption performance and durability of bio-based adsorptive concrete with the goal of improving P-removal capacity from stormwater runoff. The selection and manufacture of highly adsorptive aggregate, the modification of adsorptive cement paste, the structure optimization of adsorptive concrete and the degradation of bio-based mortar are analyzed and discussed in this work. The presented findings can be used to improve the P-removal capacity and service life of sustainable bio-based adsorptive concrete. Nonetheless, the following are some relevant open questions for future research:

1. The effects of a weakly acidic phosphate solution on the long-term performance of adsorptive concrete should be investigated in future work. Moreover, porous adsorptive concrete is frequently in contact with contaminated water, and the effects of wastewater on the durability of adsorptive concrete should be considered. Besides, due to the porous structure and nutrient capture capacity, the potential of adsorptive concrete to foster lush plant growth for low-carbon ecological city development or to refresh the air temperature during the hot season should be explored.

2. Stormwater runoff contains a variety of pollutants, including N, P and heavy metals, etc. Precipitate mechanisms for various pollutions may be different in adsorptive concrete, and thus, other pollutant removal experiments such as nitrate, organic matter and heavy metals should be performed in future work to gain a better understanding of the adsorption performance and pollutant removal mechanism of porous adsorptive

concrete.

3. All adsorbent materials will reach saturation after a certain service life. Therefore, it is necessary to consider how to extend the service life of porous adsorptive concrete after saturation. The recovery of absorbed nutrients (N, P, K) should be considered in future work, for example, to collect absorbed P for using it as fertilizer for plant growth in vegetal (ecological) concrete, or to cultivate microbial communities in micropores to decompose absorbed organic matter.

Bibliography

[1] M. Gizińska-Górna, K. Jóźwiakowski, M. Marzec, A. Pytka, Analysis of the influence of a hybrid constructed wetland wastewater treatment plant on the water quality of the receiver, Annu. Set Environ. Prot. 19 (2017) 370–393.

[2] K. Jayaswal, V. Sahu, B.R. Gurjar, Water Pollution, Human Health and Remediation, in: S. Bhattacharya, A. Gupta, A. Gupta, A. Pandey (Eds.), Water Remediat. Energy, Environ. Sustain., Springer, Singapore, (2018)11–27. http://www.springer.com/series/15901.

[3] G. Ding, J. Yu, F. Liu, Water shortage and pollution in China, Acad. J. Environ. Sci. 4 (2016) 18–19. https://doi.org/10.15413/ajes.2016.0403.

[4] R.T. Bannerman, D.W. Owens, R.B. Dodds, N.J. Hornewer, Sources of pollutants in Wisconsin stormwater, Water Sci. Technol. 28 (1993) 241–259.

[5] T. Park, V. Ampunan, S. Maeng, E. Chung, Application of steel slag coated with sodium hydroxide to enhance precipitation-coagulation for phosphorus removal, Chemosphere. 167 (2017) 91–97. https://doi.org/10.1016/j.chemosphere.2016.09.150.

[6] S. Wang, Y. Xu, N. Norbu, Z. Wang, Remediation of biochar on heavy metal polluted soils, IOP Conf. Ser. Earth Environ. Sci. 108 (2018). https://doi.org/10.1088/1755-1315/108/4/042113.

[7] G.F. Rizzo, Use of biochar geostructures for urban stormwater water cleanup, University of Southern Queensland, (2015). https://eprints.usq.edu.au/29161/1/Rizzo_G_Craig.pdf.

[8] Y. Seida, Y. Nakano, Removal of phosphate by layered double hydroxides containing iron, Water Res. 36 (2002) 1306–1312. https://doi.org/10.1016/S0043-1354(01)00340-2.

[9] G. Li, S. Gao, G. Zhang, X. Zhang, Enhanced adsorption of phosphate from aqueous solution by nanostructured iron(III)-copper(II) binary oxides, Chem. Eng. J. 235 (2014) 124–131. https://doi.org/10.1016/j.cej.2013.09.021.

[10] M.M. Mekonnen, A.Y. Hoekstra, Global anthropogenic phosphorus loads to freshwater and associated grey water footprints and water pollution levels: A high-resolution global study, Water Resour. Res. 54 (2018) 345–358. https://doi.org/10.1002/2017WR020448.

[11] N.I. Vázquez-Rivera, L. Soto-Pérez, J.N. St John, O.I. Molina-Bas, S.S. Hwang, Optimization of pervious concrete containing fly ash and iron oxide nanoparticles and its application for phosphorus removal, Constr. Build. Mater. 93 (2015) 22–28. https://doi.org/10.1016/j.conbuildmat.2015.05.110.

[12] N.M. Agyei, C.A. Strydom, J.H. Potgieter, The removal of phosphate ions from aqueous solution by fly ash, slag, ordinary Portland cement and related blends, Cem. Concr. Res. 32 (2002) 1889–1897. https://doi.org/10.1016/S0008-8846(02)00888-8.

[13] A.N. Shabalala, S.O. Ekolu, S. Diop, F. Solomon, Pervious concrete reactive barrier for removal of heavy metals from acid mine drainage − column study, J. Hazard. Mater. 323 (2017) 641–653. https://doi.org/10.1016/j.jhazmat.2016.10.027.

[14] M. Jo, L. Soto, M. Arocho, J. St John, S. Hwang, Optimum mix design of fly ash geopolymer paste and its use in pervious concrete for removal of fecal coliforms and phosphorus in water, Constr. Build. Mater. 93 (2015) 1097–1104. https://doi.org/10.1016/j.conbuildmat.2015.05.034.

[15] F. Wu, Q. Yu, F. Gauvin, H.J.H. Brouwers, C. Liu, Phosphorus removal from aqueous solutions by adsorptive concrete aggregates, J. Clean. Prod. 278 (2021) 123933. https://doi.org/10.1016/j.jclepro.2020.123933.

[16] I. Lewandowski, J. Clifton-brown, A. Kiesel, A. Hastings, Y. Iqbal, 2.Miscanthus, in: Perenn. Grasses Bioenergy Bioprod., (2018) 35–59. https://doi.org/10.1016/B978-0-12-812900-5.00002-3.

[17] Y. Lv, G. Ye, G. De Schutter, Utilization of miscanthus combustion ash as internal curing agent in cement-based materials: Effect on autogenous shrinkage, Constr. Build. Mater. 207 (2019) 585–591. https://doi.org/10.1016/j.conbuildmat.2019.02.167.

[18] F. Ntimugura, R. Vinai, A.B. Harper, P. Walker, Environmental performance of miscanthus-lime lightweight concrete using life cycle assessment: Application in external wall assemblies, Sustain. Mater. Technol. 28 (2021) e00253. https://doi.org/10.1016/j.susmat.2021.e00253.

[19] Z. Shen, Y. Zhang, F. Jin, D.S. Alessi, Y. Zhang, F. Wang, O. McMillan, A. Al-Tabbaa, Comparison of nickel adsorption on biochars produced from mixed softwood and Miscanthus straw, Environ. Sci. Pollut. Res. 25 (2018) 14626–14635. https://doi.org/10.1007/s11356-018-1674-2.

[20] W. Yuan, X. Zhang, J. Zhao, Q. Li, C. Ao, T. Xia, W. Zhang, C. Lu, Ultra-lightweight and highly porous carbon aerogels from bamboo pulp fibers as an effective sorbent for water treatment, Results Phys. 7 (2017) 2919–2924. https://doi.org/10.1016/j.rinp.2017.08.011.

[21] M. Inyang, E. Dickenson, The potential role of biochar in the removal of organic and microbial contaminants from potable and reuse water: A review, Chemosphere. 134 (2015) 232–240. https://doi.org/10.1016/j.chemosphere.2015.03.072.

[22] K. Kochová, Mechanical and physical properties of fibre-cement composites using alternative natural fibres, Eindhoven University of Technology, (2022).

[23] F.R. Oliveira, A.K. Patel, D.P. Jaisi, S. Adhikari, H. Lu, S.K. Khanal, Environmental application of biochar: Current status and perspectives, Bioresour. Technol. 246 (2017) 110–122. https://doi.org/10.1016/j.biortech.2017.08.122.

[24] T. Uysal, G. Duman, Y. Onal, I. Yasa, J. Yanik, Production of activated carbon and fungicidal oil from peach stone by two-stage process, J. Anal. Appl. Pyrolysis. 108 (2014) 47–55. https://doi.org/10.1016/j.jaap.2014.05.017.

[25] C. Niyigena, S. Amziane, A. Chateauneuf, Multicriteria analysis demonstrating the impact of shiv on the properties of hemp concrete, Constr. Build. Mater. 160 (2018) 211–222. https://doi.org/10.1016/j.conbuildmat.2017.11.026.

[26] J. Page, S. Amziane, M. Gomina, C. Djelal, F. Audonnet, Using linseed oil as flax fibre coating for fibre-reinforced cementitious composite, Ind. Crops Prod. 161 (2021) 113168. https://doi.org/10.1016/j.indcrop.2020.113168.

[27] L.I. Bowden, A.P. Jarvis, P.L. Younger, K.L. Johnson, Phosphorus removal from waste waters using basic oxygen steel slag, Environ. Sci. Technol. 43 (2009) 2476–2481. https://doi.org/10.1021/es801626d.

[28] T. Tho-In, V. Sata, P. Chindaprasirt, C. Jaturapitakkul, Pervious high-calcium fly ash geopolymer concrete, Constr. Build. Mater. 30 (2012) 366–371. https://doi.org/10.1016/j.conbuildmat.2011.12.028.

[29] A. Drizo, C.A. Frost, J. Grace, K.A. Smith, Physico-chemical screening of phosphate-removing substrates for use in constructed wetland systems, Water Res. 33 (1999) 3595–3602. https://doi.org/10.1016/S0043-1354(99)00082-2.

[30] L. Johansson, J.P. Gustafsson, Phosphate removal using blast furnace slags and opoka-mechanisms, Water Res. 34 (2000) 259–265. https://doi.org/10.1016/S0043-1354(99)00135-9.

[31] B. Kostura, H. Kulveitová, J. Leško, Blast furnace slags as sorbents of phosphate from water solutions, Water Res. 39 (2005) 1795–1802. https://doi.org/10.1016/j.watres.2005.03.010.

[32] S.M. Ragheb, Phosphate removal from aqueous solution using slag and fly ash, HBRC J. 9 (2013) 270–275. https://doi.org/10.1016/j.hbrcj.2013.08.005.

[33] L. Mo, S. Yang, B. Huang, L. Xu, S. Feng, M. Deng, Preparation, microstructure and property of carbonated artificial steel slag aggregate used in concrete, Cem. Concr. Compos. 113 (2020) 103715.

https://doi.org/10.1016/j.cemconcomp.2020.103715.

[34] J.C.O. Zepper, S.R. van der Laan, K. Schollbach, H.J.H. Brouwers, Reactivity of BOF slag under autoclaving conditions, Constr. Build. Mater. 364 (2023) 129957. https://doi.org/10.1016/j.conbuildmat.2022.129957.

[35] Q. Wang, P. Yan, Hydration properties of basic oxygen furnace steel slag, Constr. Build. Mater. 24 (2010) 1134–1140. https://doi.org/10.1016/j.conbuildmat.2009.12.028.

[36] A.M. Kaja, A. Delsing, S.R. van der Laan, H.J.H. Brouwers, Q. Yu, Effects of carbonation on the retention of heavy metals in chemically activated BOF slag pastes, Cem. Concr. Res. 148 (2021) 106534. https://doi.org/10.1016/j.cemconres.2021.106534.

[37] C. Shi, J. Qian, High performance cementing materials from industrial slags-A review, Resour. Conserv. Recycl. 29 (2000) 195–207. https://doi.org/10.1016/S0921-3449(99)00060-9.

[38] A.M. Kaja, K. Schollbach, S. Melzer, S.R. van der Laan, H.J.H. Brouwers, Q. Yu, Hydration of potassium citrate-activated BOF slag, Cem. Concr. Res. 140 (2021) 106291. https://doi.org/10.1016/j.cemconres.2020.106291.

[39] A.N. Shilton, I. Elmetri, A. Drizo, S. Pratt, R.G. Haverkamp, S.C. Bilby, Phosphorus removal by an 'active' slag filter–a decade of full scale experience, Water Res. 40 (2006) 113–118. https://doi.org/10.1016/J.WATRES.2005.11.002.

[40] J.H. Park, S.H. Kim, R.D. Delaune, B.H. Kang, S.W. Kang, J.S. Cho, Y.S. Ok, D.C. Seo, Enhancement of phosphorus removal with near-neutral pH utilizing steel and ferronickel slags for application of constructed wetlands, Ecol. Eng. 95 (2016) 612–621. https://doi.org/10.1016/j.ecoleng.2016.06.052.

[41] K. Okano, M. Uemoto, J. Kagami, K. Miura, T. Aketo, M. Toda, K. Honda, H. Ohtake, Novel technique for phosphorus recovery from aqueous solutions using amorphous calcium silicate hydrates (A-CSHs), Water Res. 47 (2013) 2251–2259. https://doi.org/10.1016/j.watres.2013.01.052.

[42] K. Hosni, S. Ben Moussa, A. Chachi, M. Ben Amor, The removal of PO_4^{3-} by calcium hydroxide from synthetic wastewater: optimisation of the operating conditions, Desalination. 223 (2008) 337–343. https://doi.org/10.1016/j.desal.2007.01.213.

[43] C. Barca, C. Gérente, D. Meyer, F. Chazarenc, Y. Andrès, Phosphate removal from synthetic and real wastewater using steel slags produced in Europe, Water Res. 46 (2012) 2376–2384. https://doi.org/10.1016/j.watres.2012.02.012.

[44] N. Bellier, F. Chazarenc, Y. Comeau, Phosphorus removal from wastewater by mineral apatite, Water Res. 40 (2006) 2965–2971. https://doi.org/10.1016/j.watres.2006.05.016.

[45] D. Claveau-Mallet, B. Courcelles, Y. Comeau, Phosphorus removal by steel slag filters:Modeling dissolution and precipitation kinetics to predict longevity, Environ. Sci. Technol. 48 (2014) 7486–7493. https://doi.org/10.1021/es500689t.

[46] L. Haselbach, C. Poor, J. Tilson, Dissolved zinc and copper retention from stormwater runoff in ordinary portland cement pervious concrete, Constr. Build. Mater. 53 (2014) 652–657. https://doi.org/10.1016/j.conbuildmat.2013.12.013.

[47] M. Jo, L. Soto, M. Arocho, J.S. John, S. Hwang, Optimum mix design of fly ash geopolymer paste and its use in pervious concrete for removal of fecal coliforms and phosphorus in water, Constr. Build. Mater. 93 (2015) 1097–1104. https://doi.org/10.1016/j.conbuildmat.2015.05.034.

[48] Y. Han, S. Park, C. Lee, J. Park, N. Choi, S. Kim, Phosphate removal from aqueoussolution by aluminum (Hydr)oxide-coated sand, Environ.Eng.Res. 14 (2009) 164–169.

[49] G.M. Kim, J.G. Jang, H.R. Khalid, H.K. Lee, Water purification characteristics of pervious concrete fabricated with CSA cement and bottom ash aggregates, Constr. Build. Mater. 136 (2017) 1–8.

https://doi.org/10.1016/j.conbuildmat.2017.01.020.

[50] X. Chen, Y. Guo, S. Ding, H. Zhang, F. Xia, J. Wang, M. Zhou, Utilization of red mud in geopolymer-based pervious concrete with function of adsorption of heavy metal ions, J. Clean. Prod. 207 (2019) 789–800. https://doi.org/10.1016/j.jclepro.2018.09.263.

[51] X. Chen, Z. Niu, H. Zhang, M. Lu, Y. Lu, M. Zhou, B. Li, Design of a chitosan modifying alkali-activated slag pervious concrete with the function of water purification, Constr. Build. Mater. 251 (2020) 118979. https://doi.org/10.1016/j.conbuildmat.2020.118979.

[52] C. Xie, L. Yuan, H. Tan, Y. Zhang, M. Zhao, Y. Jia, Experimental study on the water purification performance of biochar-modified pervious concrete, Constr. Build. Mater. 285 (2021) 122767. https://doi.org/10.1088/1755-1315/113/1/012126.

[53] E. Teymouri, S.F. Mousavi, H. Karami, S. Farzin, M. Hosseini Kheirabad, Municipal wastewater pretreatment using porous concrete containing fine-grained mineral adsorbents, J. Water Process Eng. 36 (2020) 101346. https://doi.org/10.1016/j.jwpe.2020.101346.

[54] V. Ducman, L. Korat, I. Netinger, I. Barišic, Draining capability of single-sized pervious concrete, Constr. Build. Mater. 169 (2018) 252–260. https://doi.org/10.1016/j.conbuildmat.2018.03.037.

[55] F. Wu, Q. Yu, F. Gauvin, H.J.H. Brouwers, A facile manufacture of highly adsorptive aggregates using steel slag and porous expanded silica for phosphorus removal, Resour. Conserv. Recycl. (2021) 105238. https://doi.org/10.1016/j.resconrec.2020.105238.

[56] G.T. Fasick, J. Liu, Lab scale studies of miscanthus mechanical conditioning and bale compression, Biosyst. Eng. 200 (2020) 366–376. https://doi.org/10.1016/j.biosystemseng.2020.10.011.

[57] K. Kochova, K. Schollbach, F. Gauvin, H.J.H. Brouwers, Effect of saccharides on the hydration of ordinary Portland cement, Constr. Build. Mater. 150 (2017) 268–275. https://doi.org/10.1016/j.conbuildmat.2017.05.149.

[58] E. Boix, E. Gineau, O. Joan, G. Mouille, P. Navard, Influence of chemical treatments of miscanthus stem fragments on polysaccharide release in the presence of cement and on the mechanical properties of bio-based concrete materials, Cem. Concr. Compos. 105 (2020) 1–8. https://doi.org/10.1016/j.cemconcomp.2019.103429.

[59] F. Wu, C. Liu, L. Zhang, Y. Lu, Y. Ma, Comparative study of carbonized peach shell and carbonized apricot shell to improve the performance of lightweight concrete, Constr. Build. Mater. 188 (2018) 758–771. https://doi.org/10.1016/j.conbuildmat.2018.08.094.

[60] J. Clifton-Brown, A. Hastings, M. Mos, Progress in upscaling Miscanthus biomass production for the European bio-economy with seed-based hybrids, GCB Bioenergy. 9 (2017) 6–17. https://doi.org/10.1111/gcbb.12357.

[61] F. Wu, C. Liu, Z. Diao, B. Feng, W. Sun, X. Li, S. Zhao, Improvement of mechanical properties in polypropylene- and glass-gibre-reinforced peach shell lightweight concrete, Adv. Mater. Sci. Eng. 2018 (2018) 1–11. https://doi.org/10.1155/2018/6250941.

[62] Y. Chen, Q.L. Yu, H.J.H. Brouwers, Acoustic performance and microstructural analysis of bio-based lightweight concrete containing miscanthus, Constr. Build. Mater. 157 (2017) 839–851. https://doi.org/10.1016/j.conbuildmat.2017.09.161.

[63] L. Courard, V. Parmentier, Carbonated miscanthus mineralized aggregates for reducing environmental impact of lightweight concrete blocks, Sustain. Build. 2 (2017) 1–9. https://doi.org/10.1051/sbuild/2017004.

[64] D. Waldmann, V. Thapa, F. Dahm, C. Faltz, Masonry blocks from lightweight concrete on the basis of miscanthus as aggregates, in: S. Barth, D. Murphy-Bokern, O. Kalinina, G. Taylor, M. Jones (Eds.), Perenn. Biomass Crop. a Resour. World, Springer International Publishing, Cham, (2016) 273–295.

[65] F. Wu, Q. Yu, C. Liu, Durability of thermal insulating bio-based lightweight concrete: Understanding of heat treatment on bio-aggregates, Constr. Build. Mater. 269 (2021) 121800. https://doi.org/10.1016/j.conbuildmat.2020.121800.

[66] I. Merta, E.K. Tschegg, Fracture energy of natural fibre reinforced concrete, Constr. Build. Mater. 40 (2013) 991–997. https://doi.org/10.1016/j.conbuildmat.2012.11.060.

[67] L.K. Aggarwal, J. Singh, Effect of plant fibre extractives on properties of cement, Cem. Concr. Compos. 12 (1990) 103–108. https://doi.org/10.1016/0958-9465(90)90047-2.

[68] Z.Y. Qu, Q.L. Yu, Synthesizing super-hydrophobic ground granulated blast furnace slag to enhance the transport property of lightweight aggregate concrete, Constr. Build. Mater. 191 (2018) 176–186. https://doi.org/10.1016/j.conbuildmat.2018.10.018.

[69] Y. Luo, L. Zhao, H. Meng, X. Xiang, X. Zhao, G. Li, Q. Lin, Physio-chemical characterization of biochars pyrolyzed from miscanthus under two different temperatures, Trans. Chinese Soc. Agric. Eng. 29 (2013) 208–217.

[70] T. Wu, X. Yang, H. Wei, X. Liu, Mechanical properties and microstructure of lightweight aggregate concrete with and without fibers, Constr. Build. Mater. 199 (2019) 526–539. https://doi.org/10.1016/j.conbuildmat.2018.12.037.

[71] S. Yuan, L. Zhao, H. Meng, Y. Shen, The main types of biochar and their properties and expectative researches, J. Plant Nutr. Fertil. 34 (2017) 543–549.

[72] E.Y. Nakanishi, V. Dos Santos, M.R. Cabral, S.F. Santos, M.S. Rodrigues, M. Frías, H. Savastano Junior, Hot water treatment effect in the elephant grass ashes calcinated at different temperatures, Rev. Mater. 23 (2018) 1–10. https://doi.org/10.1590/S1517-707620180003.0543.

[73] F. Wu, Q. Yu, H.J.H. Brouwers, Long-term performance of bio-based miscanthus mortar, Constr. Build. Mater. 324 (2022) 126703. https://doi.org/10.1016/j.conbuildmat.2022.126703.

[74] H. Yang, Y. Xu, X. Fang, D. Wu, Analysis on element composition，cellulose content and crystalliulty of the common nut shells, J. Anhui Agri．Sci. 44 (2016) 21–23.

[75] Y. Chen, F. Wu, Q. Yu, H.J.H. Brouwers, Bio-based ultra-lightweight concrete applying Miscanthus fibers: Acoustic absorption and thermal insulation, Cem. Concr. Compos. 114 (2020) 103829.

[76] A. Akhtar, A.K. Sarmah, Novel biochar-concrete composites: Manufacturing, characterization and evaluation of the mechanical properties, Sci. Total Environ. 616–617 (2018) 408–416. https://doi.org/10.1016/j.scitotenv.2017.10.319.

[77] S. Gupta, A. Kashani, Utilization of biochar from unwashed peanut shell in cementitious building materials – Effect on early age properties and environmental benefits, Fuel Process. Technol. 218 (2021) 106841. https://doi.org/10.1016/j.fuproc.2021.106841.

[78] M. Aslam, P. Shafigh, M.Z. Jumaat, Drying shrinkage behaviour of structural lightweight aggregate concrete containing blended oil palm bio-products, J. Clean. Prod. 127 (2016) 183–194. https://doi.org/10.1016/j.jclepro.2016.03.165.

[79] M. Bederina, M. Gotteicha, B. Belhadj, R.M. Dheily, M.M. Khenfer, M. Queneudec, Drying shrinkage studies of wood sand concrete - Effect of different wood treatments, Constr. Build. Mater. 36 (2012) 1066–1075. https://doi.org/10.1016/j.conbuildmat.2012.06.010.

[80] J. Liu, N. Farzadnia, C. Shi, X. Ma, Shrinkage and strength development of UHSC incorporating a hybrid system of SAP and SRA, Cem. Concr. Compos. 97 (2019) 175–189. https://doi.org/10.1016/j.cemconcomp.2018.12.029.

[81] P.K. Mehta, P.J.M. Monteiro, Concrete: Microstructure, Properties, and Materials, 4th ed., McGraw Hill, (2013).

[82] W. Li, Z. Huang, G. Hu, W. Hui Duan, S.P. Shah, Early-age shrinkage development of ultra-high-performance concrete under heat curing treatment, Constr. Build. Mater. 131 (2017) 767–774. https://doi.org/10.1016/j.conbuildmat.2016.11.024.

[83] H. Ye, Mitigation of drying and carbonation shrinkage of cement paste using magnesia, J. Adv. Concr. Technol. 16 (2018) 476–484. https://doi.org/10.3151/jact.16.476.

[84] W. Li, Z. Huang, T. Zu, C. Shi, W.H. Duan, S.P. Shah, Influence of nanolimestone on the hydration, mechanical strength, and autogenous shrinkage of ultrahigh-performance concrete, J. Mater. Civ. Eng. 28 (2016) 1–9. https://doi.org/10.1061/(ASCE)MT.1943-5533.0001327.

[85] S. Medjigbodo, A.Z. Bendimerad, E. Rozière, A. Loukili, How do recycled concrete aggregates modify the shrinkage and self-healing properties?, Cem. Concr. Compos. 86 (2018) 72–86. https://doi.org/10.1016/j.cemconcomp.2017.11.003.

[86] C. Sun, Y. Zhu, J. Guo, Y. Zhang, G. Sun, Effects of foaming agent type on the workability, drying shrinkage, frost resistance and pore distribution of foamed concrete, Constr. Build. Mater. 186 (2018) 833–839. https://doi.org/10.1016/j.conbuildmat.2018.08.019.

[87] X. Zhu, D. Tang, K. Yang, Z. Zhang, Q. Li, Q. Pan, C. Yang, Effect of $Ca(OH)_2$ on shrinkage characteristics and microstructures of alkali-activated slag concrete, Constr. Build. Mater. 175 (2018) 467–482. https://doi.org/10.1016/j.conbuildmat.2018.04.180.

[88] S.M.A. Kabir, U.J. Alengaram, M.Z. Jumaat, S. Yusoff, A. Sharmin, I.I. Bashar, Performance evaluation and some durability characteristics of environmental friendly palm oil clinker based geopolymer concrete, J. Clean. Prod. 161 (2017) 477–492. https://doi.org/10.1016/j.jclepro.2017.05.002.

[89] C. Martínez-García, B. González-Fonteboa, F. Martínez-Abella, D. Carro- López, Performance of mussel shell as aggregate in plain concrete, Constr. Build. Mater. 139 (2017) 570–583. https://doi.org/10.1016/j.conbuildmat.2016.09.091.

[90] H. Zhu, T. Yu, D. Wei, X. Wang, T. He, Y.; Wu, J. Qi, The adsorption of phosphorus in simulated wastewater by immersing and annealing modified attapulgite, Res. Environ. Sci. 31 (2018) 765–773.

[91] C. Guo, H. Li, F. Fang, Y. Ji, Y.; Xing, Y. Fan, Y. Liu, Study on distribution of phosphorus fractions and adsorption-desorption characteristics in surface sediments of the Yellow River by molybdenum antimony spectrophotometry, Spectrosc. Spectr. Anal. 38 (2018) 218–223. https://doi.org/10.3964/j.issn.1000-0593(2018)01-0218-06.

[92] P. Taylor, G.H. Safari, M. Zarrabi, M. Hoseini, H. Kamani, Desalination and water treatment trends of natural and acid-engineered pumice onto phosphorus ions in aquatic environment: adsorbent preparation, characterization, and kinetic and equilibrium modeling, Desalin. Water Treat. (2014) 37–41. https://doi.org/10.1080/19443994.2014.915385.

[93] M.A. Nkansah, A.A. Christy, T. Barth, G.W. Francis, The use of lightweight expanded clay aggregate (LECA) as sorbent for PAHs removal from water, J. Hazard. Mater. 217–218 (2012) 360–365. https://doi.org/10.1016/j.jhazmat.2012.03.038.

[94] S.A. Dastgheib, D.A. Rockstraw, Pecan shell activated carbon: Synthesis, characterization, and application for the removal of copper from aqueous solution, Carbon N. Y. 39 (2001) 1849–1855. https://doi.org/10.1016/S0008-6223(00)00315-8.

[95] A.I. Osman, A.T. Ahmed, C.R. Johnston, D.W. Rooney, Physicochemical characterization of miscanthus and its application in heavy metals removal from wastewaters, Environ. Prog. Sustain. Energy. 37 (2018) 1058–1067. https://doi.org/10.1002/ep.12783.

[96] S. Yaghoobi, K. Sharafie, H. Biglari, Mucilage of Plantago ovata as natural coagulation – flocculation aid in an electrocoagulation process for phosphate removal from aqueous environments, Desalin. Water Treat.

99 (2017) 21475. https://doi.org/10.5004/dwt.2017.21475.

[97] D. Naghipour, K. Taghavi, J. Jaafari, Y. Mahdavi, M.G. Ghozikali, R. Ameri, A. Jamshidi, Statistical modeling and optimization of the phosphorus biosorption by modified Lemna minor from aqueous solution using response surface methodology (RSM), Desalin. Water Treat. 3994 (2015) 1–12. https://doi.org/10.1080/19443994.2015.1100555.

[98] C. Shi, Steel slag - Its production, processing, characteristics, and cementitious properties, J. Mater. Civ. Eng. 16 (2004) 230–236. https://doi.org/10.1061/(ASCE)0899-1561(2004)16:3(230).

[99] A. Kaasik, C. Vohla, R. Mõtlep, Ü. Mander, K. Kirsimäe, Hydrated calcareous oil-shale ash as potential filter media for phosphorus removal in constructed wetlands, Water Res. 42 (2008) 1315–1323. https://doi.org/https://doi.org/10.1016/j.watres.2007.10.002.

[100] C. Jiang, L. Jia, B. Zhang, Y. He, G. Kirumba, Comparison of quartz sand, anthracite, shale and biological ceramsite for adsorptive removal of phosphorus from aqueous solution, J. Environ. Sci. 26 (2014) 466–477. https://doi.org/10.1016/S1001-0742(13)60410-6.

[101] J. Rouquerol, F. Rouquerol, P. Llewellyn, G. Maurin, K.S.W. Sing, Adsorption by powders and porous solids: principles, methodology and applications, 2nd ed., Academic Press, (2013).

[102] K.W. Jung, M.J. Hwang, K.H. Ahn, Y.S. Ok, Kinetic study on phosphate removal from aqueous solution by biochar derived from peanut shell as renewable adsorptive media, Int. J. Environ. Sci. Technol. 12 (2015) 3363–3372. https://doi.org/10.1007/s13762-015-0766-5.

[103] G. Lin, J. Jiang, K. Wu, Z. Cai, K. Sun, X. Lu, Pore structure analysis and methane adsorption of self-form granular activated carbon by phosporic acid activation, Chem. Ind. For. Prod. 36 (2016) 101–106. https://doi.org/10.3969/j.issn.0253-2417.2016.05.015.

[104] Y. Zhang, G. Li, Principle and application of activated carbon-nanofiltration in treatment of Mmicro-polluted source water, Science Press, Beijing, (2011).

[105] H. Yin, Y. Yun, Y. Zhang, C. Fan, Phosphate removal from wastewaters by a naturally occurring, calcium-rich sepiolite, J. Hazard. Mater. 198 (2011) 362–369. https://doi.org/10.1016/j.jhazmat.2011.10.072.

[106] K.R. Helyar, D.N. Munns, R.G. Burau, Adsorption of phosphate by gibbsite I. effects of neutral chloride salts of calcium, magnesium, sodium, and potassium, J. Soil Sci. 27 (1976) 307–314.

[107] K.R. Helyar, D.N. Munns, R.G. Burau, Adsorption of phosphate by gibbsite II. formation of a surface complex involving divalent cations, J. Soil Sci. 27 (1976) 315–323.

[108] J.J. Lehr, J.C. Van Wesemael, The influence of neutral salts on the solubilityof soil phosphate with special reference to the effect of the nitrates of sodium and calcium, J. Soil Sci. 3 (1952) 125–135.

[109] X. Tan, Y. Liu, G. Zeng, X. Wang, X. Hu, Y. Gu, Z. Yang, Application of biochar for the removal of pollutants from aqueous solutions, Chemosphere. 125 (2015) 70–85. https://doi.org/10.1016/j.chemosphere.2014.12.058.

[110] M. Ghaedi, A. Hassanzadeh, S.N. Kokhdan, Multiwalled carbon nanotubes as adsorbents for the kinetic and equilibrium study of the removal of Alizarin red S and morin, J. Chem. Eng. Data. 56 (2011) 2511–2520. https://doi.org/10.1021/je2000414.

[111] J.H. Park, J.J. Wang, S.H. Kim, J.S. Cho, S.W. Kang, R.D. Delaune, D.C. Seo, Phosphate removal in constructed wetland with rapid cooled basic oxygen furnace slag, Chem. Eng. J. 327 (2017) 713–724. https://doi.org/10.1016/j.cej.2017.06.155.

[112] Y. Yang, Y.Q. Zhao, A.O. Babatunde, L. Wang, Y.X. Ren, Y. Han, Characteristics and mechanisms of phosphate adsorption on dewatered alum sludge, Sep. Purif. Technol. 51 (2006) 193–200. https://doi.org/10.1016/j.seppur.2006.01.013.

[113] N.S. Bolan, J.K. Syers, R.W. Tillman, Ionic strength effects on surface charge and adsorption of phosphate

and sulphate by soils, J. Soil Sci. 37 (1986) 379–388.

[114] L. Ruixia, G. Jinlong, T. Hongxiao, Adsorption of fluoride, phosphate, and arsenate ions on a new type of ion exchange fiber, J. Colloid Interface Sci. 248 (2002) 268–274. https://doi.org/10.1006/jcis.2002.8260.

[115] F. Gan, J. Zhou, H. Wang, C. Du, X. Chen, Removal of phosphate from aqueous solution by thermally treated natural palygorskite, Water Res. 43 (2009) 2907–2915. https://doi.org/10.1016/j.watres.2009.03.051.

[116] A. Drizo, C. Forget, R.P. Chapuis, Y. Comeau, Phosphorus removal by electric arc furnace steel slag and serpentinite, Water Res. 40 (2006) 1547–1554. https://doi.org/10.1016/j.watres.2006.02.001.

[117] C. Han, Z. Wang, H. Yang, X. Xue, Removal kinetics of phosphorus from synthetic wastewater using basic oxygen furnace slag, J. Environ. Sci. 30 (2015) 21–29. https://doi.org/10.1016/j.jes.2014.11.003.

[118] G. Zhao, Q. Zhou, X. Li, Adsorption of phosphorus from aqueous solution on steel converter slags, J. Tongji Univ. (Natural Sci.) 35 (2007) 1510–1514.

[119] Z. Asadi Zeidabadi, S. Bakhtiari, H. Abbaslou, A.R. Ghanizadeh, Synthesis, characterization and evaluation of biochar from agricultural waste biomass for use in building materials, Constr. Build. Mater. 181 (2018) 301–308. https://doi.org/10.1016/j.conbuildmat.2018.05.271.

[120] B. Kaynak, H. Topal, A.T. Atimtay, Peach and apricot stone combustion in a bubbling fluidized bed, Fuel Process. Technol. 86 (2005) 1175–1193. https://doi.org/10.1016/j.fuproc.2004.12.007.

[121] W. De Jong, A. Pirone, M.A. Wójtowicz, Pyrolysis of miscanthus giganteus and wood pellets: TG-FTIR analysis and reaction kinetics, Fuel. 82 (2003) 1139–1147. https://doi.org/10.1016/S0016-2361(02)00419-2.

[122] D. Xu, J. Xu, J. Wu, A. Muhammad, Studies on the phosphorus sorption capacity of substrates used in constructed wetland systems, Chemosphere. 63 (2006) 344–352. https://doi.org/10.1016/j.chemosphere.2005.08.036.

[123] S. Tanada, M. Kabayama, N. Kawasaki, T. Sakiyama, T. Nakamura, M. Araki, T. Tamura, Removal of phosphate by aluminum oxide hydroxide, J. Colloid Interface Sci. 257 (2003) 135–140. https://doi.org/10.1016/S0021-9797(02)00008-5.

[124] S. Ramola, T. Mishra, G. Rana, R.K. Srivastava, Characterization and pollutant removal efficiency of biochar derived from baggase, bamboo and tyre, Environ. Monit. Assess. 186 (2014) 9023–9039. https://doi.org/10.1007/s10661-014-4062-5.

[125] J.S. Han, S.H. Min, Y.K. Kim, Removal of phosphorus using AMD-treated lignocellulosic material, For. Prod. J. 55 (2005) 48–53.

[126] K. Riahi, B. Ben Thayer, A. Ben Mammou, A. Ben Ammar, M.H. Jaafoura, Biosorption characteristics of phosphates from aqueous solution onto Phoenix dactylifera L. date palm fibers, J. Hazard. Mater. 170 (2009) 511–519. https://doi.org/10.1016/j.jhazmat.2009.05.004.

[127] M.S. Legnoverde, E.I. Basaldella, Influence of particle size on the adsorption and release of cephalexin encapsulated in mesoporous silica SBA-15, Mater. Lett. 181 (2016) 331–334. https://doi.org/10.1016/j.matlet.2016.06.053.

[128] F. Wu, Q. Yu, C. Liu, H.J.H. Brouwers, L. Wang, Effect of surface treatment of apricot shell on the performance of lightweight bio-concrete, Constr. Build. Mater. 229 (2019) 116859. https://doi.org/10.1016/j.conbuildmat.2019.116859.

[129] W.K. Kim, T. Shim, Y.S. Kim, S. Hyun, C. Ryu, Y.K. Park, J. Jung, Characterization of cadmium removal from aqueous solution by biochar produced from a giant Miscanthus at different pyrolytic temperatures, Bioresour. Technol. 138 (2013) 266–270. https://doi.org/10.1016/j.biortech.2013.03.186.

[130] J. Hao, H. Tian, Z. Hu, Co-pyrolysis characteristics of miscanthus corn stalks and lignite, Coal Convers. 42

(2019) 22–30.

[131] X. Peng, Y. Zhou, R. Jia, W. Wang, Y. Wu, Preparation of non-sintered lightweight aggregates from dredged sediments and modification of their properties, Constr. Build. Mater. 132 (2017) 9–20. https://doi.org/10.1016/j.conbuildmat.2016.11.088.

[132] G.C. Hoff, Guide for the use of low density concrete in civil works projects, Geotechnical and Structures Laboratory (U.S.), Washington, 2002. http://hdl.handle.net/11681/10540.

[133] P.C. Lau, D.C.L. Teo, M.A. Mannan, Mechanical, durability and microstructure properties of lightweight concrete using aggregate made from lime-treated sewage sludge and palm oil fuel ash, Constr. Build. Mater. 176 (2018) 24–34. https://doi.org/10.1016/j.conbuildmat.2018.04.179.

[134] T.Y. Lo, H. Cui, S.A. Memon, T. Noguchi, Manufacturing of sintered lightweight aggregate using high-carbon fly ash and its effect on the mechanical properties and microstructure of concrete, J. Clean. Prod. 112 (2016) 753–762. https://doi.org/10.1016/j.jclepro.2015.07.001.

[135] X.F. Gao, Y.T. Lo, C.M. Tam, Investigation of micro-cracks and microstructure of high performance lightweight aggregate concrete, 37 (2002) 485–489.

[136] A. Sayari, S. Hamoudi, Y. Yang, Applications of pore-expanded mesoporous silica. 1. Removal of heavy metal cations and organic pollutants from wastewater, Chem. Mater. 17 (2005) 212–216. https://doi.org/10.1021/cm048393e.

[137] H.W. Lee, H.J. Cho, J.H. Yim, J.M. Kim, J.K. Jeon, J.M. Sohn, K.S. Yoo, S.S. Kim, Y.K. Park, Removal of Cu(II)-ion over amine-functionalized mesoporous silica materials, J. Ind. Eng. Chem. 17 (2011) 504–509. https://doi.org/10.1016/j.jiec.2010.09.022.

[138] Y. Xue, H. Hou, S. Zhu, Characteristics and mechanisms of phosphate adsorption onto basic oxygen furnace slag, J. Hazard. Mater. 162 (2009) 973–980. https://doi.org/10.1016/j.jhazmat.2008.05.131.

[139] A. Mehmood, M.S. Akhtar, M. Imran, S. Rukh, Soil apatite loss rate across different parent materials, Geoderma. 310 (2018) 218–229. https://doi.org/10.1016/j.geoderma.2017.09.036.

[140] Dutch Soil Quality Regulation, Maximum composition and emission values for building materials, Regeling Bodemkwaliteit. (2015). http://wetten.overheid.nl/BWBR0023085/2015-07-01#B.

[141] M.A. Imteaz, A. Arulrajah, S. Horpibulsuk, A. Ahsan, Environmental suitability and carbon footprint savings of recycled tyre crumbs for road applications, Int. J. Environ. Res. 12 (2018) 693–702. https://doi.org/10.1007/s41742-018-0126-7.

[142] T.A. Kua, M.A. Imteaz, A. Arulrajah, S. Horpibulsuk, Environmental and economic viability of Alkali Activated Material (AAM) comprising slag, fly ash and spent coffee ground, Int. J. Sustain. Eng. 12 (2019) 223–232. https://doi.org/10.1080/19397038.2018.1492043.

[143] X. Gao, Q.L. Yu, Effects of an eco-silica source based activator on functional alkali activated lightweight composites, Constr. Build. Mater. 215 (2019) 686–695. https://doi.org/10.1016/j.conbuildmat.2019.04.251.

[144] G. Liu, K. Schollbach, S. van der Laan, P. Tang, M.V.A. Florea, H.J.H. Brouwers, Recycling and utilization of high volume converter steel slag into CO2 activated mortars – The role of slag particle size, Resour. Conserv. Recycl. 160 (2020) 104883. https://doi.org/10.1016/j.resconrec.2020.104883.

[145] P.S. Humbert, J. Castro-Gomes, CO2 activated steel slag-based materials: A review, J. Clean. Prod. 208 (2019) 448–457. https://doi.org/10.1016/j.jclepro.2018.10.058.

[146] L. Barcelo, J. Kline, G. Walenta, E. Gartner, Cement and carbon emissions, Mater. Struct. Constr. 47 (2014) 1055–1065. https://doi.org/10.1617/s11527-013-0114-5.

[147] P. Bartocci, G. Bidini, P. Saputo, F. Fantozzi, Biochar pellet carbon footprint, Chem. Eng. Trans. 50 (2016) 217–222. https://doi.org/10.3303/CET1650037.

[148] R.F.W. Boarder, P.L. Owens, J.M. Khatib, Sustainability of Construction Materials: 10-The sustainability

of lightweight aggregates manufactured from clay wastes for reducing the carbon footprint of structural and foundation concrete, Second, Elsevier Ltd., (2016). https://doi.org/10.1016/b978-0-08-100370-1.00010-x.

[149] W. Zappa, Pilot-scale experimental work on the production of precipitated calcium carbonate (PCC) from steel slag for CO_2 fixation, Aalto University, (2014).

[150] S. Zhuang, Q. Wang, Inhibition mechanisms of steel slag on the early-age hydration of cement, Cem. Concr. Res. 140 (2021) 106283. https://doi.org/10.1016/j.cemconres.2020.106283.

[151] X. Ma, X. Hao, X. Chen, Z. Gao, chao D. Wei, B. Zhou, Study on biochar properties analysis with scanning electron microscope-energy dispersive X-ray spectroscopy (SEM-EDX), Spectrosc. Spectr. Anal. 36 (2016) 1670–1673.

[152] S. Kourounis, S. Tsivilis, P.E. Tsakiridis, G.D. Papadimitriou, Z. Tsibouki, Properties and hydration of blended cements with steelmaking slag, Cem. Concr. Res. 37 (2007) 815–822. https://doi.org/10.1016/j.cemconres.2007.03.008.

[153] T. Le Ngoc Huyen, M. Queneudec T'Kint, C. Remond, B. Chabbert, R.M. Dheilly, Saccharification of Miscanthus x giganteus, incorporation of lignocellulosic by-product in cementitious matrix, Comptes Rendus - Biol. 334 (2011) 837.e1-837.e11. https://doi.org/10.1016/j.crvi.2011.07.008.

[154] Y. Ling, K. Wang, W. Li, G. Shi, P. Lu, Effect of slag on the mechanical properties and bond strength of fly ash-based engineered geopolymer composites, Compos. Part B Eng. 164 (2019) 747–757. https://doi.org/10.1016/j.compositesb.2019.01.092.

[155] S.D.C. Gomes, J.L. Zhou, W. Li, F. Qu, Recycling of raw water treatment sludge in cementitious composites: effects on heat evolution, compressive strength and microstructure, Resour. Conserv. Recycl. 161 (2020) 104970. https://doi.org/10.1016/j.resconrec.2020.104970.

[156] F. Wu, C. Liu, W. Sun, Y. Ma, L. Zhang, Effect of peach shell as lightweight aggregate on mechanics and creep properties of concrete, Eur. J. Environ. Civ. Eng. 0 (2019) 1–21. https://doi.org/10.1080/19648189.2018.1515667.

[157] P. Shafigh, H. Mahmud, M.Z. Jumaat, Effect of steel fiber on the mechanical properties of oil palm shell lightweight concrete, Mater. Des. 32 (2011) 3926–3932. https://doi.org/10.1016/j.matdes.2011.02.055.

[158] A. Akkaoui, S. Caré, M. Vandamme, Experimental and micromechanical analysis of the elastic properties of wood-aggregate concrete, Constr. Build. Mater. 134 (2017) 346–357. https://doi.org/10.1016/j.conbuildmat.2016.12.084.

[159] P. Shafigh, H. Ghafari, H. Bin Mahmud, M.Z. Jumaat, A comparison study of the mechanical properties and drying shrinkage of oil palm shell and expanded clay lightweight aggregate concretes, Mater. Des. 60 (2014) 320–327. https://doi.org/10.1016/j.matdes.2014.04.001.

[160] K. Ghavami, Bamboo as reinforcement in structural concrete elements, Cem. Concr. Compos. 27 (2005) 637–649. https://doi.org/10.1016/j.cemconcomp.2004.06.002.

[161] R. Ylmén, U. Jäglid, B.M. Steenari, I. Panas, Early hydration and setting of Portland cement monitored by IR, SEM and Vicat techniques, Cem. Concr. Res. 39 (2009) 433–439. https://doi.org/10.1016/j.cemconres.2009.01.017.

[162] B. Yilmaz, A. Olgun, Studies on cement and mortar containing low-calcium fly ash, limestone, and dolomitic limestone, Cem. Concr. Compos. 30 (2008) 194–201. https://doi.org/10.1016/j.cemconcomp.2007.07.002.

[163] D. Vaičiukynienė, G. Skripkiūnas, M. Daukšys, V. Sasnauskas, Cement hydration with zeolite-based additive, Chemija. 24 (2013) 271–278.

[164] J. Li, Q. Yu, J. Wei, T. Zhang, Structural characteristics and hydration kinetics of modified steel slag, Cem. Concr. Res. 41 (2011) 324–329. https://doi.org/10.1016/j.cemconres.2010.11.018.

[165] M.A. Trezza, A.E. Lavat, Analysis of the system 3CaO·Al2O3-CaSO4· 2H2O-CaCO3-H2O by FT-IR spectroscopy, Cem. Concr. Res. 31 (2001) 869–872. https://doi.org/10.1016/S0008-8846(01)00502-6.

[166] I. García Lodeiro, D.E. Macphee, A. Palomo, A. Fernández-Jiménez, Effect of alkalis on fresh C-S-H gels. FTIR analysis, Cem. Concr. Res. 39 (2009) 147–153. https://doi.org/10.1016/j.cemconres.2009.01.003.

[167] M.A.M. Ariffin, M.A.R. Bhutta, M.W. Hussin, M. Mohd Tahir, N. Aziah, Sulfuric acid resistance of blended ash geopolymer concrete, Constr. Build. Mater. 43 (2013) 80–86. https://doi.org/10.1016/j.conbuildmat.2013.01.018.

[168] R.J. Galán-Arboledas, J. Álvarez de Diego, M. Dondi, S. Bueno, Energy, environmental and technical assessment for the incorporation of EAF stainless steel slag in ceramic building materials, J. Clean. Prod. 142 (2017) 1778–1788. https://doi.org/10.1016/j.jclepro.2016.11.110.

[169] S. Duan, H. Liao, F. Cheng, H. Song, H. Yang, Investigation into the synergistic effects in hydrated gelling systems containing fly ash, desulfurization gypsum and steel slag, Constr. Build. Mater. 187 (2018) 1113–1120. https://doi.org/10.1016/j.conbuildmat.2018.07.241.

[170] Q. Wang, M. Shi, J. Yang, Influence of classified steel slag with particle sizes smaller than 20 μm on the properties of cement and concrete, Constr. Build. Mater. 123 (2016) 601–610. https://doi.org/10.1016/j.conbuildmat.2016.07.042.

[171] C.F. Chang, J.W. Chen, The experimental investigation of concrete carbonation depth, Cem. Concr. Res. 36 (2006) 1760–1767. https://doi.org/10.1016/j.cemconres.2004.07.025.

[172] K. Ćosić, L. Korat, V. Ducman, I. Netinger, Influence of aggregate type and size on properties of pervious concrete, Constr. Build. Mater. 78 (2015) 69–76. https://doi.org/10.1016/j.conbuildmat.2014.12.073.

[173] M. Carsana, F. Tittarelli, L. Bertolini, Use of no-fines concrete as a building material: Strength, durability properties and corrosion protection of embedded steel, Cem. Concr. Res. 48 (2013) 64–73. https://doi.org/10.1016/j.cemconres.2013.02.006.

[174] T.K. Ostrom, A.P. Davis, Evaluation of an enhanced treatment media and permeable pavement base to remove stormwater nitrogen, phosphorus, and metals under simulated rainfall, Water Res. 166 (2019) 115071. https://doi.org/10.1016/j.watres.2019.115071.

[175] S. Harada, M. Yanbe, Adsorption by and artificial release of zinc and lead from porous concrete for recycling of adsorbed zinc and lead and of porous concrete to reduce urban non-point heavy metal runoff, Chemosphere, 197 (2018) 451–456. https://doi.org/10.1016/j.chemosphere.2018.01.044.

[176] R.R. Holmes, M.L. Hart, J.T. Kevern, Heavy metal removal capacity of individual components of permeable reactive concrete, J. Contam. Hydrol. 196 (2017) 52–61. https://doi.org/10.1016/j.jconhyd.2016.12.005.

[177] S. Kang, J. Lee, S.M. Park, D.S. Alessi, K. Baek, Adsorption characteristics of cesium onto calcium-silicate-hydrate in concrete powder and block, Chemosphere, 259 (2020) 127494. https://doi.org/10.1016/j.chemosphere.2020.127494.

[178] L. Liu, J. Ji, Y. Guo, J. Chen, Use of ecological concrete for nutrient removal in coastal sediment and its effects on sediment microbial communities, Mar. Pollut. Bull. 162 (2021) 111911. https://doi.org/10.1016/j.marpolbul.2020.111911.

[179] A.R. Lori, A. Hassani, R. Sedghi, Investigating the mechanical and hydraulic characteristics of pervious concrete containing copper slag as coarse aggregate, Constr. Build. Mater. 197 (2019) 130–142. https://doi.org/10.1016/j.conbuildmat.2018.11.230.

[180] X. Liang, S. Cui, H. Li, A. Abdelhady, H. Wang, H. Zhou, Removal effect on stormwater runoff pollution of porous concrete treated with nanometer titanium dioxide, Transp. Res. Part D Transp. Environ. 73 (2019) 34–45. https://doi.org/10.1016/j.trd.2019.06.001.

[181] J. Yang, G. Jiang, Experimental study on properties of pervious concrete pavement materials, Cem. Concr. Res. 33 (2003) 381–386. https://doi.org/10.1016/S0008-8846(02)00966-3.

[182] M. Grazia, L. F. M. Sanchez, R. C. O. Romano, R. G. Pileggi, Investigation of the use of continuous particle packing models (PPMs) on the fresh and hardened properties of low-cement concrete (LCC) systems, Constr. Build. Mater. 195 (2019) 524–536. https://doi.org/10.1016/j.conbuildmat.2018.11.051.

[183] S.H. Chu, C.S. Poon, C.S. Lam, L. Li, Effect of natural and recycled aggregate packing on properties of concrete blocks, Constr. Build. Mater. 278 (2021) 122247. https://doi.org/10.1016/j.conbuildmat.2021.122247.

[184] D.H. Nguyen, M. Boutouil, N. Sebaibi, F. Baraud, L. Leleyter, Durability of pervious concrete using crushed seashells, Constr. Build. Mater. (2017). https://doi.org/10.1016/j.conbuildmat.2016.12.219.

[185] M.S. Sumanasooriya, N. Neithalath, Pore structure features of pervious concretes proportioned for desired porosities and their performance prediction, Cem. Concr. Compos. 33 (2011) 778–787. https://doi.org/10.1016/j.cemconcomp.2011.06.002.

[186] C. Lian, Y. Zhuge, Optimum mix design of enhanced permeable concrete - An experimental investigation, Constr. Build. Mater. 24 (2010) 2664–2671. https://doi.org/10.1016/j.conbuildmat.2010.04.057.

[187] M.S. Sumanasooriya, D.P. Bentz, N. Neithalath, Planar image-based reconstruction of pervious concrete pore structure and permeability prediction, ACI Mater. J. 107 (2010) 413–421.

[188] Z. Wang, D. Zou, T. Liu, A. Zhou, M. Shen, A novel method to predict the mesostructure and performance of pervious concrete, Constr. Build. Mater. 263 (2020) 120117. https://doi.org/10.1016/j.conbuildmat.2020.120117.

[189] N.S. Klein, L.A. Lenz, W. Mazer, Influence of the granular skeleton packing density on the static elastic modulus of conventional concretes, Constr. Build. Mater. 242 (2020) 118086. https://doi.org/10.1016/j.conbuildmat.2020.118086.

[190] W. Yeih, T.C. Fu, J.J. Chang, R. Huang, Properties of pervious concrete made with air-cooling electric arc furnace slag as aggregates, Constr. Build. Mater. 93 (2015) 737–745. https://doi.org/10.1016/j.conbuildmat.2015.05.104.

[191] S. Wang, G. Zhang, B. Wang, M. Wu, Mechanical strengths and durability properties of pervious concretes with blended steel slag and natural aggregate, J. Clean. Prod. 271 (2020) 122590. https://doi.org/10.1016/j.jclepro.2020.122590.

[192] T. Liu, Z. Wang, D. Zou, A. Zhou, J. Du, Strength enhancement of recycled aggregate pervious concrete using a cement paste redistribution method, Cem. Concr. Res. 122 (2019) 72–82. https://doi.org/10.1016/j.cemconres.2019.05.004.

[193] P. Shen, H. Zheng, S. Liu, J.X. Lu, C.S. Poon, Development of high-strength pervious concrete incorporated with high percentages of waste glass, Cem. Concr. Compos. 114 (2020) 103790. https://doi.org/10.1016/j.cemconcomp.2020.103790.

[194] P. Mehrabi, M. Shariati, K. Kabirifar, M. Jarrah, H. Rasekh, N.T. Trung, A. Shariati, S. Jahandari, Effect of pumice powder and nano-clay on the strength and permeability of fiber-reinforced pervious concrete incorporating recycled concrete aggregate, Constr. Build. Mater. 287 (2021) 122652. https://doi.org/10.1016/j.conbuildmat.2021.122652.

[195] G. Xu, W. Shen, X. Huo, Z. Yang, J. Wang, W. Zhang, X. Ji, Investigation on the properties of porous concrete as road base material, Constr. Build. Mater. 158 (2018) 141–148. https://doi.org/10.1016/j.conbuildmat.2017.09.151.

[196] S.B. Park, M. Tia, An experimental study on the water-purification properties of porous concrete, Cem. Concr. Res. 34 (2004) 177–184. https://doi.org/10.1016/S0008-8846(03)00223-0.

[197] A.K. Chandrappa, K.P. Biligiri, Pervious concrete as a sustainable pavement material-Research findings and future prospects: A state-of-the-art review, Constr. Build. Mater. 111 (2016) 262–274. https://doi.org/10.1016/j.conbuildmat.2016.02.054.

[198] Z. Ma, R. Xue, J. shan Li, Y. Zhao, Q. Xue, Z. Chen, Q. Wang, C.S. Poon, Use of thermally modified waste concrete powder for removal of Pb (II) from wastewater: Effects and mechanism, Environ. Pollut. 277 (2021) 116776. https://doi.org/10.1016/j.envpol.2021.116776.

[199] D.H. Nguyen, M. Boutouil, N. Sebaibi, F. Baraud, L. Leleyter, Durability of pervious concrete using crushed seashells, Constr. Build. Mater. 135 (2017) 137–150. https://doi.org/10.1016/j.conbuildmat.2016.12.219.

[200] M.A. González-Ortega, S.H.P. Cavalaro, G. Rodríguez de Sensale, A. Aguado, Durability of concrete with electric arc furnace slag aggregate, Constr. Build. Mater. 217 (2019) 543–556. https://doi.org/10.1016/j.conbuildmat.2019.05.082.

[201] B. Pang, Z. Zhou, X. Cheng, P. Du, H. Xu, ITZ properties of concrete with carbonated steel slag aggregate in salty freeze-thaw environment, Constr. Build. Mater. 114 (2016) 162–171. https://doi.org/10.1016/j.conbuildmat.2016.03.168.

[202] F. Gong, S. Jacobsen, Modeling of water transport in highly saturated concrete with wet surface during freeze/thaw, Cem. Concr. Res. 115 (2019) 294–307. https://doi.org/10.1016/j.cemconres.2018.08.013.

[203] O. Coussy, P.J.M. Monteiro, Poroelastic model for concrete exposed to freezing temperatures, Cem. Concr. Res. 38 (2008) 40–48. https://doi.org/10.1016/j.cemconres.2007.06.006.

[204] Z. Sun, G.W. Scherer, Effect of air voids on salt scaling and internal freezing, Cem. Concr. Res. 40 (2010) 260–270. https://doi.org/10.1016/j.cemconres.2009.09.027.

[205] M. Sun, D. Xin, C. Zou, Damage evolution and plasticity development of concrete materials subjected to freeze-thaw during the load process, Mech. Mater. 139 (2019). https://doi.org/10.1016/j.mechmat.2019.103192.

[206] M. Vancura, K. MacDonald, L. Khazanovich, Microscopic analysis of paste and aggregate distresses in pervious concrete in a wet, hard freeze climate, Cem. Concr. Compos. 33 (2011) 1080–1085. https://doi.org/10.1016/j.cemconcomp.2011.05.011.

[207] P.P. Li, Y.Y.Y. Cao, M.J.C. Sluijsmans, H.J.H. Brouwers, Q. Yu, Synergistic effect of steel fibres and coarse aggregates on impact properties of ultra-high performance fibre reinforced concrete, Cem. Concr. Compos. 115 (2021). https://doi.org/10.1016/j.cemconcomp.2020.103866.

[208] G. Hüsken, H.J.H. Brouwers, A new mix design concept for earth-moist concrete: A theoretical and experimental study, Cem. Concr. Res. 38 (2008) 1246–1259. https://doi.org/10.1016/j.cemconres.2008.04.002.

[209] R. Yu, P. Spiesz, H.J.H. Brouwers, Development of an eco-friendly Ultra-High Performance Concrete (UHPC) with efficient cement and mineral admixtures uses, Cem. Concr. Compos. 55 (2015) 383–394. https://doi.org/10.1016/j.cemconcomp.2014.09.024.

[210] R. Yu, P. Spiesz, H.J.H. Brouwers, Mix design and properties assessment of Ultra-High Performance Fibre Reinforced Concrete (UHPFRC), Cem. Concr. Res. 56 (2014) 29–39. https://doi.org/10.1016/j.cemconres.2013.11.002.

[211] H.J.H. Brouwers, H.J. Radix, Self-compacting concrete: Theoretical and experimental study, Cem. Concr. Res. 35 (2005) 2116–2136. https://doi.org/10.1016/j.cemconres.2005.06.002.

[212] Q.L. Yu, P. Spiesz, H.J.H. Brouwers, Development of cement-based lightweight composites – Part 1 : Mix design methodology and hardened properties, Cem. Concr. Compos. 44 (2013) 17–29. https://doi.org/10.1016/j.cemconcomp.2013.03.030.

[213] H. Karimi, H.J.H. Brouwers, A particle packing method for pumpable low shrinkage flowing concrete, ACI Mater. J. (2023) 81–92. https://doi.org/10.14359/51738685.

[214] X. Nan, Z. Wang, J. Hou, Y. Tong, B. Li, Clogging mechanism of pervious concrete: From experiments to CFD-DEM simulations, Constr. Build. Mater. 270 (2021) 1–11. https://doi.org/10.1016/j.conbuildmat.2020.121422.

[215] H. Yang, F. Wei, K. Hu, Determination of the maximum packing fraction for calculating slurry viscosity of debris flow, Mt. Res. 36 (2018) 382–390.

[216] D. Liu, H. Zhu, K. Wu, F. Wang, X. Zhao, Q. Liao, Understanding the effect of particle size of waste concrete powder on phosphorus removal efficiency, Constr. Build. Mater. 236 (2020) 117526. https://doi.org/10.1016/j.conbuildmat.2019.117526.

[217] V. Arenas-Montaño, O. Fenton, B. Moore, M.G. Healy, Evaluation of the fertiliser replacement value of phosphorus-saturated filter media, J. Clean. Prod. 291 (2021) 125943. https://doi.org/10.1016/j.jclepro.2021.125943.

[218] K. Haarstad, J. Bavor, Phosphorus Recycling from Wastes, J. Environ. Prot. (Irvine,. Calif). 08 (2017) 831–843. https://doi.org/10.4236/jep.2017.88052.

[219] G.S. dos Reis, P.S. Thue, B.G. Cazacliu, E.C. Lima, C.H. Sampaio, M. Quattrone, E. Ovsyannikova, A. Kruse, G.L. Dotto, Effect of concrete carbonation on phosphate removal through adsorption process and its potential application as fertilizer, J. Clean. Prod. 256 (2020) 120416. https://doi.org/10.1016/j.jclepro.2020.120416.

[220] D. Liu, X. Quan, H. Zhu, Q. Huang, L. Zhou, Evaluation of modified waste concrete powder used as a novel phosphorus remover, J. Clean. Prod. 257 (2020) 120646. https://doi.org/10.1016/j.jclepro.2020.120646.

[221] Y. Tsunashima, A. Iizuka, J. Akimoto, T. Hongo, A. Yamasaki, Preparation of sorbents containing ettringite phase from concrete sludge and their performance in removing borate and fluoride ions from waste water, Chem. Eng. J. 200–202 (2012) 338–343. https://doi.org/10.1016/j.cej.2012.06.064.

[222] M. Kayhanian, D. Anderson, J.T. Harvey, D. Jones, B. Muhunthan, Permeability measurement and scan imaging to assess clogging of pervious concrete pavements in parking lots, J. Environ. Manage. 95 (2012) 114–123. https://doi.org/10.1016/j.jenvman.2011.09.021.

[223] R. Zhong, K. Wille, Linking pore system characteristics to the compressive behavior of pervious concrete, Cem. Concr. Compos. 70 (2016) 130–138. https://doi.org/10.1016/j.cemconcomp.2016.03.016.

[224] W. Ten Kuo, C.C. Liu, D.S. Su, Use of washed municipal solid waste incinerator bottom ash in pervious concrete, Cem. Concr. Compos. 37 (2013) 328–335. https://doi.org/10.1016/j.cemconcomp.2013.01.001.

[225] B. Huang, H. Wu, X. Shu, E.G. Burdette, Laboratory evaluation of permeability and strength of polymer-modified pervious concrete, Constr. Build. Mater. 24 (2010) 818–823. https://doi.org/10.1016/j.conbuildmat.2009.10.025.

[226] E. Güneyisi, M. Gesoğlu, Q. Kareem, S. İpek, Effect of different substitution of natural aggregate by recycled aggregate on performance characteristics of pervious concrete, Mater. Struct. Constr. 49 (2016) 521–536. https://doi.org/10.1617/s11527-014-0517-y.

[227] S. Hesami, S. Ahmadi, M. Nematzadeh, Effects of rice husk ash and fiber on mechanical properties of pervious concrete pavement, Constr. Build. Mater. 53 (2014) 680–691. https://doi.org/10.1016/j.conbuildmat.2013.11.070.

[228] Y. Zaetang, A. Wongsa, V. Sata, P. Chindaprasirt, Use of lightweight aggregates in pervious concrete, Constr. Build. Mater. 48 (2013) 585–591. https://doi.org/10.1016/j.conbuildmat.2013.07.077.

[229] P. Shen, J.X. Lu, H. Zheng, S. Liu, C. Sun Poon, Conceptual design and performance evaluation of high

strength pervious concrete, Constr. Build. Mater. 269 (2021) 121342. https://doi.org/10.1016/j.conbuildmat.2020.121342.

[230] M. Hermassi, C. Valderrama, J. Dosta, J.L. Cortina, N.H. Batis, Evaluation of hydroxyapatite crystallization in a batch reactor for the valorization of alkaline phosphate concentrates from wastewater treatment plants using calcium chloride, Chem. Eng. J. 267 (2015) 142–152. https://doi.org/10.1016/j.cej.2014.12.079.

[231] E. Boix, F. Georgi, P. Navard, Influence of alkali and Si-based treatments on the physical and chemical characteristics of miscanthus stem fragments, Ind. Crops Prod. 91 (2016) 6–14. https://doi.org/10.1016/j.indcrop.2016.06.030.

[232] M.R. Ahmad, B. Chen, S.F. Ali Shah, Mechanical and microstructural characterization of bio-concrete prepared with optimized alternative green binders, Constr. Build. Mater. 281 (2021) 122533. https://doi.org/10.1016/j.conbuildmat.2021.122533.

[233] G.C.H. Doudart de la Grée, Q.L. Yu, H.J.H. Brouwers, Assessing the effect of CaSO4 content on the hydration kinetics, microstructure and mechanical properties of cements containing sugars, Constr. Build. Mater. 143 (2017) 48–60. https://doi.org/10.1016/j.conbuildmat.2017.03.067.

[234] J.R. Leslie, W.J. Cheesman, An ultrasonic method of studying deterioration and cracking in concrete structures, J. Am. Concr. Inst. 21 (1949) 17–36.

[235] M. Yew, M. Yew, L.H. Saw, S. Lim, J.H. Beh, T. Ng, Enhancement of durability properties and drying shrinkage of heat-treated oil palm shell species high-strength lightweight concrete, Nanosci. Nanotechnol. 2 (2018) 1–11. https://doi.org/10.18063/nn.v2i1.380.

[236] S. Gupta, H.W. Kua, S.D. Pang, Biochar-mortar composite: Manufacturing, evaluation of physical properties and economic viability, Constr. Build. Mater. 167 (2018) 874–889. https://doi.org/10.1016/j.conbuildmat.2018.02.104.

[237] M. Li, S. Si, B. Hao, Y. Zha, C. Wan, S. Hong, Y. Kang, J. Jia, J. Zhang, M. Li, C. Zhao, Y. Tu, S. Zhou, L. Peng, Mild alkali-pretreatment effectively extracts guaiacyl-rich lignin for high lignocellulose digestibility coupled with largely diminishing yeast fermentation inhibitors in Miscanthus, Bioresour. Technol. 169 (2014) 447–454. https://doi.org/10.1016/j.biortech.2014.07.017.

[238] J. Pastor-Villegas, J.F. Pastor-Valle, J.M.M. Rodríguez, M.G. García, Study of commercial wood charcoals for the preparation of carbon adsorbents, J. Anal. Appl. Pyrolysis. 76 (2006) 103–108. https://doi.org/10.1016/j.jaap.2005.08.002.

Abbreviations

A_e	Adsorption removal capacity (mg/g)
A_t	Amount of P adsorbed by the adsorbent at any time (mg/L)
AFt	Alumina, ferric oxide, trisulpate
AD	Adsorptive aggregate
B	Basalt
BET	Brunauer, Emmett and Teller
BJH	Barrett-Joyner-Halenda
C	P concentration in the solution (mg/L)
C_0	Initial P concentration (mg/L)
C_e	P concentration in the solution at equilibrium (mg/L)
CH	Calcium hydroxide
C_2S	Dicalcium silicate
C_3S	Tricalcium silicate
C-S-H	Calcium silicate hydrate
CHM	Mixture containing cement and heat-treated miscanthus
CMP	Mixture containing cement and miscanthus powder
EDX	Energy-dispersive X-ray spectroscopy
ES	Expanded silicate
FTIR	Fourier-transform infrared spectroscopy
HM	Heat-treated miscanthus
HM0.5	Heat-treated miscanthus with 0.5 wt.%
HM1	Heat-treated miscanthus with 1.0 wt.%
HM3	Heat-treated miscanthus with 3 wt.%
IC	Ion chromatography
ICP-AES	Inductively Coupled Plasma Atomic Emission Spectroscopy
ITZ	Interfacial transition zone
LOI	Loss on ignition

L/S	Liquid to solid
LWAC	Lightweight aggregate concrete
K_1	Rate constant of Lagergren pseudo-first-order kinetic models
K_2	Rate constant of Lagergren pseudo-second-order kinetic models
K_L	Adsorption constant in Langmuir isotherm
K_F	Constant of Freundlich isotherm
LWAC	Lightweight aggregate concrete
M	Miscanthus (*x* giganteus)
M0	Miscanthus with 0 wt.%
M3	Miscanthus with 3 wt.%
M-0	Untreated miscanthus
M-2	Heat-treated miscanthus for 2 hours
M-3	Heat-treated miscanthus for 3 hours
M-4	Heat-treated miscanthus for 4 hours
M-LF	Miscanthus with 2-3 cm long fibre
M-SF	Miscanthus with 0.4-1.5 cm short fibre
M-P	Miscanthus powder
N	Nitrogen
n	Heterogeneity factor of Freundlich isotherm
Q_m	Maximum adsorption capacity in Langmuir isotherm
P	Phosphate
P_d	P-desorption fraction (%)
P_R	P-removal fraction (%)
PS	Peach shell
q	P-adsorption amount (mg/g)
q_d	P-desorption amount (mg/g)
RM	Raw miscanthus
SS	Steel slag
SS5	Steel slag with 5 wt.%

SS10	Steel slag with 10 wt.%
SS25	Steel slag with 25 wt.%
SS50	Steel slag with 50 wt.%
SS75	Steel slag with 75 wt.%
SEM	Scanning Electron Microscope
SEM-EDS	Scanning Electron Microscope Energy Dispersive Spectrometer
T_P	P content in the P-saturated sample
TG	Thermal gravimetric
V	Volume
Vol.%	Volume fraction
Wt.%	Weight fraction
w/c	Water-to-cement ratio
XRD	X-ray diffraction
XRF	X-ray fluorescence

List of publications

Peer-reviewed journal papers

1. **F. Wu**, Q.L. Yu, X.Q. Chen. Unleashing the potential of bio-based concrete: Investigating its long-term mechanical strength and drying shrinkage in real climatic environments, Cement and Concrete Composites, 143, 105237, 2023.
2. **F. Wu**, Q.L. Yu, X.Q. Chen. Effects of steel fibre type and dosage on abrasion resistance of concrete against debris flow, Cement and Concrete Composites, 134, 104776, 2022.
3. **F. Wu**, Q.L. Yu, H.J.H. Brouwers. Mechanical, absorptive and freeze-thaw properties of pervious concrete applying a bimodal aggregate packing model. Construction and Building Materials, 333, 127445, 2022.
4. **F. Wu**, Q.L. Yu, H.J.H. Brouwers, F. Gauvin. Effects of treated miscanthus on performance of bio-based cement mortar. Journal of Sustainable Cement-Based Materials, 4, 12, 2022.
5. **F. Wu**, Q.L. Yu, H.J.H. Brouwers. Long-term performance of bio-based miscanthus mortar. Construction and Building Materials, 324, 126703, 2022.
6. **F. Wu**, Q.L. Yu, F. Gauvin, H.J.H. Brouwers, C.W. Liu. Phosphorus removal from aqueous solutions by adsorptive concrete aggregates. Journal of Cleaner Production, 278, 123933, 2021.
7. **F. Wu**, Q.L. Yu, F. Gauvin, H.J.H. Brouwers. A facile manufacture of highly adsorptive aggregates using steel slag and porous expanded silica for phosphorus removal. Resources, Conservation and Recycling, 66, 105238, 2021.
8. **F. Wu**, Q.L. Yu, H.J.H. Brouwers. Phosphorus removal enhancement by porous adsorptive mortar using miscanthus and steel slag for highly adsorptive concrete. Construction and Building Materials, 295, 123686, 2021.
9. Y.X. Chen, **F. Wu**, Q.L. Yu, H.J.H. Brouwers. Bio-based ultra-lightweight concrete applying Miscanthus fibers: Acoustic absorption and thermal insulation. Cement and Concrete Composites, 114, 103829, 2020.
10. **F. Wu**, Q.L. Yu, C.W. Liu, H.J.H. Brouwers, L.F. Wang, D.F. Liu. Effect of fibre type and content on performance of bio-based concrete containing heat-treated apricot shell. Materials and Structures, 53, 137, 2020.
11. **F. Wu**, Q.L. Yu, C.W. Liu, H.J.H. Brouwers. Effect of surface treatment of apricot shell on the performance of lightweight bio-concrete. Construction and Building Materials, 229, 116859, 2019.
12. **F. Wu**, Q.L. Yu, H.J.H. Brouwers. Improvement of phosphorus removal capacity of pervious concrete using highly adsorptive aggregates (Manuscript).

13. **F. Wu**, X.Q. Chen, Q.L. Yu, H.J.H. Brouwers. Water and fertilizer retention enhancement of sustainable bio-based aggregate concrete for plant growth (Manuscript).
14. **F. Wu**, X.Q. Chen, Q.L. Yu, H.J.H. Brouwers. Application of miscanthus to enhance plant growth adaptability of bio-based vegetal concrete (Manuscript).

Conference proceedings

1. **F. Wu**, Q.L. Yu, H.J.H Brouwers. Phosphorus removal improvement of porous concrete using highly adsorptive aggregates. The 3rd International Conference of Sustainable Building Materials (ICSBM 2023), 25-27 September, Wuhan, China. 2023.
2. **F. Wu**, Q.L. Yu, H.J.H Brouwers. Effects of aggregate type on phosphorus removal of pervious concrete. The 7th International Conference: Non-traditional Cement and Concrete (NTCC 2023), 25-28 June, Brno, Czech Republic. 2023.
3. **F. Wu**, Q.L. Yu, C.W. Liu. Physico-mechanical and adsorption performance of highly adsorptive concrete. The 4th Academic and Technology Exchange Conference of China Solid Waste Treatment and Ecological Materials, 15-17 October, Wuhan, China. 2021.
4. **F. Wu**, C.W. Liu, L.W. Zhang, Y.H. Lu, Q.L. Yu. Use of peach shell as lightweight aggregate in pervious concrete. The 2nd International Conference of Sustainable Building Materials (ICSBM 2019), 12-15 August, Eindhoven, The Netherlands. 2019.

Curriculum vitae

Fan Wu was born on February 5, 1990, in Chongqing, China. He started his academic journey at Sichuan University (SCU), completing his Bachelor`s degree in Agricultural Water Conservancy Engineering in June 2013. He pursued further studies in Geotechnical Engineering at Chongqing Jiaotong University (CQJTU), obtaining his Master`s degree in June 2016, supervised by Prof. Hongkai Chen and Prof. Hongmei Tang. His Master`s thesis related to “Tree-based techniques for vegetation restoration in harsh geological environments”. In September 2016, He returned to Sichuan University (SCU) to pursue a doctorate, focusing on “physico-mechanical properties and creep characteristics of sustainable bio-based concrete”, supervised by Prof. Changwu Liu. He was awarded a scholarship from the China Scholarship Council (CSC) in October 2018, supporting his PhD studies at Eindhoven University of Technology (TU/e), the Netherlands, supervised by Prof. H.J.H. Brouwers, Prof. Qingliang Yu, and Dr. F. Gauvin. Since December 2020, he has become an Assistant Researcher at the Institute of Mountain Hazards and Environment (IMHE), Chinese Academy of Sciences (CAS) in Chengdu, China, and working on sustainable concrete technology for civil protection structures in disaster risk reduction. His research interests include bio-based concrete, vegetal (ecological) concrete, and concrete durability technology.

Bouwstenen is een publicatiereeks
van de Faculteit Bouwkunde,
Technische Universiteit Eindhoven.
Zij presenteert resultaten van
onderzoek en andere activiteiten op
het vakgebied der Bouwkunde,
uitgevoerd in het kader van deze
Faculteit.

Bouwstenen en andere proefschriften van de
TU/e zijn online beschikbaar via:
https://research.tue.nl/

Reeds verschenen in de serie
Bouwstenen

nr 1
Elan: A Computer Model for Building Energy Design: Theory and Validation
Martin H. de Wit
H.H. Driessen
R.M.M. van der Velden

nr 2
Kwaliteit, Keuzevrijheid en Kosten: Evaluatie van Experiment Klarendal, Arnhem
J. Smeets
C. le Nobel
M. Broos
J. Frenken
A. v.d. Sanden

nr 3
Crooswijk: Van 'Bijzonder' naar 'Gewoon'
Vincent Smit
Kees Noort

nr 4
Staal in de Woningbouw
Edwin J.F. Delsing

nr 5
Mathematical Theory of Stressed Skin Action in Profiled Sheeting with Various Edge Conditions
Andre W.A.M.J. van den Bogaard

nr 6
Hoe Berekenbaar en Betrouwbaar is de Coëfficiënt k in x-ksigma en x-ks?
K.B. Lub
A.J. Bosch

nr 7
Het Typologisch Gereedschap: Een Verkennende Studie Omtrent Typologie en Omtrent de Aanpak van Typologisch Onderzoek
J.H. Luiten

nr 8
Informatievoorziening en Beheerprocessen
A. Nauta
Jos Smeets (red.)
Helga Fassbinder (projectleider)
Adrie Proveniers
J. v.d. Moosdijk

nr 9
Strukturering en Verwerking van Tijdgegevens voor de Uitvoering van Bouwwerken
ir. W.F. Schaefer
P.A. Erkelens

nr 10
Stedebouw en de Vorming van een Speciale Wetenschap
K. Doevendans

nr 11
Informatica en Ondersteuning van Ruimtelijke Besluitvorming
G.G. van der Meulen

nr 12
Staal in de Woningbouw, Korrosie-Bescherming van de Begane Grondvloer
Edwin J.F. Delsing

nr 13
Een Thermisch Model voor de Berekening van Staalplaatbetonvloeren onder Brandomstandigheden
A.F. Hamerlinck

nr 14
De Wijkgedachte in Nederland: Gemeenschapsstreven in een Stedebouwkundige Context
K. Doevendans
R. Stolzenburg

nr 15
Diaphragm Effect of Trapezoidally Profiled Steel Sheets: Experimental Research into the Influence of Force Application
Andre W.A.M.J. van den Bogaard

nr 16
Versterken met Spuit-Ferrocement: Het Mechanische Gedrag van met Spuit-Ferrocement Versterkte Gewapend Betonbalken
K.B. Lubir
M.C.G. van Wanroy

nr 17
De Tractaten van Jean Nicolas Louis Durand
G. van Zeyl

nr 18
Wonen onder een Plat Dak: Drie Opstellen over Enkele Vooronderstellingen van de Stedebouw
K. Doevendans

nr 19
Supporting Decision Making Processes: A Graphical and Interactive Analysis of Multivariate Data
W. Adams

nr 20
Self-Help Building Productivity: A Method for Improving House Building by Low-Income Groups Applied to Kenya 1990-2000
P. A. Erkelens

nr 21
De Verdeling van Woningen: Een Kwestie van Onderhandelen
Vincent Smit

nr 22
Flexibiliteit en Kosten in het Ontwerpproces: Een Besluitvormingondersteunend Model
M. Prins

nr 23
Spontane Nederzettingen Begeleid: Voorwaarden en Criteria in Sri Lanka
Po Hin Thung

nr 24
Fundamentals of the Design of Bamboo Structures
Oscar Arce-Villalobos

nr 25
Concepten van de Bouwkunde
M.F.Th. Bax (red.)
H.M.G.J. Trum (red.)

nr 26
Meaning of the Site
Xiaodong Li

nr 27
Het Woonmilieu op Begrip Gebracht: Een Speurtocht naar de Betekenis van het Begrip 'Woonmilieu'
Jaap Ketelaar

nr 28
Urban Environment in Developing Countries
editors: Peter A. Erkelens
George G. van der Meulen (red.)

nr 29
Stategische Plannen voor de Stad: Onderzoek en Planning in Drie Steden
prof.dr. H. Fassbinder (red.)
H. Rikhof (red.)

nr 30
Stedebouwkunde en Stadsbestuur
Piet Beekman

nr 31
De Architectuur van Djenné: Een Onderzoek naar de Historische Stad
P.C.M. Maas

nr 32
Conjoint Experiments and Retail Planning
Harmen Oppewal

nr 33
Strukturformen Indonesischer Bautechnik: Entwicklung Methodischer Grundlagen für eine 'Konstruktive Pattern Language' in Indonesien
Heinz Frick arch. SIA

nr 34
Styles of Architectural Designing: Empirical Research on Working Styles and Personality Dispositions
Anton P.M. van Bakel

nr 35
Conjoint Choice Models for Urban Tourism Planning and Marketing
Benedict Dellaert

nr 36
Stedelijke Planvorming als Co-Produktie
Helga Fassbinder (red.)

nr 37
Design Research in the Netherlands
editors: R.M. Oxman
M.F.Th. Bax
H.H. Achten

nr 38
Communication in the Building Industry
Bauke de Vries

nr 39
Optimaal Dimensioneren van Gelaste Plaatliggers
J.B.W. Stark
F. van Pelt
L.F.M. van Gorp
B.W.E.M. van Hove

nr 40
Huisvesting en Overwinning van Armoede
P.H. Thung
P. Beekman (red.)

nr 41
Urban Habitat: The Environment of Tomorrow
George G. van der Meulen
Peter A. Erkelens

nr 42
A Typology of Joints
John C.M. Olie

nr 43
Modeling Constraints-Based Choices for Leisure Mobility Planning
Marcus P. Stemerding

nr 44
Activity-Based Travel Demand Modeling
Dick Ettema

nr 45
Wind-Induced Pressure Fluctuations on Building Facades
Chris Geurts

nr 46
Generic Representations
Henri Achten

nr 47
Johann Santini Aichel: Architectuur en Ambiguiteit
Dirk De Meyer

nr 48
Concrete Behaviour in Multiaxial Compression
Erik van Geel

nr 49
Modelling Site Selection
Frank Witlox

nr 50
Ecolemma Model
Ferdinand Beetstra

nr 51
Conjoint Approaches to Developing Activity-Based Models
Donggen Wang

nr 52
On the Effectiveness of Ventilation
Ad Roos

nr 53
Conjoint Modeling Approaches for Residential Group preferences
Eric Molin

nr 54
Modelling Architectural Design Information by Features
Jos van Leeuwen

nr 55
A Spatial Decision Support System for the Planning of Retail and Service Facilities
Theo Arentze

nr 56
Integrated Lighting System Assistant
Ellie de Groot

nr 57
Ontwerpend Leren, Leren Ontwerpen
J.T. Boekholt

nr 58
Temporal Aspects of Theme Park Choice Behavior
Astrid Kemperman

nr 59
Ontwerp van een Geïndustrialiseerde Funderingswijze
Faas Moonen

nr 60
Merlin: A Decision Support System for Outdoor Leisure Planning
Manon van Middelkoop

nr 61
The Aura of Modernity
Jos Bosman

nr 62
Urban Form and Activity-Travel Patterns
Daniëlle Snellen

nr 63
Design Research in the Netherlands 2000
Henri Achten

nr 64
Computer Aided Dimensional Control in Building Construction
Rui Wu

nr 65
Beyond Sustainable Building
editors: Peter A. Erkelens
Sander de Jonge
August A.M. van Vliet
co-editor: Ruth J.G. Verhagen

nr 66
Das Globalrecyclingfähige Haus
Hans Löfflad

nr 67
Cool Schools for Hot Suburbs
René J. Dierkx

nr 68
A Bamboo Building Design Decision Support Tool
Fitri Mardjono

nr 69
Driving Rain on Building Envelopes
Fabien van Mook

nr 70
Heating Monumental Churches
Henk Schellen

nr 71
Van Woningverhuurder naar Aanbieder van Woongenot
Patrick Dogge

nr 72
Moisture Transfer Properties of Coated Gypsum
Emile Goossens

nr 73
Plybamboo Wall-Panels for Housing
Guillermo E. González-Beltrán

nr 74
The Future Site-Proceedings
Ger Maas
Frans van Gassel

nr 75
Radon transport in Autoclaved Aerated Concrete
Michel van der Pal

nr 76
The Reliability and Validity of Interactive Virtual Reality Computer Experiments
Amy Tan

nr 77
Measuring Housing Preferences Using Virtual Reality and Belief Networks
Maciej A. Orzechowski

nr 78
Computational Representations of Words and Associations in Architectural Design
Nicole Segers

nr 79
Measuring and Predicting Adaptation in Multidimensional Activity-Travel Patterns
Chang-Hyeon Joh

nr 80
Strategic Briefing
Fayez Al Hassan

nr 81
Well Being in Hospitals
Simona Di Cicco

nr 82
Solares Bauen: Implementierungs- und Umsetzungs-Aspekte in der Hochschulausbildung in Österreich
Gerhard Schuster

nr 83
Supporting Strategic Design of Workplace Environments with Case-Based Reasoning
Shauna Mallory-Hill

nr 84
ACCEL: A Tool for Supporting Concept Generation in the Early Design Phase
Maxim Ivashkov

nr 85
Brick-Mortar Interaction in Masonry under Compression
Ad Vermeltfoort

nr 86
Zelfredzaam Wonen
Guus van Vliet

nr 87
Een Ensemble met Grootstedelijke Allure
Jos Bosman
Hans Schippers

nr 88
On the Computation of Well-Structured Graphic Representations in Architectural Design
Henri Achten

nr 89
De Evolutie van een West-Afrikaanse Vernaculaire Architectuur
Wolf Schijns

nr 90
ROMBO Tactiek
Christoph Maria Ravesloot

nr 91
External Coupling between Building Energy Simulation and Computational Fluid Dynamics
Ery Djunaedy

nr 92
Design Research in the Netherlands 2005
editors: Henri Achten
Kees Dorst
Pieter Jan Stappers
Bauke de Vries

nr 93
Ein Modell zur Baulichen Transformation
Jalil H. Saber Zaimian

nr 94
Human Lighting Demands: Healthy Lighting in an Office Environment
Myriam Aries

nr 95
A Spatial Decision Support System for the Provision and Monitoring of Urban Greenspace
Claudia Pelizaro

nr 96
Leren Creëren
Adri Proveniers

nr 97
Simlandscape
Rob de Waard

nr 98
Design Team Communication
Ad den Otter

nr 99
Humaan-Ecologisch Georiënteerde Woningbouw
Juri Czabanowski

nr 100
Hambase
Martin de Wit

nr 101
Sound Transmission through Pipe Systems and into Building Structures
Susanne Bron-van der Jagt

nr 102
Het Bouwkundig Contrapunt
Jan Francis Boelen

nr 103
A Framework for a Multi-Agent Planning Support System
Dick Saarloos

nr 104
Bracing Steel Frames with Calcium Silicate Element Walls
Bright Mweene Ng'andu

nr 105
Naar een Nieuwe Houtskeletbouw
F.N.G. De Medts

nr 106 and 107
Niet gepubliceerd

nr 108
Geborgenheid
T.E.L. van Pinxteren

nr 109
Modelling Strategic Behaviour in Anticipation of Congestion
Qi Han

nr 110
Reflecties op het Woondomein
Fred Sanders

nr 111
On Assessment of Wind Comfort by Sand Erosion
Gábor Dezsö

nr 112
Bench Heating in Monumental Churches
Dionne Limpens-Neilen

nr 113
RE. Architecture
Ana Pereira Roders

nr 114
Toward Applicable Green Architecture
Usama El Fiky

nr 115
Knowledge Representation under Inherent Uncertainty in a Multi-Agent System for Land Use Planning
Liying Ma

nr 116
Integrated Heat Air and Moisture Modeling and Simulation
Jos van Schijndel

nr 117
Concrete Behaviour in Multiaxial Compression
J.P.W. Bongers

nr 118
The Image of the Urban Landscape
Ana Moya Pellitero

nr 119
The Self-Organizing City in Vietnam
Stephanie Geertman

nr 120
A Multi-Agent Planning Support System for Assessing Externalities of Urban Form Scenarios
Rachel Katoshevski-Cavari

nr 121
Den Schulbau Neu Denken, Fühlen und Wollen
Urs Christian Maurer-Dietrich

nr 122
Peter Eisenman Theories and Practices
Bernhard Kormoss

nr 123
User Simulation of Space Utilisation
Vincent Tabak

nr 125
In Search of a Complex System Model
Oswald Devisch

nr 126
Lighting at Work: Environmental Study of Direct Effects of Lighting Level and Spectrum on Psycho-Physiological Variables
Grazyna Górnicka

nr 127
Flanking Sound Transmission through Lightweight Framed Double Leaf Walls
Stefan Schoenwald

nr 128
Bounded Rationality and Spatio-Temporal Pedestrian Shopping Behavior
Wei Zhu

nr 129
Travel Information: Impact on Activity Travel Pattern
Zhongwei Sun

nr 130
Co-Simulation for Performance Prediction of Innovative Integrated Mechanical Energy Systems in Buildings
Marija Trčka

nr 131
Niet gepubliceerd

nr 132
Architectural Cue Model in Evacuation Simulation for Underground Space Design
Chengyu Sun

nr 133
Uncertainty and Sensitivity Analysis in Building Performance Simulation for Decision Support and Design Optimization
Christina Hopfe

nr 134
Facilitating Distributed Collaboration in the AEC/FM Sector Using Semantic Web Technologies
Jacob Beetz

nr 135
Circumferentially Adhesive Bonded Glass Panes for Bracing Steel Frame in Façades
Edwin Huveners

nr 136
Influence of Temperature on Concrete Beams Strengthened in Flexure with CFRP
Ernst-Lucas Klamer

nr 137
Sturen op Klantwaarde
Jos Smeets

nr 139
Lateral Behavior of Steel Frames with Discretely Connected Precast Concrete Infill Panels
Paul Teewen

nr 140
Integral Design Method in the Context of Sustainable Building Design
Perica Savanović

nr 141
Household Activity-Travel Behavior: Implementation of Within-Household Interactions
Renni Anggraini

nr 142
Design Research in the Netherlands 2010
Henri Achten

nr 143
Modelling Life Trajectories and Transport Mode Choice Using Bayesian Belief Networks
Marloes Verhoeven

nr 144
Assessing Construction Project Performance in Ghana
William Gyadu-Asiedu

nr 145
Empowering Seniors through Domotic Homes
Masi Mohammadi

nr 146
An Integral Design Concept for Ecological Self-Compacting Concrete
Martin Hunger

nr 147
Governing Multi-Actor Decision Processes in Dutch Industrial Area Redevelopment
Erik Blokhuis

nr 148
A Multifunctional Design Approach for Sustainable Concrete
Götz Hüsken

nr 149
Quality Monitoring in Infrastructural Design-Build Projects
Ruben Favié

nr 150
Assessment Matrix for Conservation of Valuable Timber Structures
Michael Abels

nr 151
Co-simulation of Building Energy Simulation and Computational Fluid Dynamics for Whole-Building Heat, Air and Moisture Engineering
Mohammad Mirsadeghi

nr 152
External Coupling of Building Energy Simulation and Building Element Heat, Air and Moisture Simulation
Daniel Cóstola

nr 153
Adaptive Decision Making In Multi-Stakeholder Retail Planning
Ingrid Janssen

nr 154
Landscape Generator
Kymo Slager

nr 155
Constraint Specification in Architecture
Remco Niemeijer

nr 156
A Need-Based Approach to Dynamic Activity Generation
Linda Nijland

nr 157
Modeling Office Firm Dynamics in an Agent-Based Micro Simulation Framework
Gustavo Garcia Manzato

nr 158
Lightweight Floor System for Vibration Comfort
Sander Zegers

nr 159
Aanpasbaarheid van de Draagstructuur
Roel Gijsbers

nr 160
'Village in the City' in Guangzhou, China
Yanliu Lin

nr 161
Climate Risk Assessment in Museums
Marco Martens

nr 162
Social Activity-Travel Patterns
Pauline van den Berg

nr 163
Sound Concentration Caused by Curved Surfaces
Martijn Vercammen

nr 164
Design of Environmentally Friendly Calcium Sulfate-Based Building Materials: Towards an Improved Indoor Air Quality
Qingliang Yu

nr 165
Beyond Uniform Thermal Comfort on the Effects of Non-Uniformity and Individual Physiology
Lisje Schellen

nr 166
Sustainable Residential Districts
Gaby Abdalla

nr 167
Towards a Performance Assessment Methodology using Computational Simulation for Air Distribution System Designs in Operating Rooms
Mônica do Amaral Melhado

nr 168
Strategic Decision Modeling in Brownfield Redevelopment
Brano Glumac

nr 169
Pamela: A Parking Analysis Model for Predicting Effects in Local Areas
Peter van der Waerden

nr 170
A Vision Driven Wayfinding Simulation-System Based on the Architectural Features Perceived in the Office Environment
Qunli Chen

nr 171
Measuring Mental Representations Underlying Activity-Travel Choices
Oliver Horeni

nr 172
Modelling the Effects of Social Networks on Activity and Travel Behaviour
Nicole Ronald

nr 173
Uncertainty Propagation and Sensitivity Analysis Techniques in Building Performance Simulation to Support Conceptual Building and System Design
Christian Struck

nr 174
Numerical Modeling of Micro-Scale Wind-Induced Pollutant Dispersion in the Built Environment
Pierre Gousseau

nr 175
Modeling Recreation Choices over the Family Lifecycle
Anna Beatriz Grigolon

nr 176
Experimental and Numerical Analysis of Mixing Ventilation at Laminar, Transitional and Turbulent Slot Reynolds Numbers
Twan van Hooff

nr 177
Collaborative Design Support: Workshops to Stimulate Interaction and Knowledge Exchange Between Practitioners
Emile M.C.J. Quanjel

nr 178
Future-Proof Platforms for Aging-in-Place
Michiel Brink

nr 179
Motivate: A Context-Aware Mobile Application for Physical Activity Promotion
Yuzhong Lin

nr 180
Experience the City: Analysis of Space-Time Behaviour and Spatial Learning
Anastasia Moiseeva

nr 181
Unbonded Post-Tensioned Shear Walls of Calcium Silicate Element Masonry
Lex van der Meer

nr 182
Construction and Demolition Waste Recycling into Innovative Building Materials for Sustainable Construction in Tanzania
Mwita M. Sabai

nr 183
Durability of Concrete with Emphasis on Chloride Migration
Przemysław Spiesz

nr 184
Computational Modeling of Urban Wind Flow and Natural Ventilation Potential of Buildings
Rubina Ramponi

nr 185
A Distributed Dynamic Simulation Mechanism for Buildings Automation and Control Systems
Azzedine Yahiaoui

nr 186
Modeling Cognitive Learning of Urban Networks in Daily Activity-Travel Behavior
Şehnaz Cenani Durmazoğlu

nr 187
Functionality and Adaptability of Design Solutions for Public Apartment Buildings in Ghana
Stephen Agyefi-Mensah

nr 188
A Construction Waste Generation Model for Developing Countries
Lilliana Abarca-Guerrero

nr 189
Synchronizing Networks: The Modeling of Supernetworks for Activity-Travel Behavior
Feixiong Liao

nr 190
Time and Money Allocation Decisions in Out-of-Home Leisure Activity Choices
Gamze Zeynep Dane

nr 191
How to Measure Added Value of CRE and Building Design
Rianne Appel-Meulenbroek

nr 192
Secondary Materials in Cement-Based Products: Treatment, Modeling and Environmental Interaction
Miruna Florea

nr 193
Concepts for the Robustness Improvement of Self-Compacting Concrete: Effects of Admixtures and Mixture Components on the Rheology and Early Hydration at Varying Temperatures
Wolfram Schmidt

nr 194
Modelling and Simulation of Virtual Natural Lighting Solutions in Buildings
Rizki A. Mangkuto

nr 195
Nano-Silica Production at Low Temperatures from the Dissolution of Olivine - Synthesis, Tailoring and Modelling
Alberto Lazaro Garcia

nr 196
Building Energy Simulation Based Assessment of Industrial Halls for Design Support
Bruno Lee

nr 197
Computational Performance Prediction of the Potential of Hybrid Adaptable Thermal Storage Concepts for Lightweight Low-Energy Houses
Pieter-Jan Hoes

nr 198
Application of Nano-Silica in Concrete
George Quercia Bianchi

nr 199
Dynamics of Social Networks and Activity Travel Behaviour
Fariya Sharmeen

nr 200
Building Structural Design Generation and Optimisation including Spatial Modification
Juan Manuel Davila Delgado

nr 201
Hydration and Thermal Decomposition of Cement/Calcium-Sulphate Based Materials
Ariën de Korte

nr 202
Republiek van Beelden:
De Politieke Werkingen van het Ontwerp in Regionale Planvorming
Bart de Zwart

nr 203
Effects of Energy Price Increases on Individual Activity-Travel Repertoires and Energy Consumption
Dujuan Yang

nr 204
Geometry and Ventilation:
Evaluation of the Leeward Sawtooth Roof Potential in the Natural Ventilation of Buildings
Jorge Isaac Perén Montero

nr 205
Computational Modelling of Evaporative Cooling as a Climate Change Adaptation Measure at the Spatial Scale of Buildings and Streets
Hamid Montazeri

nr 206
Local Buckling of Aluminium Beams in Fire Conditions
Ronald van der Meulen

nr 207
Historic Urban Landscapes:
Framing the Integration of Urban and Heritage Planning in Multilevel Governance
Loes Veldpaus

nr 208
Sustainable Transformation of the Cities:
Urban Design Pragmatics to Achieve a Sustainable City
Ernesto Antonio Zumelzu Scheel

nr 209
Development of Sustainable Protective Ultra-High Performance Fibre Reinforced Concrete (UHPFRC):
Design, Assessment and Modeling
Rui Yu

nr 210
Uncertainty in Modeling Activity-Travel Demand in Complex Uban Systems
Soora Rasouli

nr 211
Simulation-based Performance Assessment of Climate Adaptive Greenhouse Shells
Chul-sung Lee

nr 212
Green Cities:
Modelling the Spatial Transformation of the Urban Environment using Renewable Energy Technologies
Saleh Mohammadi

nr 213
A Bounded Rationality Model of Short and Long-Term Dynamics of Activity-Travel Behavior
Ifigeneia Psarra

nr 214
Effects of Pricing Strategies on Dynamic Repertoires of Activity-Travel Behaviour
Elaheh Khademi

nr 215
Handstorm Principles for Creative and Collaborative Working
Frans van Gassel

nr 216
Light Conditions in Nursing Homes: Visual Comfort and Visual Functioning of Residents
Marianne M. Sinoo

nr 217
Woonsporen: De Sociale en Ruimtelijke Biografie van een Stedelijk Bouwblok in de Amsterdamse Transvaalbuurt
Hüseyin Hüsnü Yegenoglu

nr 218
Studies on User Control in Ambient Intelligent Systems
Berent Willem Meerbeek

nr 219
Daily Livings in a Smart Home: Users' Living Preference Modeling of Smart Homes
Erfaneh Allameh

nr 220
Smart Home Design: Spatial Preference Modeling of Smart Homes
Mohammadali Heidari Jozam

nr 221
Wonen: Discoursen, Praktijken, Perspectieven
Jos Smeets

nr 222
Personal Control over Indoor Climate in Offices: Impact on Comfort, Health and Productivity
Atze Christiaan Boerstra

nr 223
Personalized Route Finding in Multimodal Transportation Networks
Jianwe Zhang

nr 224
The Design of an Adaptive Healing Room for Stroke Patients
Elke Daemen

nr 225
Experimental and Numerical Analysis of Climate Change Induced Risks to Historic Buildings and Collections
Zara Huijbregts

nr 226
Wind Flow Modeling in Urban Areas Through Experimental and Numerical Techniques
Alessio Ricci

nr 227
Clever Climate Control for Culture: Energy Efficient Indoor Climate Control Strategies for Museums Respecting Collection Preservation and Thermal Comfort of Visitors
Rick Kramer

nr 228
Fatigue Life Estimation of Metal Structures Based on Damage Modeling
Sarmediran Silitonga

nr 229
A multi-agents and occupancy based strategy for energy management and process control on the room-level
Timilehin Moses Labeodan

nr 230
Environmental assessment of Building Integrated Photovoltaics: Numerical and Experimental Carrying Capacity Based Approach
Michiel Ritzen

nr 231
Performance of Admixture and Secondary Minerals in Alkali Activated Concrete: Sustaining a Concrete Future
Arno Keulen

nr 232
World Heritage Cities and Sustainable Urban Development:
Bridging Global and Local Levels in Monitoring the Sustainable Urban Development of World Heritage Cities
Paloma C. Guzman Molina

nr 233
Stage Acoustics and Sound Exposure in Performance and Rehearsal Spaces for Orchestras:
Methods for Physical Measurements
Remy Wenmaekers

nr 234
Municipal Solid Waste Incineration (MSWI) Bottom Ash:
From Waste to Value Characterization, Treatments and Application
Pei Tang

nr 235
Large Eddy Simulations Applied to Wind Loading and Pollutant Dispersion
Mattia Ricci

nr 236
Alkali Activated Slag-Fly Ash Binders: Design, Modeling and Application
Xu Gao

nr 237
Sodium Carbonate Activated Slag: Reaction Analysis, Microstructural Modification & Engineering Application
Bo Yuan

nr 238
Shopping Behavior in Malls
Widiyani

nr 239
Smart Grid-Building Energy Interactions: Demand Side Power Flexibility in Office Buildings
Kennedy Otieno Aduda

nr 240
Modeling Taxis Dynamic Behavior in Uncertain Urban Environments
Zheng Zhong

nr 241
Gap-Theoretical Analyses of Residential Satisfaction and Intention to Move
Wen Jiang

nr 242
Travel Satisfaction and Subjective Well-Being: A Behavioral Modeling Perspective
Yanan Gao

nr 243
Building Energy Modelling to Support the Commissioning of Holistic Data Centre Operation
Vojtech Zavrel

nr 244
Regret-Based Travel Behavior Modeling: An Extended Framework
Sunghoon Jang

nr 245
Towards Robust Low-Energy Houses: A Computational Approach for Performance Robustness Assessment using Scenario Analysis
Rajesh Reddy Kotireddy

nr 246
Development of sustainable and functionalized inorganic binder-biofiber composites
Guillaume Doudart de la Grée

nr 247
A Multiscale Analysis of the Urban Heat Island Effect: From City Averaged Temperatures to the Energy Demand of Individual Buildings
Yasin Toparlar

nr 248
Design Method for Adaptive Daylight Systems for buildings covered by large (span) roofs
Florian Heinzelmann

nr 249
Hardening, high-temperature resistance and acid resistance of one-part geopolymers
Patrick Sturm

nr 250
Effects of the built environment on dynamic repertoires of activity-travel behaviour
Aida Pontes de Aquino

nr 251
Modeling for auralization of urban environments: Incorporation of directivity in sound propagation and analysis of a framework for auralizing a car pass-by
Fotis Georgiou

nr 252
Wind Loads on Heliostats and Photovoltaic Trackers
Andreas Pfahl

nr 253
Approaches for computational performance optimization of innovative adaptive façade concepts
Roel Loonen

nr 254
Multi-scale FEM-DEM Model for Granular Materials: Micro-scale boundary conditions, Statics, and Dynamics
Jiadun Liu

nr 255
Bending Moment - Shear Force Interaction of Rolled I-Shaped Steel Sections
Rianne Willie Adriana Dekker

nr 256
Paralympic tandem cycling and handcycling: Computational and wind tunnel analysis of aerodynamic performance
Paul Fionn Mannion

nr 257
Experimental characterization and numerical modelling of 3D printed concrete: Controlling structural behaviour in the fresh and hardened state
Robert Johannes Maria Wolfs

nr 258
Requirement checking in the building industry: Enabling modularized and extensible requirement checking systems based on semantic web technologies
Chi Zhang

nr 259
A Sustainable Industrial Site Redevelopment Planning Support System
Tong Wang

nr 260
Efficient storage and retrieval of detailed building models: Multi-disciplinary and long-term use of geometric and semantic construction information
Thomas Ferdinand Krijnen

nr 261
The users' value of business center concepts for knowledge sharing and networking behavior within and between organizations
Minou Weijs-Perrée

nr 262
Characterization and improvement of aerodynamic performance of vertical axis wind turbines using computational fluid dynamics (CFD)
Abdolrahim Rezaeiha

nr 263
In-situ characterization of the acoustic impedance of vegetated roofs
Chang Liu

nr 264
Occupancy-based lighting control: Developing an energy saving strategy that ensures office workers' comfort
Christel de Bakker

nr 265
Stakeholders-Oriented Spatial Decision Support System
Cahyono Susetyo

nr 266
Climate-induced damage in oak museum objects
Rianne Aleida Luimes

nr 267
Towards individual thermal comfort: Model predictive personalized control of heating systems
Katarina Katic

nr 268
Modelling and Measuring Quality of Urban Life: Housing, Neighborhood, Transport and Job
Lida Aminian

nr 269
Optimization of an aquifer thermal energy storage system through integrated modelling of aquifer, HVAC systems and building
Basar Bozkaya

nr 270
Numerical modeling for urban sound propagation: developments in wave-based and energy-based methods
Raúl Pagán Muñoz

nr 271
Lighting in multi-user office environments: improving employee wellbeing through personal control
Sanae van der Vleuten-Chraibi

nr 272
A strategy for fit-for-purpose occupant behavior modelling in building energy and comfort performance simulation
Isabella I. Gaetani dell'Aquila d'Aragona

nr 273
Een architectuurhistorische waardestelling van naoorlogse woonwijken in Nederland: Het voorbeeld van de Westelijke Tuinsteden in Amsterdam
Eleonore Henriette Marie Mens

nr 274
Job-Housing Co-Dependent Mobility Decisions in Life Trajectories
Jia Guo

nr 275
A user-oriented focus to create healthcare facilities: decision making on strategic values
Emilia Rosalia Catharina Maria Huisman

nr 276
Dynamics of plane impinging jets at moderate Reynolds numbers – with applications to air curtains
Adelya Khayrullina

nr 277
Valorization of Municipal Solid Waste Incineration Bottom Ash - Chemical Nature, Leachability and Treatments of Hazardous Elements
Qadeer Alam

nr 278
Treatments and valorization of MSWI bottom ash - application in cement-based materials
Veronica Caprai

nr 279
Personal lighting conditions of office workers - input for intelligent systems to optimize subjective alertness
Juliëtte van Duijnhoven

nr 280
Social influence effects in tourism travel: air trip itinerary and destination choices
Xiaofeng Pan

nr 281
Advancing Post-War Housing: Integrating Heritage Impact, Environmental Impact, Hygrothermal Risk and Costs in Renovation Design Decisions
Lisanne Claartje Havinga

nr 282
Impact resistant ultra-high performance fibre reinforced concrete: materials, components and properties
Peipeng Li

nr 283
Demand-driven Science Parks: The Perceived Benefits and Trade-offs of Tenant Firms with regard to Science Park Attributes
Wei Keat Benny Ng

nr 284
Raise the lantern; how light can help to maintain a healthy and safe hospital environment focusing on nurses
Maria Petronella Johanna Aarts

nr 285
Modelling Learning and Dynamic Route and Parking Choice Behaviour under Uncertainty
Elaine Cristina Schneider de Carvalho

nr 286
Identifying indoor local microclimates for safekeeping of cultural heritage
Karin Kompatscher

nr 287
Probabilistic modeling of fatigue resistance for welded and riveted bridge details. Resistance models and estimation of uncertainty.
Davide Leonetti

nr 288
Performance of Layered UHPFRC under Static and Dynamic Loads: Effects of steel fibers, coarse aggregates and layered structures
Yangyueye Cao

nr 289
Photocatalytic abatement of the nitrogen oxide pollution: synthesis, application and long-term evaluation of titania-silica composites
Yuri Hendrix

nr 290
Assessing knowledge adoption in post-disaster reconstruction: Understanding the impact of hazard-resistant construction knowledge on reconstruction processes of self-recovering communities in Nepal and the Philippines
Eefje Hendriks

nr 291
Locating electric vehicle charging stations: A multi-agent based dynamic simulation
Seheon Kim

nr 292
De invloed van Lean Management op de beheersing van het bouwproces
Wim van den Bouwhuijsen

nr 293
Neighborhood Environment and Physical Activity of Older Adults
Zhengying Liu

nr 294
Practical and continuous luminance distribution measurements for lighting quality
Thijs Willem Kruisselbrink

nr 295
Auditory Distraction in Open-Plan Study Environments in Higher Education
Pieternella Elizabeth Braat-Eggen

nr 296
Exploring the effect of the sound environment on nurses' task performance: an applied approach focusing on prospective memory
Jikke Reinten

nr 297
Design and performance of water resistant cementitious materials– Mechanisms, evaluation and applications
Zhengyao Qu

nr 298
Design Optimization of Seasonal Thermal Energy Storage Integrated District Heating and Cooling System: A Modeling and Simulation Approach
Luyi Xu

nr 299
Land use and transport: Integrated approaches for planning and management
Zhongqi Wang

nr 300
Multi-disciplinary optimization of building spatial designs: co-evolutionary design process simulations, evolutionary algorithms, hybrid approaches
Sjonnie Boonstra

nr 301
Modeling the spatial and temporal relation between urban land use, temperature, and energy demand
Hung-Chu Chen

nr 302
Seismic retrofitting of masonry walls with flexible deep mounted CFRP strips
Ömer Serhat Türkmen

nr 303
Coupled Aerostructural Shape and Topology Optimization of Horizontal-Axis Wind Turbine Rotor Blades
Zhijun Wang

nr 304
Valorization of Recycled Waste Glass and Converter Steel Slag as Ingredients for Building Materials: Hydration and Carbonation Studies
Gang Liu

nr 305
Low-Carbon City Development based on Land Use Planning
Gengzhe Wang

nr 306
Sustainable energy transition scenario analysis for buildings and neighborhoods - Data driven optimization
Shalika Saubhagya Wickramarachchi Walker

nr 307
In-between living and manufactured: an exploratory study on biobuilding components for building design
Berrak Kirbas Akyurek

nr 308
Development of alternative cementitious binders and functionalized materials: design, performance and durability
Anna Monika Kaja

nr 309
Development a morphological approach for interactive kinetic façade design: Improving multiple occupants' visual comfort
Seyed Morteza Hosseini

nr 310
PV in urban context: modeling and simulation strategies for analyzing the performance of shaded PV systems
Ádám Bognár

nr 311
Life Trajectory, Household Car Ownership Dynamics and Home Renewable Energy Equipment Adoption
Gaofeng Gu

nr 312
Impact of Street-Scale Built Environment on Walking/Cycling around Metro Stations
Yanan Liu

nr 313
Advances in Urban Traffic Network Equilibrium Models and Algorithms
Dong Wang

nr 314
Development of an uncertainty analysis framework for model-based consequential life cycle assessment: application to activity-based modelling and life cycle assessment of multimodal mobility
Paul Martin Baustert

nr 315
Variable stiffness and damping structural joints for semi-active vibration control
Qinyu Wang

nr 316
Understanding Carsharing-Facilitating Neighborhood Preferences
Juan Wang

nr 317
Dynamic alignment of Corporate Real Estate to business strategies: An empirical analysis using historical data and in-depth modelling of decision making
Howard Cooke

nr 318
Local People Matter: Towards participatory governance of cultural heritage in China
Ji Li

nr 319
Walkability and Walkable Healthy Neighborhoods
Bojing Liao

nr 320
Light directionality in design of healthy offices: exploration of two methods
Parisa Khademagha

nr 321
Room acoustic modeling with the time-domain discontinuous Galerkin method
Huiqing Wang

nr 322
Sustainable insulating lightweight materials for enhancing indoor building performance: miscanthus, aerogel and nano-silica
Yuxuan Chen

nr 323
Computational analysis of the impact of façade geometrical details on wind flow and pollutant dispersion
Xing Zheng

nr 324
Analysis of urban wind energy potential around high-rise buildings in close proximity using computational fluid dynamics
Yu-Hsuan Jang

nr 325
A new approach to automated energy performance and fault detection and diagnosis of HVAC systems: Development of the 4S3F method
Arie Taal

nr 326
Innovative Admixtures for Modifying Viscosity and Volume Change of Cement Composites
Hossein Karimi

nr 327
Towards houses with low grid dependency: A simulation-based design optimization approach
Zahra Mohammadi

nr 328
Activation of demand flexibility for heating systems in buildings: Real-life demonstration of optimal control for power-to-heat and thermal energy storage
Christian Finck

nr 329
A computational framework for analysis and optimisation of automated solar shading systems
Samuel B. de Vries

nr 330
Challenges and potential solutions for cultural heritage adaptive reuse: a comparative study employing the Historic Urban Landscape approach
Nadia Pintossi

nr 331
Shared control in office lighting systems
Tatiana Aleksandrovna Lashina

nr 332
Comfort in Urban Public Spaces
You Peng

nr 333
Numerical modelling of metal soap formation in historical oil paintings
Gerardus Johannes Anna Maria Eumelen

nr 334
A transdisciplinary decision-making approach to food-water-energy nexus: A guide towards sustainable development
Maryam Ghodsvali

nr 335
Numerical modelling of transient low-frequency sound propagation and vibration in buildings
Indra Sihar

nr 336
Characterization of impact sound from lightweight joist floors
Yi Qin

nr 337
Cities for Children: Supporting Children and Caregivers in Participatory Urban Planning
Özlemnur Ataol

nr 338
Engaging the unengaged: Exploring citizen participation in nature-based solutions in China
Li Dai

nr 339
Municipal Solid Waste Incineration Residues: analysis, treatments, and applications
Ekaterina Loginova

nr 340
Enhancing the Uptake of Nature-Based Solutions in Urban Settings: An Information Systems Approach
Shahryar Ershad Sarabi

nr 341
Work Schedule Arrangements in Two-Adult Households with Children
Bilin Han

nr 342
Increasing awareness of urban cultural heritage using digital technologies: empirical design and analysis of a new multi-media web platform
Benshuo Wang

nr 343
Mechanical and physical properties of fibre-cement composites using alternative natural fibres
Katerina Kochova

nr 344
Numerical and experimental investigation of urban microclimate in a real compact heterogeneous urban area
Nestoras Antoniou

nr 345
Examining in-class activities to facilitate academic achievement in higher education: A framework for optimal indoor environmental conditions
Henk W. Brink

nr 346
High-temperature resistant geopolymers: composition, microstructure and performance
Kinga Malgorzata Klima

nr 347
Individual and household decision-making in shared parking
Qianqian Yan

nr 348
In-situ formation of LDHs in Alkali activated binders
Tao Liu

nr 349
Condition assessment of concrete sewer pipes through an integrated experimental-numerical approach
Irene C. Scheperboer

nr 350
In situ PU-based characterization of sound absorbing materials for room acoustic modeling purposes
Baltazar Briere de La Hosseraye

nr 351
Uncertainty analysis and management in building energy data mining: A bottom-up approach considering the temporal and spatial aspect of data
Waqas Khan

nr 352
Personalized Heating Control Systems to improve thermal comfort and reduce energy consumption
Michal Veselý

nr 353
Restorative value of the urban greenscape: Urban residential streets as restorative environments
Robert P. van Dongen

nr 354
Urban ventilation and the compact Mediterranean city: numerical investigations of the dynamic relationships between density, morphology and wind flow
Olga Palusci

nr 355
Data science for buildings: a multi-scale approach bridging occupants to smart-city energy planning
Julien Leprince

nr 356
Class Association Rule Models for Predicting Transportation Mode Choice
Jiajia Zhang

nr 357
Acceptance and use of autonomous vehicles
Zhihui Tian

nr 358
Consumer Acceptance of Crowdshipping Services
Chenyu Wang

nr 359
Determinants of habitual participation in leisure-time physical activity and active travel in life trajectories
Xiaoyue Chen

nr 360
Analysis of Citizens' Motivation and Intention Using Modern Information Technology in Urban Planning Public Participation
Wenshu Li

nr 361
Linking smart and physical port cities. Port-city interface areas: from obsolete/isolated to smart environments.
Mercè de Miguel Capdevila

nr 362
Assessment and improvement of indoor thermal comfort and energy demand of Chinese heritage apartment buildings under climate change
Muxi Lei

nr 363
Indoor airflow and heat transfer in a cross-ventilated generic building: wind tunnel experiments and computational fluid dynamics analyses
Katarina Kosutova

nr 364
A Robotic Construction Simulation Platform for Light-weight Prefabricated Structures.
Aiyu Zhu

nr 365
Lifetime prediction of vertical-axis wind turbines based on CFD simulations and high-cycle fatigue modeling
Feiyu Geng

nr 366
Computational modeling of convective heat transfer at building surfaces
Samy Iousef

nr 367
Numerical simulation of the atmospheric boundary layer with application to natural ventilation
Vasaturo Raffaele

nr 368
Bouwen zonder scrupules. De Nederlandse bouwnijverheid tijdens de bezetting en de eerste jaren van wederopbouw (1940-1950)
Geert-Jan Mellink

nr 369
Factors Promoting a Positive Experienced Neighborhood Public Space--A Virtual Environment-based analysis.
Yuwen Zhao

nr 370
Place quality making in high-speed railway station areas. Devising place quality indicators for urban design, beyond the transport-land use divide.
Jinglun Du

Urban surfaces such as streets, parking lots and roofs are regarded as critical channels of aqueous contaminant transport. Various pollutants such as nitrate, phosphate, and heavy metals are carried by stormwater runoff to enter nearby rivers during the rainy season. Phosphorus (P) is one of the main pollutants in stormwater runoff from farmland, industry, domestic sewage and atmospheric pollution sediments, etc. The pollution level of the water body will be reduced if pollutants from stormwater runoff can be effectively removed by adsorption and physical filtration by pervious pavements. Conventional pervious concrete needs improvements to meet the requirements of sustainable and ecological cities. This work aims to develop bio-based adsorptive concretes that can reduce accelerated stormwater runoff and remove P from stormwater runoff to improve underlying water quality. The adopted research idea is to replace conventional cementitious composites with highly adsorptive materials to produce porous bio-based adsorptive concrete, and the investigated characteristics focus on adsorptive cementitious composites, performance evaluation and durability of bio-based adsorptive concrete.

DEPARTMENT OF THE BUILT ENVIRONMENT

TU/e EINDHOVEN UNIVERSITY OF TECHNOLOGY